EXPERIMENTAL AND NUMERICAL STUDY OF MICROSTRUCTURE FORMATION AND THE ORIGIN OF CRYSTALLOGRAPHIC MISORIENTATION IN Al-Zn-Si ALLOY COATINGS

THÈSE N^O 3863 (2007)

PRÉSENTÉE LE 20 JUILLET 2007

À LA FACULTÉ DES SCIENCES ET TECHNIQUES DE L'INGÉNIEUR

Laboratoire de simulation des matériaux

PROGRAMME DOCTORAL EN SCIENCE ET GÉNIE DES MATÉRIAUX

ÉCOLE POLYTECHNIQUE FÉDÉRALE DE LAUSANNE

POUR L'OBTENTION DU GRADE DE DOCTEUR ÈS SCIENCES

PAR

Christoph NIEDERBERGER

ingénieur en scences des matériaux diplômé EPF
de nationalité suisse et originaire de Wolfenschiessen (NW)

acceptée sur proposition du jury:

Prof. H. J. Mathieu, président du jury
Dr A. Jacot, Dr J. Michler, directeurs de thèse
Prof. J. Dantzig, rapporteur
Prof. P. Stadelmann, rapporteur
Dr A. Sémoroz, rapporteur

EPFL

ÉCOLE POLYTECHNIQUE
FÉDÉRALE DE LAUSANNE

Suisse
2007

CONTENTS

ABSTRACT

Al-Zn-Si alloy coatings are widely used for the corrosion protection of steel sheets. In addition to the favorable corrosion properties, the Al-43wt%Zn-1.6wt%Si coatings present several features which are of metallurgical interest. The first one is their surface appearance dominated by the typical spangle morphology exhibiting dull and shiny areas on the coating surface. Further on, the dendrite tips do apparently not grow along the $\langle 100 \rangle$ crystallographic directions that are typical for *fcc*-metals, but rather along directions in between $\langle 100 \rangle$ and $\langle 110 \rangle$. In addition, continuous variations of the crystallographic orientation, up to 35°, are observed within individual grains of Al-Zn-Si coatings [Sémoroz1 01].

The objective of the present study is to establish a better understanding of the microstructure development which is responsible for the formation of both the characteristic spangle pattern and the important variations of crystallographic orientation within the grains. In order to elucidate these questions, the present study includes three main axes, (i) a detailed microstructure characterization of industrially solidified samples, (ii) modeling work which encompasses microstructure modeling by the phase field method and a geometrical model, as well as the determination of the solid-liquid interfacial energy anisotropy by an inverse method, and (iii) re-solidification experiments aimed at studying the behavior of Al-Zn-Si layers under modified solidification conditions.

The results show that the dendrite network spreads quickly in the coating layer at a temperature between 530 to 535°C. During growth, the dendrite tips are separated from the confining boundaries by a thin, solute-rich liquid film. It was found that the preferred dendrite growth directions are in between $\langle 100 \rangle$ and $\langle 110 \rangle$, 28.5° from $\langle 100 \rangle$. Further on, a mathematical expression for the interfacial energy anisotropy of the considered alloy has been determined. The combination of the geometrical model and surface topography measurements allowed concluding that the spangle pattern is due to preferential dendrite growth along one of the two boundaries confining the melt layer. In addition, the new experimental evidence forced to discard the mechanisms previously proposed for the formation of intragranular crystallographic misorientations. The experimental findings acquired during this study indicate that the solidification shrinkage occurring in the area of the grain envelope is the driving force for the formation of the observed intragranular

misorientations. The solidification shrinkage leads to the development of tensile stresses in the oxide film covering the coating while it solidifies. These stresses apply on the dendrite network and lead to plastic deformation in the tip area of the growing dendrite arms.

Keywords: microstructure formation, dendrite, Al-Zn-Si, phase field method, crystallographic misorientation, solidification shrinkage

VERSION ABREGEE

Des revêtements d'Al-43Zn-1.6Si (%poids) sont appliqués couramment sur les tôles d'acier pour les protéger contre la corrosion. En plus de leurs bonnes propriétés protectrices, les revêtements d'Al-Zn-Si présentent d'autres caractéristiques intéressantes du point de vue métallurgique. La première est une apparence de surface typique qui présente une alternance de secteurs brillants et mats à la surface des revêtements. Une autre particularité de l'alliage Al-Zn-Si est une croissance dendritique selon des directions cristallographiques entre ⟨100⟩ et ⟨110⟩ au lieu de ⟨100⟩. Une autre caractéristique intéressante est la présence d'importantes variations d'orientation cristallographique au sein des grains. Des variations d'orientation continues et cumulatives pouvant atteindre jusqu'à 35° dans un même grain [Sémoroz1 01].

L'objectif de cette étude est d'améliorer la compréhension de la formation de la microstructure dans les revêtements d'Al-Zn-Si. Les phénomènes décrits ci-dessus sont en effet étroitement liés au développement de la microstructure. Dans l'intention d'apporter une réponse aux questions posées, la présente étude est articulée autour des trois axes suivants: (i) la caractérisation détaillée de la microstructure d'échantillons industriels de revêtement d'Al-Zn-Si, (ii) la simulation de la formation de la microstructure par un modèle de champ de phase, un modèle géométrique et des simulations inverses pour la détermination d'une fonction d'anisotropie de l'énergie d'interface solide-liquide, et (iii) des expériences de re-solidification ayant pour objectif l'étude du comportement de revêtements d'Al-Zn-Si sous des conditions de solidification modifiées.

Les expériences réalisées montrent que le réseau dendritique se propage rapidement dans le revêtement à une température entre 530 et 535°C. Pendant la croissance, les pointes de dendrite sont séparées des frontières du revêtement par un film de liquide riche en soluté. Les simulations inverses on montré que les directions de croissance préférées des pointes de dendrite sont situées entre ⟨100⟩ et ⟨110⟩, à 28.5° de ⟨100⟩, et ont permis de déterminer une expression mathématique pour l'anisotropie de l'énergie d'interface solide-liquide. Les résultats du modèle géométrique et des mesures de topographie ont permis de conclure que l'apparence de surface typique est due à la croissance préférentielle des bras de dendrite le long d'une des deux frontières qui limitent le revêtement. En outre, de nouveaux résultats expérimentaux ont permis de réfuter les mécanismes préalablement

proposés pour la formation des désorientations cristallographiques intragranulaires. Les résultats expérimentaux acquis pendant cette étude indiquent que le retrait de solidification accumulé dans la région de l'enveloppe de grain est probablement la force motrice pour la formation des désorientations intragranulaires. Le retrait de solidification provoque des contraintes de traction dans le film d'oxyde qui couvre le revêtement pendant la solidification. Ces contraintes appliquées au réseau dendritique conduisent à une déformation plastique dans la région des pointes de dendrites en croissance, générant ainsi des désorientations.

keywords: formation de microstructure, dendrite, Al-Zn-Si, methode de champ de phase, desorientation cristallographique, retrait de solidification

ACKNOWLEDGEMENTS

CHAPTER I

INTRODUCTION

Virtually all metal processing starts at the liquid state since metals and alloys are generally smelted form ore. The liquid metal is then solidified by continuous or semi-continuous casting processes into slabs and billets. These semi-finished products are subsequently transformed to finished or semi-finished products either by mechanical processing or by re-melting and casting into the final shape. In any case, solidification is an essential step in the processing of metallic materials. The resulting solidification microstructure influences the properties of the material and often also the performance of the final product. Defects formed during the solidification step can limit the properties of the material. Such defects include porosities, hot cracking, oxide inclusions, the presence of undesired phases, macrosegregation and depending on the application also variations of the crystallographic orientation within individual grains.

Variations of the crystallographic orientation within a given grain is a phenomenon which is relatively common in solidification microstructures. In some cases, such intragranular misorientations can affect the properties and performance of the final component. A typical example are single crystal turbine blades solidified from Ni-base superalloys, which are used in the first turbine stages of aeronautic and land-based gas turbines. In these single grain components, variations of the crystallographic orientation of

5-10° are commonly observed between the bottom and the top of the blade. The variations of orientation lead to subgrain or low-angle boundaries in between areas of different orientation. The presence of subgrains boundaries has a detrimental effect on the mechanical properties of the material by facilitating creep through diffusion in subgrain-boundaries. Moreover, the presence of subgrains leads to thermomechanical stresses under service conditions due to the pronounced anisotropy of the elastic properties of the crystal. Another alloy system in which substantial intragranular misorientations have been discovered recently are Al-Zn-Si coatings (nominal composition: Al-43.4Zn-1.6Si in wt.% or Al-24Zn-2Si in at.%). Misorientations of up to 35° have been reported across individual grains in Al-Zn-Si coatings of coarse grain structure [Sémoroz1 01]. Both in Al-Zn-Si coatings and superalloys, the knowledge about the mechanisms leading to the formation of such intragranular crystallographic misorientations is only fragmentary. For the present study of the intergranular misorientations, the Al-Zn-Si coating system has been selected as a model system since it presents very pronounced misorientations that can be readily analyzed by electron backscatter diffraction (EBSD). The almost two dimensional nature of the Al-Zn-Si coatings avoids the complex characterization of 3D structures.

Al-Zn-Si coatings are applied to steel substrates by the so-called hot-dipping process. In this process, a layer of Al-Zn-Si melt is applied on a steel sheet and subsequently solidified. In the solidification of alloys, the solid and liquid phases can coexist in equilibrium in a certain temperature interval. For most solidification processes, this leads to the formation of a two phase region composed of solid dendrites and interdendritic liquid. The dendrite growth is often followed by the formation of other solid phases by eutectic or peritectic reactions. The microstructure formation in Al-Zn-Si coatings is dominated by the growth of Al-rich dendrite arms into the undercooled melt layer. As already mentioned by Sémoroz et al., the formation of intragranular misorientations is likely to be closely related to the development of the microstructure in the coating layer. Numerous aspects of the microstructure formation of Al-Zn-Si coatings have not been studied yet or only partially. These aspects include:

- the selection of the dendrite growth directions in the confined melt layer of the coating.

- the geometry and kinetics of the dendrite tips interacting with the confining boundaries.

- the formation of the topography and surface appearance on the free surface of the

coating.

■ the distribution of the solute in the coating layer.

■ the effect of the thermomechanical stresses developing between coating and substrate during solidification and cooling.

■ and finally the mechanisms that lead to the formation of crystallographic misorientations within the grains of the coating which have not been clearly identified.

The goal of the present dissertation is to propose answers to these questions. The methods which have been applied for this purpose can be divided in the three following categories: characterization of the coatings, modeling, and re-solidification experiments. The characterization of the coatings after solidification and cooling is a key element for the discussion of the formation of the microstructure and the intragranular misorientations during solidification. The different microstructural constituents have been characterized by metallographic methods including optical microscopy, scanning electron microscopy (SEM) and transmission electron microscopy (TEM). The distribution of the chemical species within the coating layer has been analyzed by X-ray spectroscopy (WDS and EDS) as well as glow discharge optical emission spectroscopy (GD-OES). The surface of the Al-Zn-Si coatings has been assessed with respect to their surface topography by laser profilometry and atomic force microscopy (AFM). Finally, the intragranular crystallographic misorientations have been studied in detail by EBSD, which established itself as the method of choice for crystal orientation determination in materials science within the last 15 years.

The modeling activities pursued during this project can be divided in three topics. First, an inverse method approach has been developed for the determination of a function describing the anisotropy of the solid-liquid interfacial energy from the dendrite growth directions that are apparent in the Al-Zn-Si coatings. Further on, the inverse method allows an accurate determination of the preferred growth directions in the Al-Zn-Si system. Even though the determination of an interfacial energy function does not directly contribute to the comprehension of the microstructure formation in itself, the anisotropy function is required for 3D microstructure simulation in this alloy system by numerical methods such as the phase field method. As a second modeling activity, phase field simulations have been conducted in order to study the interaction of the dendrite tips with the two boundaries confining the melt layer. These simulations, which were finally only conducted

in 2D domains for computational reasons, allowed studying qualitatively and quantitatively the tip morphology and kinetics in the presence of a boundary. As a third modeling technique, a geometrical model which describes the development of the dendrite network in the coating layer on the scale of the grain has been developed. This last modeling activity also provides indications about the origins of the typical spangle morphology that is visible on the surface of Al-Zn-Si coatings.

In order to complete the microstructure analysis of the received industrial Al-Zn-Si coating samples and the simulations of the formation of the dendrite network, re-solidification experiments have been conducted. The experiments consisted of re-melting and re-solidifying substrate-coating composites under various solidification conditions, especially with respect to the thermomechanical stresses, the cooling rate and the presence or absence of a free coating surface. The re-solidification experiments served to study the influence of these parameters on the intragranular misorientations. Based on their results, some aspects of the microstructure formation as well as the possible mechanisms leading to the intragranular misorienations are discussed.

In order to guide the reader through this dissertation, the classical sequence of chapters, i.e. *Introduction*, *Literature survey*, *Methods*, *Results*, *Discussion* and *Conclusion* has been chosen. The chapters *Methods* and *Results* are both divided in three sections: *Characterization of coatings*, *Modeling* and *Solidification experiments* which correspond mutually. The chapter *Discussion* is, however, divided in the two thematic sections *Microstructure formation* and *Mechanism leading to intragranular misorientations* in order to allow for the discussion of the intraganular misorientations to benefits from the prior detailed discussion of the microstructure formation. This structure has also been adopted because the formation of microstructure and intragranular misorientations can only be addressed in a discussion including both experimental and simulation results.

CHAPTER II

LITERATURE SURVEY

A literature overview introducing into the solidification of Al-Zn-Si coatings is given in this chapter. The objective is to summarize the most important information concerning the microstructure formation and the application of Al-Zn-Si coatings. Further on, the basics of dendrite growth and of the influence of the interfacial energy anisotropy on dendrite growth are recalled. Finally, the state of the literature on intragranular crystallographic misorientations is presented.

2.1 Al-Zn-Si coatings

2.1.1 Corrosion protection by hot dip coatings

Protective coatings are routinely applied to low-carbon steel sheets in order to increase their resistance to corrosion. Steel sheets are particularly prone to corrosion in the presence of oxygen and moisture due to their large surface to volume ratio. The commercially most important processing techniques to protect steel sheets exposed to corrosive environments is the application of zinc alloy and aluminum alloy coatings by the so-called hot dipping process [Marder 00]. Coatings of pure Zn and lowly alloyed Zn protect the steel mainly due to a sacrificial effect. As zinc is considerably more

electronegative than steel, the zinc coating corrodes preferentially when in contact with an electrolyte and thereby protects the steel from corrosion. This type of sacrificial or cathodic protection is still effective even when part of the steel substrate is exposed to the electrolyte, e.g. after mechanical damage of the coating [Porter 91]. However, when exposed to corrosive environment, Zn coatings dissolve continuously and may lead to the corrosion of the steel once the coating has vanished.

Al coatings on the other hand offer a much higher durability as Al inherently resists to corrosion in many environments through the formation of passivating film of Al_2O_3 on its surface. However, Al coatings do not offer sacrificial or cathodic protection. If the coating is damaged mechanically, e.g. through the presence of scratches, the corrosion localizes at the now exposed steel surface. In order to combine the complementary properties of Zn and Al, Al-Zn alloy coatings have been developed and are now widely used in industry. The most widespread compositions are Zn-5wt%Al, developed by CRM Belgium and commonly known as Galfan, and Al-43.4Zn-1.6Si (in wt%) developed by Bethlehem Steel Corporation and first commercialized under the tradename Galvalume [Porter 91]. Due to its chemistry and microstructure, Al-43.4Zn-1.6Si combines the good durability of an Al coating with the sacrificial characteristics of a Zn coating. Atmospheric corrosion tests in various environments showed that the durability of Al-43.4Zn-1.6Si coatings is at least twice that of a Zn coating of equal thickness [Townsend 95]. Another study showed that the life expectancy of Al-43.4Zn-1.6Si coatings is 4 to 12 times longer than for Zn coatings in most residential environments in Australia [Willis 98]. Even though the sacrificial characteristics are less pronounced than for Zn coatings, the long service lifetime makes Al-43.4Zn-1.6Si coatings particularly suitable for applications where a service lifetime of several decades is absolutely required such as in the building sector.

2.1.2   *Industrial process of hot dipping*

The industrial samples studied in the present work have been deposited by the continuous hot dipping process. Figure 2-1 visualizes the layout of a modern hot dip coating line [Wehling 99]. In a first step, the coils of steel sheet are welded to a continuous strip (1). The spiral accumulator (2) ensures the continuity of the process while the next coil is welded. Subsequently the steel strip undergoes a pickling step (3) where residual grease and oxides are removed chemically. Then the strip is induction heated in protective atmosphere to about 500 °C in the case of Al-43.4Zn-1.6Si coatings (4). Through the snout

(5), the sheet enters into the bath of liquid coating alloy (6) which is held at 600 °C.
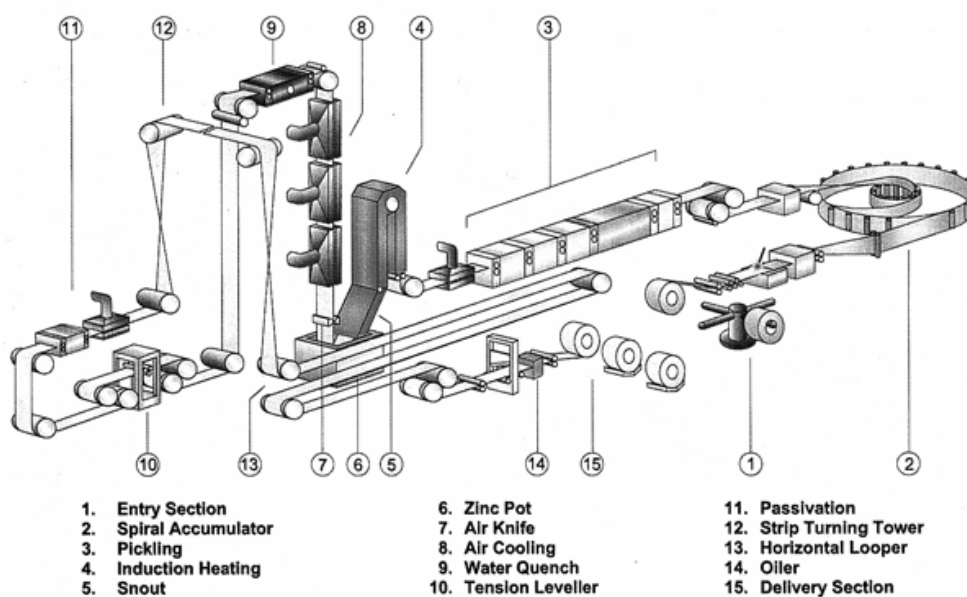
Figure 2-1 Layout of a hot dip coating line [Wehling 99].

The strip remains in the bath for 1-2 s and when leaving the bath, it is covered with a layer of liquid coating alloy. The thickness of the coating is controlled through airknifes (7) that blow away excess liquid. In the case of Al-43.4Zn-1.6Si coatings, the desired thickness is generally in the order of 20 μm. The steel sheet then enters into the cooling tower (8) where the coating layer solidifies under the action of air cooling. Once the coating is solidified, it is further cooled down in a water quencher (9). Additional operations include flattening by a tension leveler (10), and possibly a passivation or chromatation treatment for increased corrosion resistance (11). Finally, the coated steel sheet is coiled again.

2.1.3   *Intermetallic layer in Al-Zn-Si coatings*

The steel sheet and the coating alloy already react with each other when the strip is immersed into the alloy bath. Very rapidly, intermetallic phases containing Fe, Al, Si and Zn start to form at the interface between the steel strip and the liquid coating alloy. The amount and the type of intermetallics forming at the substrate-coating interface depends on the composition of the alloy bath, the time during which the steel strip is in contact with the liquid alloy and the entry temperature of the steel sheet [Marder 00]. The addition of Si

to the coating alloy is crucial as it slows down the formation of intermetallic phases. Without Si, a very strong exothermic reaction takes place at the interface which leads to the formation of $FeAl_3$ and Fe_2Al_5 and consumes the steel panel in less than 2 minutes [Selverian 88]. Silicon suppresses the exothermic reaction by forming a continuous interfacial layer that acts as a diffusion barrier or inhibition layer for the reactive species (i.e. Fe and Al). The silicon concentration in Al-43.4Zn-1.6Si coatings is high enough to limit the formation of binary intermetallics effectively, but sufficiently low in order to not deteriorate the formability and corrosion properties of the coated sheet. The thin continuous layer formed during the industrial hot dipping of Al-43.4Zn-1.6Si coatings seems to be made up of the so-called T_{5C} phase having a composition of 57 wt% Al, 30 wt% Fe, 6 wt% Si and 7 wt% Zn [Marder 00]. For short dipping times in the order of seconds, the T_{5C} phase is the only phase present [Selverian 89]. If the steel substrate is exposed to the melt for longer times, additional binary ($FeAl_3$ and Fe_2Al_5) and ternary phases form and the intermetallic layer increases in thickness [Selverian 89]. In this case, it has been reported that a continuous layer of Fe_2Al_5 forms on the steel substrate and a nearly continuous layer of $FeAl_3$ is found on top of the Fe_2Al_5 layer. Fragments of ternary and quaternary phases form then on top of the $FeAl_3$ layer and within the melt [Selverian 89].

2.1.4 Sequence of phase transformations

Microstructure and solidification sequence of Al-Zn-Si coatings (nominal composition: Al-43.4Zn-1.6Si in wt.% or Al-24Zn-2Si in at.%) have been studied by several authors [Cleary 85, Selverian 87, Marder 00, Sémoroz 01]. The most complete description of the solidification sequence has been done by Chen and Willis [Chen 05]. They compared the results of Thermo-Calc simulation combined with a Scheil solidification model to experimental observations. Their model predicted three stages in the solidification path. In the first stage, which goes from the ternary liquidus temperature of 566 °C to 520°C, primary α-Al dendrites are formed. At 520 °C, a volume fraction of liquid of 45% remains. From 520 °C to 381 °C, a binary eutectic of α-Al and Si forms. At the ternary eutectic point of 381 °C, the remaining liquid fraction (8%) solidifies into a ternary Al-Zn-Si eutectic.
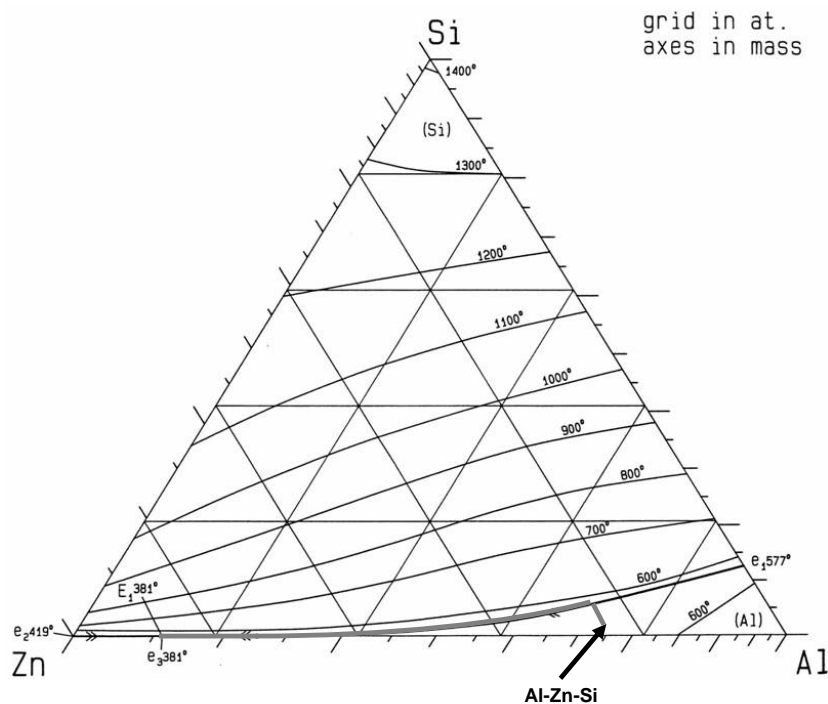
Figure 2-2 Liquidus surface of the ternary Al-Zn-Si phase diagram. Taken from [Suzuki 93].

The binary Al-Si eutectic valley that is active between 520 °C and 381 °C approaches the binary Al-Zn phase diagram during cooling. As the Si concentration is low, the volume fraction of the Si phase is accordingly low. Hence, the solidification process can be well approximated by the binary Al-Zn phase diagram, Figure 2-3, neglecting the formation of Si needles between 520 °C and 381 °C. The binary phase diagram shows that the solubility of Zn in α-Al is very pronounced, leading to a microstructure that is dominated by α-Al and which exhibits a relatively low volume fraction of eutectic in spite of the high Zn content of 43.6 wt%.
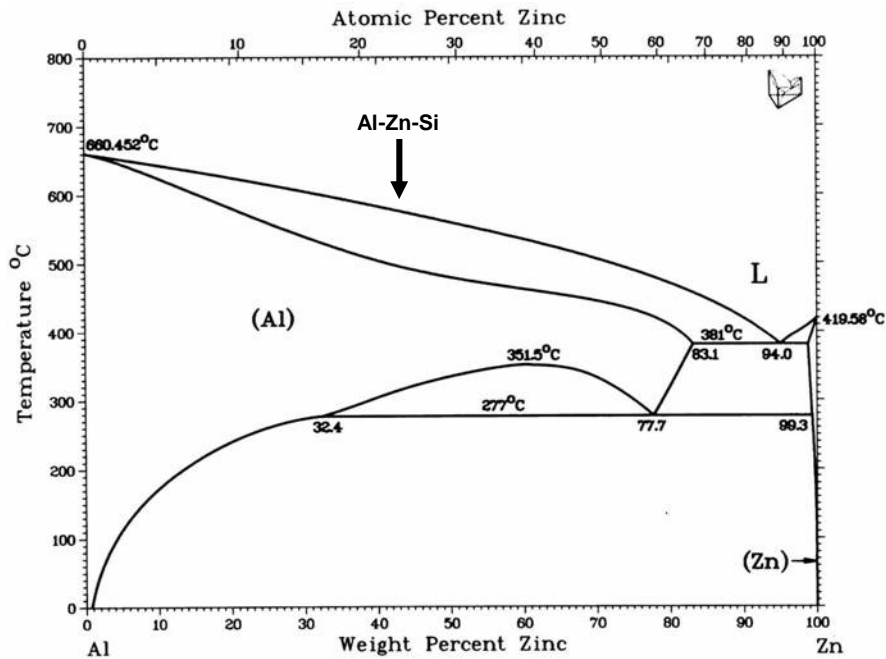
Figure 2-3 Binary Al-Zn phase diagram [Murray 83]

The solubility of Zn in the α-Al phase is very pronounced at high temperatures and decreases very much with decreasing temperature. At ambient temperature, the phase diagram (Figure 2-3) predicts that the primary α-Al phase of the dendrite arms should decompose in a two phase microstructure. According to Löffler et al. [Löffler 91], precipitation reactions in quenched Al-Zn alloys are possible at room temperature without a precipitation heat treatment. According to Simerska et al. [Simerska 78], the phase that can be expected for the precipitates is the equilibrium β-hcp phase. They showed that the GP zones transform directly into the equilibrium phase if Al-Zn alloys are aged for sufficiently long times at room temperature. The orientation relationship between matrix and precipitates was found to be [Löffler 95]:

$$\left(00.1\right)_{hex} // \left(111\right)_{cub} \quad \text{and} \quad \left[2\,\overline{1}.0\right]_{hex} // \left[1\,\overline{1}0\right]_{cub} \tag{2.1}.$$

This means that the close packed plane of the hexagonal lattice is parallel with one of the four closed packed planes of the cubic matrix, thereby leading to the different sets of precipitates observed experimentally. Further on, Löffler et al. state that the β-precipitates are delimited by planes of the $\{110\}_{cub}$ family. The intersecting planes of type $\{110\}_{cub}$ form edges of type $\langle 111 \rangle_{cub}$. Löffler et al. [Löffler 91] show that three planes of the $\{110\}_{cub}$ family are almost parallel to the three planes of type $\{10.3\}_{hex}$ and that the atomic positions fit together well. If the $(00.1)_{hex}$ plane in the precipitate is continued in the matrix

by $(111)_{cub}$, then:

$$\left(0\bar{1}.3\right)_{hex} // \left(110\right)_{cub}$$
$$\left(10.3\right)_{hex} // \left(101\right)_{cub} \tag{2.2}.$$
$$\left(\bar{1}1.3\right)_{hex} // \left(011\right)_{cub}$$

This leads to coherent β-Zn precipitates of parallelepiped shape in the α-Al matrix

2.2 Dendritic growth

Dendritic growth of the primary Al-phase is the dominant aspect of the microstructure formation in Al-Zn-Si coatings. This chapter will briefly recall some basic notions with respect to dendritic solidification of alloy systems.

2.2.1 Stability of the solid-liquid interface

The necessary condition for a solidification reaction is that the transformation from the liquid phase to the solid phase is associated with a decrease in Gibbs free energy ΔG. In the simple case of a binary alloy system, an undercooled liquid of concentration c_0 decomposes into a solid phase of concentration c_s and a liquid phase of concentration c_l, thereby reducing the total Gibbs free energy by ΔG, Figure 2-4 (a). Once a first nucleus of the solid phase is formed, the solid-liquid interface moves at the expense of the liquid phase and a concentration profile as the one displayed in Figure 2-4 (c) establishes. Unless the interface velocity is very high, the system is locally at equilibrium at the interface and the concentrations c_s and c_l are observed on the respective sides of the interface. Within the solid, the concentration is about uniform in the case of isothermal solidification, whereas the rejection of solute by the moving solid-liquid interface leads to a solute boundary layer ahead of the interface on the side of the liquid. At the solid-liquid interface, not only solute is rejected, but also the latent heat of solidification L. In the case of equiaxed solidification, the latent heat can only be evacuated into the undercooled melt leading to a negative temperature gradient G on the liquid side of the interface and a nearly constant temperature in the solid phase (bold line in Figure 2-4 (d)). The liquidus temperature $T_l(x)$, which depends on the local concentration in the liquid ahead of the

interface, exhibits the positive gradient mG_c where G_c is the solute gradient ahead of the interface and m is the liquidus slope. Therefore, the effective undercooling, $T_l(x) - T(x)$, and hence the driving force for solidification, increase ahead of the interface.
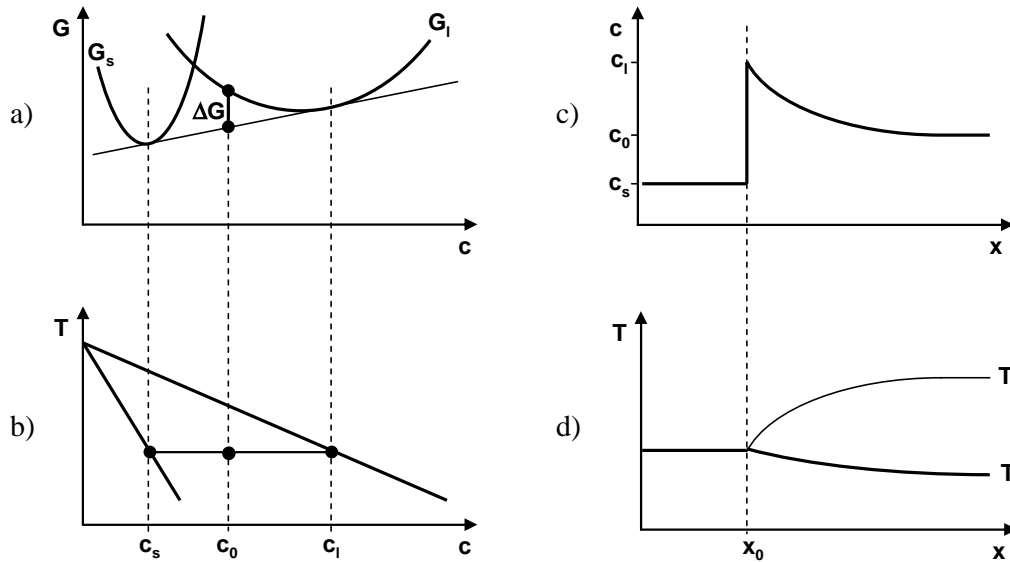
Figure 2-4 a) Gibbs free energy as a function of concentration in the solid-liquid two phase region. **b)** The corresponding binary phase diagram. **c)** Concentration profile across the moving solid-liquid interface. **d)** Temperature profile (bold) and the corresponding liquidus temperature across the interface in the case of equiaxed solidification.

If a protrusion is formed on the solid-liquid interface, one can imagine that it either continues to grow if the interface velocity at its tip is higher than in the surrounding areas or that it vanishes if the velocity at its tip is lower. In this case, the perturbed interface returns to a planar state. The necessary condition for the presence of a non-vanishing perturbation is given by the criterion for constitutional undercooling [Tiller 53, Kurz 98]:

$$G < mG_c \qquad (2.3).$$

As mentioned above, the condition of the above equation is always fulfilled in the case of equiaxed solidification as G is negative and mG_c positive. In equiaxed solidification, there exists always a zone of constitutional undercooling. Therefore, planar interfaces are inherently unstable in free equiaxed solidification. In the case of columnar solidification, G and mG_c are both positive and a planar interface may or may not destabilize depending on the magnitude of the temperature gradient.

The perturbation analysis of Mullins and Sekerka [Mullins 63, Mullins 64] provides

not only provide a criterion for destabilization, but also gives information about the characteristic length scales of the expected microstructure by taking into account the effect of the solid-liquid interfacial energy. In order to do so, they perturbed the planar interface with a sinusoid:

$$x^* = x_0 + \varepsilon \sin\left(\frac{2\pi}{\lambda} y\right)$$

(2.4),

where ε is the amplitude and λ the wavelength. The perturbation analysis shows that the amplitude of the sinusoid shrinks ($\dot{\varepsilon}/\varepsilon < 0$) for small λ and increases $\dot{\varepsilon}/\varepsilon > 0$ for large λ. The λ for which $\dot{\varepsilon}/\varepsilon = 0$ is called marginal stability wavelength:

$$\lambda_i = 2\pi \sqrt{\frac{\Gamma}{mG_c - G}}$$

(2.5),

where $\Gamma = \gamma_{sl}/\Delta s_f$ is the so-called Gibbs-Thompson coefficient. The stabilizing factor at small wavelength is the surface energy γ_{sl} which enters into play through the curvature undercooling $\Delta T_r = \Gamma K$ where K is the curvature at the tip of the protrusions. In the case of the destabilization of a spherical solid-liquid interface, the marginal stability wavelength is slightly smaller, in this case, the prefactor 2π in Eq. 2.5 is replaced by about 4.5 [Dantzig 07].

2.2.2 Stationary growth shapes

The considerations above showed that during equiaxed growth, the solid-liquid interface necessarily destabilizes if perturbations with a wavelength above λ_i are present. If $\dot{\varepsilon}/\varepsilon > 0$, the amplitude of the sinusoidal perturbation increases. Solute is easily rejected at the protrusions and accumulated in the depressions. The interface finally loses its sinusoidal character and forms deep trenches of solute-rich liquid in between cells of solid. Stationary cellular patterns may be observed in directional solidification ($G > 0$). For most growth conditions however, dendritic structures develop very quickly after destabilization of the interface. Actually, an exact distinction between cellular and dendritic patterns is difficult to make. In general, one refers to structures as cellular if they do not grow along precise crystallographic directions but rather along the thermal gradient. Dendrites on the other hand grow along well defined families of crystallographic directions along which they also develop sidebranches. In many cases, the family of crystallographic directions along which the dendrites develop is $\langle 100 \rangle$ for metals exhibiting cubic crystal structures.

However, as will be emphasized in chapter 2.3.5, other growth directions are also possible in certain alloy systems.

Over the past decades, significant progress has been made in relating characteristic length scales of the microstructure to the solidification conditions. For a more complete description of dendritic growth than the one given below, the interested reader may refer to the excellent review article of Trivedi and Kurz [Trivedi 94] and the textbook of Kurz and Fisher [Kurz 98]. The most important characteristics of a growing dendrite tip are its shape, the tip radius, the tip velocity and the tip undercooling. These quantities can be linked by calculating the diffusion fields of solute and heat (in the case of equiaxed solidification) considering also the effect of the curvature of the interface. Very early, it was shown that a parabolic interface along which concentration and temperature are constant can lead to stationary diffusion fields [Papapetrou 35]. Trivedi [Trivedi 94] showed for the case of equiaxed alloy solidification in an undercooled melt, that the undercooling ΔT can be related to the tip radius R and its velocity V through:

$$\Delta T = \frac{L}{c_l} Iv(P_t) + \frac{k\Delta T_0 Iv(P)}{1-(1-k)Iv(P)} + \frac{2\Gamma}{R} \qquad (2.6),$$

where k is the partition coefficient and ΔT_0 the solidification interval. $P_t = VR/2\alpha_t$ is the thermal Peclet number, α_t the thermal diffusivity and $P = VR/2D$ is the solutal Peclet number. $Iv(\ )$ stands for the Ivantsov function [Kurz 98]. The first term on the right hand side of the above equation contains the contribution of the diffusion of the latent heat away from the solid-liquid interface. The second term gives the part of the undercooling necessary to drive the solute diffusion and the last term adds a capillarity undercooling. By relating the undercooling ΔT to the product VR and R, Equation 2.6 does not lead to a single pair of radius and velocity but to a curve in the R-V space. An example of such a curve is given in Figure 2-5. For a while, it was believed the operating state of a dendrite tip should correspond to the maximum velocity in the R-V curve. Experimental evidence however showed that this criterion is not valid.
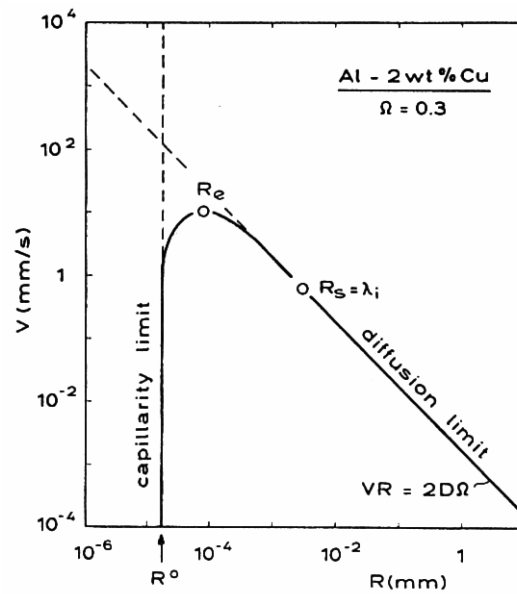
Figure 2-5 Curve showing the relationship between R and V for an Al-Cu alloy. The operating point highlighted by $R_s=\lambda_i$ corresponds to the marginal stability radius. From [Kurz 98].

A more reliable criterion for the selection of the operating state of the tip is the so-called "Ivantsov with marginal stability" model [Langer 77]. It states that the dendrite selects the marginal stability wavelength λ_i (see Equation 2.5) as the radius of the tip:

$$R_s = \sqrt{\frac{\Gamma}{\sigma^*\left(mG_c - G\right)}} \tag{2.7},$$

where σ^* is the so-called stability constant which corresponds to $1/4\pi^2$ in the case of the "Ivantsov with marginal stability" model. This concept has been developed in detail by Kurz et al. for the case of directional solidification and is known as KGT model [Kurz 86]. For the equiaxed case, a similar development has been done by Lipton et al. [Lipton 87]. However, the above models do not include the small but non-negligible effect of the anisotropy of the solid-liquid interfacial energy on tip radius and velocity. This problem is addressed by the so-called microscopic solvability theory [Langer 86, Kessler 88, Kobayashi 93]. If anisotropy is present, the stability constant deviates from the value of $1/4\pi^2$ and can be expressed as a function of the parameters describing the anisotropy of the solid-liquid interfacial energy. Saito et al. [Saito 88] for example calculated the dependence of σ^* on the anisotropy, and Muschol et al. [Muschol 92] compared stability constants determined from experimental measurements of R and V with σ^* values calculated through the solvability theory applied to experimentally determined anisotropy of the interfacial energy.

2.2.3   *Phase field modelling of dendritic growth*

The phase-field method is now one of the most popular techniques to simulate dendritic growth and moving boundary problems in general. The method is based on the introduction of an auxiliary variable, the phase field $\varphi(\mathbf{x},t)$, which is an order parameter representing the local state of the matter and is comprised between two values representing bulk liquid and bulk solid, e.g. 0 and 1. The phase field approach is based on a concept of diffuse interfaces. This means that the solid-liquid interfaces are represented by a steep but continuous transition of φ over a certain interface thickness δ, which is a parameter of the simulation. Physically, the phase field variable φ can be interpreted as an order parameter corresponding to the amplitude of the spatial atom density [Boettinger 02], see Figure 2-6. However, for practical reasons the interface thickness δ needs to be chosen bigger ($\delta \gg 1\,\mathrm{nm}$) than the actual interface thickness. As the method has the advantage that the diffuse interface is never explicitly tracked, the model can easily be formulated on a fixed grid.
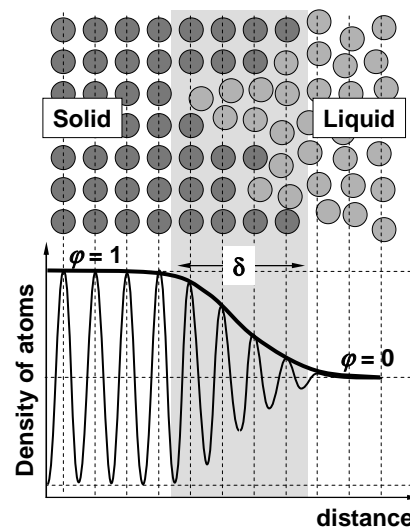
Figure 2-6 Schematic representation of a possible physical interpretation of the phase field variable φ (adapted from [Boettinger 02]).

Different formulations of phase field models have been proposed. Most phase field models are based on a thermodynamic treatment from an entropy or energy functional. The model originally proposed by Warren and Boettinger [Warren 95] for binary alloys is a typical example for such a model. Boettinger et al. propose the use of the following free

energy functional [Boettinger 02]:

$$F = \int \left[f\left(\varphi,c,T\right) + \frac{\varepsilon_C^2}{2}\left|\nabla c\right|^2 + \frac{\varepsilon_\varphi^2}{2}\left|\nabla \varphi\right|^2 \right] dV \qquad (2.8),$$

where $f\left(\varphi,c,T\right)$ is the free energy density and ε_C, ε_φ are the associated gradient energy coefficients. The functional derivatives of F with respect to the phase and the concentration field lead to two coupled partial differentiation equations describing the time evolution of these fields. The coupled partial differential equations are in general solved by either a finite difference of finite element method on a fixed grid and with an explicit time-stepping scheme. More details about the implemented partial differential equations can be found in section 3.2.2.

The phase field method has been successfully applied to the solidification of pure metals [Kobayashi 93, Karma 98], binary alloys [Warren 95, Tiaden 98, Provatas 98], eutectic growth [Plapp 02] and 3D growth [Karma 98, Henry 99]. In addition, formulations for multicomponent and multiphase systems have been porposed [Tiaden 98, Nestler 00]. Detailed comparisons have demonstrated that the dendrite tip growth kinetics predicted by phase field models are in good agreement with experimental results [Dantzig 00] and microscopic solvability theory [Karma 97], provided the interface thickness is chosen sufficiently small. However, available computer resources generally impose a lower limit for the interface thickness, which results in artificial non-equilibrium effects. In order to limit these effects, the classical phase field models have been extended by correction terms limiting these artifacts [Karma 01, Echebarria 04].

As detailed above, carefully conducted phase field modeling replicates well the analytical results for dendrites growing into the undercooled bulk melt. However, the phase field method becomes of particular interest when no analytical solution is available. The interaction of dendrite tips with boundaries confining the melt is such a case since the diffusion fields governing the growth of the dendrite tip interfere with the boundary. The application of phase field modeling to the growth of dendrites in confined spaces has been reported by Athreya et al. [Athreya 04] but only for dendrites that are aligned with the confining boundaries. The influence of the incidence angle on the kinetics of dendrite tip reaching a boundary has been addressed by Sémoroz et al. [Sémoroz 00]. A similar approach is reported here, based on a more recent phase field formulation and for conditions that are closer to those prevailing during solidification of Al-Zn-Si coatings.

2.3 Solid-liquid interfacial energy and dendrite growth directions

A key quantity in the selection of the solidification morphology is the solid-liquid interfacial energy and its anisotropy, i.e. its dependence on the local crystallographic orientation of the solid-liquid interface. The anisotropy of interfacial energy, even in non-faceted metallic systems where it is as small as 1% typically, plays an important role in pattern formation. Its effect on the radius and velocity of a dendrite tip was already discussed in subsection 2.2.2. Furthermore, it is responsible for the fact that dendrites grow in a structured way and generally exhibit well defined angles - most often 90° in cubic systems - between the primary and secondary arms.

With the emergence of quantitative numerical methods for the simulation of solidification microstructures – namely the phase field method – needs have become more acute to collect data of the solid-liquid interfacial energy and to formulate mathematical expressions describing its anisotropy. In recent years, significant progress has been made in that sense through molecular dynamics simulations [Hoyt 01, Hoyt 03, Morris 04, Davidchack 00, Laird 05] and experimental techniques [Liu 01, Napolitano 02, Napolitano 04]. Among the simulation techniques recently reviewed by Hoyt et. al. [Hoyt 03], two methods have been applied with success. The first calculates the work required to create a solid-liquid interface [Davidchack 00, Laird 05] and the second evaluates the fluctuations of the level of the crystal-melt interface which are directly related to the surface stiffness [Hoyt 01, Hoyt 03]. Experimental measurements of the anisotropy of the solid-liquid interfacial energy have been done through the determination of the equilibrium shape of a solid crystal in a melt in the case of transparent organic alloys [Glicksman 89, Muschol 92] and more recently through serial sectioning of quenched liquid droplets in metallic systems [Liu 01, Napolitano 02, Napolitano 04]. As will be detailed in section 2.3.3, the determination of $\gamma_{sl}(\mathbf{n})$ from the equilibrium shape is simple in the case of small anisotropy since the equilibrium shape of the crystal does directly correspond to the γ-plot. Such experiments require extreme caution as the anisotropy of the interfacial energy is small and the equilibrium shapes are nearly spherical. Nevertheless, reliable measurements have been reported in the (001) crystallographic plane for Al-Cu [Liu 01] and Al-Si [Liu 01, Napolitano 02] and in three dimensions for the Al-Sn system [Napolitano 04].

2.3.1 Mathematical expressions for the solid-liquid interfacial energy

In two dimensional models, the anisotropy of the interfacial energy is often described by the following expression:

$$\gamma_{sl}(\mathbf{n}) = \gamma_{sl}(\phi) = \gamma_{sl}^0 (1 + \varepsilon_4 \cos 4\phi) \tag{2.9},$$

where is ϕ the polar angle, γ_{sl}^0 is a mean interfacial energy and ε_4 is the amplitude of anisotropy. The above equation represents a 4-fold symmetry as it is often observed in the {100} planes of cubic crystals.

The orientation dependence of $\gamma_{sl}(\mathbf{n})$ in three dimensions is described as an expansion of cubic harmonics, which are a basis set of linear combinations of spherical harmonics that respect the cubic symmetry of the crystal lattice [Fehlner 76]. The anisotropic character of the solid-liquid interfacial energy can be expressed as:

$$\gamma_{sl}(\mathbf{n}) = \gamma_{sl}^0 \left[\begin{array}{l} 1 + \varepsilon_1 \left(Q - \dfrac{3}{5} \right) + \varepsilon_2 \left(3Q + 66S - \dfrac{17}{7} \right) \\ + \varepsilon_3 \left(65Q^2 - 94Q - 208S + 33 \right) + ... \end{array} \right] \tag{2.10},$$

where

$$Q = n_x^4 + n_y^4 + n_z^4 \tag{2.11},$$

and

$$S = n_x^2 n_y^2 n_z^2 \tag{2.12},$$

where n_x, n_y and n_z are the Cartesian components of the unit normal vector to the solid-liquid interface expressed in the crystallographic coordinate system. In most studies, the interfacial anisotropy has been described by expansions up to the second order, i.e. the coefficients ε_3 and higher have been neglected. This allowed the accurate description of the solid-liquid interfacial energy in systems such as Al-Cu [Asta 02] by numerical simulation or in Al-Sn [Napolitano 04] by experimental determination of the equilibrium shape. In both cases positive values have been determined for ε_1 and negative values for ε_2.

2.3.2 Interface stiffness

The influence of the interfacial energy on the equilibrium and dynamics of a solid-

liquid interface in an alloy can be quantified with the generalized Gibbs-Thomson relation:

$$T = T_{liq}(c_{liq}) - \Delta T_r - \Delta T_k \qquad (2.13),$$

which expresses the interface temperature, T, as a function of the local liquid concentration, c_{liq}, curvature undercooling, ΔT_r, and kinetic undercooling, ΔT_k. In the above Equation, $T_{liq}(c_{liq})$ expresses the liquidus temperature as a function of the concentration. For isotropic interfaces, the curvature undercooling can be expressed as:

$$\Delta T_r = \Gamma K \qquad (2.14),$$

where K is the local interface curvature and Γ is the Gibbs-Thomson coefficient. The kinetic undercooling, ΔT_k, is given by:

$$\Delta T_k = \frac{V}{\mu} \qquad (2.15),$$

where V is the interface velocity and μ is the mobility coefficient.

The undercooling terms ΔT_r and ΔT_k are related to intrinsic interfacial properties, the Gibbs-Thomson and mobility coefficients, which are anisotropic in nature, i.e. they depend on the local crystallographic orientation of the solid-liquid interface. However, under normal solidification conditions in metallic systems (moderate velocity), only ΔT_r is of importance.

If the anisotropy of the interfacial energy can be expressed as a function of the normal vector to the interface, $\mathbf{n}$, the curvature undercooling can be written as [Herring 51]:

$$\Delta T_r(\mathbf{n}) = \frac{1}{\Delta s_f}\left[\kappa_1\left(\gamma_{sl}(\mathbf{n}) + \frac{\partial^2 \gamma_{sl}(\mathbf{n})}{\partial \vartheta_1^2}\right) + \kappa_2\left(\gamma_{sl}(\mathbf{n}) + \frac{\partial^2 \gamma_{sl}(\mathbf{n})}{\partial \vartheta_2^2}\right) \right] \qquad (2.16),$$

where κ_1 and κ_2 are the principal curvatures of the solid-liquid interface and ϑ_1 and ϑ_2 are the associated angular coordinates. The terms in the parentheses are the two principal interface stiffness components. They involve the second partial derivatives of $\gamma_{sl}(\mathbf{n})$ in the planes associated with the corresponding principal curvatures by which they are multiplied.

Under the assumption of a locally spherical interface, i.e. $\kappa_1 = \kappa_2 = K/2$, the above Equation becomes [Napolitano 04]:

$$\Delta T_r\left(\mathbf{n}\right) = \kappa \Gamma^0 \Phi_r\left(\mathbf{n}\right)$$

$$\Phi_r\left(\mathbf{n}\right) = \frac{1}{\gamma_{sl}^0}\left[\gamma_{sl}\left(\mathbf{n}\right) + \frac{1}{2}\left(\frac{\partial^2 \gamma_{sl}\left(\mathbf{n}\right)}{\partial \vartheta_1^2} + \frac{\partial^2 \gamma_{sl}\left(\mathbf{n}\right)}{\partial \vartheta_2^2}\right)\right] \qquad (2.17),$$

where $\Gamma^0 = \gamma_{sl}^0 / \Delta S_f$ is a mean Gibbs-Thomson coefficient and $\Phi_r\left(\mathbf{n}\right)$ is the normalized generalized interface stiffness as defined in [Napolitano 04], which is a scalar function of the local interface orientation and can readily be calculated if $\gamma_{sl}\left(\mathbf{n}\right)$ is known.

In general, the interface stiffness is more anisotropic than the interfacial energy. This statement is easily verified by considering the mathematical form commonly used to describe the weak anisotropy of cubic crystals in the {100} planes as given in Equation 2.7. One deduces immediately that the anisotropy of the interface stiffness, $\gamma_{sl} + \mathrm{d}^2\,\gamma_{sl}\big/\mathrm{d}\,\phi^2$ is 15 times larger than that of γ_{sl}. This interface stiffness exhibits minima along the $\langle 100\rangle$ directions which correspond exactly to the maxima of γ_{sl}. However, this match is not necessarily verified for more complex anisotropy functions [Haxhimali 06].

2.3.3   *Influence of the interfacial energy anisotropy on the equilibrium shape*

The equilibrium shape of a crystal in contact with its proper melt is the shape that minimizes the interfacial free energy under the constraint of constant volume. If the interfacial energy is anisotropic, the equilibrium shape is not a sphere, but exhibits protrusions and even corners and edges if the anisotropy is strong. The equilibrium shape influences the growth morphology as crystals presumably nucleate with their equilibrium shape [Sekerka1 2005]. In the absence of long range transport of either heat or solute, the crystal would not undergo morphological instability, see subsection 2.2.1, and remain at its equilibrium shape if the attachment kinetics are negligible as is the case for metals under realistic solidification conditions. If the condition for interface instability is met, the destabilization is presumably initiated at the minima of the interface stiffness or at the protrusions of the equilibrium shape which are very close to each other.

A very elegant way to find the equilibrium shape of a crystal is the ξ-vector formalism of Cahn and Hoffman [Hoffman 72, Cahn 74, Sekerka2 05]. In spherical coordinates, a ξ-vector can be defined as follows:

$$\xi = \gamma_{sl}\mathbf{n} + \frac{\partial\gamma_{sl}}{\partial\theta}\boldsymbol{\theta} + \frac{1}{\sin\theta}\frac{\partial\gamma_{sl}}{\partial\phi}\boldsymbol{\varphi} \qquad (2.18),$$

where θ and ϕ are the azimuthal and polar angles and $\mathbf{n}$, $\boldsymbol{\theta}$ and $\boldsymbol{\varphi}$ are the unit vectors of the spherical coordinate system. The equilibrium shape $\mathbf{r}(\mathbf{n})$ is then given by:

$$\mathbf{r}(\mathbf{n}) = P\xi(\mathbf{n}) \qquad (2.19),$$

where $P = 2T_m / \left((T_m - T) L \right)$ is a scale factor. The equilibrium shape is hence similar in shape to the ξ-plot.

2.3.4 *Influence of the interfacial energy anisotropy on the solidification morphology*

In section 2.2.2, it was already shown that the anisotropy of the interfacial energy can affect the shape and growth kinetics of a dendrite. Likewise, the effect of vanishing anisotropy on the growth morphology has been studied theoretically and experimentally. Brener et al. [Brener 96] studied the expected morphology as a function of undercooling/supersaturation and anisotropy. They found that a certain amount of anisotropy is required in order maintain a dendritic structure; otherwise, it degenerates into a seaweed pattern. The required minimum anisotropy in order to maintain a dendritic pattern increases with increasing undercooling. Interesting experimental evidence with respect to this topic has been gathered by Akamatusu et al. [Akamatsu 95] and Utter et al. [Utter 02]. They conducted solidification experiments with organic alloy systems exhibiting an anisotropy which can be accurately described by a first order (i.e. ε_1 only) cubic harmonic expansion. In such systems, the interfacial energy is highly anisotropic in {100} sections through the crystal and completely isotropic in {111} sections. Figure 2-7 shows the solidification morphology of two grains. The grain on the left has a {100} plane well aligned with the experimental cell while the grain on the right has a {111} plane parallel to the experimental cell [Akamatsu 95].
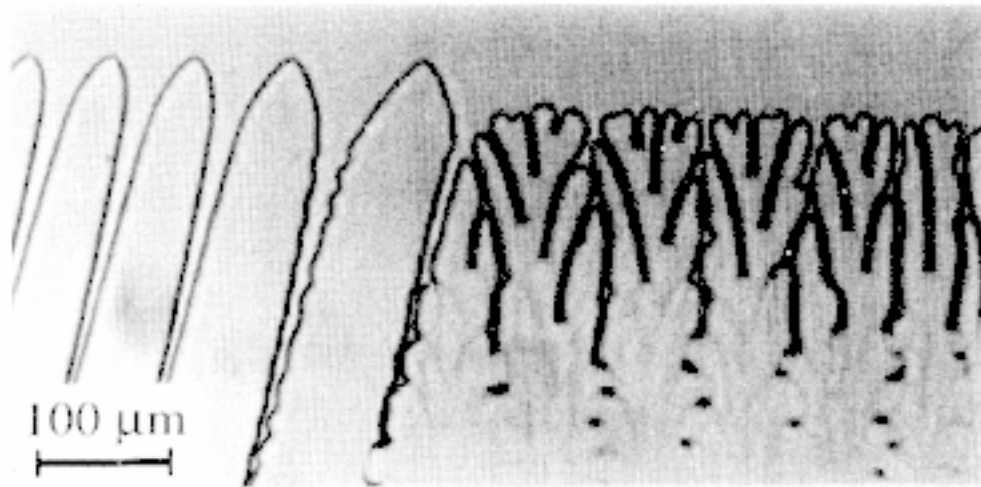
Figure 2-7 Grain boundary in organic CBr_4 8mol% C_2Cl_6 alloy. The plane of growth corresponds to (100) for the left grain and to (111) for the right grain which highlights the importance of the in-plane anisotropy on the growth morphology. From [Akamatsu 95]

It is clear that the anisotropy of the interfacial energy is responsible not only for the selection of either dendritic of seaweed pattern, but also for the selection of the dendrite growth directions. Even though some doubts remain about the exact relationship between the predominant dendrite growth directions and the interfacial energy or the interface stiffness, some links can be established between them. Different criteria for the selection of the dendrite growth directions are conceivable. Firstly, one could imagine that dendrite tips develop along the protrusions of the equilibrium shape of a crystal since the solute rejection during growth is most effective at these protrusions. On the other hand, it is also conceivable that the dendrite tips grow along the directions of minimum interface stiffness. This seems plausible from an energetic point of view as it is easiest to realize high curvatures as they occur at the dendrite tips along the minima of the interface stiffness. Thirdly, one can imagine that neither the protrusions of the equilibrium shape nor the minima of the interface stiffness are valid as a unique criterion but that the selection of the growth direction is the result of the joint action to the energetics of curved solid-liquid interface and the diffusion field.

2.3.5 *Experimentally observed dendrite growth directions*

In metals of cubic crystal structure, dendrite tips grow in most cases along the ⟨100⟩ orientations. However, it has also been reported that dendrites of *fcc* structure can grow along directions other than ⟨100⟩. Dendritic growth along ⟨110⟩ directions has been observed by Henry in Al-Mg-Mn [Henry1 98, Henry2 98] and by Napolitano in Al-Si-Sr [Napolitano 02], while Sémoroz et al. observed growth along orientations close to ⟨320⟩ in Al-Zn-Si alloys [Sémoroz1 01, Sémoroz2 01]. Recently, Gonzales et al. reported the continuous transition from ⟨100⟩ to ⟨110⟩ growth with increasing Zn content in the binary Al-Zn system [Gonzales 06]. Below a nominal composition of 25 wt% Zn the dendrites grow along the usual ⟨100⟩ directions and above 60 wt% Zn, all dendrites follow ⟨110⟩ orientations. In between these two concentrations, intermediate growth directions such as ⟨210⟩ or ⟨320⟩ have been identified (Figure 2-8). Even though the possible influence of anisotropic attachment kinetics cannot be totally excluded, as the dendrites grow at finite speed, the reported results indicate that the interfacial energy is a complex function of crystal orientation and composition, which remains to be established.
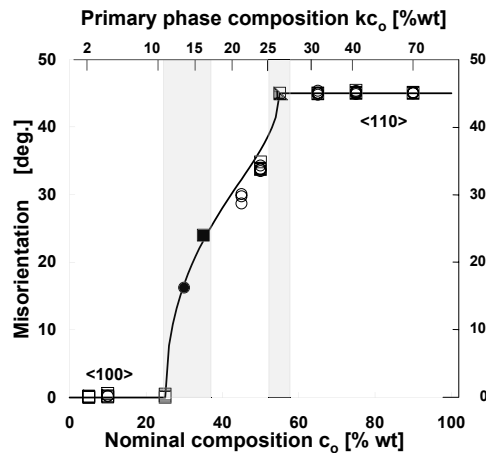
Figure 2-8 Angle between the ⟨100⟩ direction and the dendrite growth direction as a function of the Zn concentration in a binary Al-Zn alloy. A continuous transition from ⟨100⟩ to ⟨110⟩ is visible. From [Gonzales 06].

2.4 Intragranular crystallographic misorientations

Important variations of the crystallographic orientation within a given grain is a phenomenon common to several material processing techniques. Directionally solidified single crystal superalloy turbine blades for example often exhibit subgrains, which is one form of intragranular misorientation [Siredey 93, Napolitano 00]. As an example, Figure 2-9 shows a schematic representation of the subgrains present in a single crystal blade casting. Likewise, in thin films deposited by epitaxial lateral overgrowth, intragranular misorientations create structural and related electronic defects [Zytkiewicz 02]. Al-Zn-Si coatings deposited on steel by hot dipping may show large intragranular misorientations of up to 35 degrees [Sémoroz1 01, Sémoroz2 01]. Most of the studies cited further in this chapter report in some detail the observation of misorientations and low-angle boundaries, but they often do not provide clear information about the mechanisms leading to the development of such misorientations. A priori, one can imagine different mechanisms for the formation of misorientations. The changes of orientation are obviously the consequence of non-symmetrical growth conditions which may be of thermal (crystallographic growth direction not aligned with the thermal gradient), chemical (asymmetric solute field) or mechanical (fluid flow or thermal stresses) nature.
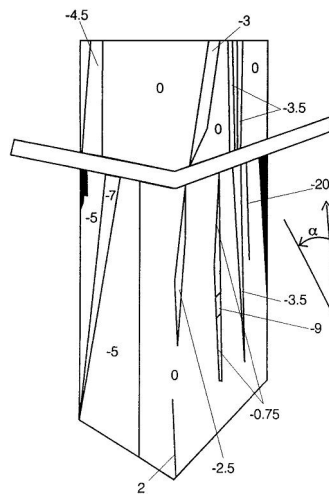
Figure 2-9 Schematic representation of a mock-up single crystal turbine blade casting in which subgrains and their misorientations with respect to the original orientation are given. From [Napolitano 00].

In the past years, some attention has been paid to the formation of crystallographic misorientations and low-angle boundaries during solidification, mainly for the case of Ni-based superalloys. The presence of subgrains or low-angle boundaries has a detrimental effect on the mechanical properties of the material by facilitating creep through diffusion

in subgrain-boundaries. Moreover, the presence of subgrains leads to thermomechanical stresses under service conditions due to the pronounced anisotropy of the elastic properties of the crystals. In the past twenty years, these grain defects have been studied in some detail, but the mechanisms responsible for their formation remain poorly understood. As early as 1986, Rappaz and Blank observed the formation of layered misorientation structures in Ni-based single-crystal castings [Rappaz 86]. The orientation is essentially constant within individual dendrites and rows of dendrites, the misorientations occur between rows of dendrites. Therefore, the authors related the misorientations to branching events during dendritic solidification.
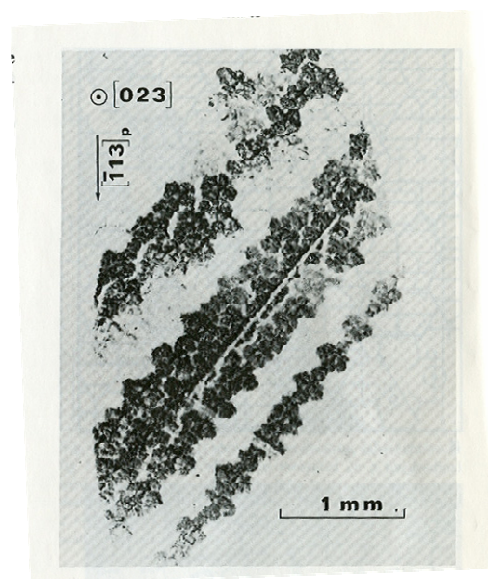
Figure 2-10 X-ray topograph of a Ni-Cr-C dendritic single crystal. Dark rows of diffracting dendrites are separated by rows which are out of diffraction. From [Rappaz 86]

In 1989, Agapova et al. reported that the overall shape of the dendritic growth front, which is dictated by the thermal gradient, is an important factor for the formation of low-angle boundaries [Agapova 89]. Paul et al. [Paul 93] correlated the relatively large liquid undercooling ahead of the growth front in the platform region of single crystal turbine blades with distortions of the crystal lattice. Siredey et al. [Siredey 93] emphasized that misorientions where already present at early stages of growth, namely at the end of the grain selector used to grow single crystal castings. The still relatively high degree of crystal perfection in the lower regions of the casting deteriorates as growth proceeds, leading to more pronounced but random misorientations in the upper part of a single crystal casting. Siredey et al. tentatively propose that the observed misorientations are due to thermomechanical stresses which build up during the γ' precipitation as the

precipitation is associated to a volume change. This may seem plausible for the AM1 nickel-base superalloy they used in their study since its precipitation temperature is only slightly below the solidus temperature.

Napolitano and Schaefer [Napolitano 00] proposed a mechanism for the formation of low-angle boundaries in the platform region of a turbine blade where the envelope of the solidification front splits into two parts. The two segments of the grain envelope rejoin later and may form a low angle boundary at the junction, Figure 2-11.
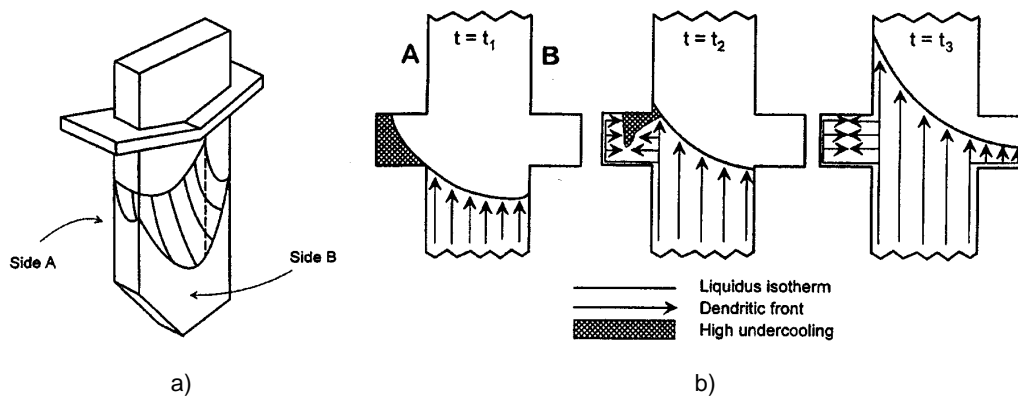
Figure 2-11 a) General shape of the isotherms. **b)** Schematic representation of growth into the platform region, illustrating the relationship between the high undercooling in the platform region and the dendritic pattern. From [Napolitano 00].

More recent studies using the EBSD technique led to a more detailed picture of the misorientations possible in single-crystal turbine blade castings. Newell et al. [Newell 05] studied misorientation in CMSX4 and CMSX10N castings. They found that under steady state growth conditions (temperature gradient and velocity of the growth front are uniform and constant), misorientations of random nature reaching a magnitude in the order of 2° are observed. In the platform area, however, Newell et al. observed continuous and cumulative misorientations of up to 6°. They do not propose a mechanism from the observed misorientations, but state that the misorientations occur in an area where secondary dendrite arms grow into the platform region where the undercooling is higher and where the dendrite tip velocity is significantly accelerated. The acceleration of the tip speed is of course also coupled with a refinement of the dendritic microstructure. D'Souza et al. [D'Souza 05] studied the same kind of misorientations in the platform region of blade castings. They suggest that the cumulative misorientations are due to contraction stresses resulting in plastic bending of the dendrite arms at intermediate solid fractions. The low

angle boundaries are subsequently produced when the independently advancing growth fronts converge as proposed by Napolitano and Schaefer [Napolitano 00]. Another interesting observation of crystallographic misorientations in Ni-based single crystal alloys has been made by Wagner et al. [Wagner 04]. They quenched castings during the directional solidification process in order to study the dendrite morphology. In the zones of extremely rapid growth ahead of the quenched dendritic front, they found very significant, continuous and cumulative misorientations of up to 20°. They suggested that these misorientations are due to thermomechanical stresses arising from the outer shell of the casting that solidifies quickly during quenching. These stresses may, according to the authors, lead to the deformation of the very fine dendrite structure in the core of the casting.

Low angle boundaries are present not only in Ni-based alloys but have also been observed in single crystal solidification of Mo-Re alloys by Agapova et al. [Agapova 97], as well as in Cu alloys by Mullis et al. [Mullis 01] and Dragnevski et al. [Dragnevski 02]. The latter two authors showed that crystallographic misorientations can arise from mechanical deformation of dendrites through fluid flow in the mushy zone. However, this effect becomes important only at very high undercoolings where the dendrite structure is very fine and where growth velocity and fluid flow are very important. Under normal, industrial solidification conditions, the mechanical effect of fluid flow on the dendrite arms remains negligible [Dragnevski 02]. Interesting experimental evidence about the bending of dendrite arms in the mushy zone has been gathered by Billia et al. [Billia 07]. They used in-situ real time synchrotron X-ray radiography to monitor the dendritic growth in Al-Ni alloys. In a directional solidification experiment, they observed how a secondary arm located shortly behind the primary tip undergoes a downward rotation of about 5°. The authors attributed the bending of the slender secondary arm to a mechanical force having its origin in earth gravity. As the density of the solid dendrite arm is higher than the one of the surrounding melt, a resulting force acts on the dendrite arm thereby causing bending and a local variation of crystal orientation in the arm.
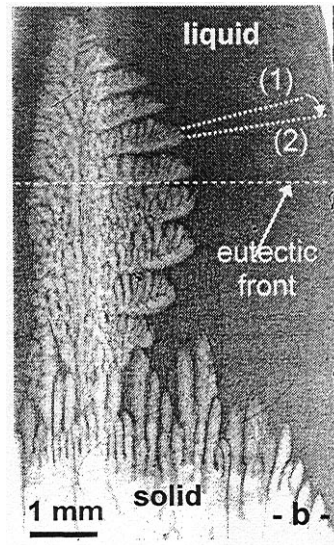
Figure 2-12 In situ synchrotron X-ray micrograph of vertical columnar dendritic growth in Al-3.5wt% Ni. It was observed that a secondary arm changes its orientation from (1) to (2), thereby rotating by about 5°. From [Billia 07].

Sémoroz et al. [Sémoroz1 01, Sémoroz2 01] found intragranular variations of crystallographic orientation in Al-Zn-Si and Zn-Al alloy coatings deposited on steel stubstrates. Their study is of particular interest as misorientations of up to 35° are observed in the coarse grained coating layers whereas misorientations of only a couple of degrees are normally observed in Ni-base single-crystal castings. This makes the Al-Zn and Zn-Al coating systems particularly suitable in order to study the mechanisms involved in the formation of intragranular variations of crystallographic orientation. Sémoroz et al. [Sémoroz1 01, Sémoroz2 01] proposed two possible mechanisms for the formation of misorientations in Al-Zn-Si coatings on steel substrates. These mechanisms are briefly presented here and will be discussed in subsequent chapters. The first mechanism assumes that the thermomechanical stresses occurring during cooling of the substrate-coating composite are responsible for the observed misorientations. The stresses are due to the difference in the thermal contraction behavior of substrate and coating, which leads to the following thermal strain:

$$\varepsilon_{th} = \left(\alpha_{coating} - \alpha_{substrate} \right) \Delta T \qquad (2.20).$$

As the expansion coefficient of the coating is considerably larger than for the substrate ($\alpha_{Al} = 2.5\,10^{-5}\,K^{-1}, \alpha_{Fe} = 1.2\,10^{-5}\,K^{-1}$) [Smithells 99], cooling from the liquidus temperature to room temperature leads to a thermal strain of about $\varepsilon_{th} = 0.7\%$. As the rigidity of the substrate is much higher than that of the thin coating, one can assume that

the strain is concentrated in the coating. In an Al-based alloy such as the Al-Zn-Si coating layer, a strain of 0.7% is certainly accompanied by plastic deformation and hence multiplication and displacement of dislocations. Sémoroz et al. pointed out that an accumulation of excess dislocations of one sign could lead to distortions of the crystal lattice and finally to misorientations, Figure 2-13 a). Considering that the coating exhibits a thickness of 20 μm and that the Burgers vector is about 0.14 nm, one excess dislocation leads to a rotation of the crystal lattice of about 4. 10^{-4} degree. In order to reach a typical misorientation rate of 5 °/mm, an excess dislocation density of 6. 10^{11} m^{-2} is required. This value is 3 to 4 orders of magnitude smaller than the dislocation density that is commonly observed in plastically deformed metals. Therefore, at first glance, it seems plausible that the observed misorientations are due to excess dislocations accumulated in the coating layer [Sémoroz2 01].

a)   b)
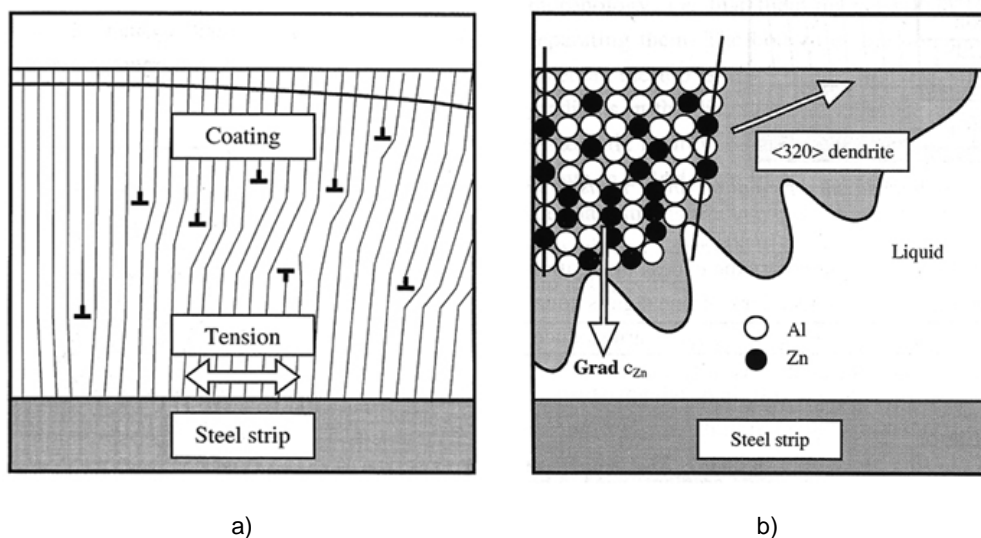
Figure 2-13 a) Schematic diagram illustrating how an accumulation of excess dislocations can lead to misorientations. **b)** Schematic diagram illustrating the concept of segregation induced misorientations. Adapted from [Sémoroz1 01]

The other hypothesis proposed by Sémoroz et al. states that solute gradients within the dendrite trunks can possibly explain the existence of the observed misorientations. According to the phase diagram (Figure 2-2, Figure 2-3), pronounced microsegregation will occur during the solidification of the Al-Zn-Si alloy coating. The Zn concentration is expected to increase substantially from the core to the periphery of a dendrite arm. Experimental data show that the lattice parameter of the Al-Zn solid solution decreases with increasing Zn content as Zn atoms are smaller than Al atoms [Murray 83], seeFigure

2-14. The difference in Zn concentration that is necessary to explain the misorientations can be calculated from the misorientation rate $\partial\eta/\partial x$ (typically 5 °/mm) and the thickness of the dendrite arm d (e.g. 10 µm) if the lattice parameter ($a \approx 0.2\,10^{-9}\,m$) and its concentration dependence ($\partial a/\partial c \approx 7.9\,10^{-12}\,m$) are known:

$$\Delta c_{Zn} = ad\,\frac{\partial\eta/\partial x}{\partial a/\partial c}$$

(2.21),

where Δc_{Zn} is the concentration difference in atomic fraction. For the values given above, this equation leads to a required concentration difference of about 4.5 at.% Zn which corresponds to about 11 wt.% Zn. Considering that the maximum solubility of Zn in the α-Al phase is 67 at.% (83 wt.% Zn), it becomes apparent that such concentration gradients can be expected within the dendrite trunks. In order to explain the systematic and continuous misorientations observed in the Al-Zn-Si coatings, the Zn concentration needed always to be higher at the substrate-coating interface than at the free surface of the coating. This implies that all dendrites should grow along the free surface as illustrated in Figure 2-13 b). The question whether this is actually the case will be addressed in some detail later in this work.
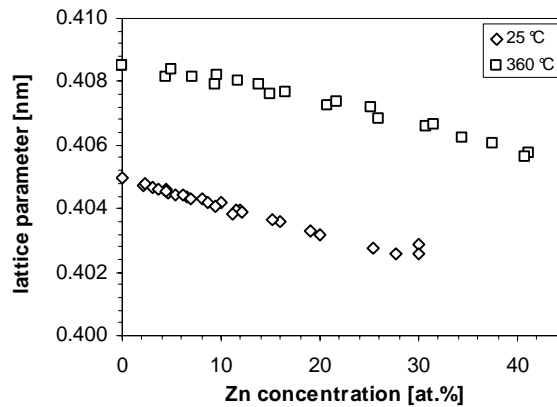
Figure 2-14 Experimental lattice parameter for a binary Al-Zn alloy at *T*=25 °C and *T*=360 °C. Data taken from [Murray 83].

Prima facie, both of the mechanisms proposed by Sémoroz et al. in order to explain the presence of such pronounced misorientations seem plausible, but neither of them is utterly convincing and many questions remain about the prevailing mechanism. An important part of this study will be dedicated to the further elucidation of the mechanisms leading to crystallographic misorientations in Al-Zn-Si coatings.

CHAPTER III

METHODS

This chapter describes the experimental and numerical methods that have been applied in this study. The chapter is divided in three sections. First, the experimental methods used for the characterization of the microstructure and the misorientations in the Al-Zn-Si coatings are introduced (section 3.1). In section 3.2, the numerical methods used to simulate distinct phenomena relevant for the microstructure formation are described. Finally, the re-solidification experiments conducted in the laboratory are introduced in section 3.3. The goal of these experiments was to determine whether intragranular misorientations can be reproduced in laboratory and to try to evidence their mechanism by modifying the solidification conditions.

3.1 Characterization of coatings

3.1.1 *Metallography and microscopy*

Preparation of sections parallel to the plane of the coating

For the analysis of the microstructure parallel to the plane of the coating, the samples underwent brief fine grinding with 1000 grit size and subsequently with 2400 and 4000 grit

size SiC papers using water as lubricant. Then, diamond polishing with 6 µm, 1 µm and 0.25 µm grits on Struers DP-Mol and DP-Nap cloths followed, using red DP lubricant from Struers or ethanol as lubricant.

For samples on which only EBSD analysis was conducted, the fine grinding steps on SiC paper were omitted. Starting directly with 6 µm diamond grits leads to less plastic deformation beneath the surface of the sample, improving thereby the quality of the EBSD diffraction pattern and hence the indexing rate of the automated EBSD analysis. However, starting directly with diamond polishing has the inconvenience that the polished surfaces will not be completely flat. In order to perform EBSD analysis on Al-Zn-Si samples, a subsequent electropolishing step is required in any case as the mechanical polishing, even if only conducted with diamond grits, leaves behind a plastically deformed surface layer. Electropolishing was carried out with a microprocessor controlled LectroPol-5 apparatus from Struers. As electrolyte, a solution equivalent to Struers A2 consisting of 720 ml ethanol, 200 ml 2-butyloxyethanol ($C_6H_{14}O_2$) and 80 ml perchloric acid ($HClO_4$, 70%) was used. Best EBSD results were achieved for an applied voltage of 25 V and a polishing time of 2 to 3 s. Due to the short polishing time, no temperature control needs to be applied to the electrolyte even though the heat release is significant during electropolishing. The electropolishing step leads to some surface roughness since not all phases dissolve at the same rate. The dissolution rate is particularly high for the eutectic β-Zn which is the most electronegative of all phases present. The Si particles on the other hand are hardly affected at all by the electropolishing step. As the electropolishing step does hence reveal well the different phases, electropolished samples were used not only for EBSD analysis but also for the characterization of the microstructure by SEM.

Preparation of cross sections through the coating

In order to prepare cross sections through the substrate-coating composite, the samples were embedded by hot mounting. The resin of choice was the thermosetting Konductomet of Buehler, which is suitable for SEM and EBSD analysis as it contains conducting carbon filler. Fine grinding was realized with SiC papers ranging from 320 to 4000 grit size. For the entire grinding sequence, ethanol was used as lubricant. The use of water would lead to a preferential dissolution of the coating layer and especially the Zn-rich areas as the thin coating is much more electronegative than the much thicker steel substrate. For the subsequent diamond polishing steps with 6 µm, 1 µm and 0.25 µm grits, the water-free yellow DP lubricant from Struers was used.

For EBSD analysis, mechanical polishing is not sufficient. Electropolishing, the method of choice for the preparation of sections parallel to the coating plane, is not practicable on cross sections as the material removal is much faster for the coating layer than for the underlying steel substrate. Even a short electropolishing step dissolves the coating layer significantly and leaves behind an important level difference between the steel substrate, the coating and the mounting plastic. In order to remove the plastically deformed surface layer, ion milling was chosen as an alternative approach. The samples were mounted on a rotating stage and have been exposed to an Ar ion beam impinging on the sample at a sharp angle. Thereby, the mechanically deformed surface layer was sputtered away without creating significant level differences between the substrate and the Al-Zn-Si coating.

Microscopy

For optical microscopy, Leitz Metallovert, Zeiss Axiomat and Zeiss Axioplan microscopes were used. All microscopy units were equipped with CCD cameras and image acquisition software. The main part of scanning electron micrographs were taken on a Philips XL30 FEG SEM. In addition a Zeiss DSM-962 and a Jeol JXA-8800 were also used for SE and BSE imaging. TEM lamellae were prepared on a FEI Strata DB 235 dual beam focused ion beam (FIB) milling station. The lamellae were subsequently analyzed on a Philips CM 30 transmission electron microscope which was operated at 200 kV.

3.1.2 *Crystallographic misorientations*

Formation of EBSD Kikuchi Pattern

When the electrons of the incident electron beam enter into the solid, they are diffusely scattered in all directions. If the scattered electrons fulfill the Bragg condition with respect to one family of lattice planes, they undergo diffraction. Considering that the electrons are diffusely scattered before, the Bragg condition is fulfilled for all electrons on cones with a half apex of 90-ϑ around the normal to the diffracting lattice planes where ϑ is the Bragg angle. For typical acceleration voltages used in EBSD analyses (20-30 kV), the Bragg angles corresponding to the lattice interplanar distances are on the order of 0.5°. Consequently, the apex of the diffraction cones is close to 180°, i.e. the cones are almost

flat. The conic sections of the diffraction cones on the EBSD phosphor screen are therefore nearly straight and nearly parallel lines. The whole Kikuchi EBSD pattern consists of pairs of parallel lines, each pair of parallel lines being called a Kikuchi band, Figure 3-1. The intersection of bands corresponds to zone axes. Software allows the automatic detection and indexing of the zone axes and hence the determination of the local crystallographic orientation.
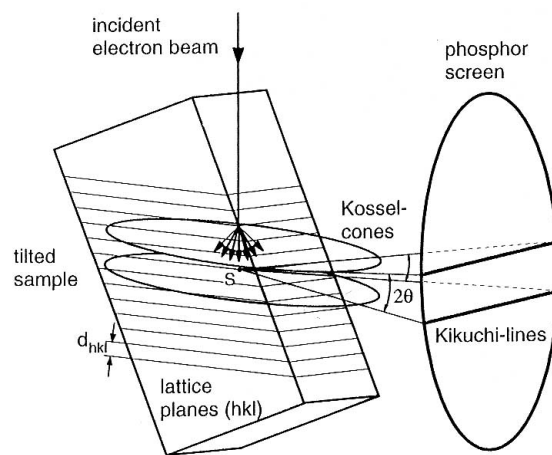
Figure 3-1 Schematic illustration of the origin of the EBSD Kikuchi lines. From [Randle 00].
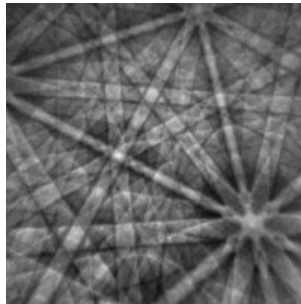
Figure 3-2 EBSD Kikuchi pattern recorded for an Al-Zn alloy.

Descriptors of orientation and misorientation

In order to specify an orientation, it is necessary to define two coordinate systems. The sample coordinate system K_S is chosen according to important surfaces or directions associated with the external form or shape of the sample. In the cases treated in this study for example, the z-axis of the sample coordinate system is always normal to the sample surface. The crystal coordinate system K_C is specified by directions of the crystal. For

crystals with cubic symmetry, the obvious choice for the axes of the crystal coordinate system are the crystallographic directions [100], [010] and [001].

Having specified the two coordinate systems, the local crystallographic orientation is then defined as the position of the crystal coordinate system with respect to the sample coordinate system, i.e.:

$$K_C = [\mathbf{M}] K_S \tag{3.1},$$

where $[M]$ is the rotation or orientation matrix embodies the rotation from the sample coordinate system into the crystal coordinate system. The orientation matrix is a 3x3 matrix:

$$[\mathbf{M}] = \begin{pmatrix} M_{11} & M_{12} & M_{13} \\ M_{21} & M_{22} & M_{23} \\ M_{31} & M_{32} & M_{33} \end{pmatrix}$$

$$= \begin{pmatrix} \cos\varphi_2 & \sin\varphi_2 & 0 \\ -\sin\varphi_2 & \cos\varphi_2 & 0 \\ 0 & 0 & 1 \end{pmatrix} \cdot \begin{pmatrix} 1 & 0 & 0 \\ 0 & \cos\phi & \sin\phi \\ 0 & -\sin\phi & \cos\phi \end{pmatrix} \cdot \begin{pmatrix} \cos\varphi_1 & \sin\varphi_1 & 0 \\ -\sin\varphi_1 & \cos\varphi_1 & 0 \\ 0 & 0 & 1 \end{pmatrix} \tag{3.2},$$

which can be written as the product of the three following consecutive rotations: φ_1 around the z-axis of the sample coordinate system, ϕ around the new x-axis and φ_2 around the new z-axis. The angles φ_1, ϕ and φ_2 are generally called Euler angles.

The orientation of a spot within the sample can be expressed not only with respect to the sample coordinate system as described above, but also with respect to the orientation of another spot on the same sample. In this way the relative orientation or misorientation between two spots can be described. The misorientation can be calculated from the orientation matrices $[\mathbf{M}^A]$ and $[\mathbf{M}^B]$ of the two spots A and B [Randle 00]:

$$[\mathbf{M}^{AB}] = [\mathbf{M}^A]^{-1} [\mathbf{M}^B] \tag{3.3},$$

where $[\mathbf{M}^{AB}]$ is the matrix which embodies the misorientation between A and B. $[\mathbf{M}^A]$ is arbitrarily chosen as the reference orientation in this case. A misorientation can also be described by a rotation axis $\mathbf{r}$ and an angle of rotation τ instead of a misorientation matrix. The axis / angle pair can be extracted from the misorientation matrix as follows [Randle 00]:

$$\tau = \arccos\left[\frac{1}{2}\left(M_{11}^{AB} + M_{22}^{AB} + M_{33}^{AB} - 1\right)\right] \tag{3.4},$$

$$\begin{aligned} r_1 &= M_{23}^{AB} - M_{32}^{AB} \\ r_2 &= M_{32}^{AB} - M_{13}^{AB} \\ r_3 &= M_{12}^{AB} - M_{21}^{AB} \end{aligned} \tag{3.5}.$$

The misorientation axis **r** given here is expressed in the crystal coordinate system of A. In order to have the misorientation axis in the sample coordinate system, $\left[M^A\right]^{-1}$ needs to be applied on **r** . It is usually not necessary to ascribe a handedness to the rotation, as it is conventionally described as a right handed screw operation. The angle τ is hence always positive.

EBSD instrument

The EBSD measurements were conducted on a Philips XL30 FEG SEM equipped with Nordlys EBSD detector from HKL. The recorded Kikuchi pattern were treated with a HKL Channel 5 acquisition and data processing software. The Channel 5 software controls both the displacement of the electron beam and the stage of the microscope which allows mappings up to the cm^2 range. For most measurements, an acceleration voltage of 20 kV was used. In some cases with poor EBSD pattern quality, higher acceleration voltages allowed improving the pattern. Depending on the desired spatial resolution and the size of the zone to be analyzed, step sizes between 40 nm and 40 µm have been chosen.

3.1.3   *Surface topography measurements*

To investigate the topography of coating samples in the as-solidified state, two approaches were selected. In order to get an overview on the surface topography on the scale of the grain, optical profilometry using a AltiSurf-500 white light profilometer of Cotec was conducted. This method allowed assessing areas up to $1mm^2$ and has maximum lateral resolution of 1 µm and a maximum vertical resolution of 100 nm. For more detailed measurements of the topography on the scale of individual dendrite arms a TopoMetrix Explorer TMX 1000 atomic force microscope (AFM) was used. Measurements have been realized by scanning areas measuring 100x100 µm and 20x20 µm with a maximum z-displacement of 12 µm, thereby realizing a lateral resolution of 20nm. The measured data

have been processed with Mountains Map Universal and Matlab software.

3.1.4   Segregation of chemical species

For concentration measurements, two different methods were used. The Glow Discharge Optical Emission Spectroscopy (GD-OES) technique served to assess concentration profiles normal to the coating surface. By applying an Ar plasma on the sample to be analyzed, atoms of the specimen are sputtered away and ionized. When electron recombination occurs, radiation of wavelengths characteristic for the chemical element is emitted. The emitted light is analyzed in an optical spectrometer and the concentration at the surface of the specimen is determined thereby, Figure 3-3. As the sputtering process continuously ablates material from the surface of the sample, depth profiles of the concentration can be established. It has the advantage of a very high resolution in the z-direction (~nm) when the surface is flat, however, the lateral extension of the measurement spot is very large. The GD-OES analysis was conducted using a JY 5000 RF instrument manufactured by Jobin-Yvon Horiba and equipped by a glow discharge source of 4 mm diameter.
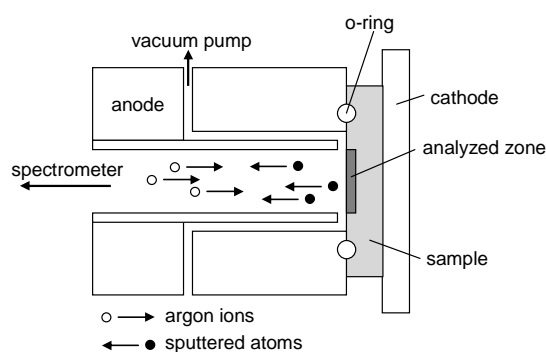
Figure 3-3 Schematic representation of the GD-OES process for the acquisition of concentration profiles.

WDS and EDS microprobe analysis was used to make quantitative measurements in spots and semi-quantitative concentration mappings. WDS and EDS are both based on X-ray emission, but WDS has the advantage of a higher concentration resolution. For the WDS analysis, a Jeol JXA-8800 electron probe microanalyzer equipped with 4 wavelength dispersive X-ray spectrometers was used. This allowed to measure in parallel the X-ray intensities of the four main constituents of the substrate-coating system: Al, Zn, Si and Fe. Analysis has been done with an acceleration voltage of 20 kV in order to measure the k_α

signals of all four elements. Depending on the size of the mappings, lateral step sizes between 0.3 and 10 μm and dwell times in the order of 60 ms have been chosen. EDS has been used for concentration measurements in spots and for the identification of the phases of the microstructural constituents. The measurements were conducted on a Prism-2000 instrument of Princeton Gamma-Tech mounted on a Philips XL30 FEG SEM.

3.2 Modeling

In this section, three numerical methods are presented. They address three different aspects that are of relevance in the microstructure formation of Al-Zn-Si coatings. A first subsection describes an inverse method, which was applied in order to determine a mathematical function for the anisotropy of the solid-liquid interfacial energy of the Al-Zn-Si alloy. As has been shown in section 2.3, the anisotropic solid-liquid interfacial energy is a physical property of key importance in solidification. The availability of an appropriate anisotropy function is a prerequisite for realistic 3D phase field simulations of the given alloy. In a second subsection, the phase field method, which was used to simulate the interaction of the dendrite tips with the confining boundaries, is described. The objectives of the phase field simulations are to gather information about the morphology of the dendrites growing in interaction with the confining boundaries in terms of the tip shape, the thickness of the dendrite arms and the development of secondary branches. It provides an estimation of these quantities which may play a significant role in the formation of misorientations and which are difficult to obtain experimentally as they change considerably during solidification. Another objective is to determine the influence of the boundaries on the dendrite tip kinetics. The tip kinetics determined by phase field simulations are then implemented into a geometrical model of dendrite growth that is described in a third subsection. The geometrical model simulates the formation of the dendrite network in the thin coating layer on the scale of a grain. It is used to investigate the origin of the visual aspect of the samples.

3.2.1 *Inverse modeling for the determination of the interfacial energy anisotropy*

In the Al-Zn-Si system, uncommon dendrite growth directions have been reported in literature [Sémoroz1 01, Gonzales 06], see section 2.3.5. As has been discussed in section 2.3.4, the anisotropy of the solid-liquid interfacial energy is responsible for the selection of

the crystallographic dendrite growth directions. For the Al-Zn-Si alloy system, no mathematical expression is available for the solid-liquid interfacial energy. However, the availability of such an expression is a necessary prerequisite for 3D microstructure simulations by the phase field method. In this section, a method for the determination of the anisotropy function is described. The fact that the dendrite growth is confined by two boundaries in the Al-Zn-Si coating layers allows extracting more information about the interfacial energy than is the case in bulk samples of the same alloy. Further, the inverse method described below serves also to determine more accurately the preferred crystallographic growth direction in the Al-Zn-Si system, growth directions which do not necessarily need to follow low Miller index directions such as $\langle 320 \rangle$.

The method used to characterize the anisotropy of the interfacial energy is based on the observation of dendrite growth directions in the Al-Zn-Si coatings. The microstructure of such coatings is composed of Al-rich dendrites of fcc crystal structure that grow in the confined volume of the thin coating, Figure 3-4 a). As the preferred crystallographic dendrite growth directions are in general not aligned with the plane of the coating and as the coating is thin, the dendrite tips are forced to grow along the two boundaries confining the melt. The growth directions of the dendrites that are visible at the free surface (or in a parallel section a few microns underneath) hence in most cases do not correspond to the crystallographic growth directions of an ideal dendrite tip growing in the bulk melt. For bulk dendrites, we assume that the growth directions correspond to the minima of the generalized interface stiffness, $\Phi_r(\mathbf{n})$, see section 2.3.4. In the case of growth in a thin coating layer, it is much more plausible that the dendrite tips grow along the directions that correspond to local minima of the surface stiffness within the coating plane. This concept is illustrated in Figure 3-4 b), which displays a typical 3D plot of the interface stiffness having the same orientation with respect to the coating plane as the grain of Figure 3-4 a). The local minima within the plane of the coating, which are determined from the trace of the stiffness plot in this plane, Figure 3-4 c), correspond well to the growth directions observed in Figure 3-4 a).

The assumption that dendrite tips grow along the in-plane minima of the interface stiffness also relies on experimental observations and phase field simulations detailed later in chapters 4.1.4 and 4.2.2, which show that the dendrite tips remain separated from the confining boundaries by a thin layer of solute enriched liquid. Since the dendrite tips are separated from the boundaries, the interfacial energies between the solid and the substrate or between the solid and the air should not influence the dendrite tip kinetics. Therefore, it

is plausible that the interface stiffness is the only factor for the selection of the dendrite growth directions.
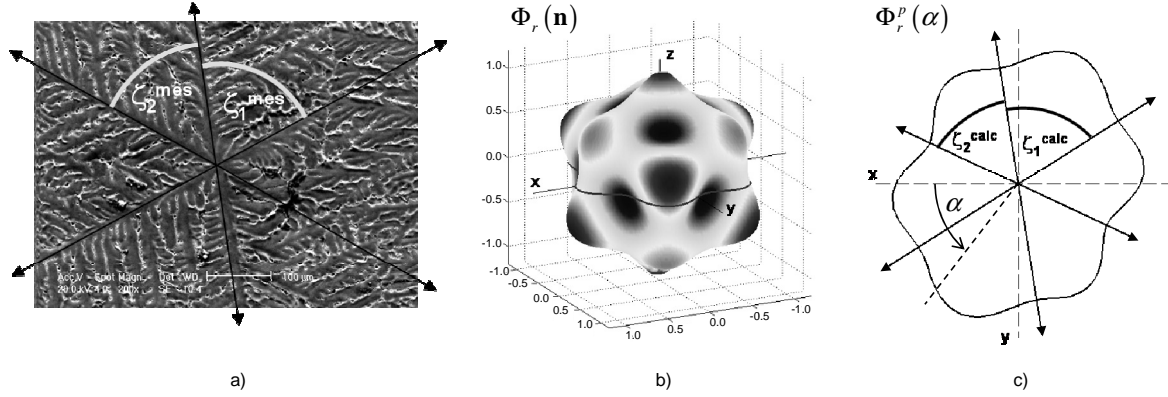
Figure 3-4 Schemtic illustration of how $\{\zeta^{mes}\}$ and $\{\zeta^{calc}\}$ angles are determined. **a)** Typical microstructure observed a few microns underneath the surface of an Al-Zn-Si coating. The angles $\{\zeta^{mes}\}$ are measured between the primary dendrite arms. **b)** Stiffness plot computed with arbitrary anisotropy parameters ε_1, ε_2, and ε_3 for the crystallographic orientations of the grain shown in a). The coordinate axes correspond to the coordinate system of the sample where z is normal to the coating plane. The circumferential line in the (x,y) plane corresponds to the intersection of the stiffness plot with the coating plane. **c)** The local minima of the in-plane stiffness plot allow determining the $\{\zeta^{calc}\}$ angles.

Experimental observations have shown that either 6 or 8 primary dendrite branches are present in the plane of the coating [Sémoroz1 01]. The number of growth directions and the angles between them, $\{\zeta^{mes}\}$, depend of the crystallographic orientation of the grain with respect to the coating plane. In the case of 6 growth directions, two angles, ζ_1^{mes} and ζ_2^{mes}, completely describe the orientation of the growth directions with respect to each other, see Figure 3-4 a). In the case of 8 growth directions, three ζ^{mes} angles are required.

The anisotropy of the solid-liquid interfacial energy is described by a third order cubic harmonics expansion, Eq. 2.10. For a given grain orientation and a given set of coefficients of the cubic harmonic expansion, $\boldsymbol{\varepsilon} = (\varepsilon_1, \varepsilon_2, \varepsilon_3)$, the angles between the expected growth directions in the coating plane, $\{\zeta^{calc}(\boldsymbol{\varepsilon})\}$, can be obtained by determining the local minima in the corresponding plane of the stiffness plot, Figure 3-4 b) and c). More precisely, the growth directions in the coating plane are obtained by solving the following equation:

$$\frac{\mathrm{d}\Phi_r^p(\alpha)}{\mathrm{d}\alpha} = 0 \quad \text{with} \quad \frac{\mathrm{d}^2\Phi_r^p(\alpha)}{\mathrm{d}\alpha^2} > 0 \tag{3.6},$$

where $\Phi_r^p(\alpha)$ expresses the trace of the interface stiffness in the coating plane as a function of the in-plane azimuthal angle α, see Figure 3-4 c). This function is obtained by the following operation:

$$\Phi_r^p(\alpha) = \Phi_r\left(\mathbf{n}(\alpha)\right) = \Phi_r\left(\left[\mathbf{M}\right]\cdot\begin{pmatrix}\cos\alpha\\\sin\alpha\\0\end{pmatrix}\right) \qquad (3.7),$$

where $\Phi_r(\mathbf{n})$ is the normalized generalized interface stiffness expressed in the crystallographic coordinate system and defined by Equation 2.17. $\left[\mathbf{M}\right]$ is the transformation matrix describing the transition from the sample coordinate system to the crystallographic coordinate system given by Equation 3.2. The three Euler angles that are necessary to define $\left[\mathbf{M}\right]$ can be obtained from electron backscattering diffraction (EBSD) measurements. The vector to which the transformation matrix is applied, is the in-plane unit vector. It has a zero z-component as the z-axis of the sample coordinate system is normal to the plane of the coating. The solution of Equation 3.6 is obtained numerically using a very fine mapping of $\Phi_r^p(\alpha)$.

By applying the procedure described above for a series of grains, an inverse method can be formulated in order to determine the most likely set of anisotropy coefficients. Following the inverse method described by Rappaz et al. [Rappaz 95] which is based on the work of Beck et al. [Beck 77], the procedure consists of looking for the anisotropy coefficients, $\boldsymbol{\varepsilon} = (\varepsilon_1, \varepsilon_2, \varepsilon_3)$, which minimize the mean square deviation $S(\boldsymbol{\varepsilon})$ between measured angles $\left\{\zeta^{mes}\right\}$ and calculated angles $\left\{\zeta^{calc}\right\}$:

$$S(\boldsymbol{\varepsilon}) = \sum_{i=1}^{N}\left[\zeta_i^{mes} - \zeta_i^{calc}(\boldsymbol{\varepsilon})\right]^2 \qquad (3.8),$$

where N is the number of angles that have been determined experimentally.

As the locations of the minima of the stiffness plot depend only on the relative magnitude of the anisotropy coefficients and not on their absolute values, the condition for a local minimum of $S(\boldsymbol{\varepsilon})$ can be expressed as a function of only two anisotropy parameters:

$$\frac{\partial S}{\partial \varepsilon_2} = 0$$

$$\frac{\partial S}{\partial \varepsilon_3} = 0 \tag{3.9}.$$

The minimum of S is obtained by an iterative descent algorithm [Beck 77, Rappaz 95], which consists of linearizing $\zeta_i^{calc}(\boldsymbol{\varepsilon})$ and using numerical estimations of the sensitivity coefficients, $\partial \zeta_i^{calc}/\partial \varepsilon_2$ and $\partial \zeta_i^{calc}/\partial \varepsilon_3$ to calculate the increments of the unknowns between two successive iterations. As the method involves only 2 out of the 3 anisotropy coefficients, it does not allow determination of the absolute magnitude of the anisotropy. The objective is therefore restricted to the determination of the shape of the interface stiffness and interfacial energy functions.

3.2.2 2D phase field modeling of dendrite tips on confining boundaries

The phase field method has been applied to study the interaction of dendrite tips and arms with the boundaries confining the melt. As the thickness of the coating is only 20 μm, the effect of the substrate-coating interface and of the free surface on the dendrite morphology are considerable and can not be neglected. These two interfaces are subsequently termed as boundaries of the modeling domain. The influence of the boundaries on the dendrite tip velocities can not be described by analytical models as it is the case for unconstrained dendrite tips. If boundaries are present in the vicinity of growing dendrite tips, analytical relationships such as those presented in chapter 2.2.2 are not valid anymore since the solute diffusion field in the liquid is heavily affected by the boundaries.

As described in section 2.2.3, partial differential equations describing the time evolution of the phase and concentration fields can be derived from a free energy or entropy functional. Details on the derivation from the free energy functional to the partial differential equations stated below can be found in [Tiaden 98, Beckermann 99 and Boettinger 02]. The equations given here are those implemented in the phase field model that has been used to simulate solidification in binary alloys during this project. The time derivative of the phase field is described by:

$$\frac{1}{\mu_k}\frac{\partial \varphi}{\partial t} = \Gamma \eta_4^2 \nabla^2 \varphi - \Gamma \frac{2\varphi(1-\varphi)(1-2\varphi)}{4\delta^2} - \frac{5\sqrt{2}}{2}\frac{\varphi^2(1-\varphi)^2}{\delta}\left(T_{liq}(c_L)-T\right) + \Gamma K_{aniso} \tag{3.10},$$

where $\eta_4 = \left(1 + \varepsilon_4 \cos 4\phi\right)$, K_{aniso} is taken from [Warren 95]:

$$
\begin{aligned}
K_{aniso} = \eta_4 \frac{\mathrm{d}\eta_4}{\mathrm{d}\phi} & \left[2\cos\left(2\phi\right)\frac{\partial^2 \varphi}{\partial x \partial y} + \sin\phi\cos\phi\left(\frac{\partial^2 \varphi}{\partial y^2} - \frac{\partial^2 \varphi}{\partial x^2}\right) \right] \\
& - \frac{1}{2}\left[\left(\frac{\mathrm{d}\eta_4}{\mathrm{d}\phi}\right)^2 + \eta_4 \frac{\mathrm{d}^2\eta_4}{\mathrm{d}\phi^2} \right]\left[2\sin\left(2\phi\right)\frac{\partial^2 \varphi}{\partial x \partial y} - \nabla^2\varphi - \cos\left(2\phi\right)\left(\frac{\partial^2 \varphi}{\partial y^2} - \frac{\partial^2 \varphi}{\partial x^2}\right) \right]
\end{aligned}
\tag{3.11}
$$

and where μ_k is a mobility coefficient related to the characteristic time of attachment of the atoms at the interface, $\Gamma = \gamma_{sl}^0 / \Delta s_f$ is the Gibbs Thomson coefficient, T_m the melting point of the pure substance and c_L the local liquid concentration. $T_{liq}(c_L)$ is the liquidus temperature associated to the local concentration of the liquid. The first term on the right hand side of Equation 3.10 tends to coarsen the microstructure and widen the interface by diffusion whereas the second confines the interface width to the predefined value of δ. The third term includes the thermodynamic driving force for the phase transformation through the local undercooling. In interface areas, random noise is applied on the terms number 2 and 3 on the right hand side of Equation 3.10. This noise is necessary in order to initiate the formation of secondary branches.

The evolution of the concentration field is obtained through the following conservation equation which uses the phase field variable as a weighting factor for the concentrations of solid and liquid in the interface [Tiaden 98]:

$$
\frac{\partial c}{\partial t} = \nabla \cdot \left[\varphi D_S \nabla c_S + \left(1 - \varphi\right) D_L \nabla c_L \right]
\tag{3.12}
$$

The liquid and solid concentrations c_S and c_L can be expressed in terms of the actual local concentration through:

$$
c_L = \frac{c}{\left(1 - \varphi\right) + k\varphi} \quad \text{and} \quad c_S = \frac{kc}{\left(1 - \varphi\right) + k\varphi}
\tag{3.13}
$$

where k is the solute partition coefficient. The coupled phase and concentration equations are solved sequentially on a fixed square grid of uniform mesh size by using an explicit time stepping scheme.

Calculations have been conducted for the binary Al-Zn phase diagram. Liquidus and solidus as a function of temperature were extracted from ThermoCalc and tabulated in a file. The influence of Si on the dendrite morphology has hence been neglected. This

approach can be justified by the fact that the nominal Zn concentration of 43.4 wt.% (24 at.%) is much higher than the Si concentration of 1.6 wt.% (2 at.%). Considering the Zn partition coefficient is not close to 1 at typical solidification temperatures, see Figure 2-3, it becomes apparent that the Zn diffusion field due to the rejection of solute at the solid-liquid interface is by far dominating over the Si diffusion field.

For the present study, only the partial differential equations relating concentration and phase field have been solved. The diffusion of heat has been neglected; the temperature field is set uniform in the modeling domain but may vary in time. Firstly, heat diffusion is much faster than solute diffusion. Further on, the Al-Zn-Si coating (2 x 20 μm) is thin with respect to the steel substrate (0.5 mm). Therefore, it is reasonable to assume that the temperature evolution during cooling is dominated by the heat capacity of the steel substrate rather than the rejection of latent heat in the coating. This seems all the more convincing when considering that the latent heat is released over the large solidification interval between 580 °C (liquidus temperature for the nominal concentration) and 381 °C (ternary eutectic temperature). In addition, Sémoroz [Sémoroz2 01] showed that the Biot number of the substrate-coating composite is small (~0.05):

$$Bi = \frac{h\,d}{\kappa} \tag{3.14},$$

where h is the heat transfer coefficient at the surface of the coating, d the coating thickness and κ the thermal conductivity of the sample. A small Biot number means that the cooling of the sample is limited by the heat transfer across the coating-air interface and not by the diffusion of heat within the sample. Therefore, it is reasonable to assume that the temperature gradients within the coating-substrate composite are negligible.

As initial condition for the solidification simulations, spherical nuclei were positioned within the modelling domain. Their concentration was set to the solidus concentration at the given temperature, whereas the concentration of the surrounding liquid was set to the nominal concentration of the alloy. In order to study the interaction of the dendrite arms with the boundaries confining the melt, modified boundary conditions that allow simulating wetting have been applied following the approach proposed by Sémoroz et al. [Sémoroz 00]. The introduction of phase field values for an additional layer of virtual nodes outside the modelling domain allows predefining the angle between the phase field isovalue lines and the boundary. This angle β corresponds to the "wetting" angle of the solid on the boundary as the solid-liquid interface is parallel to the phase field isovalue

lines. For the case of a boundary on the left of the modelling domain, Figure 3-5, a value φ_W needs to be calculated from a given β. If the mesh is regular one finds that:

$$\mathrm{ctg}(\beta) = \frac{\partial\varphi/\partial x}{\partial\varphi/\partial y} = \frac{\varphi_E - \varphi_W}{\varphi_N - \varphi_S} \tag{3.15},$$

where φ_E, φ_W, φ_N and φ_S are the first neighbors on the east, west, north and south side of the concerned node respectively. Hence:

$$\varphi_W = \varphi_E - (\varphi_N - \varphi_S)\mathrm{ctg}(\beta) \tag{3.16}.$$

For the boundaries on the top, bottom and right side of the modelling domain, similar expressions can be found.
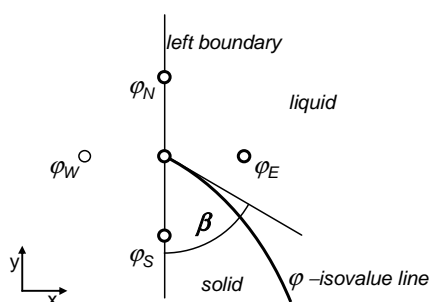
Figure 3-5 Mesh detail on the left boundary. A phase field value φ_W is introduced at a virtual node outside the modeling domain in order to impose a wetting angle β. Adapted from [Sémoroz 00].

For the solute field, homogeneous Neumann boundary conditions are applied in order to ensure conservation of the solute species:

$$\frac{\partial c}{\partial \mathbf{n}} = 0 \tag{3.17},$$

where $\mathbf{n}$ is the normal to the boundary.

The phase field model is two dimensional and incorporates the standard 4-fold anisotropy expression for the solid-liquid interfacial energy given in Equation 2.9. This situation corresponded to dendrites arms growing along the 6 (4 in 2D) $\langle 100 \rangle$ directions. An important parameter of the phase field simulation is the angle between the preferred crystallographic growth direction and the boundary along which the tip is forced to grow. This quantity is subsequently termed as incidence angle α.

As it was already mentioned in section 2.3.5, actual Al-Zn-Si dendrites do not grow

along the $\langle 100 \rangle$ directions but rather along some directions in between $\langle 100 \rangle$ and $\langle 110 \rangle$. The corresponding interfacial energy function is a considerably more complicated 3 dimensional expression as the one given in Equation 2.10. In order to provide a more accurate description of the interaction between a growing tip and a confining boundary, simulations needed to be conducted in a 3 dimensional domain which is associated with a very high demand in computational resources. The conducted 2D simulations do nevertheless provide a first approximation of the influence of the crystallographic orientation with respect to the confining boundary.

3.2.3   *Geometrical model for the microstructure formation on the grain scale*

One of the goals of this project is to better understand the development of the dendrite network during solidification in Al-Zn-Si coatings and possibly to explain the spangle morphologies observed at the surface of coated samples. A numerical model was developed for that purpose. To capture the mechanisms that lead to the formation of the characteristic surface appearance in Al-Zn-Si coatings, a model needs to describe the development of the dendritic network in the three dimensions of the coating layer. In order to model the formation of the dendrite skeleton on the grain scale, a geometrical model which takes into account the influence of the coating boundaries on the tip growth kinetics has been developed. In this model, the evolution of the dendrite skeleton is calculated in a 3D domain which corresponds to a coating layer of about 20 µm thickness and a lateral extension of several millimeters. The dendrite arms are described as vector type elements that do not have any lateral extension. In order to model the capture of the volume by the dendrite branches, the calculation domain is enmeshed with a regular grid of cubic elements, which can take the liquid or solid states. A cell goes from liquid to solid as it is reached by a dendrite vector, and the growth of a dendrite vector is stopped when it reaches a solid cell.
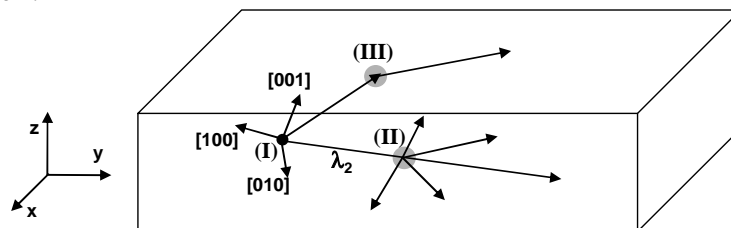
Figure 3-6 Schematic development of the dendrite skeleton in the confined space of the coating. Nucleation occurs at position (I). The vector type dendrite arms emit branches every λ_2, (II). If a dendrite arm hits one of the coating boundaries, it is projected onto the boundary, (III).

First, a nucleus with a distinct crystallographic orientation, which is represented by the Euler angles φ_1, ϕ and φ_2, is positioned within the domain, (I) of Figure 3-6. From the nucleus, 24 primary dendrite arms of the $\langle 320 \rangle$ family are emitted. After a distance λ_2, which is a parameter of the model, the primary branches emit secondary arms, (II) of Figure 3-6. Secondary branches emit again tertiary branches after having covered the distance λ_2. The branching mechanism is considerably more complicated in the case of growth along the 24 $\langle 320 \rangle$ directions than in the case of growth along the six $\langle 100 \rangle$ directions. In $\langle 100 \rangle$ growth, the four lateral growth directions that form a 90° angle with the primary dendrite arm generally give rise to side branches. In $\langle 320 \rangle$ growth, 22 side-branches can be imagined a priori but only a limited number of them will be activated. This requires introducing a branching criterion. Out of the 22 possible directions, the 12 branches forming an angle equal or larger than 90° with the primary arm are excluded, as secondary branches growing forwards into the undercooled melt are considerably more favored than branches pointing towards the interior of the grain. Thereby only the 10 $\langle 320 \rangle$ directions depicted with black squares in Figure 3-7 remain. A second branching criterion is used to account for the orientation with respect to the free surface. The directions forming an angle larger than 35° with the plane of the coating layer are not considered, as they are likely to be quickly eliminated at a boundary.
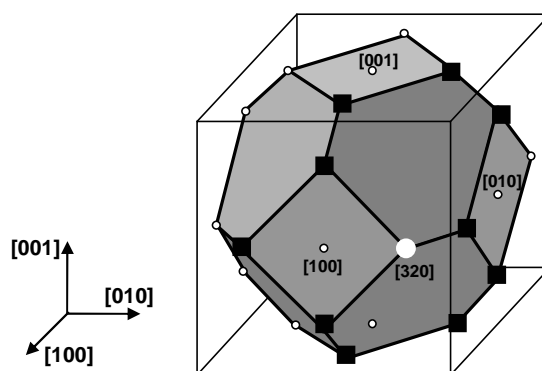
Figure 3-7 The 24 summits of the cube-octahedron represent the 24 $\langle 320 \rangle$ dendrite growth directions observed in the Al-Zn-Si alloy. For a given primary arm direction, e.g. [320] (white circle), only the 10 $\langle 320 \rangle$ directions forming an angle smaller than 90° with the primary arm (black squares) are considered for secondary arms.

As the coating layer is only about 20 μm thick, the dendrite arms will frequently reach the upper and lower boundary of the domain, (III) of Figure 3-6. In this case, the dendrite is projected onto the plane of the boundary and the tip growth velocity is modified according to a relationship determined by phase field simulations.

3.3   Re-solidification experiments

Re-solidification experiments have been conducted in order to determine whether intragranular misorientations can be reproduced in laboratory experiments and to try to identify the mechanisms responsible for the misorientations by modifying the solidification conditions. In a first subsection, the two different furnaces used for the re-melting and re-solidification experiments are described. In a second subsection, a setup which was designed in order to modify the stress/strain state of the coating during the thermal cycle in the infrared furnace is presented. In a third subsection, re-solidification experiments aimed at studying the influence of the free boundary on the misorientations are described.

3.3.1   *Re-melting / re-solidification of coatings*

Induction melting

A first series of re-melting and re-solidification experiments has been conducted with an induction heating apparatus. The objective was to study the morphology and microstructure of the coating formed under laboratory solidification conditions, in particular the influence of re-melting and re-solidification on the crystallographic misorientations. A 15 by 25 mm substrate-coating sample was positioned in the center of a Helmholtz coil. The Helmholtz coil having a radius and an interspace of 5 cm is supposed to generate a uniform magnetic field. The sample is hold by two ceramic tubes in which K-type thermocouple wires are inserted. Two thermocouples were spot welded to either side of the sample and one additional to the center of the sample, which allows monitoring temperature gradients developing within the sample. In order to guarantee good weld joints, the Al-Zn-Si coating has been removed on the lower side of the sample. The substrate-coating sample is induction heated with a frequency of 300 kHz until the coating liquefies. Subsequently, the sample is cooled with the assistance of the Ar flux provided by a cooling nozzle located beneath the Helmholtz coil.
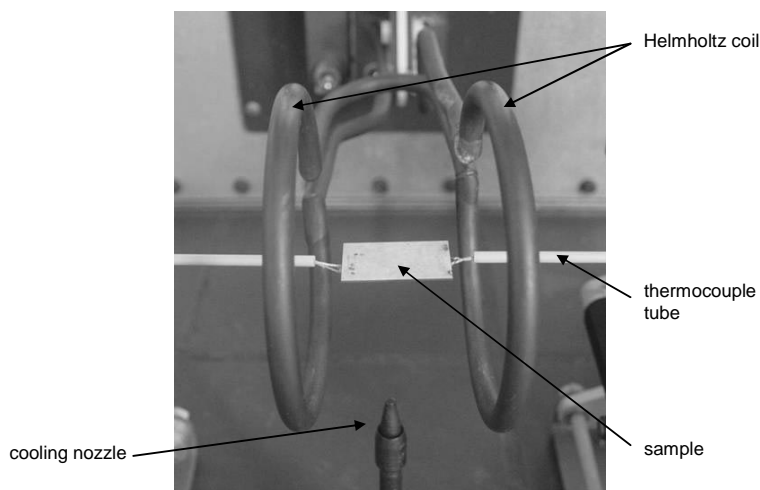
Figure 3-8 Experimental setup for the re-melting and re-solidification of Al-Zn-Si coatings by induction heating.

The cooling rate of the sample can be controlled by the flow rate of the cooling gas. As mentioned above, the coating is removed on the lower side of the sample before the re-melting and re-solidification step. On the upper side of the sample - the side to be analyzed - a short polishing of the surface is done in order to remove surface topography. After the re-solidification experiment, the sample is prepared for metallographic and EBSD analysis according to the procedures described in chapter 3.1.

Melting in the infrared furnace

The major part of the re-melting / re-solidification experiments have been conducted with an infrared furnace which allows a better uniformity of the temperature in the sample and a better control of the temperature sequence. The infrared furnace VHT-E48 of Ulvac-Riko uses four filaments emitting infrared radiation as a heat source. The four filaments of a length of 225 mm are positioned in the focal points of elliptic mirrors. The mirrors reflect the emitted radiation and focus it on the central axis of the furnace which corresponds to the other focal point of the elliptical mirrors, Figure 3-9.

a)   b)
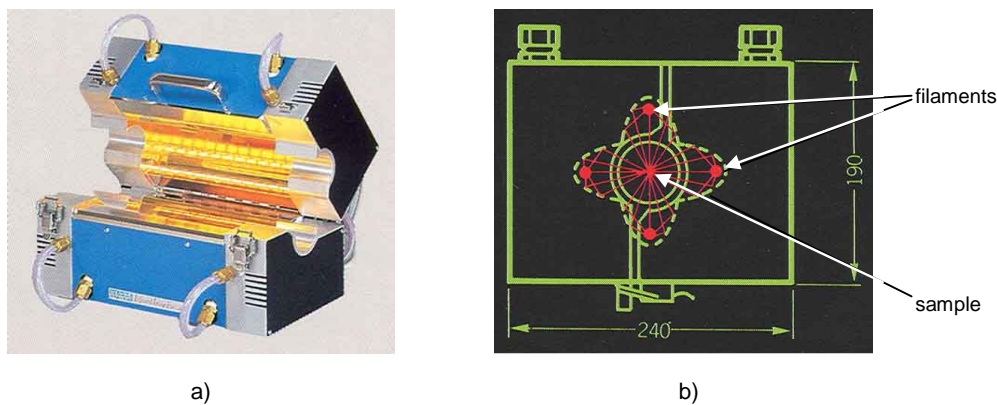
Figure 3-9 a) Illustration of the infrared furnace in the opened state. **b)** Schematic section across the infrared furnace showing the optical path of the radiation that is emitted from the filaments and reflected by the elliptical mirrors.

A quartz tube of 40 mm diameter is positioned along the central axis of the furnace. As the re-melting / re-solidification experiments need to take place within this quartz tube, the sample size is limited. In combination with the rated power output of 24000 W, the small sample size allows reaching high temperatures in very short time. Simple re-solidification experiments comparable to the ones conducted with the induction apparatus have been realized in the infrared furnace. As in the case described previously, the samples were held in position by the ceramic tubes that served as sleeves for the thermocouple wires. As the tubular shape of the experimental chamber does not allow the access to the sample from below or above, the cooling gas was led to the sample from both sides, i.e. parallel to the thermocouple sleeves. The temperature pattern is controlled by an OMRON ES100P console that allows predefining temperature sequences at will (supposed an adequate set of P-I-D values are available).

3.3.2   Solidification under modified stress conditions

The goal of this section is to describe the experiments that have been conducted in order to study the influence of the thermomechanical stresses on the formation of intragranular crystallographic misorientations. A substrate-coating sample on which no external mechanical force is applied is subject to a strain of about $\varepsilon = 0.7\%$ during cooling from the liquidus temperature to room temperature. This strain is due to different thermal contraction behaviour of the steel substrate and the Al-Zn-Si coating and can be quantified by Equation 2.20. As the rigidity of the relatively thick steel substrate is much higher than the one of the thin coating, the strain leads to plastic deformation only in the coating under

normal processing conditions. The chosen experimental approach was to modify the strain to which the Al-Zn-Si coating is exposed during solidification and the subsequent cooling to ambient temperature. Therefore, a setup applying a strain that is comparable to the natural thermal contraction of the coating was designed. By imposing a higher contraction on the steel substrate, the difference in thermomechanical strain between substrate and coating (Equation 2.20) and hence the plastic deformation of the coating is reduced. Samples solidified under such conditions are then analyzed by EBSD and the amount of intragranular crystallographic misorientation found is compared to samples solidified under non-modified solidification conditions.

The basic idea is to constrain a substrate-coating sample in between two massive plates of a material exhibiting a coefficient of thermal expansion close to the one of the Al-Zn-Si coating. The size of the plates surrounding the sample is however limited by the size of the infrared furnace, i.e. the quartz tube of 40 mm diameter, which is used to conduct the re-melting and re-solidification cycle. For the plates, a material with a high coefficient of thermal expansion and sufficient mechanical strength at high temperatures is required. Among all metals used for structural applications, Al and Zn have of the highest coefficients of thermal expansion. Classical engineering metals such as Nickel, Titanium and Copper alloys exhibit coefficients of thermal expansion that are much closer to that of steel than to Al alloys. One of the few exceptions are $\alpha + \beta$ brasses. Their coefficients of thermal expansion are not exactly as high as the ones of Al-alloys, but much closer to them than to the ones of steels. For the constraining plates, CuZn37Pb3 brass was therefore chosen. The physical properties of this alloy are given in Table 3-1. Its thermal expansion coefficient of $21.4 \ 10^{-6} \ \mathrm{K}^{-1}$ (between 20 and 300 °C) is relatively close to the value of Al ($23.5 \ 10^{-6} \ \mathrm{K}^{-1}$).

	T_l [°C]	T_s [°C]	α [K^{-1}]	ρ [kg m^{-1}]	C_p [J kg^{-1} K^{-1}]	κ [W m^{-1} K^{-1}]	E [Gpa]	σ_y [MPa]	R_m [MPa]
Al-Zn-Si	665	487	$23.5 \ 10^{-6}$ [*]				70 [*]		
CuZn39Pb3	890	885	$21.4 \ 10^{-6}$	$8.47 \ 10^3$	398	123	97		80 [**]
carbon steel			$12 \ 10^{-6}$	$7.87 \ 10^3$	482	55	210	335	500

[*] values for pure Al
[**] at 475 °C

Table 3-1 Properties of the Al-Zn-Si coating, the brass plates and the steel substrate. Data for CuZn39Pb3 from [Werkstoff 05], data for carbon steel from [Smithells 99].

When defining the geometry of the brass plates constraining the sample, several

considerations need to be taken into account. First, the setup must be sufficiently small in order to fit into the quartz tube of the infrared furnace. However, the area of the coating solidified under modified conditions needs to be sufficiently large to display a minimum number of grains for the EBSD analysis. Secondly, the thermal inertia of the system must be small so that fast heating and cooling of the sample is possible without having important thermal gradients within the setup. Further, the setup must allow the positioning of thermocouples at several spots of the substrate-coating sample, but also on the outside of the brass plates. And of course, the brass plates must be sufficiently rigid in order to impose their deformation / contraction behavior on the steel substrate which means that the inevitable plastic deformation needs to occur in the steel substrate and not in the brass plates. In order to calculate the thickness required for the brass plates, the mechanical equilibrium condition of the brass-sample-brass sandwich needs to be considered:

$$\sigma_{steel} \, d_{steel} = \sigma_{brass} \, d_{brass} \qquad (3.18),$$

where d_{steel} is the thickness of the steel substrate and d_{brass} is the total thickness of the two brass plates, see Figure 3-10. In order to avoid plastic deformation of the brass disks, its stress level must remain below the yield point. In the literature, values for the mechanical properties of the given brass alloy are reported up to 475 °C [Werkstoff 05]. By extrapolating these data to higher temperatures (up to 600 °C), a maximum acceptable stress of 20 MPa was determined. The stress level in the steel substrate, where plastic deformation is desired, was set to maximum stress at room temperature, 500 MPa, see Table 3-1. From these values and the thickness of the steel substrate (0.5 mm), the minimum thickness of the brass plates was calculated to be 12.5 mm by Equation 3.18. For the final setup, two brass disk of 7 mm thickness where chosen. The relatively small safety margin is justified by the fact that the setup needs to fit into the 40 mm quartz tube. The two brass plates are machined into circular shape and connected by 6 screws of the same material. In the center of the upper disk, a cavity of 7 mm diameter is machined in order to provide room for the Al-Zn-Si coating. Further on, channels are machined into the brass blocs in order to guide thermocouple wires to the central area of the sample. The present setup allows fixing up to four thermocouples on different spots of the substrate-coating composite.

a)   b)
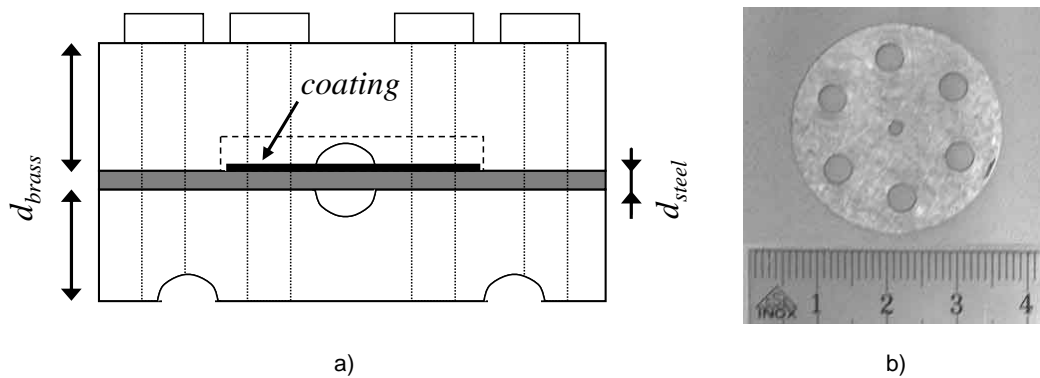
Figure 3-10 a) Schematic side view of the setup constraining the thermal contraction of the steel substrate. Two brass disks of 7 mm thickness and 30mm diameter are positioned above and below the steel substrate. They are held together by 6 screws. A cavity is machined at the center of the upper plate in order to make room for the Al-Zn-Si coating. The thermocouple wires are led to the inner cavity through channels machined into the brass plates. **b)** Top view of a substrate-coating sample exhibiting a diameter of 30 mm. 6 holes are machined into the sample for the screws holding together the brass disks.

The substrate-coating samples are machined to the same shape, exhibiting 6 holes for the screws connecting the brass blocks, Figure 3-10 b). On the lower side of the samples, the Al-Zn-Si coating is totally removed by grinding, on the upper side it is removed by dissolution with hydrochloric acid except in the central area which fits into the cavity of the upper brass disk. Therefore, the brass plates are not in contact with the coating but only with the steel substrate. In order to study the influence of the rigidity of the steel substrate, experiments have been conducted not only with substrates of the initial thickness (~0.5 mm) but also with also with substrates of reduced thickness (0.1 - 0.15 mm).

In the quartz tube of the infrared furnace, the brass-sample-brass sandwich is centered by a sample holder made of Macor glass ceramics, see Figure 3-11 c). To control the cooling rate of the setup, helium cooling gas is applied on the brass setup through the Macor tubes from both sides.

The infrared furnace allows reaching a uniform temperature of 600°C within the brass / sample setup in 80 s. At this temperature, the Al-Zn-Si coating layer is liquid. Subsequently, the setup is cooled by the He gas flow. Experiments with cooling rates in the range of 1 to 15 K/s were realized. The re-solidified coatings were then analyzed as it was described in chapter 3.1.
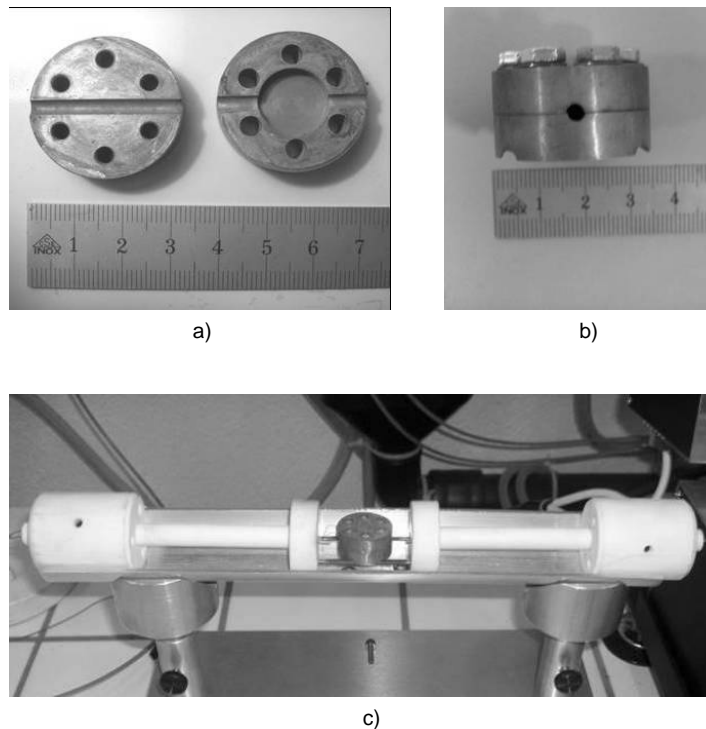
Figure 3-11 a) The inner sides of the two brass plates displaying the thermocouple channels and the central cavity. **b)** the two brass plates screwed together (without a sample in between them). **c)** Setup ready to be inserted into the infrared furnace. The brass plates are held in position by a ceramic sample holder. The two lateral ceramic tubes conduct the cooling gas and the thermocouple sleeves.

3.3.3   *Solidification of Al-Zn-Si layers with no free boundary*

Further experiments have been conducted in order to determine the influence of the free surface on the intragranular crystallographic misorientations. The idea is to compare re-solidified Al-Zn-Si coatings with Al-Zn-Si layers confined by two steel substrates and re-solidified under identical conditions. Normal coatings of course exhibit an interface between the coating layer and the ambient air, which is not the case for Al-Zn-Si interlayers confined between two steel layers. This difference may be of importance as the solidification shrinkage is accommodated differently in the two cases. The challenging step is to produce Al-Zn-Si interlayers confined by steel on both sides. In order to reproduce as well as possible the microstructure found in coatings, it was chosen to prepare steel / Al-Zn-Si / steel sandwiches by joining two Al-Zn-Si coated steel substrates on their coated side. The simple superposition of two coating layers would not lead to a single, compact Al-Zn-Si interlayer upon re-melting since the two coatings would remain separated by the oxide films at their surfaces. During the subsequent re-solidification step, the solidification

shrinkage would be accommodated by creating voids in between the two oxide skins which would be equivalent to what happens at the surface of a simple Al-Zn-Si coating. In order to truly eliminate the free surface during the re-solidification step, the two coating layers need to be joined beforehand by a method that destroys oxide skins at their surfaces without promoting growth of the intermetallic layer at the coating-substrate interface. The method chosen for this joining step is ultrasonic metal welding. In this process, the substrate-coating samples are placed between a fixed machine part, i.e. the anvil, and the sonotrode, which oscillates horizontally during the welding process at high frequency of 20 kHz. Unlike in other welding processes, the parts to be welded are not heated to melting point, but are connected by applying pressure and high-frequency mechanical vibrations. Ultrasonic metal welding involves static forces and oscillating shearing forces breaking the oxide skins into pieces and stirring them into the coating. Meanwhile, the temperature increase during the welding process is only moderate.

For the re-melting / re-solidification experiments on ultrasonic welded samples, the same sample geometry was chosen as for the experiments described in the previous section. Prior to welding, the samples where polished down to 1 μm diamond grits in order to remove all surface roughness. A rectangular weld spots of 8 x 10 mm was applied in the center of the 30 mm sample disks by TELSONIC AG Bronschhofen, Switzerland. Subsequently, the samples underwent re-melting and re-solidification in the setup described in the previous section in order to guarantee comparable temperature but without tightening the screws between the brass blocs.

CHAPTER IV

RESULTS

In this chapter, the experimental and simulation results are presented. The results are structured in methodic sections that are aligned with the structure of chapter 3. In section 4.1, the results of the characterization of the coatings are shown. Section 4.2 summarizes the results of the three modeling approaches described in section 3.2 and section 4.3 shows the results of the re-solidification experiments. Since chapter 5 (*Discussion*) is structured in two thematic sections, *Microstructure formation* and *Mechanism leading to intragranular misorientations*, it will not follow point by point the results that are presented here. As a consequence, this chapter not only presents raw data but contains already some elements of interpretation in order to provide a sufficient basis for the following *Discussion* chapter.

4.1 Characterization of industrial coatings

This sections aims at giving an overview of the microstucture in Al-Zn-Si coatings. A first subsection presents the phases and their morphology that are observed in the coating system. Further on, results on the surface appearance and surface topography as well as the microsegregation and the intragranular misorientation are presented as far as they are of relevance for the discussion of the microstructure formations and especially the

formation of intragranular misorientations.

4.1.1 *Phases and morphology of phases in Al-Zn-Si coatings*

In order to study the microstructure and the phases present in Al-Zn-Si coatings produced industrially by BHP Steel, today BlueScope Steel, metallographic sections have been prepared in the plane of the coating and perpendicular to the coating as described in section 3.1.1. Figure 4-1 shows an assembly of micrographs of an Al-Zn-Si coating surface after mechanical and electropolishing. It becomes apparent that the grain size is in the order of millimetres. From the micrograph, one can directly discern the nucleation centres (dots) and the dendrite structure for each grain (dashed lines).
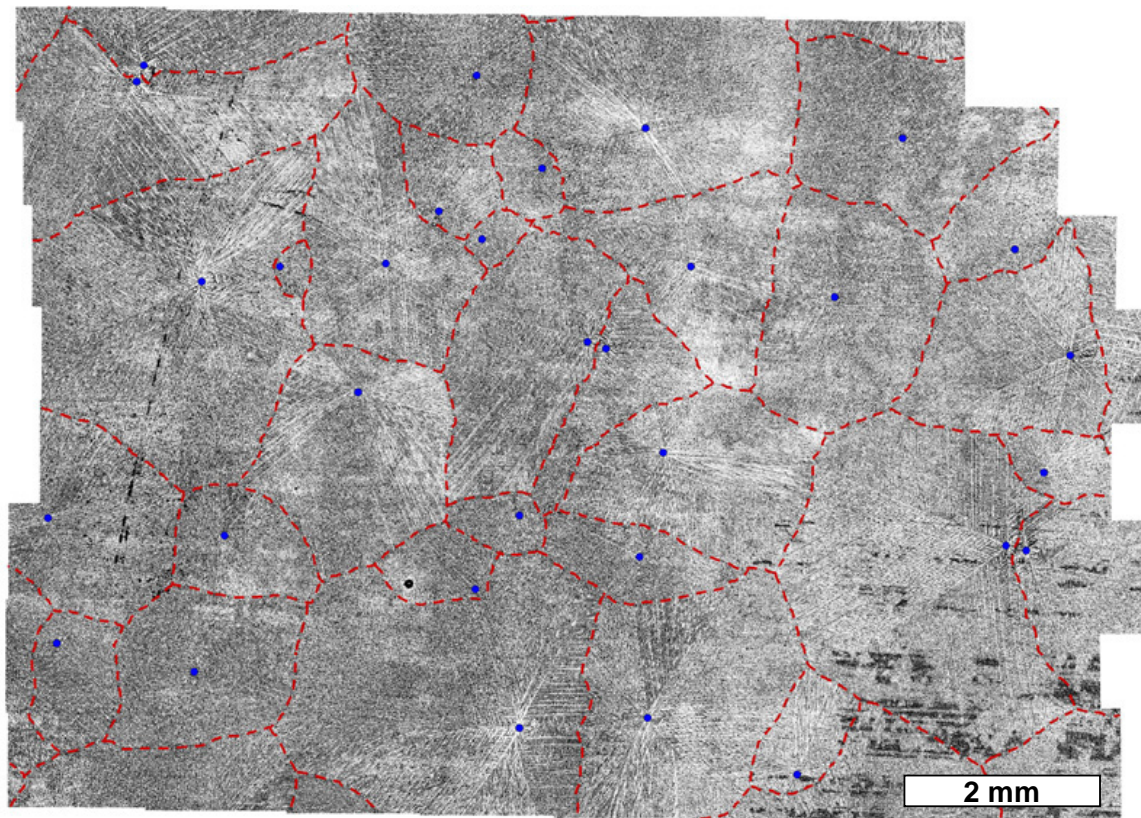
Figure 4-1 Optical micrograph of the surface of an Al-Zn-Si coating after mechanical and electropolishing. Grain boundaries are highlighted with dashed lines, nucleation centers with dots. Within the grains, the dendrite structure is visible to some extent.

After mechanical polishing of the coating surface, dark Si particles in the form of platelets or needles randomly scattered in the coating are revealed under the optical microscope, Figure 4-2 a). If upon the mechanical polishing, an electropolishing step is

added, the dendrite structure becomes exposed, Figure 4-2 b). On the electropolished samples, the dendrite arms spacing λ_2 has been determined by conducting measurements on optical micrographs. For industrial coatings, a mean dendrite arm spacing of 11.2 μm has been found. During the electropolishing step, the Zn-rich interdendritic areas are dissolved preferentially whereas the Si-needles are not etched at all. It is apparent in Figure 4-2 b) that the dark Si particles are in general located in the interdendritic areas. In order to analyze the interdendritic areas, scanning electron microscopy (SEM) has been performed. As Al and Si have a low atomic number, they produce a chemical contrast with respect to Zn even in the secondary electron mode. Figure 4-2 c) and d) show secondary electron micrographs of mechanically polished coating surfaces. Besides the dark Si needles and platelets, the internal structure of the interdendritic eutectic becomes visible. The eutectic islands have an irregular structure displaying the Zn-rich phase in bright and the Al-rich phase in dark tones. The eutectic islands are surrounded by a zone in which coarse Zn-rich precipitates (bright) are embedded in an Al-rich matrix. Within the core of the dendrites, however, no precipitates can be detected by the means of SEM on mechanically polished surfaces.
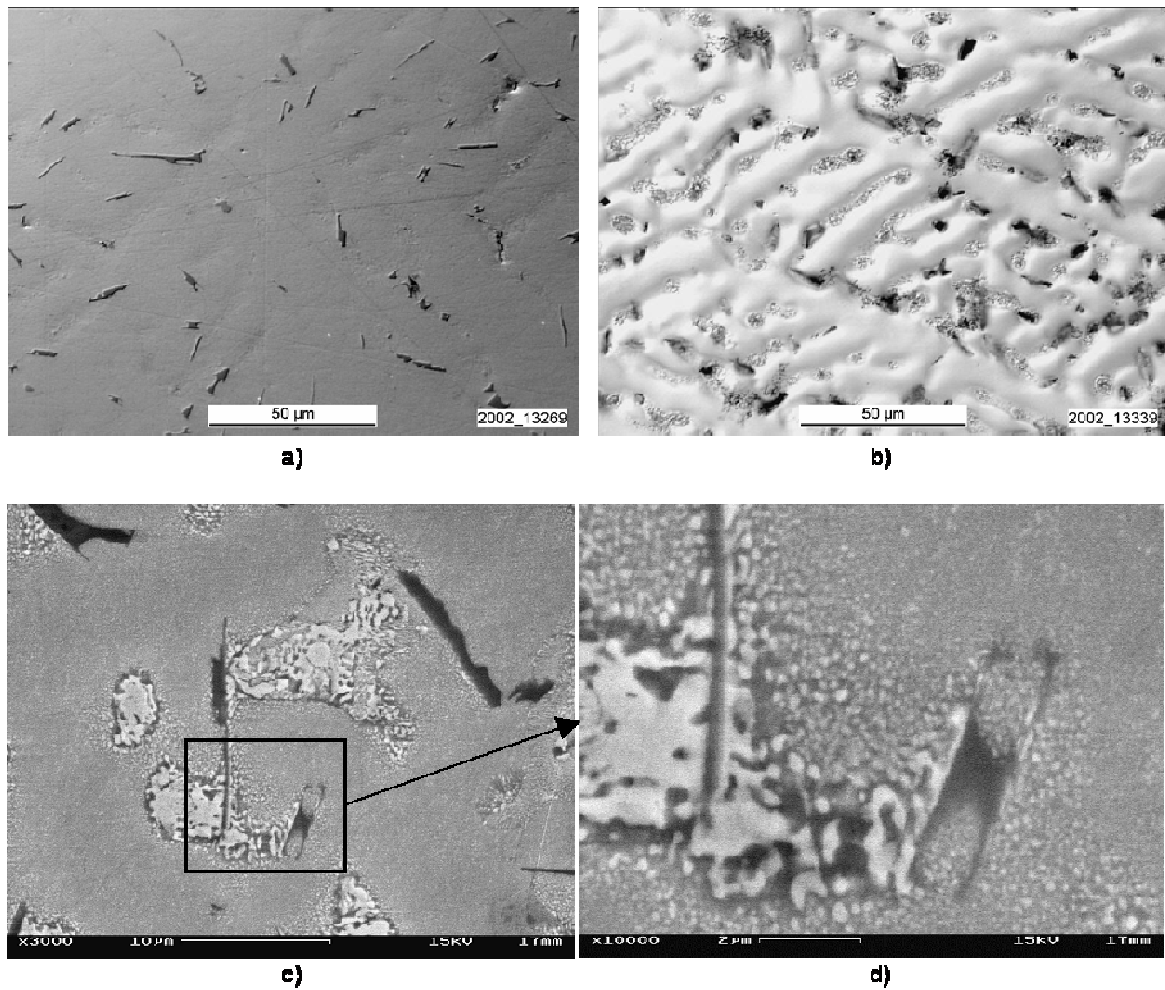
Figure 4-2 Microstructure in sections parallel to the coating plane. **a)** Optical micrograph after mechanical polishing, **b)** after additional electropolishing. **c, d)** scanning electron micrographs.

Further information about the microstructure can be gathered through the examination of metallographic cross-sections through the substrate-coating composite, Figure 4-3. It is found that in general, the Al-Zn-Si coating has a thickness of about 20 μm. On an optical micrograph of a polished cross-section, the only microstructural features visible are again the Si-particles (Figure 4-3 a). Si-particles are dispersed in the coating layer but many of them are connected to the substrate-coating interface, or rather to the intermetallic layer present at this interface. A closer look to the situation at the substrate-coating interface is obtained through SEM observation of a Focused Ion Beam (FIB) – prepared lamella, Figure 4-3 b). The figure displays two neighboring Al-rich dendrite arms(1) and the steel substrate (2). On top of the Al-Zn-Si coating, a Pt layer (3) has been applied in order to protect the coating during the ion-milling process. In between the two dendrite cores, there is an area where the two dendrites coalesced. The higher

concentration of Zn in this area is revealed by the presence of coarse Zn-rich precipitates (4). The intermetallic layer (5) is continuous and of an irregular thickness of less than 1 μm in most places. At a spot where the intermetallic layer is particularly thick, the following composition was measured by EDS: 48.4Al 28.6Fe 13.9Zn and 9.2Si (in wt.%). The only Si particle visible on this micrograph (6) is located on the intermetallic layer. Also, it can be seen that the dendrite cores are not in direct contact with the substrate-coating interface. They are separated by a layer of eutectic (7), which spreads along the boundary between the intermetallic layer and the dendritic microstructure.
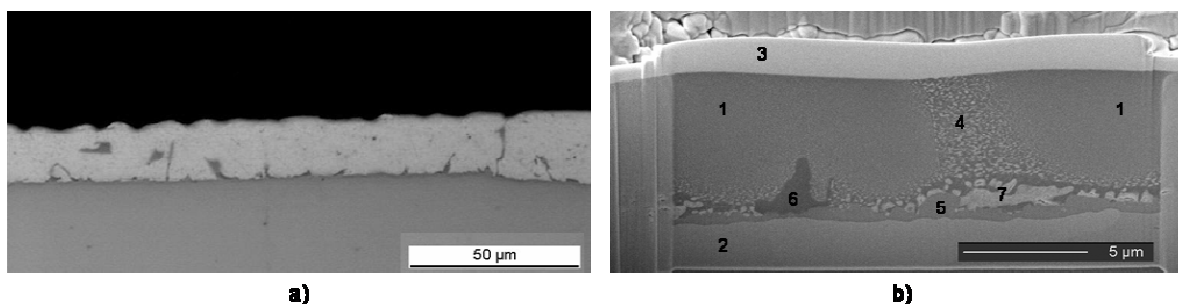
Figure 4-3 a) Optical micrograph of a cross-section through a substrate-coating composite. **b)** SE-electron micrograph of a FIB-prepared lamella showing the interface between substrate and coating.

In order to gain a better understanding of the structure within the dendrite arms and at the boundary between substrate and coating, TEM analyses have been performed on lamellae prepared by FIB. Assemblies of bright field micrographs of two TEM lamellae are shown in Figure 4-4. Both lamellae are cut perpendicular to the coating plane. In the lower part of the images, the steel substrate is visible. It is covered by an Al-Fe-Si-Zn intermetallic layer of irregular thickness. Above the intermetallic layer, the dendritic microstructure of the Al-Zn-Si coating is displayed. Note that the top of the lamella does not correspond to the free surface of the coating, since a top layer of the coating was removed by polishing before the lamellae were milled. On both micrographs, two dendrite arms belonging to the same grain, one to the left and one to the right, are visible. The two dendrites in Figure 4-4 a) impinged on each other during growth and coalesced before the ternary eutectic temperature. The vertical line visible in the center separates the two dendrite arms. The two dendrite arms in Figure 4-4 b) remained separated by interdendritic liquid until the ternary eutectic temperature was reached. The gap between the two dendrites is therefore filled with Al-Zn(-Si) eutectic. Due to the mass-thickness contrast, the Zn-rich β-phase is dark and the Al-rich α-phase appears bright.
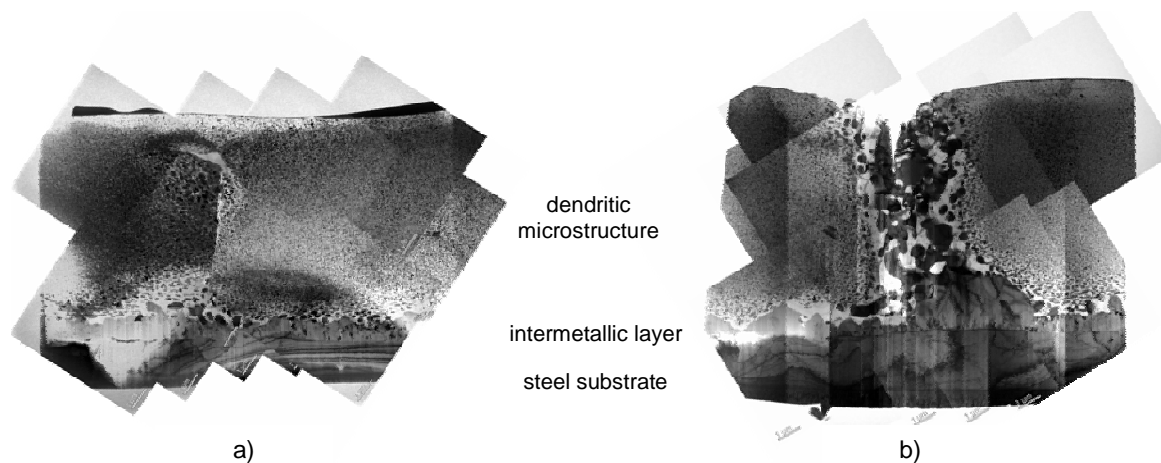
Figure 4-4 Assemblies of cross-sectional TEM bright field micrographs of Al-Zn-Si coatings.

The contrast visible within the dendrite arms is due to precipitates that are scattered in the fcc-matrix of the dendrites. The precipitates make up a considerable volume fraction even in the dendrite core which is not surprising considering the important solubility of Zn at high temperatures in the α-Al phase. The size of the precipitates depends to a certain extent on the position within the dendrite arm. In the dendrite core, the size of the precipitates varies typically between 20 and 50 μm. The precipitates display an oblate parallelogram shape (Figure 4-5 a), indicating that they are of irregular parallelepiped shape. The orientation of the precipitates is not random with respect to the matrix. By changing the diffraction conditions in the bright field mode, i.e. by reorienting the lamella with respect to the electron beam, different sets of precipitates can be identified. This means that: (i) there is an orientation relationship between the matrix and the precipitates and (ii) the different sets are due to different possible orientation relationships between the precipitates and the α-fcc-matrix.
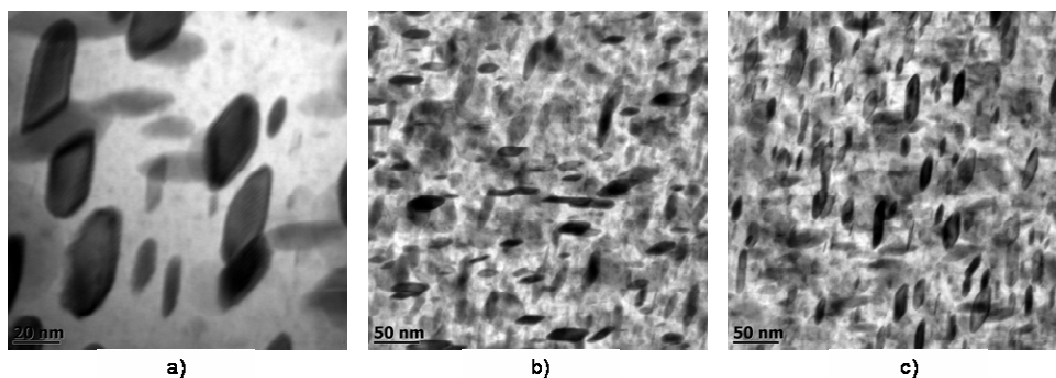
Figure 4-5 a) Typical precipitate morphology in the core of a dendrite arm. **b, c)** Bright field TEM micrographs of the same area taken under different diffraction conditions.

The presence of different but closely related sets of parallelepipedic precipitates displaying orientation relationships with the α-Al matrix corresponds well to what has been described in section 2.1.4 and what was reported by [Simerska 78] and [Löffler 91]. One can assume that the precipitates are coherent and that the cubic $(111)_{cub}$ planes are aligned with the hexagonal $(00.1)_{hex}$ planes. Since there are 4 $(111)_{cub}$ planes but only one $(00.1)_{hex}$ plane, several sets of precipitates can be formed.

At the periphery of the dendrite arms, the precipitates are larger and do not exhibit the typical parallelepiped shape, see also Figure 4-6 f). This is probably due to the fact that Zn concentration is locally higher as the periphery solidified later in the solidification path. The higher Zn concentration may lead to larger precipitates and a loss of the coherency between matrix and precipitates.

Further information on the microstructure formation in Al-Zn-Si alloy coatings can be obtained from SEM on coatings in the as-solidified state, i.e. coatings that were neither polished nor etched. In the area shown in Figure 4-6 a), which is close to the nucleation center of an α-Al grain, most typical microstructural features of Al-Zn-Si coatings are present. There are first the cores of dendrite arms (1) and primary phase areas which formed later in the solidification path and therefore exhibit a coarser precipitation structure (2). An eutectic island of non-lamellar internal structure (3) is visible in between the dendrite trunks. Further on, one can observe the rare case of a facetted intermetallic particle (4) that is even visible at the free surface of the coating. The intermetallic particle has been identified as such by EDS. From the experimental evidence, it is not possible to say whether it is a coincidence that the nucleation center of the α-Al grain is located so close to a prominent intermetallic particle. Some authors have argued that intermetallic particles might serve as nucleation centers for α-Al grains [Sémoroz2 01]. In addition the micrograph also displays a faceted Si particle (5). The Si particle is located in the interdendritic area, which seems obvious considering the fact that the Si phase is a secondary phase which appears in the solidification sequence after the development of the dendrite network. It is apparent that the Si particle is connected to the intermetallic particle. It is uncertain whether this is a coincidence or whether the intermetallic particle can serve as a nucleation center also for the Si phase. Another interesting observation is that the Si phase is surrounded by bright Zn particles. It seems that Zn-rich β precipitates preferentially nucleate at the Si- α-Al interface.

From the surface micrographs, it can also be seen that two different eutectic microstructures are possible in Al-Zn-Si coatings. In most cases, divorced eutectic structures are observed. In some cases however, coupled, lamellar eutectics are also possible. Figure 4-6 d) and e) show zones where both forms are present. In Figure 4-6 d), divorced eutectic is visible along the dendrite arm located in the lower left corner of the image. It is characterized by the dark, eutectic α-Al phase that forms epitaxially on the α-Al dendrite. Big nuggets of β-Zn form on top of the α-Al. Figure 4-6 d) shows the transition from a divorced to a fine, coupled eutectic. β-Zn lamellae grow out of the β-Zn nuggets whereas α-Al lamellae seem to develop from them. The increasing undercooling due to the considerable cooling rate during the eutectic reaction may be the origin of this transition as the coupled growth mode becomes more competitive at higher undercoolings. The same phenomenon can be observed in Figure 4-6 e) where a zone of coupled eutectic is embedded in divorced eutectic.

Figure 4-6 f) shows in detail the transition from fine precipitates in the dendrite core, to coarse precipitates at the periphery of the dendrite arms and eutectic areas. The transition from dendrite core with its fine, oriented precipitate microstructure to the coarser precipitates of the dendrite periphery is quite sharp whereas it is not easy to exactly identify the boundary between coarse precipitates and the divorced eutectic.

In summary, it is observed that:

- the microstructure is dominated by a network of α-Al dendrites

- in the interdendritic areas, Si particles form as a secondary phase

- eutectic islands of α-Al and β-Zn are observed in between the dendrite arms. Both, divorced and lamellar eutectic structures can occur.

- within the dendrite arms, a high volume fraction of precipitates is present. In the core of the dendrite arms, the precipitates are fine and coherent whereas they are much coarser in the periphery of the dendrite arms.
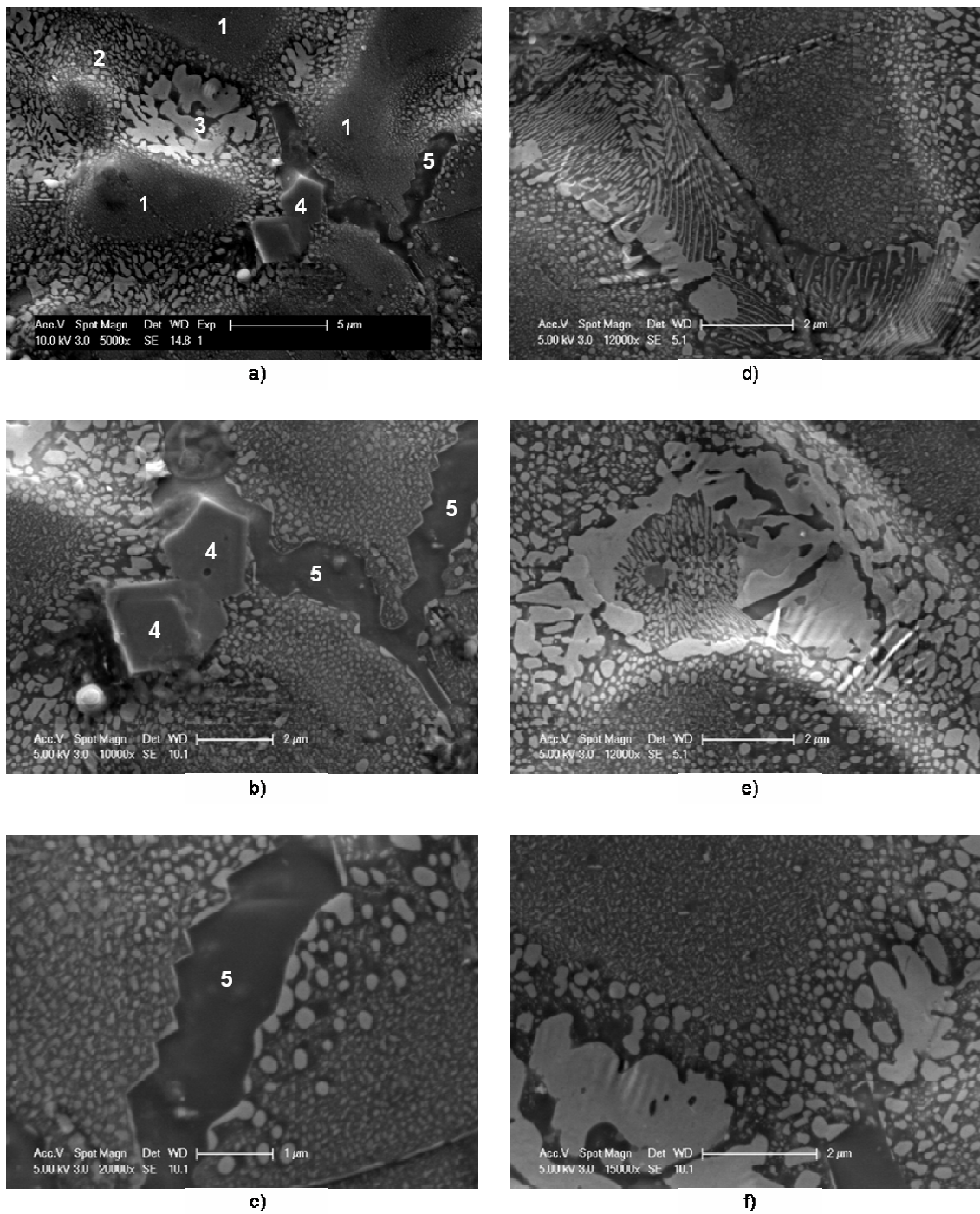
Figure 4-6 Secondary electron micrographs of the coating surface in the as-solidified state (no polishing or etching).

4.1.2 Visual surface appearance

As seen in the previous subsection, Al-Zn-Si coatings typically present large grains with diameters in the order of millimetres. Upon visual inspection by naked eye, the grain structure, or spangle structure as it is often termed, is readily visible. The goal of this subsection is to report some basic findings about the spangle structure.

The spangle structure is made up of alternating dull and shiny areas or sectors within the equiaxed grains, Figure 4-7. One grain consists in general of 6 to 8 sectors. The nucleation centre of the grain can readily be identified as it is the spot where the sectors of one grain meet. The dendritic nature of the coating is directly apparent on the optical micrographs, Figure 4-8, especially in the shiny sectors of the grains. The boundaries between the sectors normally correspond to the primary dendrite arms emitted from the nucleation centre of the grain.
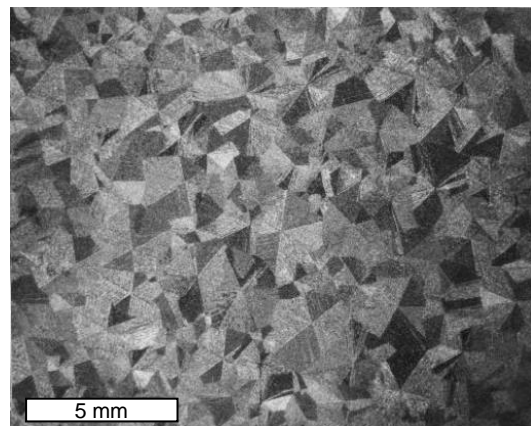
Figure 4-7 Typical sprangle structure as it is observed by visual inspection of Al-Zn-Si coatings.
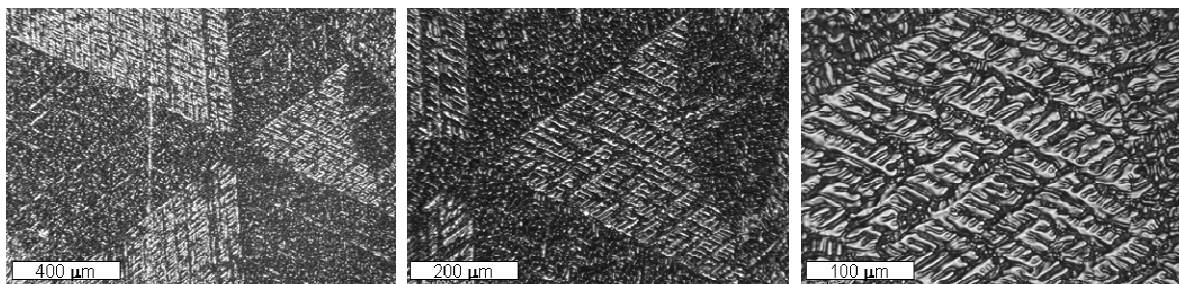
Figure 4-8 Shiny and dull sectors within a grain on optical micrographs.

Another interesting feature of the microstructure that is already visible by naked eye is the number of primary dendrite growth directions present in the coatings. As it was

already highlighted by Sémoroz et al. [Sémoroz1 01], 6 or 8 dendrite growth directions can be present in the plane of the Al-Zn-Si coating. Sémoroz et al. explained this "anomaly" by the proposition that the dendrite tips grow along the $\langle 320 \rangle$ crystallographic directions in the Al-Zn-Si alloy system instead of the $\langle 100 \rangle$ directions that are usually observed in fcc metals. Indeed, this result was confirmed in the present study. By comparing the dendrite growth directions visible on optical micrographs with $\langle 320 \rangle$ EBSD pole figures of the same grain, Figure 4-9, it becomes apparent that the growth directions correspond well to the $\langle 320 \rangle$ orientations which exhibit a small angle with the coating plane. The EBSD analysis also shows that 6 distinct dendrite growth directions are present when the normal to the coating is either close to a $\langle 110 \rangle$ or to a $\langle 111 \rangle$ crystallographic direction (Figure 4-9 a). Eight dendrite growth directions are observed for grains having $\langle 100 \rangle$ close to the coating normal (Figure 4-9 b).

a)   b)
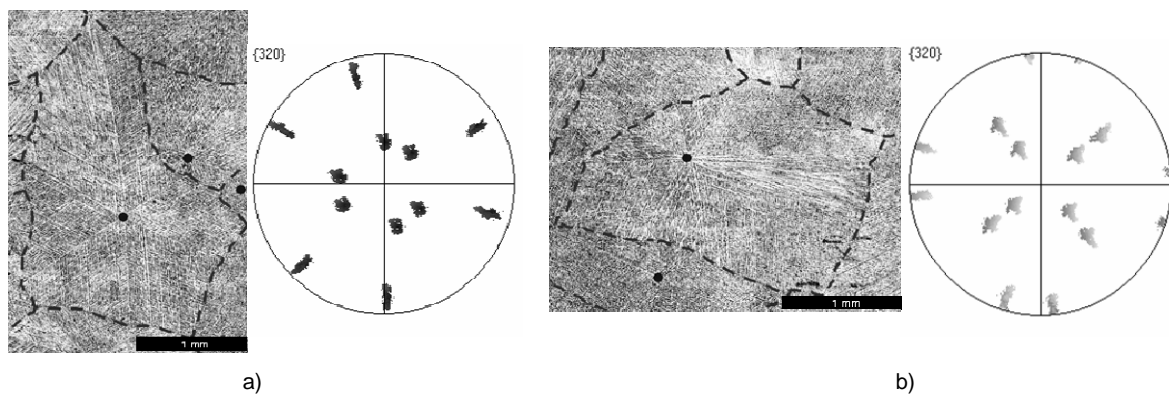
Figure 4-9 Micrographs revealing the dendrite structure and corresponding $\langle 320 \rangle$ EBSD pole figures. **a)** a grain with [111] as coating normal, **b)** a grain with [100] as coating normal.

4.1.3   Surface topography

The surface topography of an untreated (as-solidified) Al-Zn-Si coating was measured by laser profilometry. Figure 4-10 a) shows a false color map of the surface topography of $1mm^2$ area around the nucleation center of a grain exhibiting 6 predominant dendrite growth directions and 6 alternating dull and shiny sectors that are typical for a grain having an $\langle 111 \rangle$ orientation aligned with the coating normal. The dendrite structure visible on the optical micrograph, Figure 4-10 b) is clearly reflected in the topography map. As expected, elevations correspond to dendrite arms and depressions to interdendritic areas. Moreover, the six sectors between the six primary dendrite trunks do not all have the same overall height level. The three dull sectors are lower (green dominates), the three shiny sectors are higher (yellow dominates). For the different sectors, r_a values were

measured in order to quantify the roughness. The results indicate that the more elevated (yellow) sectors are in general smoother. However, roughness measurements on these surfaces are delicate as the dendrite arms are oriented. Therefore the r_a measurement results could vary depending on the direction in which the measurement was done.
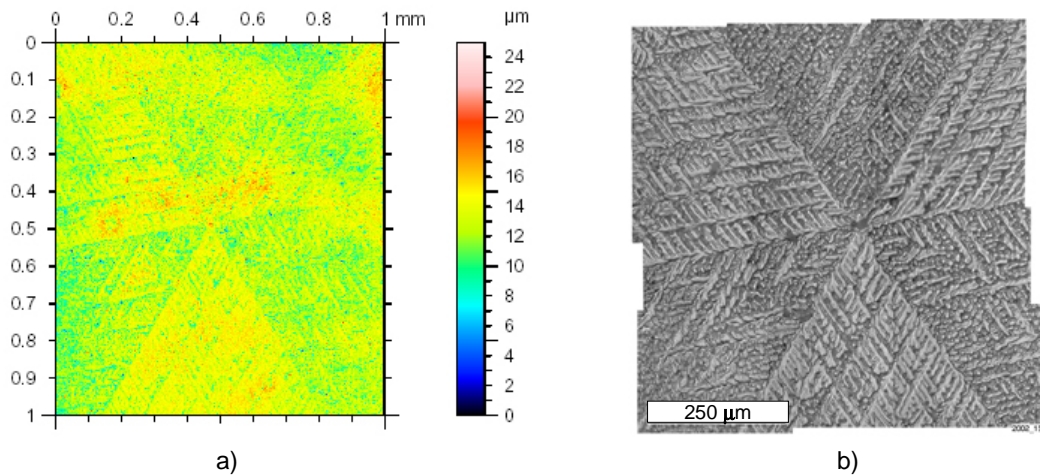
Figure 4-10 a) False color map representing the surface topography at the center of a grain. **b)** Corresponding optical micrograph.

In order to get more detailed information on the surface topography, AFM mapping of the coating surface has been performed. Figure 4-11 shows an AFM map of an area where both shiny and dull morphologies are present. The shiny part in the upper half shows dendrite arms grown along the surface of the coating, whereas the dendritic nature of the structure is much less apparent in the lower dull part. In the dull part, the surface topography is dominated by hillocks and dimples. Unlike the case of the shiny area, the dendrite arms obviously did not grow along the surface of the coating, but rather in the center or at the substrate-coating interface. It seems sensible to assume that the surface topography of hillocks and dimples is the result of ternary dendrite arms growing towards the surface from within the coating.

a)   b)
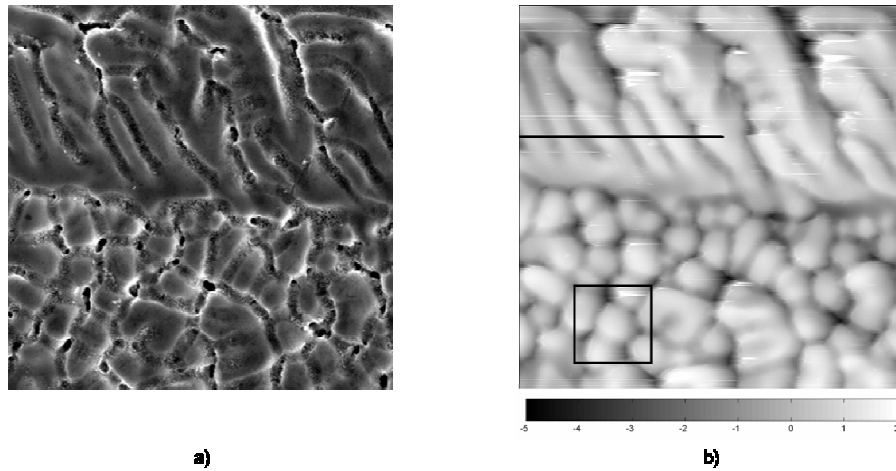
Figure 4-11 a) SE micrograph and **b)** AFM topography map of a selected area of the coating surface displaying shiny morphology in the upper part and dull morphology in the lower part. The AFM mapping covers an area of 100 x 100 µm.

From the AFM map of Figure 4-11, topography profiles have been extracted. Figure 4-12 shows the profile along the black line indicated in the shiny zone of Figure 4-11 b). The profile is taken almost perpendicular to the local predominant growth direction of secondary arms. It clearly shows the individual dendrite arms as elevations and the intermediate interdendritic areas as depressions. Given the fact that the scales of the x and y axis are equivalent, it is striking that the local inclination at the coating surface can be significant, even though the interdendritic depressions are not as deep as in other parts of the coating and not filled with eutectic which indicates that the dendrite arms coalesced before the ternary eutectic temperature was reached. In other areas, especially also in the dull sectors, even much deeper depressions can be found.
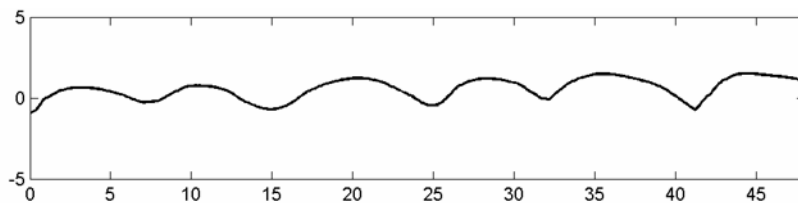
Figure 4-12 Surface topography profile measured along the black line in Figure 4-11. Units in µm.

Further inspection of the microstructure in the shiny sectors shows that the dendrite arms obviously growing along the free surface are not continuous over long distances. After a couple of 100 µm at the largest, the dendrite arms at the surface are overtaken by other dendrite arms emerging from within the coating, Figure 4-13.
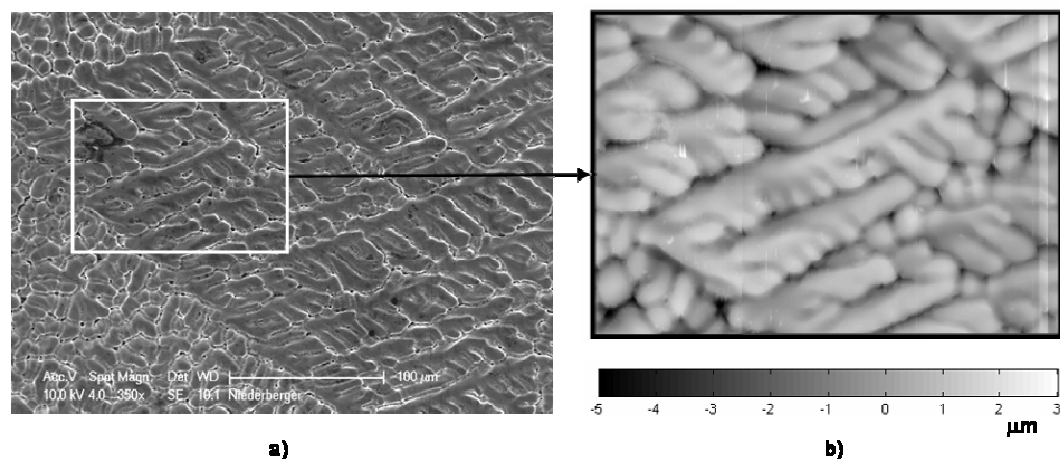
Figure 4-13 a) SE-micrograph showing a dull area in the lower left corner and a shiny area in the rest. **b)** AFM topography map in the shiny area. The size of the AFM mapping is 100 x 140 μm.

Figure 4-14 shows a higher resolution AFM mapping of a 20 x 20 μm area which is representative of a dull sector. The analyzed zone corresponds to the black frame displayed in Figure 4-11 b). Firstly, the presence of deep depressions in between the humps can be noted. When shadowing is applied to the topography map, Figure 4-14 b), wrinkle structures become visible in the depressions separating the humps. The same wrinkles can also be observed as fine lines on SE-micrographs of the corresponding area, Figure 4-14 c). The wrinkles typically occur in spots where one of the principal curvatures of the surface is positive and the other is negative. The wrinkles are then in general aligned along the direction of negative curvature. This also explains why such wrinkle structures are more abundant in dull areas than in shiny ones. Shiny areas are dominated by well aligned, parallel dendrite arms where one of the principal curvatures is always close to zero.
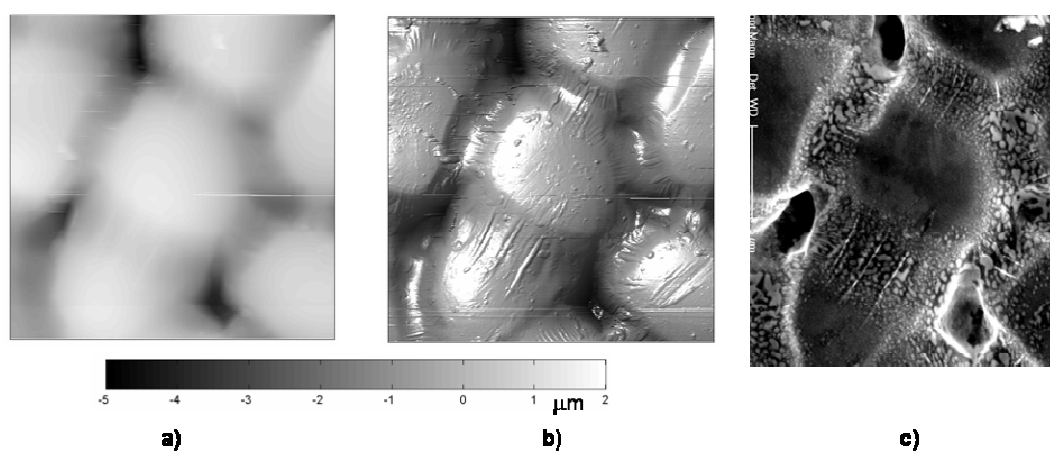
Figure 4-14 a) AFM topography map of 20 x 20 μm area in a dull sectors. **b)** Upon the application of

shadowing, wrinkle structures become visible on the topography map. **c)** SE-micrograph of the corresponding area.

In summary:

- shiny and dull sectors are visible on the surface of Al-Zn-Si coatings

- the dominant dendrite growth directions are close to ⟨320⟩ as it has already been shown by Sémoroz et al. [Sémoroz1 01].

- laser profilometry shows a slight overall level difference between shiny and dull sectors.

- AFM measurements show a pronounced relief at the surface of the coating. The local inclination of the surface can be substantial.

- the dendrite arms in shiny sectors are not continuous but repeatedly undergo branching.

- wrinkle structures are observed on the surface of the coatings.

As will be seen in section 5.2, the surface relief, the repeated branching and the wrinkle structures observed in this subsection provide valuable information for the discussion of the misorientation mechanisms.

4.1.4   *Solute distribution in the coating*

Figure 4-15 shows typical concentration profiles measured by GDOES. It shows that the concentration is not homogeneous in the Al-Zn-Si coating. Maxima of the Al-concentration are observed close to the surface of the coating and towards the substrate-coating interface. In the centre and at the very surface of the coating, maxima of Zn concentration are observed. Figure 4-15 b) shows also the profile of silicon. It appears that silicon is present throughout the coating layer, but its composition increases towards the interface with the substrate, which is in good agreement with the metallographic observation that Si particles are often attached to the intermetallic layer. At the substrate-coating interface, the transition of the concentration profiles seems quite smooth. In part, the intermetallic layer that is composed of Fe, Al, Si and Zn may be responsible for this, but the blurring of the interface is certainly also due to the topography which is already

present in the beginning at the surface of the coating and that subsequently propagates during the sputtering process. However, it seems clear that the origin of the concentration differences within the coating is microsegregation. The maxima of Al concentration observed in the vicinity of the two boundaries confining the coating layer show that these are the preferred areas for the growth of the primary α-Al dendrites during the formation of the dendrite network.
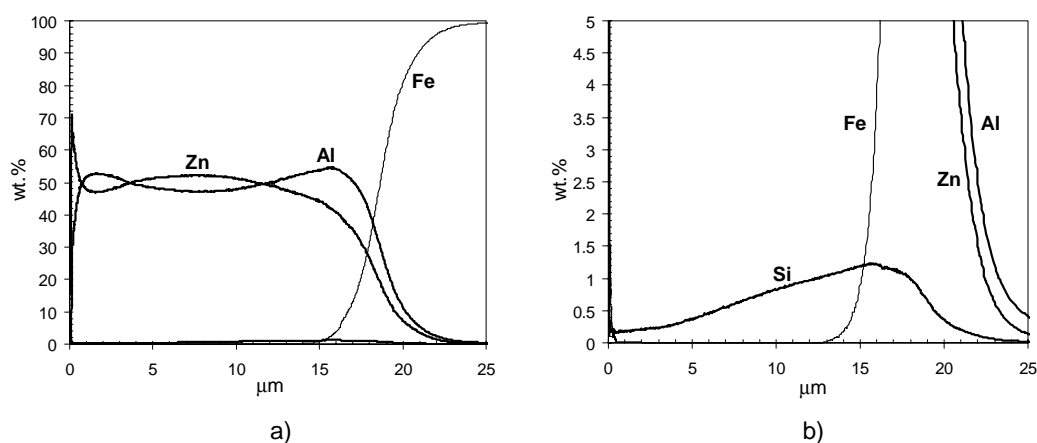
Figure 4-15 GD-OES depth profile of the concentration within the Al-Zn-Si coating. **a)** and **b)** show the same curves but with different concentration scales.

Wavelength dispersive microprobe mappings have been made on samples polished parallel to the coating surface in order to gain a better understanding of the microsegregation within the plane of the coating. Figure 4-16 shows a false color map giving the intensity of k_α-Al X-ray signal. Unfortunately, no fully quantitative analysis of such large mappings is possible. The concentration map shows one grain having its nucleation spot about centered in the mapping. The dendritic nature of the microstructure is clearly visible. The Al-rich dendrite trunks are displayed in pink and red colors whereas the interdendritic areas are green and yellowish. From the center of the grain to the periphery, there is no systematic change in concentration. The overall concentration in the center and at the fringes of the grain are about the same. However, a structure of sectors meeting in the nucleation center seems to be discernable on the concentration mapping. Three sectors are more reddish and exhibit a higher overall Al concentration than the three other sectors.
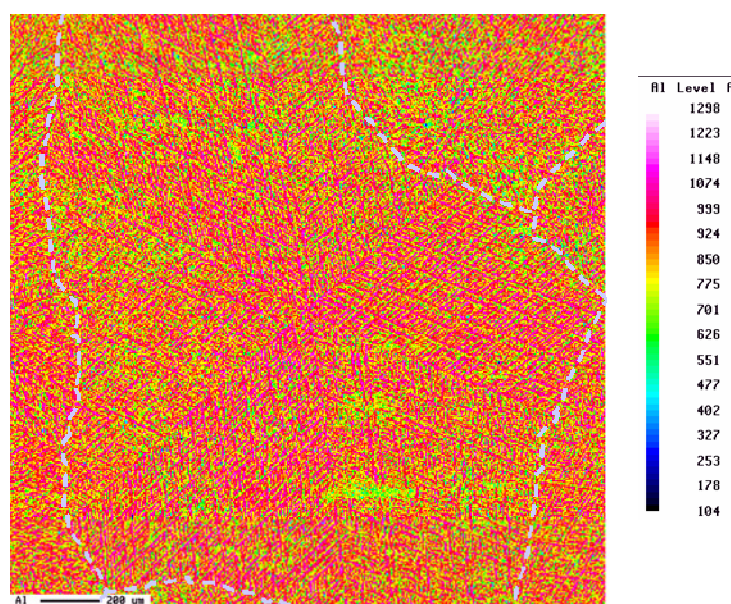
Figure 4-16 Semiquantitative map of the Al concentration within the plane of the coating realized by WDS. Pink/red color indicate high Al concentration, Blue/green color indicates low Al concentration. The dashed gray line represents the grain boundary. The map corresponds to an area of 2 x 2 mm.

The alternating sequence of the sectors indicates that the solute distribution is different in the shiny and dull sectors described beforehand. The analyzed sample has only been polished slightly in order to get rid of the surface topography and we estimate therefore that the concentration measurements have been performed close the surface or at least in the upper half of the coating layer. It is hence sensible to assume that the sectors with higher Al concentration correspond to shiny sectors where the dendrite arms seem to grow along the surface of the coating.

WDS mappings have also been recorded on cross-sections through the coating. The concentration mapping displayed in Figure 4-17 a) shows an area on which both shiny and dull surface appearances are present. Examination of the coating free surface adjacent to the cross-section allowed for the determination of the corresponding surface appearance of the mapped area. On the left hand side, the surface appears dull whereas it is shiny on the right hand side. The two sectors are separated by a primary dendrite arm growing almost perpendicular to the displayed section. As it is very difficult to orient the cross-section along the predominant growth direction in one sector and it is absolutely impossible to do this for both of the adjacent sectors, the Al-intensity mapping exhibits an irregular, patchy structure with dendrite arms intersecting the plane of observation at different angles. The surface appearance can be related to some extent to the dendritic network observed in the cross-section where dendrites seem to follow the free surface only in the shiny sector. Near

the center of the map, just right of the vertical bar separating dull and shiny sector, a dendrite arm was emitted close to the substrate and grew to the right with an inclination of about 7° before reaching the free boundary. This may be regarded as a transient regime before growth could really take place along the free surface (right hand side of the shiny sector).

In order to have more quantitative description of the microsegregation pattern, the measured intensities were averaged along x and displayed as a function of z in Figure 4-17 b) for the dull sector and Figure 4-17 c) for the shiny sector. Note that the "transient" zone on the left hand side of the shiny sector was not considered for the analysis. For both the dull and shiny sectors, local maxima of the Al signal are observed at about ¼ and ¾ of the coating thickness. However, for the dull sector, the global maximum is close to the substrate whereas it is close to the free surface for the shiny region. This observation tends to confirm the assumption that the dendrite tips primarily grow along the free surface in the shiny sectors and along the substrate for the dull appearing areas. The averaged profiles of Figure 4-17 b, c) do not show a sharp drop of the Al-intensity at the upper and lower boundary of the coating. This is due to several reasons. First, the boundaries exhibit some roughness. Moreover, there is a thin intermetallic layer at the interface between substrate and coating which may influence the measurement. Finally, very close to the boundary, the quantity of emitted X-ray photons may not be representative for the actual concentration as the interaction volume of the electrons interferes with the boundaries. Nevertheless, it is clearly visible on the mapping that the highest Al concentrations, i.e. the cores of the dendrite arms, are not found directly at the boundaries.
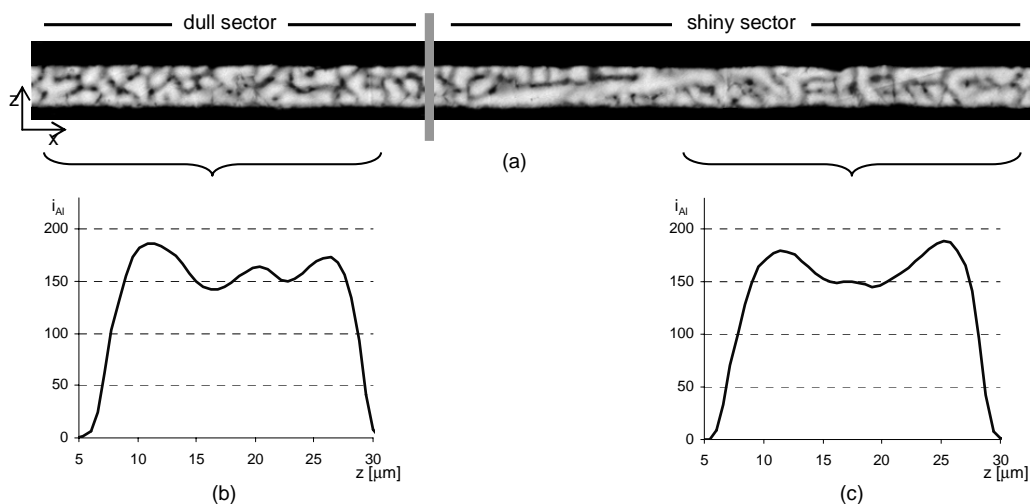
Figure 4-17 a) Mapping of the intensity of the k_α-Al signal recorded by WDS on a cross-section trough the

Al-Zn-Si coating. Bright gray areas correspond to high Al concentrations. The lower boundary corresponds to the substrate-coating interface, the upper boundary to the free surface. **b)** and **c)** averaged Al-intensity profiles in the dull and shiny sector, respectively.

In summary:

- GD-OES shows maxima of the Al concentration close to the boundaries but not exactly on the boundaries.

- Si is accumulated toward the coating-substrate interface.

- the WDS mappings show that the global maximum of the Al concentration is close the free boundary in shiny sectors, whereas it is close to the substrate boundary in dull areas.

- the WDS mappings confirm that the maxima of Al concentration are not located on the boundaries.

As will be seen in section 5.2, the results presented here are of particular importance for the discussion of the influence of the microsegregation on the intragranular misorientations.

4.1.5   *Intragranular crystallographic misorientations*

This subsection presents the results of the characterization of the intragranular crystallographic misorientations. The main emphasis is laid on the qualitative description of the different misorientation phenomena that are observed in the Al-Zn-Si coatings and that are of relevance for the discussion of the mechanisms responsible for the formation of misorientations in section 5.2.

The crystallographic orientation of the coating was assessed by electron backscattering diffraction (EBSD) as described in section 3.1.2. Figure 4-18 a) shows the misorientation map large grain in an Al-Zn-Si coating. The reference orientation (blue) has been assigned to the nucleation center of the grain. The rainbow color code shows that between the center and the periphery of the grain, variations of orientation of up to 16° are present. This results confirms the important variations of crystallographic orientation

within single grains of up to 35° that were reported by Sémoroz et al. [Sémoroz1 01]. Further experiments showed that the variation of crystallographic orientation follows distinct pattern that are in most cases closely related to the dendrite skeleton of the coating layer. At first sight, one can distinguish three different types of intragranular misorientations, which are indicated by the encircled zones on Figure 4-18 b):

- Misorientations due to a continuous change of orientation along a dendrite arm as it occurs in many spots on Figure 4-18 where continuous changes of color from blue to green, from green to yellow or from yellow to red are visible. In Figure 4-18 b) this is for example the case for the transition from yellow to orange that is labeled with (1). Misorientation rates of 4 to 5 °/mm are typically observed in such cases.

- Misorientations leading to sharp subgrain boundaries originating in one distinct dendrite arm and propagating into the areas that have subsequently grown from this arm. Three spots where such subgrain boundaries originated are labeled with (2) in Figure 4-18 b). One may divide this type of misorientations into two sub-groups. The first one, which is labeled (2a) in Figure 4-18 b), is characterized by small misorientations of less than 2 or 3 °. The rotation axis and the sense of rotation of these misorientations are often related to the local dendrite morphology as will be detailed further in the text. On the other hand, more pronounced misorientations of up to 10° are sometimes observed. In this case, the misorientation axis is usually not related to the growth morphology. A typical example for the latter case is the subgrain boundary observed between the blue and the yellow zone near the nucleation center of the grain in Figure 4-18 which is labeled (2b).

- Misoriented areas of band like shape that are not directly related to the grain and dendrite structure (3).

The characteristics of these three types of misorientations will be described in detail on the following pages in order to gather a maximum of information with respect to the mechanisms which are responsible for the formation of such misorientations. The subsection is divided into four part according the four different types of misorientaitons.
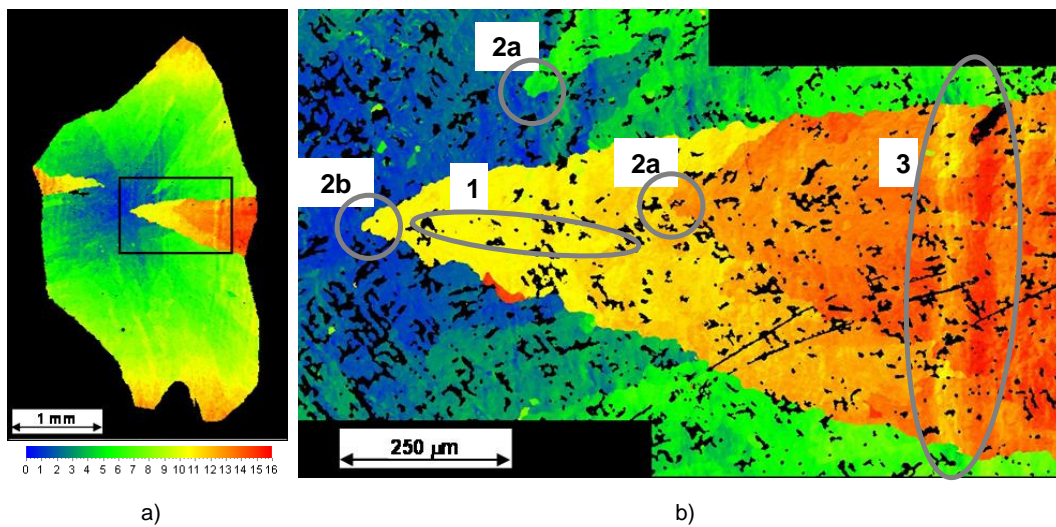
Figure 4-18 a) EBSD misorientation map of one grain in an Al-Zn-Si coating. **b)** On a higher resolution mapping, different kinds of misorientations can be observed. As a reference orientation of the misorientation mapping, the orientation of the nucleus has been chosen.

Systematic continuous misorientations

Continuous misorientations (type 1) are responsible for a significant part of the misorientations observed in Al-Zn-Si coatings, and therefore, they are presented here in some detail. Figure 4-19 shows another grain with significant misorientations. Here again, the orientation of the nucleus identified from an optical micrograph has been selected as the reference orientation of the misorientation mapping. Therefore, the central region of the grain is displayed in blue. In addition, subgrain boundaries are drawn as black lines. The black lines are generated automatically in spots where two areas meet whose respective orientation is different by more than 5 °. This explains the presence of black spots scattered all over the map, they may actually stem from regions where (non-epitaxial) eutectic α-Al contributed to the diffraction pattern. Figure 4-19 shows that it is possible to have true, continuous subgrain boundaries even without the presence of a sharp origin across a dendrite arm as described above. Subgrain boundaries can appear in between dendrite arms growing from the same nucleus but undergoing only continuous misorientations that are different for the two dendrite arms. This is for example the case for the subgrain boundary to the left of the nucleus in Figure 4-19 a). Even when the subgrain boundary originates in a sharp misorientation as it is the case for the subgrain boundary upwards from the nucleus, the misorientation across the boundary can considerably increase when the neighbouring dendrite arms undergo additional continuous misorienation. When comparing the black lines representing subgrain boundaries to the dendrite structure which can easily be

extracted from optical micrographs, it turns out that the subgrain boundaries almost exclusively lay in the interdendritic areas. During the formation of the dendrite network, these areas were still liquid, at least to the point where coalescence between neighbouring arms occurs. It is possible that the misorientations develop independently in the uncoalesced neighbouring dendrite branches during the growth. Another interesting feature is that in several spots, subgrain boundaries are present between closely spaced, parallel dendrite arms in between which no secondary dendrite arms are visible.
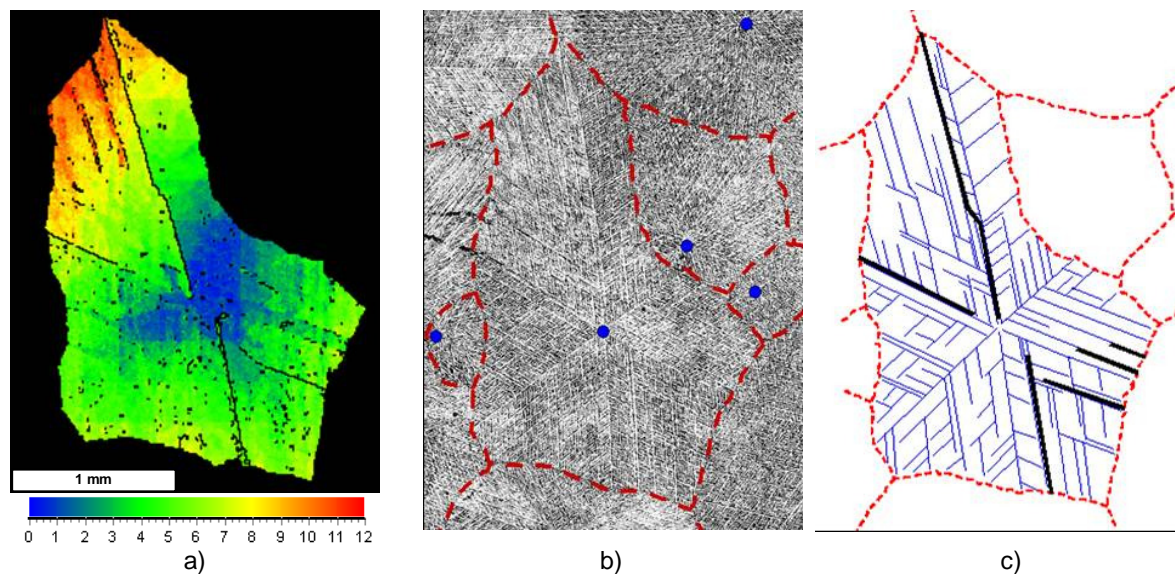
Figure 4-19 a) EBSD misorientation map of a grain showing subgrain boundaires of more than 5° as black lines. **b)** Assembly of optical micrographs showing the dendrite structure of the grain. Nucleation centers are highlighted with blue dots and grain boundaries as red, dashed lines. **c)** Schematic representation of the predominant dendrite growth directions in blue and the subgrain boundaries in black.

The continuous misorientations are not random in their nature but the axis of rotation and the sense of rotation are in general related to the dendritic pattern from which they arise. A visual illustration of this is given in Figure 4-20 b) which shows the $\langle 111 \rangle$ pole figure of the grain. A close-up view of the central pole is given in Figure 4-20 c). The color scale is the same as for Figure 4-20 a). This means that areas close to the nucleation center which are displayed blue on the EBSD map correspond to blue orientations in the EBSD pole figure. It can be shown that distinct areas in the $\langle 111 \rangle$ pole correspond to the sectors of the grain which are labelled form A to E. The zone labelled A in Figure 4-20 c) corresponds to the sector labelled A in Figure 4-20 a). It becomes apparent that the evolution of orientation from the nucleus to the periphery of the grain follows a quite uniform pattern within one sector (e.g. A), whereas the evolution is significantly different

in another sector (e.g. B), even if they are adjacent and only separated by the above-mentioned subgrain boundary. The observation that the central pole moves radially away from the pole corresponding to the nucleation center is confirmed in many grains. In other words, this means that crystallographic planes being parallel to the coating plane in the nucleation center are bent towards the substrate-coating interface when moving away from the nucleation center, leading to a convex shape of such crystallographic planes within one grain. When describing the misorientation along a dendrite arm in terms of a rotation axis and a rotation angle, this corresponds to an axis which is laying in the coating plane or close to it and approximately normal to the predominant dendrite growth direction.
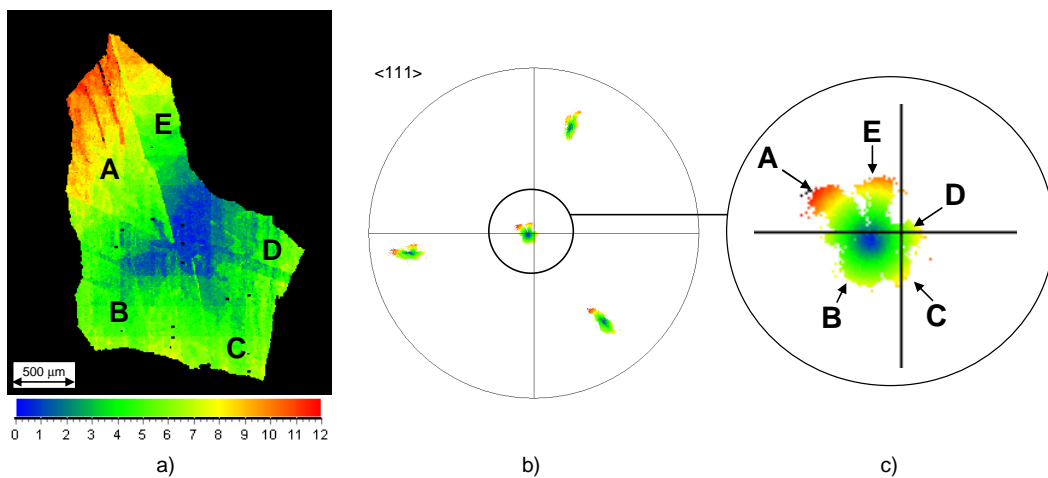
Figure 4-20 a) EBSD misorientation map. **b)** ⟨111⟩ EBSD pole figure of the corresponding grain. **c)** detail view of the central pole. It can be shown that distinct areas of the central pole correspond to the sectors of the grain in a).

Figure 4-21 shows however that the misorienation axis along a dendrite arms is determined not only by its proper growth direction but also by its environment. The three long and continuous dendrite arms highlighted with black lines in Figure 4-21 a) show different rotation axes even though the three arms are strictly parallel. For dendrite (1), the unit vector representative of the rotation axis is (0.98 -0.20 -0.04), for dendrite (2) (0.73 -0.68 -0.02) and for dendrite (3) (0.18, -0.98, -0.06) where the components are given in the sample coordinate system.

a)   b)
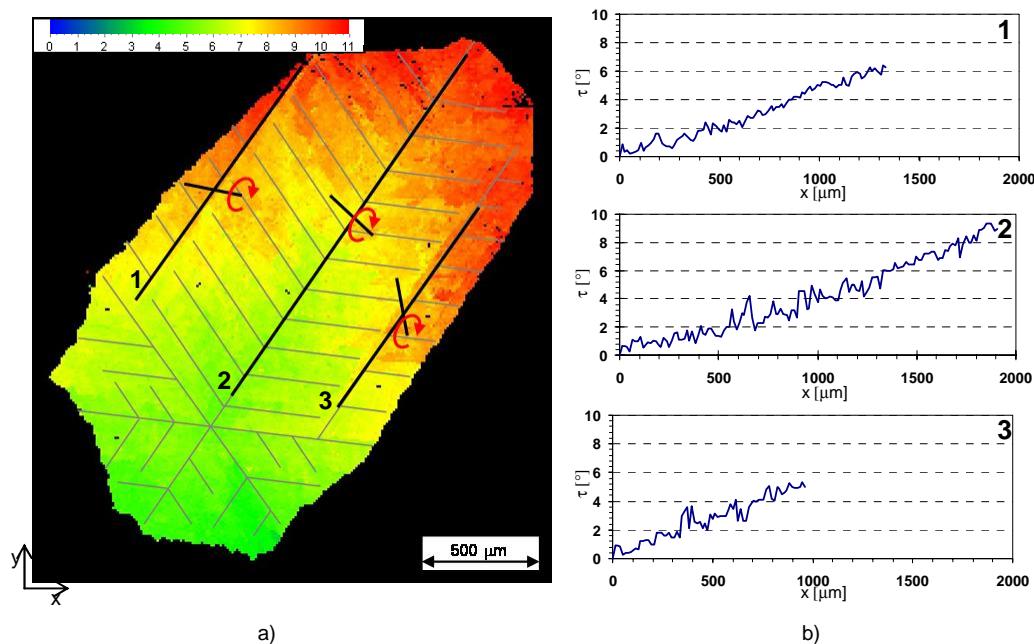
Figure 4-21 a) EBSD misorientation map of a grain. The predominant dendrite growth direction are schematically given by gray lines. There are three areas in the upper part of the grain that grew from three different but parallel "pseudo-primary" dendrite arms. The line segments crossing these arms highlighted in black indicate the axis of rotation, the red arrows the sense of rotation along the dendrite arm. **b)** The misorientation profiles along these three arms.

As one can see, the component normal to the coating plane is very small in the three cases and the misorientation axes lay approximately in the plane of the coating. For this reason, the rotation axes can easily be represented by the black line segments crossing the examined dendrite arms. When looking at the predominant growth direction which are schematically represented by grey lines in Figure 4-21 a), it becomes apparent that dendrite arm (1) emits secondary branches only towards the left, arm (2) to both sides and arm (3) only to the right. The presented experimental results indicate that the orientation of the rotation axis does in fact also depend on the secondary branches emitted by a dendrite arm. It seems that the rotation axis is neither perpendicular to the primary arm nor to the secondary arms but located somewhere in between. Figure 4-21 b) shows the misorientation profiles along the three evaluated primary dendrite arms. Even though the rotation axes are different, the misorientation rate is very similar and located between 4 and 5 °/mm as it is typical for continuous misorientations. In the profiles, some steps corresponding to localized orientation changes of up to 2° are observed. More detailed mappings with a spatial resolution of 1 μm, Figure 4-22, show that no subgrain boundaries of more than 1° misorientation stretches completely across the primary dendrite arm. One can therefore still consider that the misorientation is truly continuous along the given

dendrite arm. The noise in the profiles of Figure 4-21 b) originate from individual pixels or isolated clusters of pixels within the dendrite trunk that are misoriented with respect to the rest of the dendrite arm. The origin of the isolated, misoriented clusters within a dendrite arm may be different from the origin of the continuous misorientations observed over long distances along dendrite arms. In addition to the physically present misorientations, part of fluctuations in the profiles of Figure 4-21 b) may also be due to the noise of the measurement method.
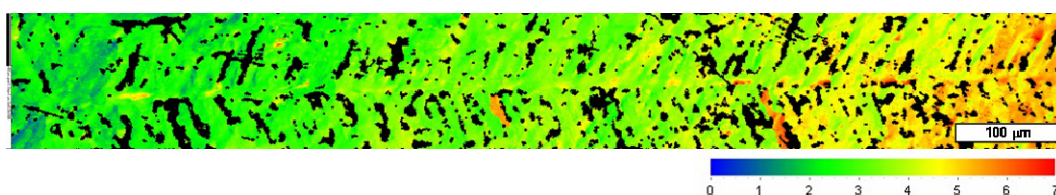
Figure 4-22 EBSD misorientation map of the first half of the dendrite arm number (2) of Figure 4-21. The nucleation center of the grain is visible on the left side of the map, the dendrite arm is growing to the right, emitting secondary arms on both sides. The black spots correspond to non-indexed interdendritic / eutectic areas.

Small and systematic discrete misorientations

As mentioned in chapter 4.1.3, dendrite arms continuously growing over large distances without undergoing branching are the exception rather than the rule in Al-Zn-Si coatings where the dendrites are confined to grow within the thin volume of the coating. In many cases, frequent branching occurs and therefore, continuous, straight dendrites over distances as long as millimeters are not observed. Figure 4-23 shows the microstructure of an area where two dendrite growth directions are competing for the lead in the pattern formation. The two dendrite growth directions point from the bottom left to the top right and from the bottom right to the top left. Figure 4-23 a) shows the resulting misorientation map. The misorientations observed are not completely continuous, but subgrain boundaries highlighted by the red lines are present. Most of subgrain boundaries showing misorientations of a few degrees at maximum are oriented along the two dendrite growth directions and lying in the interdendritic areas of the coating. The resulting characteristic misorientation pattern could be described as a "tile-pattern". Globally, the nature of these misorientation follows the same principles as in the case of the continuous misorientations described above: they are cumulative, their misorientation axis is approximately perpendicular to the predominant growth directions and the sense of rotation is always towards the substrate-coating interface when measuring from the nucleus of the grain

towards the periphery.
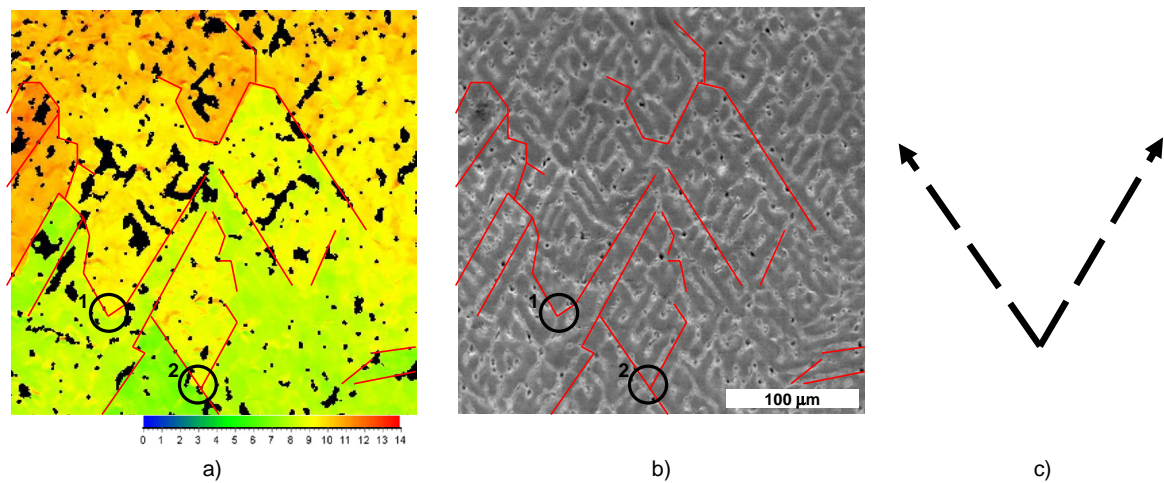
Figure 4-23 a) Close-up EBSD misorientation map of an area in the upper part of Figure 4-18a). Misorientations form a "tile-pattern" where subgrain boundaries highlighted in red are present in different directions. **b)** The SE micrograph shows that the subgrain boundaries are aligned with the dendrite growth directions and lay in the interdendritic areas. The numbers indicate two spots for which are discussed in detail on the subsequent pages. **c)** The arrows indicate the two dominant dendrite growth directions.

New "tiles" exhibiting an orientation different from its parent dendrites originate in distinct spots such as the ones highlighted by black circles in Figure 4-23 a) and b). In the case of spot (1), one finds the situation displayed in Figure 4-24 a) where to the origin of the tile seems to be associated with a neck in a dendrite arm growing from the lower left to the upper right. A detailed EBSD mapping with a point resolution of 200 nm, Figure 4-24 b), allows identifying a sharp subgrain boundary between the light orange and the dark orange areas. The misorientation measured between the two grain is about 2°. When drawing the detected subgrain boundary into a micrograph, Figure 4-24 c), it becomes apparent that the boundary is not at the spot where the neck seems narrowest. At the narrowest spot of the neck, a morphology of coarse precipitates is present. That indicates that the concentration of the solid solution was locally higher there and that solidification occurred late in the solidification sequence. This means that the narrowest spot on the micrograph does not correspond to the actual neck as it is formed during the branching of the primary dendrite. The actual neck may be above or below the plane of observation which lies within the coating as the sample underwent polishing and electropolishing before observation. It remains hence reasonable to assume that the observed subgrain boundary is associated with a branching neck in the dendrite morphology.
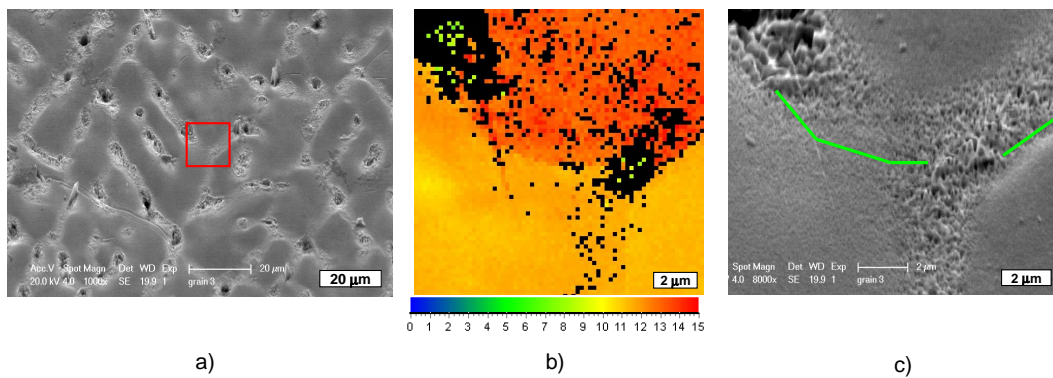
Figure 4-24 a) SE-micrograph of the area around spot (1) of Figure 4-23. **b)** EBSD misorientation map of the area in the red frame of a). **c)** SE-micrograph of the same area. The subgrain boundary is drawn in green.

Similar observation can be made for spot (2) of Figure 4-23. Figure 4-25 shows the origin of this subgrain boundary. In Figure 4-25 a), the neck in the main dendrite arm growing from the lower right to the upper left which is visible in the center of the microrograph corresponds to a subgrain boundary. The subgrain boundary shows a misorientation of a bit more than 1° leading to a contrast between bright orange and dark orange in Figure 4-25 b). A second subgrain boundary from yellow to dark orange is also visible on the left hand side of Figure 4-25 b). It is probably not associated to a branching neck, but rather to the coalescence of two neighboring dendrite arms exhibiting slightly different orientations. This seems plausible considering the branching pattern shown in Figure 4-25 a).

Another interesting feature is the eutectic island displayed at the bottom center of Figure 4-25 b) and c). Some of the eutectic α-Al phase is also indexed as either yellow or dark orange which means that there is an epitaxial relationship between the primary dendrites and the eutectic α-Al. Furthermore, the presence of both yellow and dark orange areas in the eutectic suggests that the orientations of both neighboring dendrite arms do not change anymore once the ternary eutectic temperature is reached, otherwise they could not transmit their orientation to the α-Al phase of the eutectic.
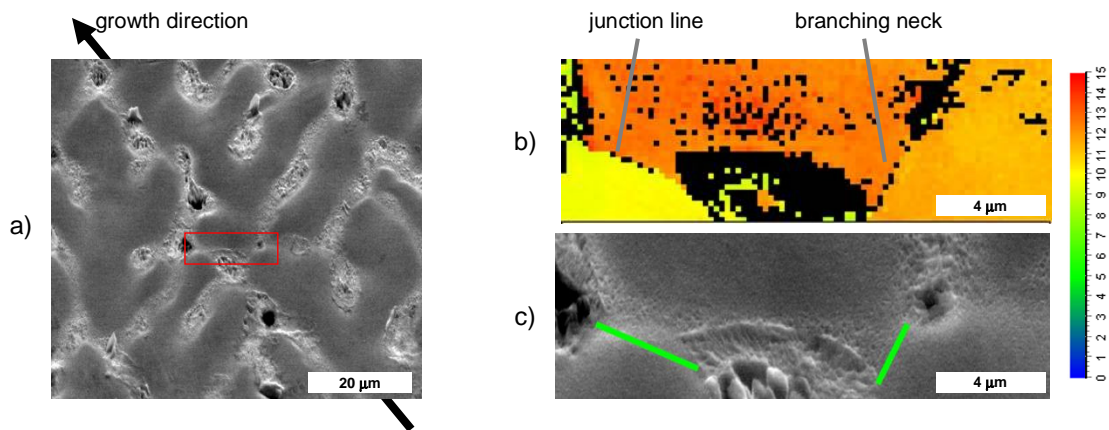
Figure 4-25 a) SE-micrograph of the area around spot (2) of Figure 4-23. **b)** EBSD misorientation map of the area in the red frame of a). **c)** SE-micrograph of the same area. The subgrain boundaries are drawn in green.

Large and non-systematic discrete misorientations

In some cases, misorientations originating at sharp subgrain boundaries across dendrite arms and then propagating into the areas that have subsequently grown from this arm can be much more pronounced as in the cases presented in the two previous figures. In these cases, the axis of misorientation is usually not in the coating plane and perpendicular to the dominant growth direction but random. A typical example is the subgrain boundary observed between the blue and the yellow area near the nucleation center of the grain in Figure 4-18. The EBSD mappings of Figure 4-26 show that this subgrain boundary originates very close to the nucleation center, probably in the neck that formed when the nucleus destabilized. The misorientation across the subgrain boundary is more than 10° and the axis of misorientation is almost normal to the coating plane which is very different from the systematic misorientations described above. The detailed EBSD mapping of Figure 4-26 c) exhibiting a pixel size of 40 nm shows that the boundary is seamed by a layer of 1 to 4 non-indexed pixels. The subgrain boundary can hence be considered as sharp at least up to the spatial resolution of the EBSD technique.

a)   b)   c)
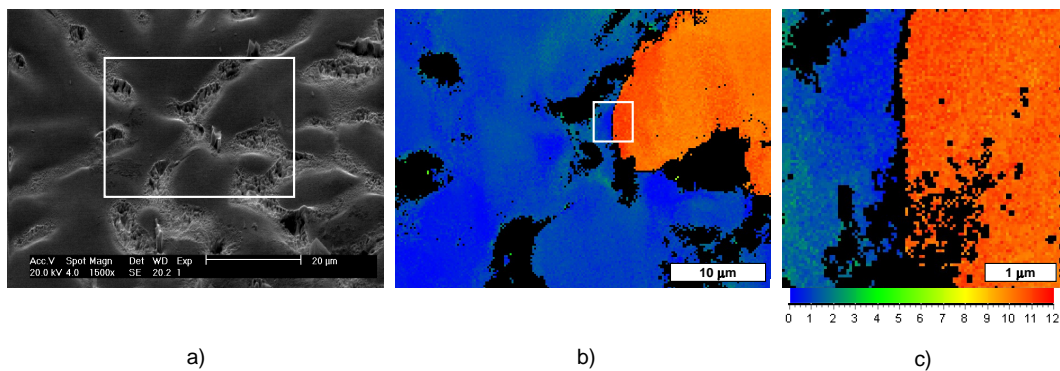
Figure 4-26 a) SE micrograph of the nucleus area of the grain depicted in Figure 4-18. EBSD misorientation mappings with a spot resolution of 200 nm (**b**) and 40 nm (**c**) show that the subgrain boundaries are sharp at least to the resolution limit of the EBSD method.

Misorientation bands

As described in the beginning of chapter 4.1.5, there is a third kind of misorientation pattern that is frequently observed in Al-Zn-Si coatings. It is characterized by the presence of band-shaped misoriented areas which do not follow or even propagate along the dendrite structure. A banded structure equivalent to the one displayed in the plane of the coating in Figure 4-18 was also found in metallographic sections across the coating-substrate composite. An example is shown in Figure 4-27 which shows a cross-section where a primary dendrite arm is lying almost parallel to the plane of the image. The WDS Al-intensity map (b) clearly reveals the dendrite pattern within the coating. From the almost horizontal Al-rich primary arm centered in the coating layer, a series of secondary arms are emitted towards both the substrate-coating and the free boundary.
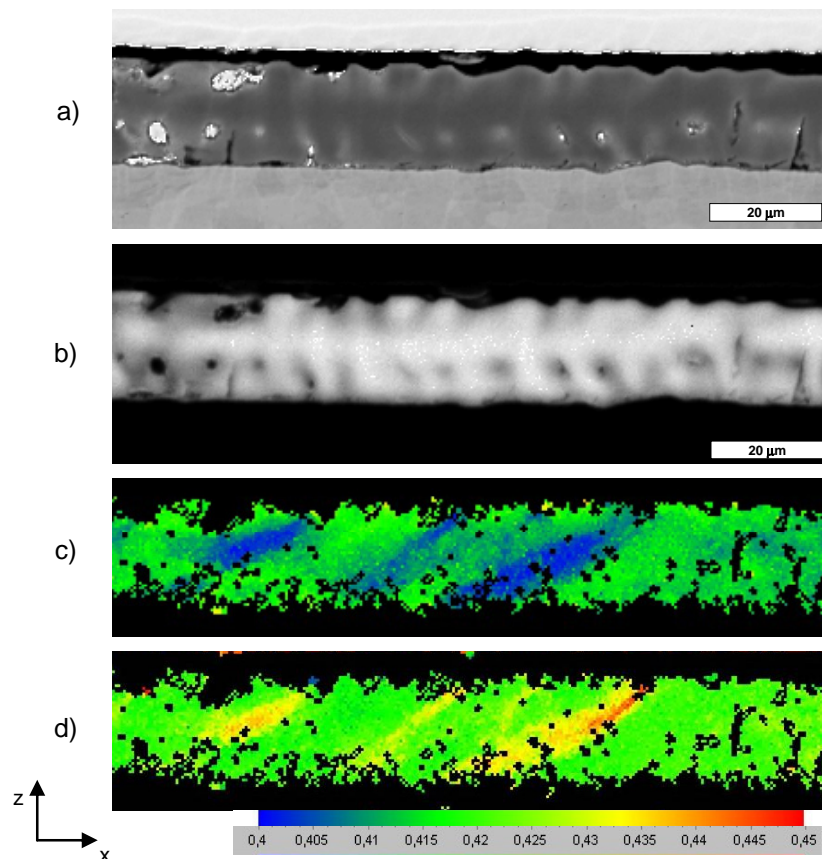
Figure 4-27 a) BSE micrograph of a cross section through the coating-substrate composite. The section is taken almost parallel to a primary dendrite arm visible in the center of the coating. The steel substrate (light gray) is below the coating (dark gray). **b)** WDS intensity map of the k_α-Al peak. Brighter gray tones correspond to higher Al concentration. **c)** EBSD misorientation map showing a banded misorientation pattern (step size 500 nm). **d)** Schmid factor map for an applied load along the x-axis.

The EBSD misorientation map of the same area, Figure 4-27 c), shows an array of inclined, misoriented zones (blue) which are not at all related to the dendrite structure displayed in b). The displayed misorientations are not cumulative, the orientation is approximately the same on the left and on the right of the displayed mapping. In order to gain a better understanding of the isolated misorientations, the Schmid factor has been calculated from the Euler angle data. For a supposed applied load along the primary arm of the dendrite (x-axis in Figure 4-27), the slip system $\left[01\overline{1}\right]\left(1\overline{1}\overline{1}\right)$ displays the highest resolved shear stress. The Schmid factor for this slip system is displayed in Figure 4-27 d). The Schmid factor is largest in the isolated misoriented areas, thereby indicating that plastic deformation is concentrated there.

In summary, one observes:

- continuous misorientations along dendrite arms. In general, the misorienation axis is perpendicular to the growth direction and lays in the coatings plane. In some cases it is however influenced by the secondary dendrite arms. The rotation occurs always towards the coating plane.

- repeated discrete but cumulative misorientations. The misorientation axes are similar to the previous case. The small discrete misorientations are located at the branching necks of the dendrite network.

- large, discrete misorientations that are also located at the branching necks. No relationship between the axis of misorientation and the dendrite growth directions or the coating plane was detected.

- banded misorientation structures in which misoriented zones alternate with non-misoriented zones.

The detailed description of the misorientation pattern given in this subsection will provide the basis for the discussion of the mechanisms responsible for their formation that will follow in section 5.2.

4.2 Modeling

In this section, the results of the three numerical methods that were applied are presented. The numerical simulations allowed determining an anisotropy function for the solid-liquid interfacial energy of the Al-43.4Zn-1.6Si (wt.%) alloy, as well as studying the interaction of the dendrite tips with the confining boundaries and the development of the dendrite network on the scale of the grain.

4.2.1 *Assessment of the gamma anisotropy by inverse modeling*

By applying the inverse method technique described in chapter 3.1.1, it is attempted to determine a mathematical function describing the anisotropy of the solid-liquid interfacial energy. In the present work, a set of 5 randomly selected grains has been investigated. The crystallographic orientations of the grains were determined by electron backscattering diffraction (EBSD). The Euler angles have been reported in Table 4-1, and the inverse pole figure of Figure 4-28 shows the orientation of the normal to the coating plane in the crystallographic reference frame of the 5 grains. Three grains exhibit 6 primary growth directions while the two others show 8 primary arms, which leads thereby to a total number of $N = 12$ measured angles, ζ^{mes}.

	φ_1	ϕ	φ_2	ζ^{mes}	ζ^{calc}
grain 1	118.1°	52.0°	39.9°	67.5	71.75
				47.5	44.00
grain 2	230.6°	31.1°	55.7°	41.4	37.50
				65.0	66.75
grain 3	38.4°	9.8°	45.4°	25.0	31.25
				54.5	56.75
				46.5	35.25
grain 4	83.7°	13.5°	40.8°	30.0	33.50
				39.5	45.00
				50.5	50.00
grain 5	142.1°	32.0°	85.2°	74.0	74.25
				41.0	36.25

Table 4-1 Euler angles as well as measured and calculated ζ angles for the grains used in the inverse method analysis.

The inverse method was applied to this set of data, starting with the following initial

guess for the anisotropy parameters: $\varepsilon_1 = 0.025$, $\varepsilon_2 = -0.007$ and $\varepsilon_3 = -0.0005$. Keeping ε_1 constant, the iterative procedure converged towards $\varepsilon_2 = -0.00469$ and $\varepsilon_3 = -0.000194$, which corresponds to the following ratios: $\varepsilon_2/\varepsilon_1 = -0.188$ and $\varepsilon_3/\varepsilon_1 = -0.00776$. Tests have shown that the initial choice for ε has no influence on the solution as long as chosen within reasonable limits, e.g. $\Phi_r(\mathbf{n}) > 0 \quad \forall \mathbf{n}$, which is the condition for non-facetted crystal growth. The interfacial energy $\gamma_{sl}(\mathbf{n})/\gamma_{sl}^0$ and the normalized general stiffness $\Phi_r(\mathbf{n})$ corresponding to the optimized anisotropy parameters are shown in Figure 4-29. The calculated growth direction angles, ζ^{calc}, corresponding to this anisotropy function are given in Table 1, where they can be compared with the corresponding measured angles, ζ^{mes}.
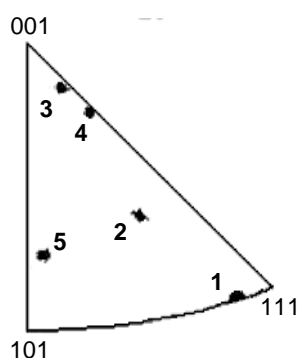
Figure 4-28 Inverse pole figure giving the orientation of the normal to the coating plane in the crystallographic reference frame of the five grains used for the inverse method analysis.

The interfacial energy shown in Figure 4-29 a) as a function of the interface orientation exhibits its lowest value for interfaces having their normal corresponding approximately to the $\langle 111 \rangle$ directions (blues spots), i.e. for interfaces that are parallel to the dense packed planes of the *fcc* structure. The maximum of interfacial energy (dark red) is observed for $\{100\}$ interfaces, whereas saddle points are found for $\{110\}$ (orange). The sections through the $\gamma_{sl}(\mathbf{n})$ plots shown in Figure 4-29 b), c), d) indicate that amplitude of the anisotropy in a given plane strongly depends on its orientation. The interfacial energy within the $(\bar{1}10)$ plane, Figure 4-29 c), exhibits 2 global maxima of the [001] family and 4 global minima of the [111] family. For sections that are parallel to the (001) plane, Figure 4-29 b), however, the in-plane anisotropy is substantially weaker as the difference of interfacial energy between [100] and [110] is considerably smaller than between [001] and [111]. The in-plane anisotropy of $\gamma_{sl}(\mathbf{n})$ is even weaker within the (111) section, Figure 4-29 d).

The present case is an example of an interfacial energy function whose maxima do not correspond to the minima of the surface stiffness. The stiffness plot exhibits global maxima along $\langle 111 \rangle$ and local maxima along $\langle 100 \rangle$, Figure 4-29 e). Again, saddle points can be found for the $\langle 110 \rangle$ orientations. The global minima of the stiffness are however located between the $\langle 100 \rangle$ and $\langle 110 \rangle$ directions, forming a 28.5° angle with the $\langle 100 \rangle$ orientations. In consequence, there are in total 24 minima of the stiffness and hence also 24 possible dendritic growth directions. The 2D section through the stiffness plot shown in Figure 4-29 f) clearly reveals that the in-plane anisotropy is very weak for {001} sections.
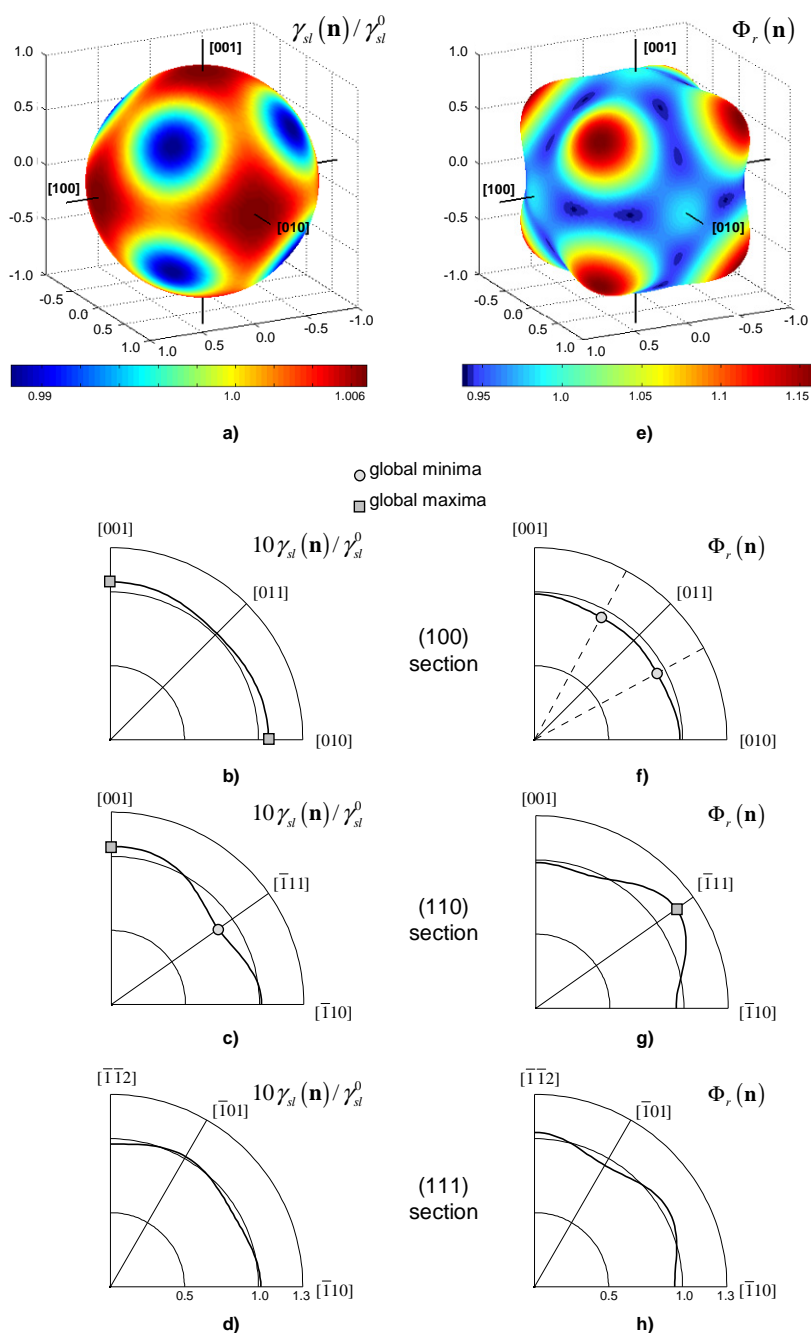
Figure 4-29 Plots of $\gamma_{sl}(\mathbf{n})/\gamma_{sl}^0$ (**a**) and $\Phi_r(\mathbf{n})$ (**e**) vs. the crystallographic orientation for the optimized values of anisotropy $\varepsilon_2 = -0.188\varepsilon_1$ and $\varepsilon_3 = -0.00776\varepsilon_1$ with $\varepsilon_1 = 0.025$. The maxima of the interfacial energy are reached for the $\langle 100 \rangle$ directions whereas the minima of the stiffness are located in between $\langle 100 \rangle$ and $\langle 110 \rangle$. The coordinate axes correspond to the crystallographic $\langle 100 \rangle$ directions. 2D sections of interfacial energy and stiffness are given in (**b**) and (**f**) respectively for the (001) plane, in (**c**) and (**g**) for the (110) plane and in (**d**) and (**h**) for the (111) plane. For the 2D plots of the interfacial energy (**b-d**), the magnitude of the anisotropy was increased by a factor 10 as no minima and maxima are discernable otherwise. The 2D plots of the interface stiffness (**e-g**) were not amplified.

Since the dendrites are confined to grow in the thin coating layer, the selected growth pattern depends not only on ε_1, ε_2 and ε_3 but also on the orientation of the crystal with respect to the coating plane. As mentioned above, the dendrites in the coating layer are assumed to grow along the directions for which the intersection of the stiffness plot and the plane of the coating exhibits local minima. Depending on the crystallographic orientation with respect to the coating, the magnitude of this in-plane anisotropy may be very variable. Strong in-plane anisotropy is observed for crystals having a {110}, Figure 4-29 g) or {111}, Figure 4-29 h) crystallographic plane nearly parallel to the coating plane. In this case, the microstructure shows a very well defined dendritic pattern with 6 dendrite growth directions that can be distinctly identified. An example of a grain having the (111) plane almost aligned with the coating plane is given in Figure 4-30 a, b) (The exact orientation of this grain can be seen in Figure 4-28 where it is labeled "1"). If, however, a {100} plane is approximately parallel to the coating plane (grain 3 on Figure 4-28), the effective in-plane anisotropy is much weaker and 8 minima of the stiffness are present, see Figure 4-30 c). On the corresponding micrograph, Figure 4-30 d), 8 dendrite growth directions can be identified, but the dendrite growth directions are sometimes blurred and smooth transitions form one growth direction to another seem to be possible. This corresponds well to the weak effective in-plane anisotropy observed for surface stiffness in the (100) plane, Figure 4-29 f).
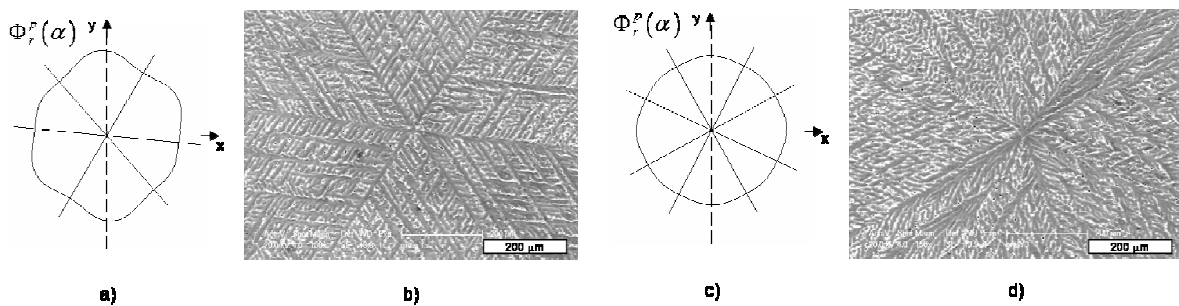
Figure 4-30 a) In-plane stiffness plot for a grain having a {111} crystallographic plane close to the coating plane. The minima of the stiffness are highlighted by the radial lines. **b)** The micrograph of the corresponding grain shows a well-defined dendrite structure. **c)** In-plane stiffness plot for a grain having a {100} crystallographic plane close to the coating plane. The anisotropy is weaker than in a) and leads to a dendrite pattern with poorly defined growth directions **d)**.

The results of this subsection summarize as follows:

- A mathematical expression of the anisotropic solid-liquid interfacial energy has been determined from the dendrite growth directions measured on Al-Zn-Si coatings. The anisotropy function can be expressed in terms of a third order cubic harmonics expansion.

- The minima of the interface stiffness, and hence the dendrite growth directions of the bulk alloy, are located in between the neighboring [100] and [110] directions at 28.5° from [100].

- The amount of in-plane anisotropy, which depends on the orientation of the crystal with respect to the coating plane, correlates well with the sharpness of the dendrite pattern.

These results will be further discussed in section 5.1.2.

4.2.2   *Interaction of dendrite tips with confining boundaries - 2D phase field modeling*

2D phase field modeling can provide valuable information about the morphological evolution of a dendrite confined within the Al-Zn-Si coating layer. In this subsection, the following aspects are addressed:

- behavior of a dendrite nucleated on a boundary as a function of the wetting angle β

- behavior of a dendrite nucleated in the bulk as function of the wetting angle β as it approaches the boundary

- influence of the domain thickness on the tip kinetics of the dendrite

- dependence of the dendrite tip kinetics on the incidence angle α i.e. the crystallographic orientation of the dendrite arm with respect to the boundary

- development of secondary branches behind the dendrite tip and their interaction with the boundaries

For the reason of computational efficiency, calculations are easier to conduct for high supersaturations Ω:

$$\Omega = \frac{c_l - c_0}{c_l - c_s} \tag{4.1}.$$

For the first three points listed above supersaturations higher than those expected in the real solidification process were used. This can be justified considering that the information extracted from these simulations is only of qualitative nature. Given that the qualitative behavior of the dendrite tips is not expected to change for lower undercoolings, the findings are considered valid for the entire domain of undercoolings. For the simulation of the dependence of the dendrite tip kinetics on the crystallographic orientation, smaller undercoolings representative for the actual solidification process are also selected since the calculated results are subsequently used in the simulation of the microstructure on the grain scale. Likewise, the simulations of the secondary dendrite arm formation has been conducted at realistic supersaturations since the respective results serve to elucidate to the mechanism responsible for the formation of crystallographic misorientations.

The physical properties used for the phase field simulations are given in Table 4-2.

c_0 [at.% Zn]	D_S [m^2/s]	D_L [m^2/s]	ρc_p [J/Km^3]	L [J/m^3]	Γ [Km]	V_m [m^3/mol]	ε_4 [-]	μ_k [m/Ks]
24	1.0 10^{-12}	3.0 10^{-9}	3.1 10^6	1.0 10^9	2.5 10^{-7}	1.0 10^{-5}	0.01	0.0036

Table 4-2 Parameters used in the phase field simulations.

Dendrite arms nucleated on the boundary

Figure 4-31 a) shows the morphological evolution of a dendrite nucleated in the center of the undercooled melt. This serves as a reference case for the comparison with dendrites interacting with boundaries. The dendrite shown here displays four-fold symmetry and has its preferred ⟨100⟩ growth directions 11° off the horizontal and vertical directions. Dendrites nucleated on a boundary with wetting angles β ranging from 60° to 120° are shown in Figure 4-31 b-f). The simulation conditions are exactly the same as for Figure 4-31 a) except that the lower half of the modeling domain has been omitted. The following observations can be made:

- For wetting angles 90°, the primary arm growing towards the left side follows the boundary whereas the primary arm growing towards the right sides detaches from the boundary and growing along its preferred growth direction which is 11° off the horizontal boundary. If the wetting angle is smaller than 90°, even the primary arm growing towards the right follows the boundary and not the preferential growth direction.

- For wetting angles smaller than 90°, the velocity of the tips growing along the boundary increases with decreasing β. This observation was already made by Sémoroz et al. [Sémoroz 00].

- For wetting angles 90° however, the envelope of the growing dendrite seems to be independent of the wetting condition. The dendrites grown with β =90°, 105° and 120° differ only in their configuration of secondary arms which is governed by random noise.
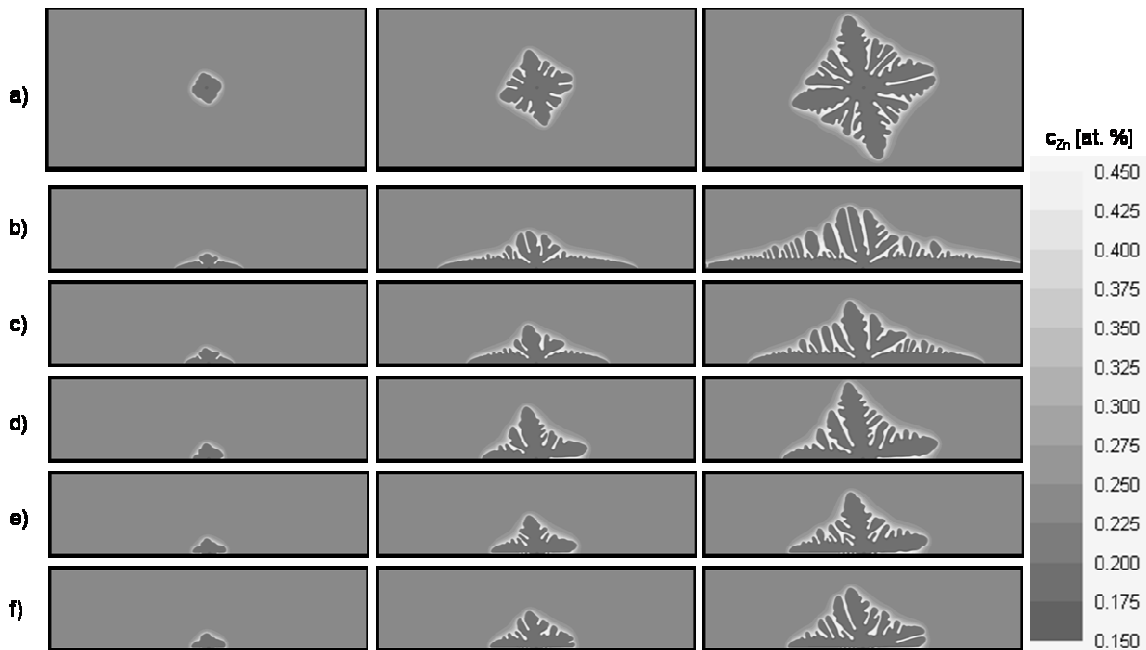
Figure 4-31 a) Concentration fields for a dendrite nucleated in the bulk, and, b-f) for grains nucleated on the boundary with wetting angles β of 60°, 75°, 90°, 115° and 120° respectively. The incidence angle α is 11° in all cases. The supersaturation Ω is set to 0.73 (T=530 °C), the mesh size is 10 nm, the modeling domain measures 5 x 20 μm and snapshots are displayed for 0.025, 0.075 and 0.125 ms after nucleation.

By taking a closer look, one can, however, find an important difference between the dendrite growing at β=90° and the dendrites growing at β>90°. Figure 4-32 shows that for a wetting angle equal to 90°, the tip is in contact with the boundary whereas for a wetting anglesof 105°, a liquid film rich in solute remains in between the dendrite and the boundary. As the observed liquid layer is several mesh elements thick, it can be assumed that this is not an artifact of the numerical method. The dendrite tip seems to detach from the interface soon after nucleation. The finding that the tip velocity is independent of the wetting angle if the latter is larger than 90° is therefore not surprising since there is no solid-liquid-boundary triple point in the vicinity once the tip is detached from the boundary.
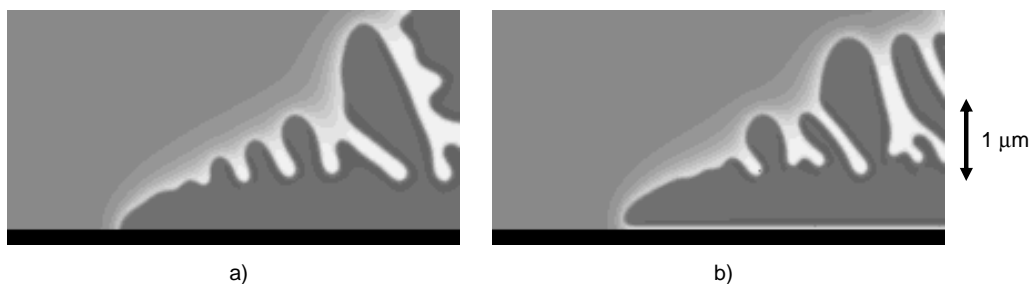
Figure 4-32 a) Detail pictures of a tip growing with a wetting angle β=90°. b) Tip growing with a wetting

angle β=105°. In both cases, the nuclei were positioned on the boundary with α=11°. A solute-rich liquid layer remains between tip and boundary for wetting angles larger than 90°. The conditions are the same as in Figure 4-31.

Dendrite arms nucleated in the bulk

An additional set of simulations has been performed with conditions equal to those displayed in Figure 4-31 except that the nucleus was positioned within the bulk of the supersaturated melt. This allows studying the influence of the wetting condition on a dendrite tip approaching the boundary from within the melt. It turns out that the tip approaches but never completely reaches the boundary. There always remains a thin liquid layer in between the growing dendrite tip and the boundary. The evolution of the dendrite morphology is therefore independent of the imposed wetting angle β as no contact is established between dendrite tip and the boundary. An example of the resulting microstructure is displayed in Figure 4-33. The situation at the tip of the dendrite arm growing along the boundary is the same as the one displayed in Figure 4-32 b).

Figure 4-33 Simulation of a dendrite nucleated in the bulk and approaching the boundary. The dendrite tip does not establish contact with the boundary regardless of the imposed wetting condition. All other simulation conditions are the same as in Figure 4-31 except the positioning of the nucleus.

Influence of the domain thickness

In order to save computation time, it is desirable to limit the size of the simulated volume. Therefore, a set of simulations was conducted to determine the influence of the domain thickness on the tip kinetics, see Figure 4-34. The velocity of the tip growing along the boundary is the same for the four chosen domain thicknesses, even for the very thin domain in the last row of Figure 4-34. In order to quantify the required minimum thickness, a domain thickness Peclet number P_d is defined:

$$P_d = \frac{V}{2D_L}d \tag{4.2}$$

where V is the tip velocity of a tip not influenced by a domain thickness, D_L is the diffusion coefficient in the liquid and d the domain thickness. The simulation run at a

supersaturation of 0.73 showed that a P_d value as small as 3.7 still allows valid calculations of the dendrite tip kinetics.
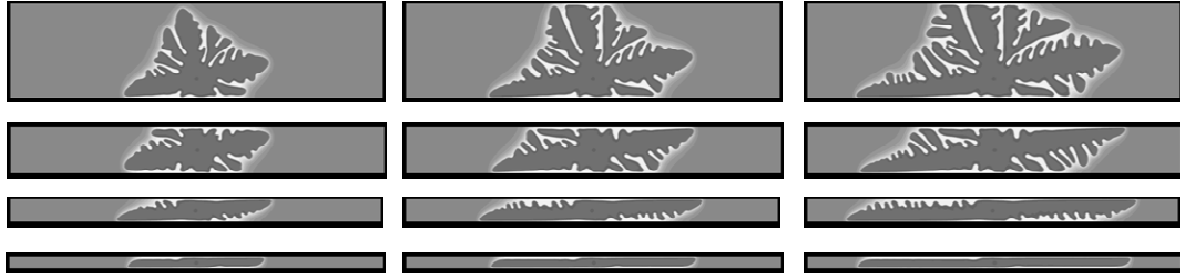
Figure 4-34 Dendrite morphology for domain thicknesses of 5, 2.5, 1.25 and 0.63 µm. Snapshots of the concentration field are displayed for 0.125, 0.175 and 0.225 ms after nucleation. All other simulation conditions are the same as in Figure 4-31.

Tip kinetics as a function of wetting and incidence angles

A series of calculations was carried out to determine the influence of the wetting angle β and the incidence angle α on the tip velocity of a dendrite growing along a boundary. For both objectives, simulations were performed at supersaturations of $\Omega = 0.73$ (T=530 °C) and $\Omega = 0.52$ (T=550 °C). The measured tip velocities were normalized with respect to the velocity of a tip freely growing into the supersaturated melt. As will be emphasized in chapter 5.1, the latter case is certainly closer to the situation in a real solidification experiment of Al-Zn-Si coatings. For the dependence on the wetting angle, β values of 75°, 82.5°, 90°, 97.5°, 105° and 112.5° have been applied on nuclei positioned on a boundary. For these simulation runs, the incidence angle α was arbitrarily set to 11° in order to ensure that the dendrite tip continues to follow the boundary and establishes a steady state morphology. The results are plotted in Figure 4-35 a). The increase in tip speed for wetting angles $\beta < 90°$ is significant for both temperatures but even more pronounced for the lower supersaturation. For $\beta = 90°$, tip velocities slightly below the velocity of a free dendrite have been measured. This is due to the fact that the incidence angle α is larger than zero. If α is set to 0° instead of 11°, the boundary corresponds to a crystallographic plane exhibiting mirror symmetry, and indeed, the measured normalized tip velocity becomes unity. For wetting angles $\beta > 90°$, the tip detaches from the boundary as it was already described above. For the lower supersaturation at 550 °C, the resulting normalized tip velocities are below unity whereas, surprisingly, the normalized tip velocities at 530°C are marginally higher than unity.

a)   b)
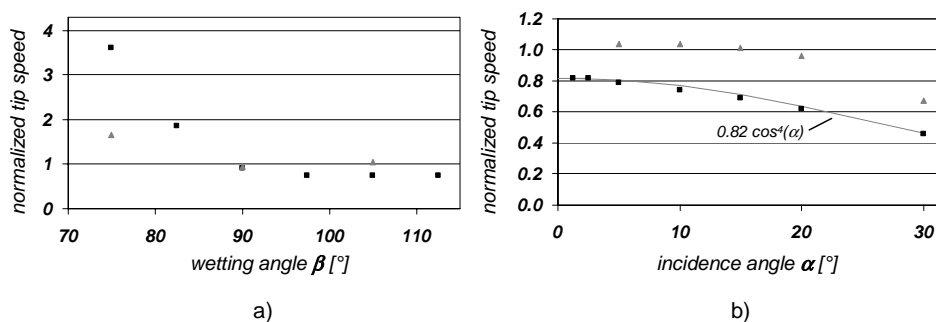
Figure 4-35 a) Normalized tip speed vs. the wetting angle β for a dendrite nucleated on the boundary. b) Normalized tip speed vs. the incidence angle α for a dendrite nucleated in the bulk of the liquid. Gray triangles stand for simulations at 530 °C, black squares for simulations at 550 °C. The tip speed vs. incidence angle curve for the more realistic 550 °C case is well fitted by a $\cos^4(\alpha)$ relationship.

The same observation can be made for dendrites nucleated in the bulk, approaching the boundary, and finally reaching a steady state morphology along the boundary, Figure 4-35 b). At the high supersaturation of 530 °C, tip velocities above unity are observed up to incidence angles of 15°. At the supersaturation corresponding to 550°C, the velocities of tips growing along the boundary are significantly smaller than for a free dendrite. In this case, which can be considered as representative for the actual growth conditions, the normalized tip velocity can be approximated by the following relationship:

$$\frac{V_{boundary}(\alpha)}{V_{bulk}} = 0.82\cos^4(\alpha) \tag{4.3}$$

Interactions of secondary branches with the boundaries

In the previous section, simulation results showing the influence of the boundaries on the velocity of dendrite tips growing along them was presented. The boundaries of the thin coating layer constrain, however, not only the dendrite tips oriented along the boundaries, but also the secondary arms emitted from such primary arms. Secondary arms can be emitted from the primary arm sidewards along directions that are close to the coating plane. In this case, the secondary behave like primary arms, i.e. they are affected by the boundary through a decrease in their tip velocity. On the other hand, secondary arms can be emitted towards the opposite boundary. In this case they include a large angle with the coating plane. Such secondary arms do not only suffer from a decrease in tip velocity but they are stopped upon impingement on the opposite boundary as shown in Figure 4-36.
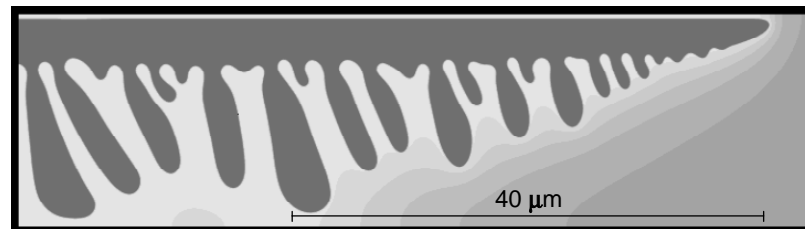
Figure 4-36 Phase field simulations showing the concentration field of a dendrite growing along a boundary and emitting secondary arms towards the opposite boundary at a realistic undercooling of 550°C. The secondary dendrite arms impinge on the opposite boundary about 40 μm behind the primary tip The supersaturation Ω is set to 0.51 (T=550 °C), the mesh size is 22.5 nm, the modeling domain measures 18 x 67.5 μm.

In the simulation result of Figure 4-36, the secondary arms impinge on the opposite boundary about 40 μm behind the primary tip. The essential part of the dendrite morphology is formed in the 40 μm between tip and the impingement of the secondary branches. There, the primary and secondary arms develop and the solid fraction increases form zero to the equilibrium value for the present temperature. Further behind, the solid fraction remains at the equilibrium value and the microstructure evolves only by maturation and thickening of the existing dendrite arms.

4.2.3 *Microstructure formation on the scale of the grain*

In order to better understand the formation of the dendrite network on the scale of the grain, a geometrical model describing the growth of the dendrites in the confined space of the Al-Zn-Si layer has been developed. As it was mentioned in section 3.2.3, the key physical parameter for the final appearance of the dendrite pattern is the crystallographic orientation of the grain with respect to the plane of the coating. In this subsection, the results of the geometrical model for two distinct orientations representing two exemplary types of simulation results are given. Figure 4-37 a) shows the dendrite network predicted for a grain having a {111} crystallographic plane close to the coating plane. The model predicts the selection of six primary arms which are projected into the coating plane and emit secondary branches. Note that the tertiary and quaternary branches have been calculated but are not shown on Figure 4-37 a) for the sake of clarity. The secondary arms emitted from the primary dendrite arms either grow towards the boundary with the substrate or towards the free boundary. In both cases, they will reach a boundary and will be projected into the plane of the boundary. In this way, two kinds of areas are formed where the dendrite arms predominantly grow either along the substrate or along the free

surface. These two cases are represented schematically in Figure 4-37 b) where an area of growth along the substrate is highlighted in dark gray and an area with growth along the free boundary in light gray.

In Figure 4-38 a), the dendrite structure of the grain is viewed from the normal direction to the coating plane. The regions where the dendrites have grown predominantly along the substrate are colored in dark while those captured by growth along the free surface are shown with a bright tone. In both cases, tertiary branches growing towards the free surface and the substrate respectively are also present but are not displayed in the figure.

a)   b)
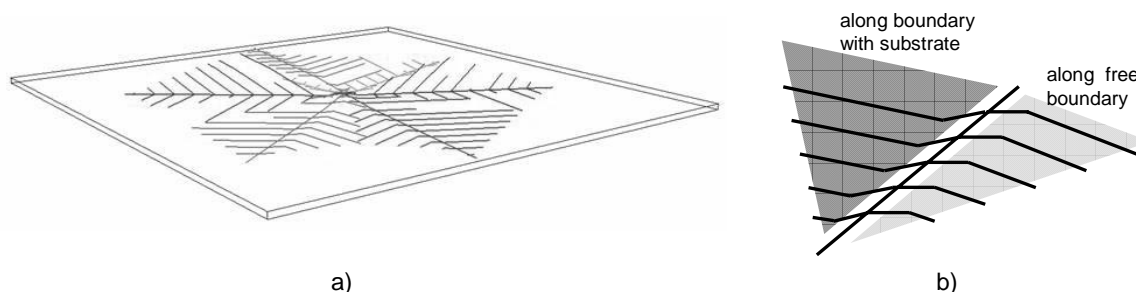
Figure 4-37 a) 3D view of a dendrite skeleton generated by the geometrical model. For the sake of clarity the ternary and quaternary branches are not displayed. **b)** Schematic representation of sectors resulting from growth along the free boundary (bright) or along the boundary with the substrate (dark).

The simulated grain is compared with the corresponding optical micrograph shown in Figure 4-38 b). As the simulation was carried out with the crystallographic orientation of the grain measured by EBSD, a direct comparison is possible. The six bright and dark sectors calculated with the model, Figure 4-38 a), correspond well to the observed shiny and dull sectors observed on the optical micrograph, Figure 4-38 b). This indicates that dendrite arms growing along the free boundary lead to a shiny and regular surface aspect, whereas dendrite arms growing along the substrate emit ternary branches that are responsible for the duller and more dimpled appearance at the free surface. In Figure 4-38 c), a surface topography map of the grain, which corresponds to the one already shown in Figure 4-10, is given. The relationship between the surface appearance and the topography that was already mentioned in section 4.1.3 will be discussed in detail in section 5.1.4.

<center>a)   b)   c)</center>
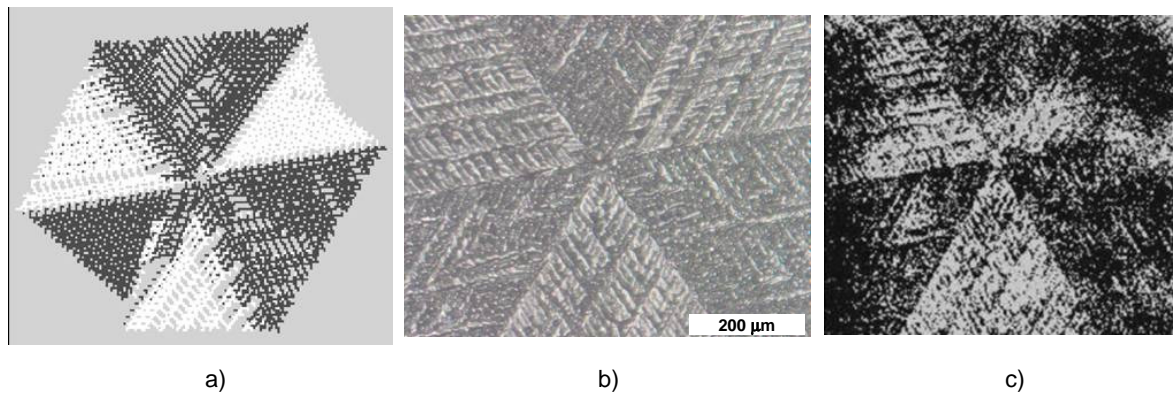
Figure 4-38 a) Shiny (bright) and dull (dark) sectors predicted with the geometrical model based on the assumption that predominant dendritic growth along the free surface leads to shiny areas, while growth along the substrate leads to dull sectors. **b)** Optical micrograph of a grain having the same crystallographic orientation with respect to the coating. **(c)** Surface topography obtained by laser profilometry. In the bright areas, the level of the surface is higher.

Figure 4-39 shows the simulation results and the corresponding optical micrograph for a grain exhibiting a {100} crystallographic plane close to the plane of the coating. Obviously, the agreement between Figure 4-39 b) and c) is poor. As can be seen from Figure 4-39 a), the geometrical model does not in all cases predict the correct predominant dendrite growth directions. As a consequence, the areas where the model predicts growth along the boundary with the substrate and the free boundary do not always correspond to the experimental observations.

<center>a)   b)   c)</center>
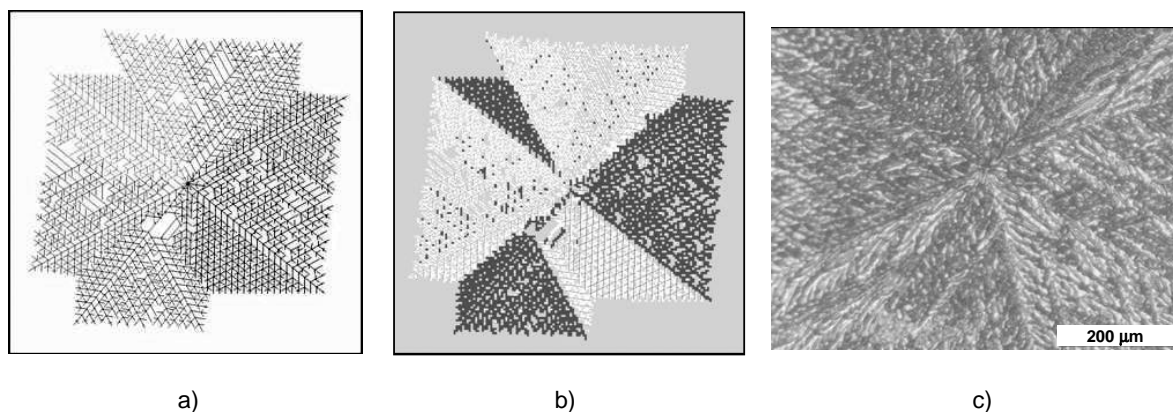
Figure 4-39 a) Dendrite network of a grain having a {100} plane close to the coating plane. **b)** Sectors of growth along the substrate and the free boundary. **c)** The corresponding optical micrograph.

For orientations similar to the ones displayed in Figure 4-38 ({111} or {110} crystallographic planes close to the coating plane), a good agreement between simulation

results and experimental observation is found in general. For orientations similar to the ones displayed in Figure 4-39 ({100} crystallographic plane close to the coating plane), the agreement is in general poor. There is no doubt that this discordance is due to imperfections in the geometrical model. The origins of these imperfections will be addressed in section 5.1.4.

4.3   Re-solidification experiments

Re-solidification experiments have been conducted in order to determine whether intragranular misorientations can be reproduced in laboratory experiments and to study the influence of the solidification and cooling conditions on the misorientations. In a first subsection, the temperature cycles that can be realized in the re-solidification experiments as well as the resulting misorientations are presented. In a second subsection, the influences of modified strain conditions during the thermal cycle and of the cooling rate on the misorientations are shown. Finally, in a third subsection, the microstructure and misorientations in Al-Zn-Si layers with no free boundary are analyzed.

4.3.1   *Re-melting / re-solidification of coatings*

The re-melting and re-solidification experiments have been conducted in order to study the microstructure of the Al-Zn-Si coating under modified solidification conditions in terms of cooling rate, thermal contraction and interaction with free surfaces. The influence of the solidification conditions on the intragranular misorientations is of particular interest. Before focusing on the formation of misorientations, the temperature patterns realized and some resulting microstructural features are described. Figure 4-40 a) and b) show temperature cycles obtained with the induction and infrared furnaces respectively. The induction apparatus (Figure 4-40 a)) has the advantage that it allows not only fast heating but also fast cooling of the samples. Without the application of cooling gas, i.e. only by the natural convection of the ambient air, cooling rates of about 10 K/s are obtained. By the gas cooling, the cooling rate can be increased up to 50 K/s. In the infrared furnace however, the efficiency of the cooling is reduced by the quartz tube in which the sample is held. Without gas cooling, the cooling rate is around 1 K/s, and even under the effect of a He gas flow, the cooling rate cannot be increased much above 20 K/s. The infrared furnace has the advantage that it leads to much smaller gradients within the sample. The gradients were estimated by comparing temperature measurements in the center and in the periphery of the samples. At maximum, a gradient of 1 K/mm is observed, in the induction heated sample however, gradients of up to 8 K/mm are reached; see the gradient curves in Figure 4-40. The reason for the strong gradients in the induction heated samples is the inhomogeneity of the Eddy currents in the sample. Therefore, the gradients disappear quickly once the induction heating is turned off. Due to the strong gradients, it is necessary to considerably superheat the center of the sample in order to melt

the coating at the periphery. Therefore, it is preferable to conduct re-solidification experiments within the infrared furnace in most cases except when particularly high cooling rates are desired. Further on, the use of the infrared furnace allows better defined temperature patterns and includes also the possibility of plateaus as shown in Figure 4-40 b).
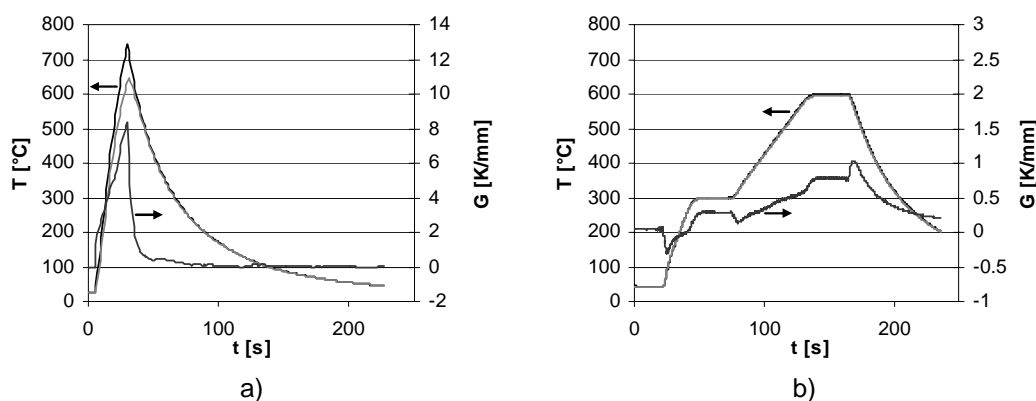
Figure 4-40 a) Re-melting / re-solidification temperature pattern realized with the induction apparatus, **b)** realized with the infrared furnace. In both cases, no cooling gas was applied. Black curves are measured in the center of the sample, grey curves on the side. The red curves give the temperature gradient between center and side. Note that the gradient reaches 8 K/mm in the induction furnace but only 1 K/mm in the infrared furnace.

An interesting observation was made in cases where the induction heating was not shut off immediately after the coating liquefied. In this case, curled fringes such as the ones showed in Figure 4-41 a) developed on the sides of the substrate. EDS analysis shows that they are made up of Al-Zn alloy. On the surface of the sample where the coating is expected to be, a structure as shown in Figure 4-41 b) remains. It turns out that the characteristic needles are silicon particles standing out of the surface. EDS measurements show that the underlying material contains not only Al, Zn and Si but also a significant amount of Fe, thereby indicating that the Al-Zn coating has completely vanished leaving behind only the intermetallic layer formed at the interface between coating and substrate. Apart from showing that significant temperature gradients remove the coating from the surface and make re-solidification experiments meaningless, this observation shows that the Si particles do not melt or dissolve into the liquid Al-Zn coating layer if the layer is maintained above the liquidus temperature for a short time only. Therefore, the liquid is less rich in Si and undergoes therefore another solidification path than the original coating.

a)   b)
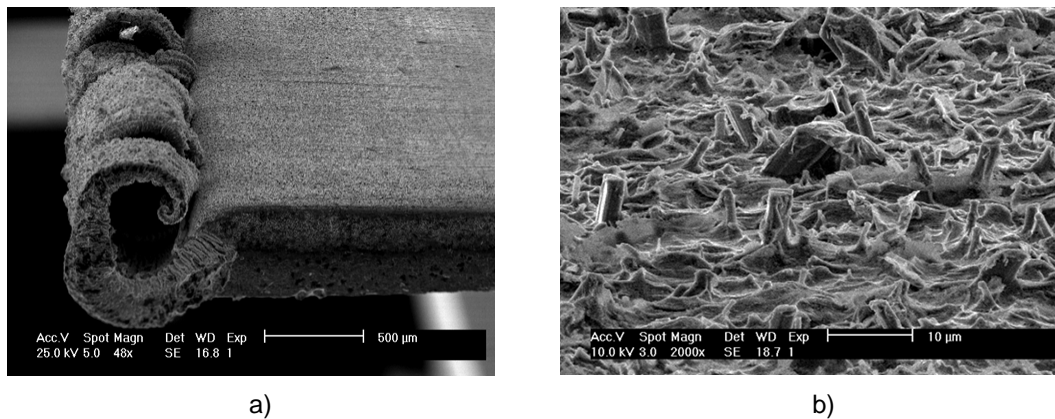
Figure 4-41 a) SE micrograph of curled Al-Zn fringes on the sides of the substrate typically observed in the induction apparatus when the coating layer is held in the liquid state for too much time. **b)** SE micrograph of the surface of the same sample where the coating is supposed to be. Si-needles and intermetallic particles wrapped by a wrinkled oxide skin remain after the Al-Zn coating has vanished.

Since the displacement of the coating layer into fringes is only observed in induction heated samples, it is reasonable to assume that the significant temperature gradients are responsible for this phenomenon. Indeed, the literature states that the solid-vapor interfacial energy decreases with increasing temperature for both Al and Zn, Figure 4-42. The surface energy of the melt is hence larger in the center of the samples than in their periphery. Therefore, it seems plausible to explain the displacement of the liquid alloy by Marangoni convection which displaces the liquid towards the colder edges of the sample.
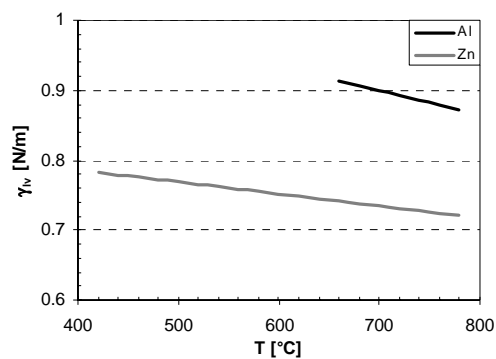
Figure 4-42 Solid vapor surface tension as a function of temperature for Al and Zn. Based on values taken from [Smithells 99].

The much less pronounced temperature gradients observed in the infrared furnace make this method more suitable at least for low cooling rates. Further on, the infrared furnace allows making temperature measurements with less noise than the induction

heating. Figure 4-43 a) shows a typical temperature pattern as it was measured in the infrared furnace and for which a He gas flow was applied in order to increase the cooling rate. Figure 4-43b) shows that the cooling rate realized is about constant in the solidification interval of the alloy. For the given He gas flow it was about 12.5 K/s.
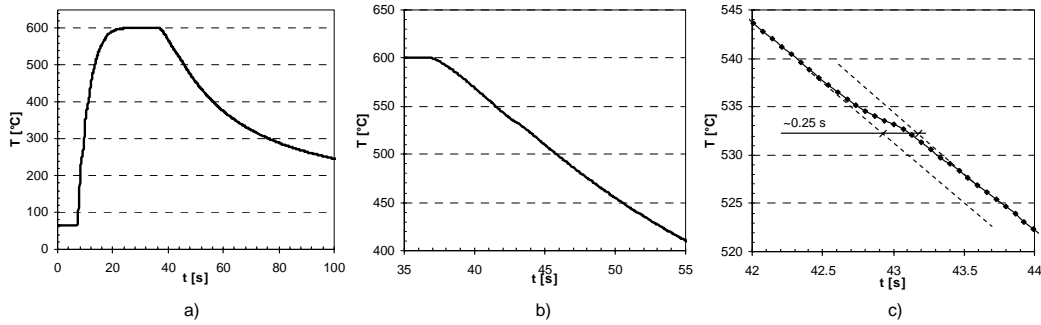
Figure 4-43 Typical temperature pattern measured at the center of a sample re-melted and re-solidified in the infrared furnace. **a)** The entire temperature pattern. **b)** Detail of a). The cooling rate (here 12.5 K/s) is constant in the solidification interval. **c)** Detail of b). Between 535 and 530 °C, a sudden decrease of the cooling rate occurs. Soon after, the cooling rate returns to its initial value. This phenomenon can be explained by the rejection of latent heat in the coating.

The cooling rate is however not completely constant. A systematic decrease in cooling rate is observed between 535 to 530 °C. After a short time, the cooling rate stabilizes again at the values already observed at higher temperatures. A typical example is given in Figure 4-43 c). In this case, the observed inflection shifts the cooling curve by about $\Delta t = 0.25$ s. It is assumed that the sudden decrease of the cooling rate is due to release of latent heat during solidification in the coating layer. From the time shift of the temperature curve, Δt, the heat flow balance due to the release of latent heat can be established:

$$\dot{T} \, \rho c_p \, d_{coated\,steel} \, \Delta t = f_s \, L \, d_{coating} \tag{4.4},$$

where $\dot{T}$ is the cooling rate, $\rho c_p = 3.8\,10^6\,\mathrm{Jm^{-3}K^{-1}}$ the volumetric specific heat, $d_{coated\,steel} = 0.5$ mm the thickness of the substrate, $L = 9.10^8\,\mathrm{Jm^{-3}}$ the latent heat of fusion of the coating, $d_{coating} = 20\,\mu\mathrm{m}$ the thickness of the coating and f_s the solid fraction. From the given equation, the solid fraction f_s that needs to be reached in order to cause the Δt can be calculated. For the given numerical values, a solid fraction f_s of about 33% is achieved during the inflection shown in Figure 4-43 c). This estimation of the solid fraction is somewhat approximate, however, the experimental observation of the inflection in the cooling curve is reproducible and always leads to solid fractions in this same order

of magnitude.

The temperatures at which solidification starts, i.e. at which the cooling curves start to deviate from the linear regime, have been determined for different cooling rates. No clear dependence on the cooling rate was found. In general the reaction starts between 537 and 531 °C. In Figure 4-43, it starts at about 536 °C.

The dendrite arm spacing λ_2 however is not independent of the cooling rate and follows a clear trend. With increasing cooling rate, the dendrite arms spacing decreases. The dependence is particularly strong at the low cooling rates realized with the infrared furnace, Figure 4-44. The dendrite arms spacing of industrially solidified samples is about 11 μm. From this information, it seems reasonable to assume that the cooling rate in the industrial process is in the order of 10 K/s or more.
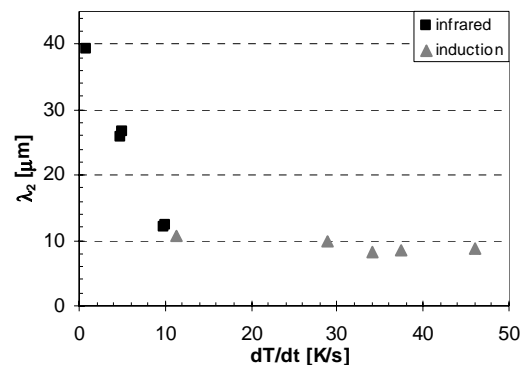
Figure 4-44 Dependence of the dendrite arm spacing on the cooling rate.

An important difference between the industrially solidified Al-Zn-Si coatings and the re-melted / re-solidified samples is the observed grain size. In re-solidified samples the grain size is significantly smaller. In industrial coatings, grains have diameters of several mm whereas re-solidified grains often have a diameter of a mm or less. Also it seems that the grain size is somewhat dependent on the cooling rate. At higher cooling rates the grains tend in general to be smaller. Figure 4-45 visualizes the difference in grain size in a particularly pronounced case: a) shows the grain structure of an industrial coating and b) the one of a coating re-solidified in the induction furnace at rate of 30 K/s.
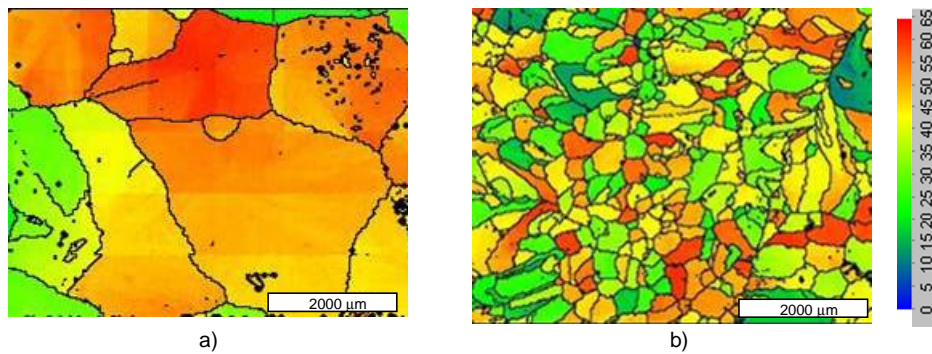
Figure 4-45 EBSD misorientation mappings showing the grain structures in Al-Zn-Si coatings. **a)** Coarse grained structure in an industrial coating. The horizontal and vertical lines are artifacts of the EBSD method. **b)** Fine grain structure in a sample re-solidified with the induction apparatus with a cooling rate of about 30 K/s.

By looking carefully at the EBSD mappings shown in Figure 4-45, intra-granular variations of orientation manifesting themselves through color gradients within grains which can be observed both in the industrial and in the re-solidified sample. As a first approximation the amount of misorientation can be characterized by taking misorientation profiles along the longest diameter of a grain. The misorientation τ with respect to the first point / origin of the profile is calculated as described in section 3.1.2. In Figure 4-46, 10 respectively 12 such profiles are shown for the industrial sample of Figure 4-45 a) and for the re-solidified sample of Figure 4-45 b). By applying a linear regression on the profiles, a misorientation rate $\mathrm{d}\tau/\mathrm{d}x$ can be determined for each profile. For the industrial sample, a mean misorientation rate of 4.2°/mm and a standard deviation of 1.8°/mm were found. In the re-solidified sample, the corresponding values were 7.7°/mm and 5.0°/mm. The misorientation rates are hence higher in the present re-solidified sample. In re-solidified samples, it is however noticeable that very strong variations of the misorientation rate occur from one grain to the other, or even within one grain when the profile is taken along different directions. In conclusion, one can say that the re-melting / re-solidification experiments also lead to pronounced variations of crystallographic orientation within grains.
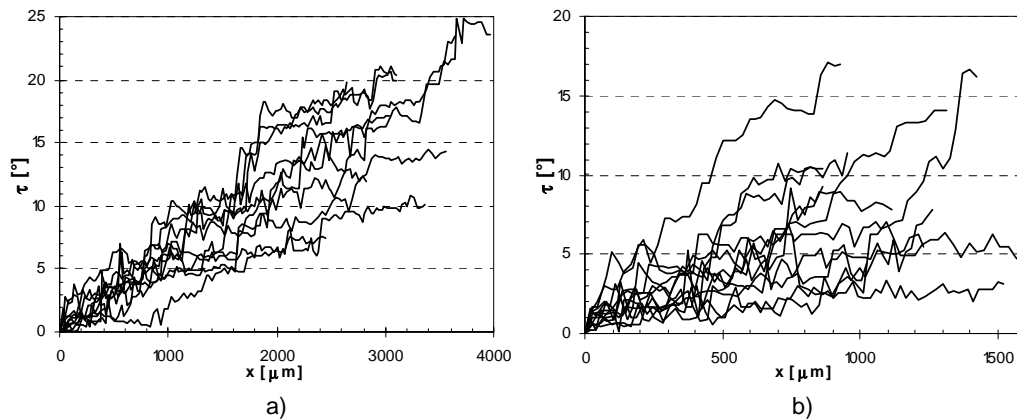
Figure 4-46 a) Misorientation profiles taken along the longest diameter of 10 grains in the industrial sample shown in Figure 4-45 a). **b)** Misorientation profiles taken for 12 grains of the re-solidified sample shown in Figure 4-45 b). Significant misorientations are also present in re- solidified grains. The misorientation rates are more scattered in the re-solidified sample.

A more detailed qualitative analysis of the given misorientations shows that the character of the misorientations found in re-solidified samples is comparable to the misorientations found in industrial samples, i.e. the misorientations develop either continuously along dendrite arms or they initiate as discrete orientation change across one dendrite arm and propagate during growth as subgrain boundaries. The presence of discrete misorientations and subgrain boundaries is well illustrated by the numerous jumps of orientation in the profiles of Figure 4-46 that are due to subgrain boundaries. The irregular nature of the profiles is also due to the fact that the profiles where not taken along primary growth directions but along the longest diameter of the grain. Therefore, it is more likely to intersect many subgrain boundaries. A more detailed description of the misorientations present in re-solidified samples is found in the subsequent section where, besides the effect of modified stress conditions, the influence of the cooling rate on the misorientations is discussed in detail.

4.3.2   *Solidification under modified stress conditions*

In order to study the influence of the thermomechanical stresses on the formation of intragranular crystallographic misorientations, re-solidification experiments have been conducted with samples mounted in the brass setup described in section 3.3.2. Samples have been re-melted and re-solidified without tightening the screws thereby providing reference samples solidified under identical conditions except that no strain is applied on

the sample by the brass disks.
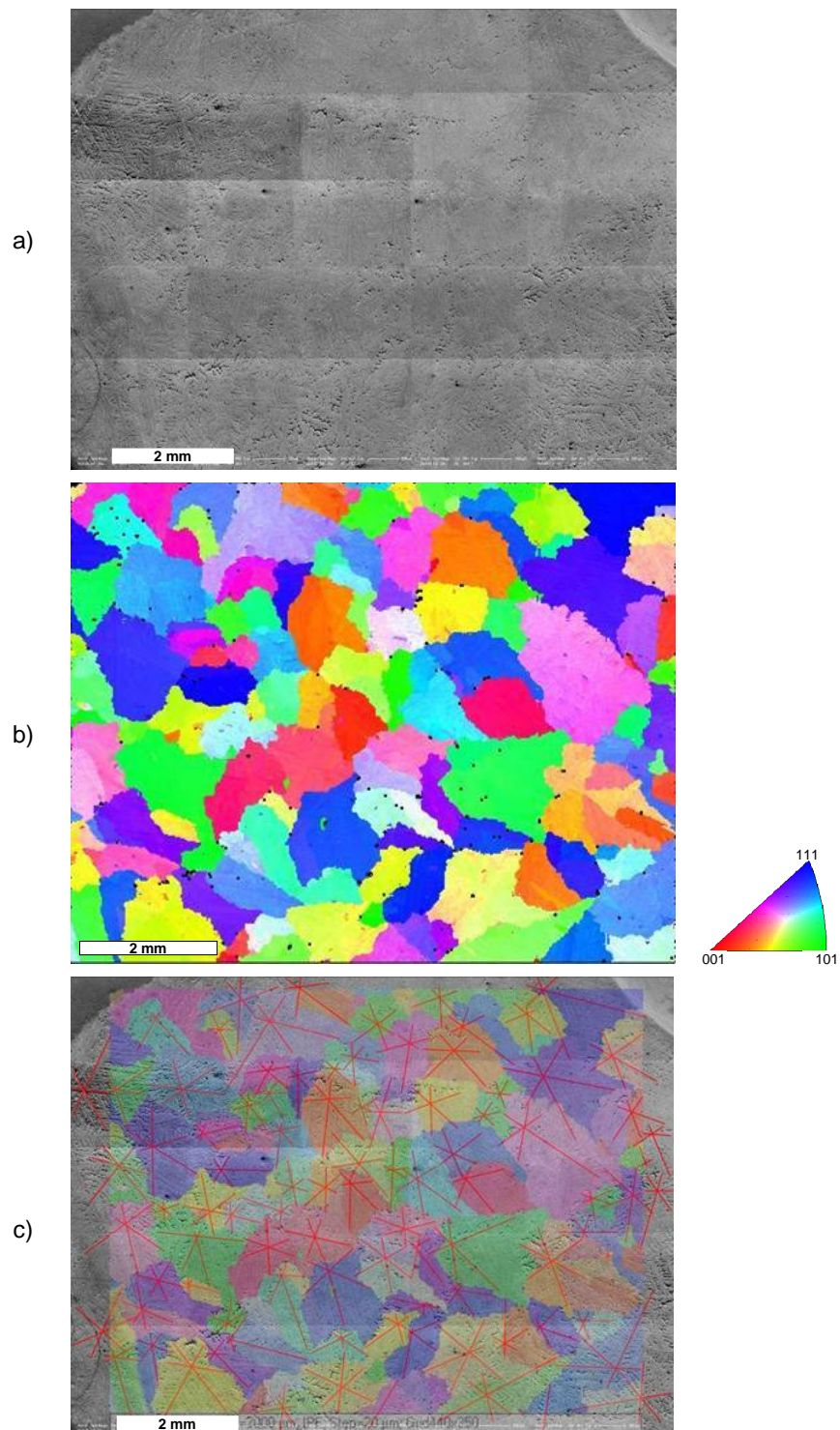
Figure 4-47 a) Assembly of SE micrographs used to identify the primary dendrite arms. **b)** EBSD inverse pole figure map of the corresponding area. **c)** Superposition of a) and b).The red lines indicate the primary dendrite arms along which the misorientation profiles have been measured.

After re-solidification, EBSD mappings have been performed on a relatively large zone of the sample, Figure 4-47. The main objective was to characterize the misorientations that are due to continuous orientation changes along the dendrite arms. For this reason, misorientation profiles have been measured along the primary dendrite arms. As the dendrite structure cannot be identified on the EBSD maps, SE micrographs of the corresponding area have been taken and assembled, Figure 4-47 a). The assembled micrographs have been superimposed onto the EBSD map in Figure 4-47 c). The red lines in Figure 4-47 c) correspond to the primary dendrite arms along which misorientation profiles have been measured. The misorientation rates extracted from the raw data are presented in Table 4-3. The misorientation rates of an industrial reference sample are compared with those of two samples re-solidified at a cooling rate of about 5 K/s with and without tightened screws. It becomes apparent that the re-solidified samples exhibit a considerably smaller misorientation rate than the industrial sample, at least for the given cooling rate. The difference between the two re-solidified cases is however small. The sample on which a strain has been imposed by the brass disk shows even a slightly higher misorientation rate than the sample where the disks were not screwed together. The difference is however small, especially when considering the high standard deviations which show that the misorientation rates vary considerably from one grain to the other and even for profiles taken in the same grain but along different directions.

	# of profiles	misorientation rate $d\tau/dx$ [°/mm]			
		minimum	maximum	mean	std. deviation
industrial reference sample	33	1.62	8.86	**4.36**	1.55
re-solidification **without** imposed strain	36	0.36	3.76	**1.86**	0.98
re-solidification **with** imposed strain	45	0.37	5.49	**2.07**	1.31

Table 4-3 Experimentally determined misorientation rates for an industrial sample and samples re-solidified without and with imposed strain. In both of these cases, the coated steel sample is placed in between the brass blocs in order to guarantee a comparable thermal history, but the contraction of the brass disks is only imposed in the latter case where the screws connecting the two brass blocs have been tightened. For the given results, the cooling rate during re-solidification was about 5 K/s.

The results reported above have been recorded on coatings positioned on steel substrates exhibiting the original thickness (~0.5 mm). As mentioned in section 3.3.2, equivalent experiments have been done on samples where the thickness of the substrates was reduced to 0.1 – 0.15 mm. These thin samples however often bulged as a reaction to the thermomechanical stresses occurring during the thermal cycle, which made the analysis

of the misorientations difficult.

From the results previously presented above, it becomes apparent that the cooling rate during re-solidification is an important parameter for the measured misorientation rate. Figure 4-48 shows that the misorientation rate distribution is heavily affected by the imposed cooling rate. In general, higher cooling rates lead to more pronounced intragranular misorientations in the coating.
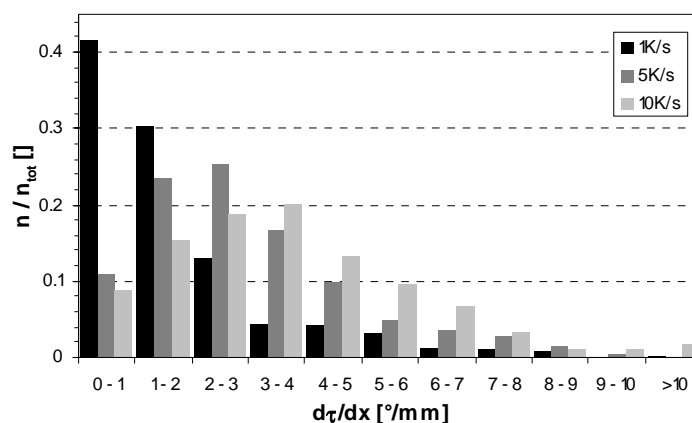
Figure 4-48 The misorientation rate distribution as a function of the cooling rate. Higher cooling rates correlate with higher misorientation rates.

In conclusion, one can therefore say that the influence of the brass setup on the intragranular misorientations is small. However, the misorientation rate correlates with the cooling rate. Likewise, there is a correlation between cooling rate and secondary arm spacing, see Figure 4-44.

4.3.3 *Solidification of Al-Zn-Si layers with no free boundary*

Microstructure after ultrasonic welding, before re-melting

Two steel sheets which are both coated with an Al-Zn-Si alloy layer of about 20 μm thickness have been joined by ultrasonic welding as described in subsection 3.3.3. The resulting structure is a sandwich of two steel sheets with an Al-Zn-Si layer (~40 μm thick) in between. Figure 4-49 shows optical micrographs of polished sections across the sandwich. On the optical micrographs, only Si particles are visible within the interlayer. The micrographs of Figure 4-49 a) and b) are taken within the welding spot which has the

size of 8 x 10 mm, while the micrograph of Figure 4-49 c) is taken outside the welding spot. In the latter case, it is clearly visible that the connection between the two Al-Zn-Si layers is poor. Within the welding spot however (Figure 4-49 a) and b)), the connection is good and no pores/cavities are visible at the initial interface between the two Al-Zn layers. In some areas, especially on Figure 4-49 b), a thin dark line remains visible at the former interface between the two layers. This feature may correspond to an oxide skin that is not completely dispersed during the welding process.
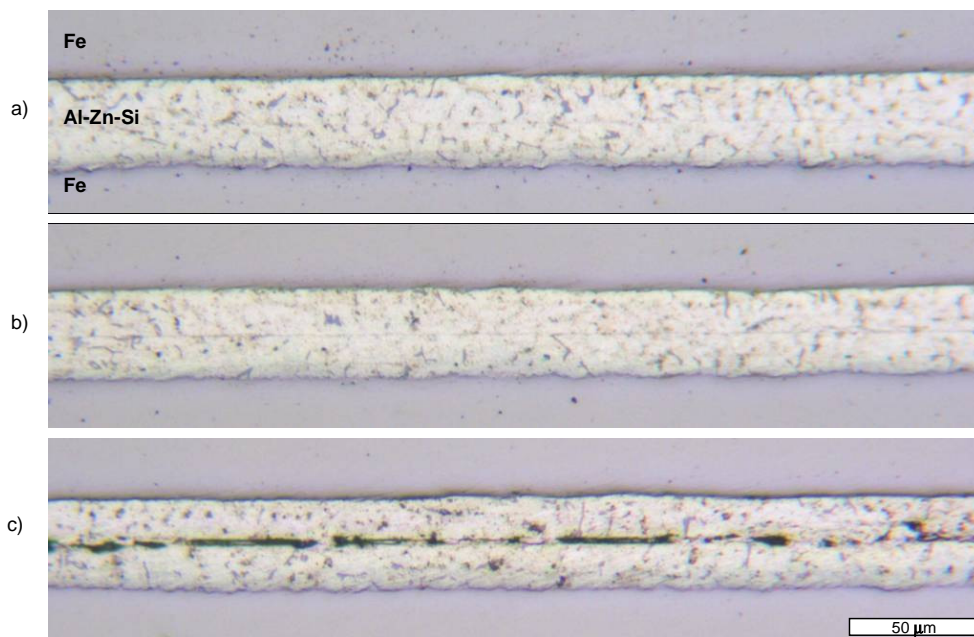
Figure 4-49 Optical micrographs of polished cross-sections after ultrasonic welding. **a, b)** Within the welding spot, **c)** outside the welding spot.

In order to gather more information about the microstructure at the weld joint, scanning electron microscopy has been performed (Figure 4-50 a-c). In most of the Al-Zn-Si coating, the typical Al-Zn-Si microstructure is preserved during the ultrasonic welding process: the black areas correspond to Si particles, α-Al dendrite arms are shown in dark gray tones and light gray areas correspond to eutectic areas and zones rich in precipitates. Within the welding spot, areas presenting different morphologies at the welding joint can be distinguished. Figure 4-50 a) shows an area where the Al-Zn-Si microstructure is entirely conserved, and the interface between the two sub-layers is displayed as a sharp, dark line. In this case, it remains questionable whether the oxide skins are properly broken at the interface. In Figure 4-50 c) the interface is made up of a broad zone where the initial Al-Zn-Si microstructure is stirred up. Dendrite arms as well as eutectic islands are severely

deformed and broken up. In this case it seems likely that the oxide skins at the interface are destroyed. Figure 4-50 b) shows a somewhat intermediate case. In the center of the welding spot, the cases of Figure 4-50 a) and Figure 4-50 c) are equally likely, whereas in the periphery of the welding spot, case a) dominates.

| a) | b) | c) |
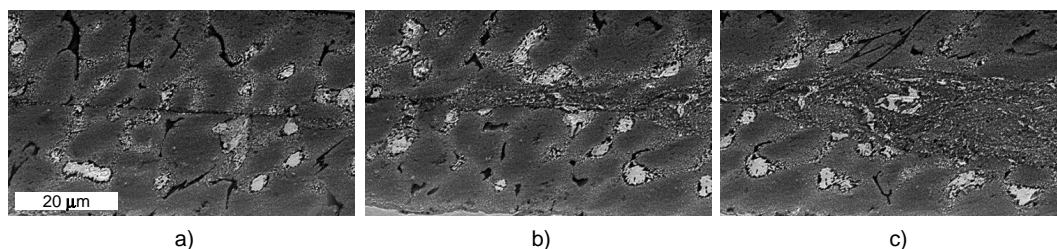
Figure 4-50 SE micrographs of the weld joint within the welding spot prior to re-melting / re-solidification. **a)** to **c)** show different qualities of the joint.

Microstructure after ultrasonic welding, after re-solidification

Re-melting / re-solidification experiments have been conducted on the samples joined by ultrasonic welding. Cross-sectional micrographs of the resulting microstructure are displayed in Figure 4-51. The micrograph of Figure 4-51 a) shows a microstructure that is typical for the welded samples after re-solidification. The most distinct features are the black lines that are partially folded to loops. They correspond to the remains of the oxide skins present at the interface between the two Al-Zn-Si sublayers prior to welding. This oxide skin is not continuous but in fragments, and in some areas, it is not present at all. However, it can be assumed that the oxide fragments affect the solidification microstructure of the Al-Zn-Si interlayer. In particular, it appears that pores and cracks form on the oxide fragments in the center of the interlayer during re-solidification. Figure 4-51 b) and c) show pores of different size which are all attached to the oxide fragments present in the central area of the interlayer.
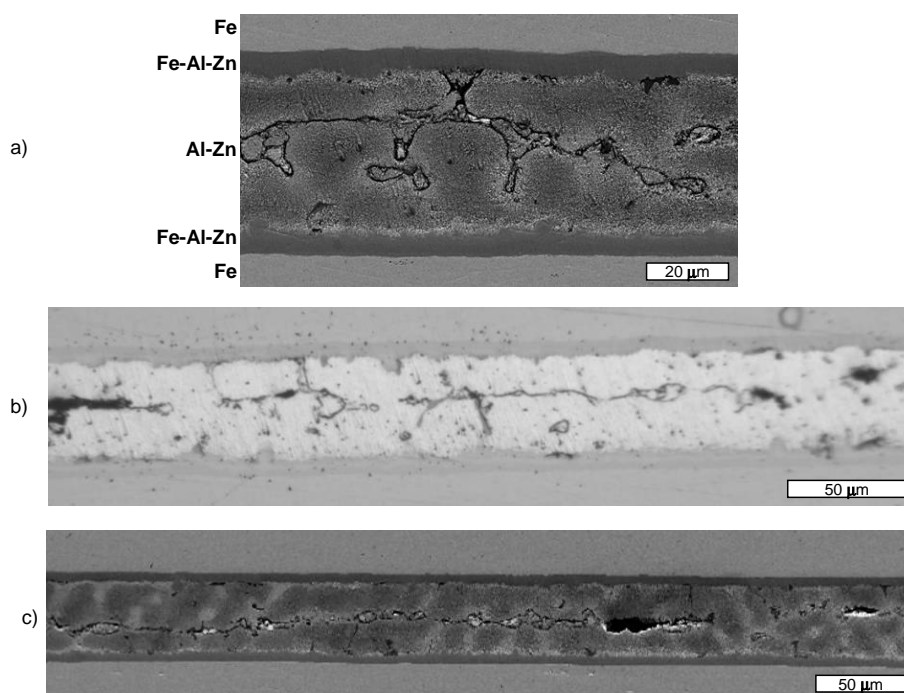
Figure 4-51 SE (a, c) and optical (b) micrographs of cross sections through the welded samples after re-solidification. Oxide skins are visible as dark, wrinkled loops at the center of the Al-Zn-Si interlayer. In **b)** and **c)**, it can be seen that porosities preferentially form on the oxide skin.

The SE micrographs of cross sections of the re-solidified samples clearly show an additional dark gray layer in between the steel substrate and the dendritic Al-Zn-Si layer. EDS analysis showed that this layer is made up of the four elements: Al, Fe, Zn, and Si. The approximate concentration of the layer is 76Al-14Fe-4.5Zn-4Si (in wt.%). The formation of such an intermetallic layer is not restricted to the re-solidification of sandwich structures but does also occur in the re-solidification of simple coatings. One can assume that this intermetallic layer forms during the time the coating Al-Zn-Si layer is liquid since the diffusivity is greatly enhanced in the liquid state as compared to the solid state. The short time of not more than a minute during which the layer is liquid is apparently sufficient in order to break up the Al-Fe-Zn-Si inhibition layer (see section 2.1.3) and to form a relatively thick intermetallic layer. In the intermetallic layer, the ratio between Al, Zn, and Si is different from in the original alloy coating. In particular, the proportions of Al and Si are higher in the intermetallic. For that reason, the remaining part of the coating alloy is finally poorer in Al and Si than the original one.

In order to assess the intragranular misorientations in the Al-Zn-Si interlayer, metallographic sections parallel to the plane of the layer must be prepared by removing one

of the steel substrates by grinding. When arriving towards the center of the interlayer, the influence of the pores displayed in Figure 4-51 becomes apparent. In the areas where there are pores, no contact between the two sublayers is established and the upper sublayer delaminates from the lower leaving behind a relief showing the dendrite structure of the lower sublayer. Figure 4-52 shows that delamination occurs on a significant fraction of the surface even in the center of the welding spot. It is, however, difficult to exactly determine in which areas the contact was good, since the delamination can only be detected in areas where the polishing plane is close to the interface between the two sublayers but still in the upper sublayer as it is the case in Figure 4-52. This situation occurs however only in a restricted part of the sample as it is extremely difficult to remove one of the steel substrates by grinding without inducing a misalignment of less than 10 μm. In all the other areas, the section either crosses the upper or the lower sublayer and no delamination and hence no indication of the quality of the weld joint is discernable.
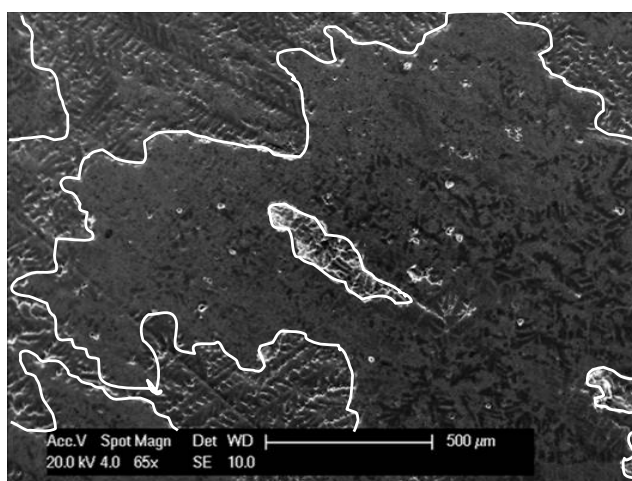
Figure 4-52 SE micrograph of a section polished parallel to the plane of the coating. Areas where a good weld contact is established show no roughness and only chemical contrast. In areas where the two sublayers delaminated during polishing, a relief reproducing the dendrite structure is observed. The white line follows the boundary between the areas of good contact and the delaminated areas.

The EBSD mapping of Figure 4-53 shows that the grain structure of the re-melted interlayer is affected by the ultrasonic welding process. Within the welding spot, the grain structure is finer and more fragmented than outside where the layer solidified under conditions that are essentially identical to the ones in a re-solidification experiment of a simple coating. The difference in grain size is clearly observed in Figure 4-53 a), where the bottom quarter of the EBSD map lays outside the welding spot and exhibits grains that are significantly larger than in the rest of the sample.

From the EBSD mappings it can also be seen that the grain structure does not show any congruence with respect to unwelded areas. This confirms that the layer of Al-Zn-Si melt is indeed continuous and that the oxides films are truly broken into pieces. It can be observed that a grain nucleated in a welded area continues subsequently in an unwelded zone and again in a zone of good contact. This means that dendrite tips of the growth front of one grain can grow around the oxide fragments that lead to the formation of pores and finally to delamination of the two sublayers.

a)   b)
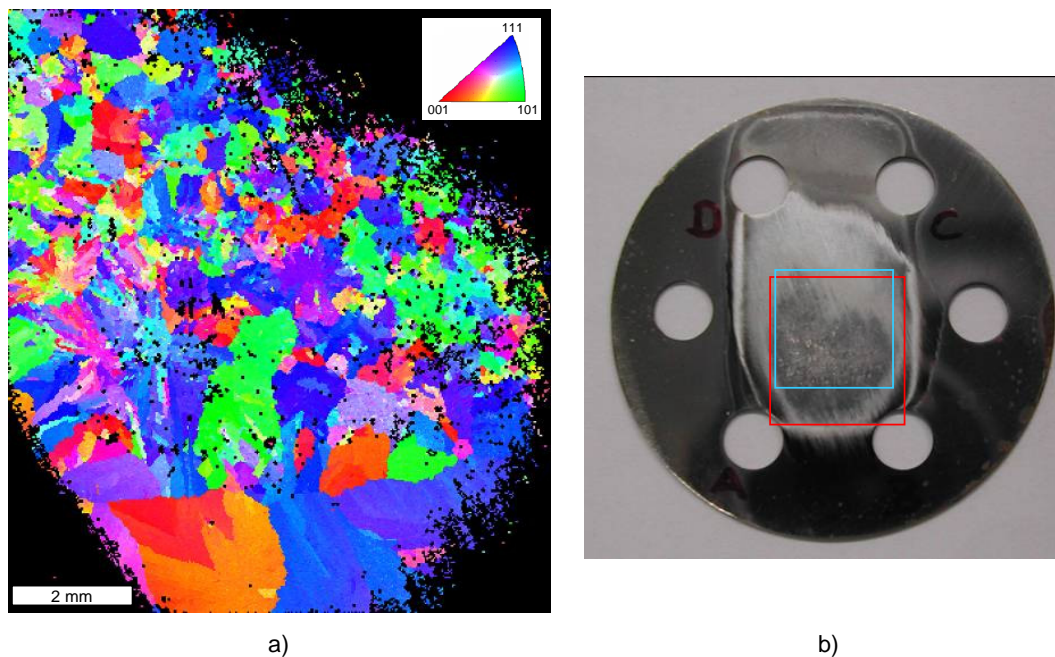
Figure 4-53 a) EBSD inverse pole figure map showing the grain structure of an Al-Zn-Si sandwich interlayer after re-solidification. The black, non-indexed areas are due to grinding down to the substrate. **b)** Sample on which the EBSD map has been taken. The red zone corresponds to the mapped area, the blue zone to the position of the ultrasonic welding spot.

The characterization of the intragranular misorientations present in the re-solidified grains within the welding spot is relatively difficult. The first reason for this is that the grain size is smaller than in the samples discussed in previous sections. However, the distribution of the misorientations is substantially different from what was observed in re-melted industrial coatings. In many grains, strong misorientations as shown in Figure 4-54 a) occur. These misorientations are however mostly made up of discrete orientation changes of several degrees propagating in the form of subgrain boundaries. The continuous

misorientations that are characteristic for industrial of re-melted samples seem negligible as compared to the pronounced discrete misorientations. Therefore, it is not meaningful to quantify the misorientations by taking misorientation profiles along the dendrite arms as was done in the previous sections. The result would be dominated by the discrete and apparently random subgrain boundaries. An extreme case is given by Figure 4-54 a) where a small grain shows an extremely scattered crystal orientation pattern. The numerous subgrain boundaries seem to follow the dendrite structure form the nucleus to the periphery of the grain, which indicates that these very pronounced misorientations are still produced within the solidification interval.
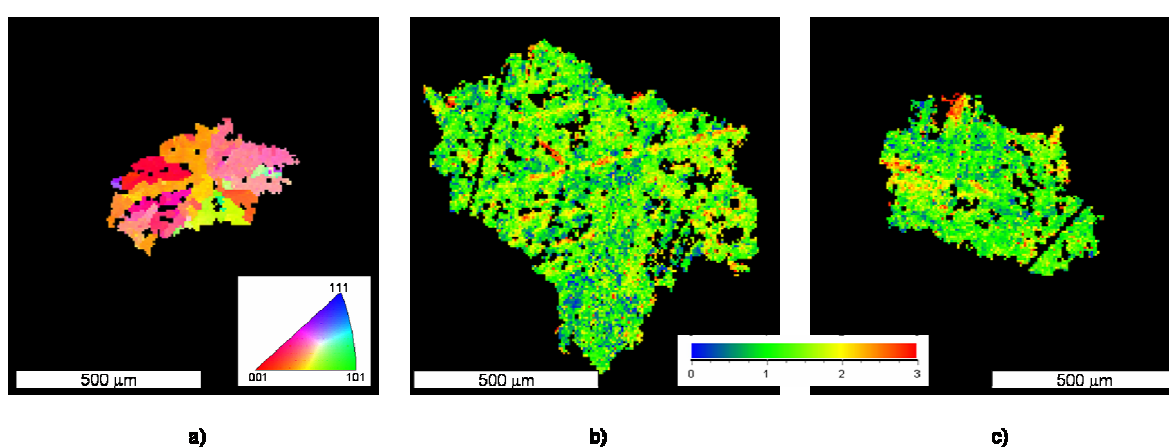
Figure 4-54 EBSD maps showing the intragraular misorientation present within individual grains in the welding spot after re-solidification. Different grains show very different misorientation pattern. **a)** Shows a grain with very pronounced, discrete misorientations, whereas the grains in **b)** and **c)** show misorientations that are extraordinarily small for Al-Zn-Si layers.

However, not all grains show such strong discrete misorientations. A minority of the grains found within the welding spot exhibit a very uniform crystal orientation. Examples for such grains are shown in Figure 4-54 b) and c). It is actually almost impossible to determine a misorientation rate across such grains independently of the direction that is chosen for the misorientation profile. As compared to the observations made on industrial and re-solidified coatings, the uniform crystal orientations observed in these grains are quite exceptional.

The question whether the presence or absence of intragranular misorientations is related to the local quality of the weld joint cannot be answered conclusively since the quality of the weld joint can only be judged in the limited area where the polished section is close enough to the former interface between the two Al-Zn-Si interlayers and where

hence delamination can occur.

The results of the re-solidification experiments can be summarized as follows:

- Cooling rates in the range of 1 to almost 50 K/s can be realized with the infrared and the induction furnace.

- Temperature gradients in the samples need to be avoided since they lead to the collapse of the coating, probably due to marangoni convection.

- Inflections in the cooling curves at the relatively low temperatures of 530-535°C are observed. They are due to the release of latent heat. From the shift of the cooling curves, it can be concluded that a substantial volume fraction is formed in a very short time at this temperature

- The grain size is in general smaller in re-solidified coatings than in industrial coatings.

- The dendrite arm spacing decreases with increasing cooling rate.

- Intragranular misorientations are also shown in the re-solidified coatings. The observed misorientation rates scatter more strongly from one grain to the other than in industrial coatings.

- The observed misorientation rate increases with an increase of the applied cooling rate.

- The observed misorientation rates do not depend significantly on whether the strain conditions during the thermal cycle are modified by the brass disks or not.

- The joining of two Al-Zn-Si coating layers by ultrasonic welding allows breaking up the oxide layers at least partially.

- The re-solidification experiments of ultrasonic welded Al-Zn-Si interlayers allows producing grains with almost no misorientations while other grains still exhibit very strong misorientations.

CHAPTER V

DISCUSSION

In this chapter, the results presented in chapter 4 are further analyzed and discussed. The chapter is divided in two sections. The first section is concerned with the microstructure formation in Al-Zn-Si coatings including the aspects of the selection of the dendrite growth directions, the formation of the dendrite network and the origin of the surface structure on the coating. Experimental and modeling results are related and jointly discussed in this section. The discussion about the microstructure formation of section 5.1, especially the development of the dendrite network, constitutes the basis for the discussion of the mechanisms that possibly lead to the formation of the intragranular misorientations. The latter aspect is treated in section 5.2. There, three different mechanisms, which could be responsible for the intragranular misorientations, are discussed.

5.1 Microstructure formation

5.1.1 Sequence of phase transformations

Upon cooling, the melt undergoes a series of phase transformations which lead to the final microstructure. The first of them is the formation of primary α-Al dendrites from the melt. The microstructure of the coating is largely dominated by the network of primary dendrites. As will be argued in section 5.2, the formation of intragranular misorientations is closely related to the growth of the primary dendrites. Therefore, the growth of the dendrites in the Al-Zn-Si coating layer will be discussed in detail in the following subsections. However, a brief discussion of the entire series of phases appearing during the microstructure formation is given here.

The experimental observations on the microstructure of Al-Zn-Si coatings are in good accordance with the results reported by Chen and Willis [Chen 05] on the solidification sequence of such coatings. The primary phase that dominates the microstructure are α-Al dendrites. As a second phase, Chen and Willis identified Si-particles that are supposed to appear at temperatures below 520 °C. This is well reflected in the microstructure by the presence of facetted Si particles that are always located in the interdendritic areas. Finally, at the ternary eutectic point at 381 °C, the hexagonal β-Zn phase appears. The interdendritic eutectic islands are essentially constituted of α-Al and β-Zn since the Si concentration approaches zero in the binary eutectic valley towards the ternary eutectic point. Most eutectic islands show a microstructure of a divorced eutectic where the α-Al phase grows epitaxially on the surrounding dendrite arms. In some cases however, the divorced eutectic abruptly changes into a coupled microstructure. Even though the kinetics of divorced eutectics are ill-defined, one can assume that the increasing driving force due to the forced cooling of the sample favors the transition to coupled eutectic growth. After cooling to room temperature, another phase transformation takes place. Within the dendrite arms, β-Zn precipitates form once the samples are cooled. As it has been shown in section 4.1.1, the β-Zn precipitates are coherent with the α-Al matrix. Considering the high volume fraction of precipitates due to the important supersaturation, it becomes apparent that important coherency stresses must develop in the dendrite arms during precipitation.

5.1.2   Interfacial energy anisotropy and the selection of dendrite growth directions

In this subsection, the results presented in subsection 4.2.1 are further discussed. The objective was to develop a mathematical expression for the solid-liquid interfacial energy and to determine more accurately the preferred growth directions in the Al-Zn-Si alloy system. Based on the assumptions that dendrite tips grow along the local (in-plane) minima of the interface stiffness and that the solid-liquid interfacial energy can be described by a cubic harmonic expansion up to the third order, an expression for the interfacial energy has been determined by inverse modeling. The corresponding minima of the interface stiffness are located in between neighboring $\langle 100 \rangle$ and $\langle 110 \rangle$ directions, 28.5° from the $\langle 100 \rangle$ directions. In consequence, there are in total 24 minima of the stiffness and hence also 24 possible dendrite growth directions. The calculated and measured growth directions reported in Table 4-1 show a good agreement, if one considers the errors associated with the measurement of the dendrite growth directions (estimated at a few degrees).

The results are also in reasonable agreement with the findings of Sémoroz et al. [Sémoroz1 01] who stated that the growth directions in the Al-Zn-Si system are approximately $\langle 320 \rangle$. The $\langle 320 \rangle$ directions include an angle of 33.7° with the neighboring $\langle 100 \rangle$ direction. The results of Sémoroz et al. deviate by only about 5° from the inverse method results, which is remarkable considering that their findings are based on the visual comparison of pole figures to micrographs of the dendrite structure. The result of the inverse modelling is also in good agreement with the recent observations of Gonzales et al. [Gonzales 06] who showed that the preferential dendrite growth directions gradually change form $\langle 100 \rangle$ to $\langle 110 \rangle$ as the Zn concentration is increased in a binary Al-Zn alloy. For an Al-50wt%Zn alloy, they reported growth directions 32.7° off the $\langle 100 \rangle$ orientations.

Further on, it has been reported in section 4.2.1 that the dendrite pattern is affected by the strength of the in-plane anisotropy of the interface stiffness. A strong in-plane anisotropy leads to a well-defined dendrite pattern, whereas a weak in-plane anisotropy leads to a more blurred / chaotic dendrite structure. Similarly, planes of strong and weak effective in-plane anisotropy have been reported in the literature for transparent organic alloys of cubic crystal structure by in-situ observation of the solidification in thin layers [Akamatsu 95, Utter 02]. The planes of strong and weak effective anisotropy are however different in the reported organic systems as compared to the Al-Zn-Si alloy considered here. In thin samples of CBr_4-C_2Cl_6 [Akamatsu 95] and succinonitrile [Utter 02], dendritic growth with distinctly pronounced arm directions is found when the experimental cell is aligned with a {100} crystallographic plane. If however the sample is aligned with a {111}

plane, unsteady seaweed growth is observed as the in-plane anisotropy of the stiffness is almost nil for this orientation. A cubic harmonics expansion considering only ε_1 and neglecting higher order terms describes therefore well the anisotropy of the interfacial energy in the mentioned organic alloys, since a first order expansion leads to pronounced anisotropy in the {100} planes but to no anisotropy in the {111} planes [Utter 02]. The behavior of the Al-Zn-Si alloy is considerably different since this system shows well-defined dendrite patterns in {111} and {110} sections and more blurred dendrites in {100} sections. This confirms the necessity to consider the additional ε_2 and ε_3 contributions in order to describe the anisotropy in the Al-Zn-Si system. The good correspondence between the strength of the in-plane anisotropy of the stiffness and the dendrite pattern further validates the expression determined for the solid-liquid interfacial energy anisotropy.

As emphasized in section 2.3.5, growth along the minima of the interface stiffness is not the only conceivable criterion for the selection of the dendrite growth directions. It has been argued that the dendrite tips could also grow along the protrusions of the equilibrium shape of a crystal in contact with its melt. Therefore, the equilibrium shape has been calculated for the anisotropy expression determined in 4.2.1 ($\varepsilon_2/\varepsilon_1 = -0.188$ and $\varepsilon_3/\varepsilon_1 = -0.00776$ with $\varepsilon_1 = 0.025$) using the ξ-vector formalism presented in section 2.3.3. As expected, the equilibrium shape, see Figure 5-1 b), is quite close to the $\gamma_{sl}(\mathbf{n})$ plot and exhibits maxima along the $\langle 100 \rangle$ directions, saddle points along the $\langle 110 \rangle$ directions and minima along the $\langle 111 \rangle$ directions. When the curvature at the surface of the equilibrium shape is determined, Figure 5-1 c), it turns out that the mean curvature $H = (\kappa_1 + \kappa_2)/2$ of the surface exhibits maxima along directions between $\langle 100 \rangle$ and $\langle 110 \rangle$ that correspond well to the minima of the interface stiffness shown in Figure 5-1 a). This is not surprising since at constant curvature undercooling, a large curvature can only be realized for orientations where the stiffness is small. From a diffusion point of view, it seems reasonable that a crystal initially at its equilibrium shape destabilizes in spots where solute can easily be rejected, i.e. in the areas of maximum curvature.

However, one should bear in mind that the assumption of dendrite growth along the directions corresponding to minima of the generalized interface stiffness, $\Phi_r(\mathbf{n})$, is not universally valid, since it is based on the assumption of equal main radii of curvature at the dendrite tip, see equations 2.14 and 2.15. This is not necessarily the case. Further on, the shape and hence the growth direction of a dendrite tip may be determined not only by energetic/capillary effects but also by diffusional aspects. Very recently, it has been shown by Haxhimali et al. [Haxhimali 06] that dendritic structures can develop along directions in

between $\langle 100 \rangle$ and $\langle 110 \rangle$ even when the minima of the interface stiffness are located at $\langle 110 \rangle$. Therefore, to better establish the relationship between the interfacial energy / interface stiffness and the observed growth directions, quantitative 3D phase field simulations would be desirable.
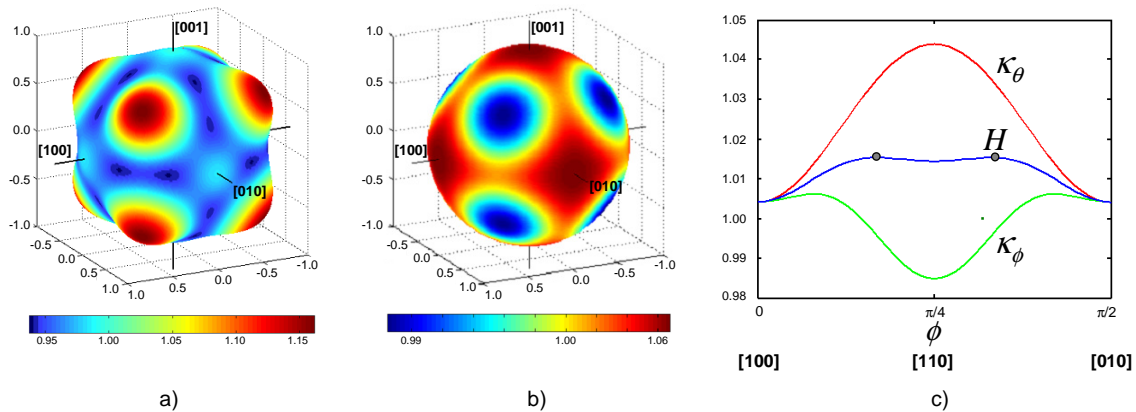
Figure 5-1 a) Interface stiffness $\Phi_r(\mathbf{n})$ vs. the crystallographic orientation for the optimized values of anisotropy (ε_2=-0.188ε_l and ε_3=-0.00776ε_l with ε_l=0.025). **b)** The corresponding equilibrium shape. **c)** The principal curvatures and the mean curvature H at the surface of the equilibrium shape between [100] and [010]. In this specific plane, the principal radii of curvature lay in the planes of ϕ and θ. The mean curvature H exhibits a maximum between [100] and [110] (dots).

The anisotropy expression determined in this project is an essential prerequisite for 3D phase field simulations of dendrite growth in the given alloy system. Unfortunately, such simulations could not be carried out during this project, but they should be a key element of future studies of Al-Zn-Si coatings.

5.1.3   Formation of the dendrite network in the coating layer

The formation of the dendrite network is a key step both for the formation of the microstructure and of the intragranular crystallographic misorientations. The first observation when inspecting the dendrite pattern is that the dendrite arm spacing is relatively fine in industrial coatings with about 11 μm, see section 4.1.1. This indicates that the growth velocity of the dendrites is high and little coarsening / ripening of the dendrite arms occurs in the semi-solid state. Even though the solidification interval is very important for the given Al-Zn-Si alloy, this is certainly true due to the high cooling rates of

10 K/s or more in the industrial coatings.

Another surprising feature is the non-uniformity of the cooling rate observed between 535 and 530 °C in the re-solidification experiments. This phenomenon is due to the release of latent heat and indicates the beginning of solidification in the coating layer. This phenomenon is observed at a temperature significantly below the liquidus temperature of the coating alloy, which is 566 °C for the nominal composition of 43.4wt% Zn and 1.6 wt% Si. This indicates that the undercooling for nucleation and growth of the dendrites would be as high as 30 K. At this undercooling, the equilibrium solid fraction is about 50%. However, such a high undercooling determined needs to be regarded with caution as the actual liquidus temperature of the melt layer in the re-solidification experiment is not exactly known since the concentration of the melt may deviate from the initial nominal concentration. Its concentration is certainly poorer in both Si and Al. The decrease in Si concentration comes from the fact that the Si-particles do not completely re-melt. The lower Si concentration leads to an even higher liquidus temperature. On the other hand, the lower Al concentration, which is due to the preferential absorption of Al in the intermetallic layer, decreases the liquidus temperature.

Another piece of evidence that confirms the high undercooling is the shift of the cooling curve associated with to the inflection observed between 535 and 530 °C. The inflection in the cooling curve is due to the release of latent heat. The shift of the cooling curve allows calculating the amount of latent heat released and hence the solid fraction that is created in very short time at this temperature. In this way it has been estimated that a solid fraction in the order of 30% is reached just behind the moving grain envelope. In order to create such a high solid fraction, a supersaturation Ω of at least as much is required. The sharp transition that produces such a high solid fraction in a fraction of a second requires that dendrite arms cover distances in the order of millimeters in this short time. For the high undercooling, it seems reasonable to assume that tip velocities of several mm/s are reached as it was already reported by Sémoroz [Sémoroz2 01]. Therefore, the dendrite network spans the entire grains in a very short time.

In order to gather more information about the dendrite growth and especially their interactions with the boundaries confining the melt volume, phase field simulations have been conducted. In general, the simulations were conducted at constant, uniform temperature. This situation corresponds well to the above described conditions in which the dendrite network is established. Key parameters for the resulting microstructure are the

concentration of the melt and the undercooling / temperature that are chosen. For the sake of simplicity, the phase field simulations have been conducted for the binary Al-43.4wt%Zn alloy. The addition of 1.6wt% Si in the real coating alloy acts primarily as a melting point depressant: due to the addition of Si, the liquidus temperature decreases from 580 to 566°C. In order to conduct simulations at a comparable supersaturation, temperatures need to be chosen higher for the binary Al-Zn system than for the ternary Al-Zn-Si system. Simulations have been done for a temperature of 530 °C corresponding to a supersaturation Ω of about 0.73 and at a temperature of 550 °C corresponding to a supersaturation of 0.5. The first case was primarily used in order to study the qualitative interaction of dendrite tips with the boundary, whereas the latter case, which is computationally more expensive, was used for qualitative estimations of microstructural features. Figure 5-2 shows that this simulation condition reproduces well the microstructure observed in industrial coatings.

a)

b)
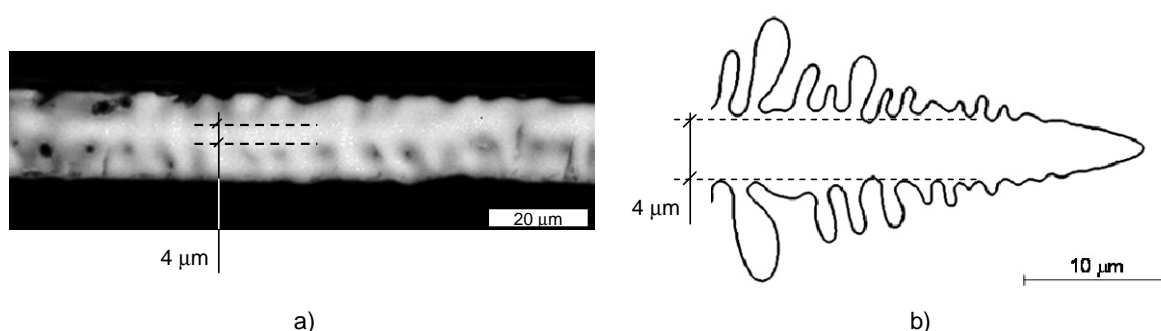
Figure 5-2 a) WDS intensity map of the k_α-Al peak in a cross section taken almost parallel to a primary dendrite arm visible in the center of the coating layer. Brighter gray tones correspond to higher Al concentration. **b)** Phase field dendrite arm growing into a binary Al-43.4wt%Zn melt at 550°C. At the given conditions, the phase field simulation reproduces well the characteristic size of the dendrite core.

The phase field simulations provided the following key findings about the qualitative interaction of the dendrite tips with the boundary confining the melt:

- If the dendrite is nucleated on the boundary and the wetting angle β is smaller than 90°, the tip velocity is increasing significantly with a decreasing wetting angle.

- If the dendrite is nucleated on the boundary and the wetting angle β is larger than 90°, the tip detaches from the boundary. The wetting angle has no influence anymore on the tip velocity.

- If a dendrite tip nucleated in the bulk melt approaches a boundary, it will not

establish contact with the boundary, but remains separated from it by a thin layer of solute-rich liquid.

The first case is easily understood when considering that the imposed sharp wetting angle greatly enhances the solute rejection sidewards from the tip as observed by previous authors in directional solidification experiments [Fabietti 91] and in phase field simulations [Sémoroz 00]. The detachment of the tip from the boundary observed for large wetting angles can be explained by the different solute gradients present at the tip and at the triple point. If one neglects diffusion in the solid, the local velocity of the solid-liquid interface is proportional to the local solute gradient on the liquid side of the moving solid-liquid interface:

$$v_{sl} = \frac{\mathbf{grad}\, c \cdot \mathbf{n}}{c_l - c_s} \tag{5.1}.$$

As the tip grows parallel to the boundary, the solute gradient and velocity are both parallel to the boundary at the tip and at the triple point. The magnitude of the gradient is however much larger at the tip since solute accumulates in the receding gap between tip and triple point. Therefore, the interface velocity is lower at the triple point than at the tip of the dendrite. The tip hence moves away from the triple point and once a steady state situation is reached, the triple point remains immobile since the gradient vanishes in the solute-rich layer separating the solid from the boundary. These observations and interpretations differ somewhat from findings previously reported by Sémoroz et al. [Sémoroz 00]. In their simulations, they observed triple points with angles $\beta > 90°$ moving along with the dendrite tips. The present author beliefs that this observation is an artifact due to i) the very high undercooling used and ii) the relatively coarse mesh size. As the thickness of the solute-rich liquid layer decreases significantly when the undercooling is increased, the tip of the dendrite comes very close to the boundary for high undercoolings. When a too large mesh size is used for the resolution of the partial differential equations, the solute-rich liquid layer between the dendrite arm and the boundary becomes indiscernible as it is in the same order of magnitude as the interface thickness.
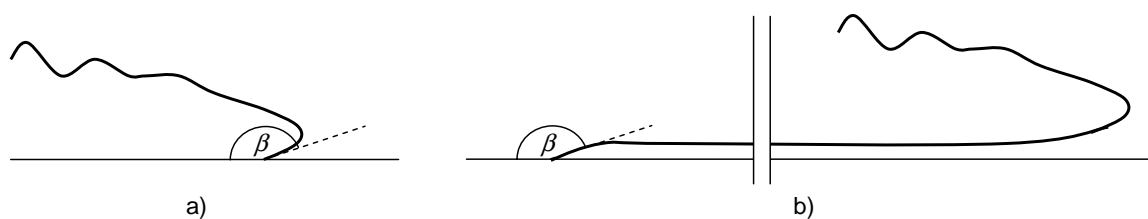
Figure 5-3 a) Schematic morphology of a non-wetting dendrite ($\beta > 90°$) soon after nucleation on the boundary. **b)** The tip detaches from the boundary and the triple point remains immobile.

The morphology adopted by dendrites impinging on the boundary from within the melt is identical to the previously discussed case of dendrites nucleated on the boundary with $\beta > 90°$. Even if the preferred crystal growth direction is strongly inclined towards the boundary, i.e. if the incidence angle α is large, the tip can not break through the solute-rich liquid layer that separates the tip form the boundary

In real Al-Zn-Si coatings, experimental evidence suggests that the tips of the dendrite arms are also detached from the boundaries confining the melt. Cross sectional WDS mappings, see Figure 4-17, show that the cores of the dendrite arms are not in direct contact with the boundaries. The areas of the dendrites where the Al concentration is highest, and where the tips of the dendrites were located, are separated from the boundaries by thin areas that are richer in Zn. This finding is confirmed by the GD-OES depth profiles showing that the maxima of Al concentration are present close to the boundaries but not exactly on the boundaries, see Figure 4-15. When interpreting the GD-OES results, one needs however to keep in mind that the accuracy of the results is blurred by the roughness of the interfaces which is considerable in the Al-Zn-Si system.

On the other hand, one can assume that the nucleation of the dendrites occurs heterogeneously on the boundaries confining the melt, i.e. either on the intermetallic layer or on the oxide skin, since the formation of nuclei is energetically more favorable on boundaries, which are very abundant in thin coatings. This means that detachment from the boundaries occurs after nucleation and that the solid α-Al phase is hence not wetting the boundaries, i.e. $\beta > 90°$. For the boundary with the ambient air, this is in good accordance with the information reported in the literature. In general one can write for metallic systems that [Woodruff 73]:

$$\gamma_{sv} > \gamma_{lv} + \gamma_{sl} \qquad (5.2).$$

The contact angle β is therefore supposed to be 180° and it is energetically

favourable for a thin liquid film to remain at the boundary. Equation 5.2 also implies that when a solid is raised to its bulk melting point, the free surface will spontaneously melt and no superheating of the solid is possible. About the wetting behaviour of a dendrite tip at the boundary with the intermetallic layer, no information is available in the literature. The high undercooling achieved in the re-solidification experiments indicates however that the contact angle must be large since a small wetting angle would lead to a lower undercooling by favouring heterogeneous nucleation.

The dendrite tip velocity has been determined for different incidence angles for the two temperatures 550 and 530°C. For the higher temperature, which is considered to be quite representative of the actual situation during the solidification of Al-Zn-Si coatings, a significant increase of the velocity with decreasing incidence angle α is observed, Figure 4-35. However, even for shallow incidence angles, tip velocities not higher than 82% of the velocity of a free tip are reached. The results at the lower temperature of 530°C, which are much less representative, indicate that the tip velocity remains slightly above the reference velocity for incidence angles α up to 15°.

The low tip velocities of dendrites growing along boundaries at 550°C can be understood when looking at the diffusion fields ahead of the corresponding dendrite tips. The isoconcentration lines displayed in Figure 5-4 a) and b) show that the solute boundary layer for a tip growing freely into the melt is sharper than for a tip growing along a boundary with a small incidence angle α. Considering that the boundary conditions of the solute equation are symmetrical, the diffusion field around a tip following the boundary can be regarded as the diffusion field of a double tip, see Figure 5-4. For an incidence angle α =0°, this situation would correspond to a doublon. The low tip velocity observed even for very small incidence angles α indicates therefore that the doublon cannot be the most favorable growth morphology at a temperature of 550°C. In Figure 5-4 c) and d), a free dendrite tip and a tip growing along a boundary are shown for a temperature of 530°C. Unlike in the previous case, the solute boundary layer ahead of the tips are of about the same size for the free and for the confined tip. Further on, it seems that the minimum radius of curvature at the tip is smaller for the confined tip than for the free tip. These observations are in good accordance with the measured higher tip speed for the confined dendrite tip. The fact that the confined dendrite tip is competitive with respect to the free dendrite tip indicates that the doublon may be a stable growth morphology at 530 °C. This is also confirmed by the spontaneous appearance of a doublon in Figure 4-31 f) where tip

splitting occurs for a dendrite tip freely growing into the supersaturated melt.
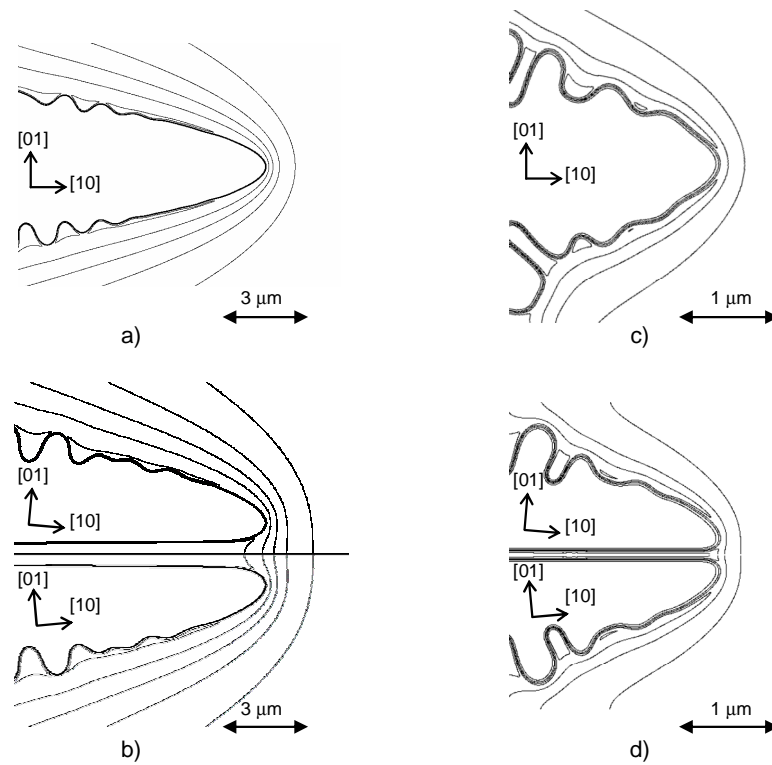
Figure 5-4 Phase field simulations showing iso-concentration lines of steady-state dendrite tips. **a)** Dendrite tip growing into the bulk melt at 550 °C. **b)** Tip growing along a boundary with α=5° at 550 °C and its mirror image across the boundary. **c, d)** same configuration as in a) and b) but at 530°C.

At the high undercooling of 530°C, the tip speed remains very high for incidence angles α up to 15°. This fact is surprising as a dendrite with a incidence angle α=15° has to grow along a direction that is considerably less favorable than a dendrite with an incidence angle of only 5°or less. Figure 5-5 displays the dendrite tip shapes for these two cases. The gap of solute-rich liquid between tip and boundary is larger for the dendrite with α = 5°. The larger incidence angle of the dendrite in Figure 5-5 b) pushes its tip closer towards the boundary thereby leading to a sharper minimum curvature at its tip. The more efficient solute rejection due to this sharper tip is apparently responsible for the equally high tip speed.

a)   b)

Figure 5-5 Stationary dendrite tip shapes growing at 530°C. **a)** $\alpha=5°$, **b)** $\alpha=15°$. For the case with $\alpha=15°$, the apex of the tip is closer to the boundary, the gap of solute-rich liquid between the solid and the boundary is thinner and the minimum curvature is smaller.

The tip speed / incidence angle relationship hence depends strongly on the temperature. It seems as if two regimes can be distinguished: At high undercoolings, maximum tip speed is reached for an incidence angle α which is small but >0°. At lower undercoolings, the maximum tip speed, which is however significantly lower than the tip speed of a free dendrite is reached for an incidence angle approaching 0°, and the tip speed is clearly decreasing with increasing incidence angle. One can try to understand this in terms of the characteristic length scales of the dendrite tip growth problem. For a hemispherical tip, the undercooling is equal to the solute Peclet number [Kurz 98]:

$$\Omega = P_c = \frac{VR}{2D} = \frac{R}{\delta_c}$$ (5.3),

which is the ratio of the tip radius R and the diffusion boundary layer thickness δ_c ahead of the growth front. For low undercoolings, δ_c is large compared to R and one can assume that the diffusion field is strongly perturbed by the boundary for a tip that is still several R away from the boundary. At higher undercoolings however, δ_c is comparable to R. The tip therefore approaches the boundary up to a distance of about R before its diffusion field starts interacting with the boundary. Under these circumstances, the tip may be forced to adopt a curvature that is locally higher than the curvature of a corresponding free dendrite. This effect may the lead to the high tip velocities reported in Figure 4-35 b) at 530°C.

All the phase field simulations of the interactions between the dendrite tip and the confining boundaries presented in this work have been conducted in two dimensions. In the actual solidification process, the diffusion field around a tip interacting with a boundary is of course three dimensional as solute is rejected also laterally. Therefore, the 2D

simulations cannot predict the exact shape of the dendrite tips. On can however assume that the qualitative phenomena observed in 2D simulations such as the presence of a solute-rich melt layer in between the tip and the boundary are also observed in the three dimensional case. However, one needs to be aware that the calculated relationship describing the influence of the incidence angle α on the tip velocity is only approximate. For a more exact relationship, 3D phase field simulations would be required. With the determination of an anisotropy function for the Al-Zn-Si system presented in sections 4.2.1 and 5.1.2, an important prerequisite for the 3D simulations is available now. In 3D phase field simulations, the incidence angle α will not be sufficient in order to describe the crystal orientation of the dendrite with respect to the boundary. A second orientation parameter would be required to define the orientation with respect to the boundary. This second orientation parameter may be of non-negligible importance since it strongly influences the in-plane anisotropy.

The phase field method allows studying in detail the interaction of the dendrite tips with confining boundaries. However, one needs to keep in mind that the general limitations of the method as it was implemented in the present study. In order to conduct simulations in a computationally feasible way, the interface thickness δ, see Equation 3.10, (and hence the mesh size) need to be selected several orders of magnitude larger than in reality where the interface thickness is in the order of 1 nm. The use of a large interface thickness leads to several non-equilibrium effects which originate from the solute transport in the artificially large interface area. These effects include an artificially large solute trapping across the interface and also an overestimation the lateral solute diffusion along the solid-liquid interface if the curvature of the interface is non-uniform. In phase field formulations that are more recent than the one used in this project, these problems can be addressed by the introduction of correction terms [Echebarria 04]. The correction of the non-equilibrium effects allow increasing the mesh size of the finite difference scheme and therefore reduces the required computation power. This is of particular importance for future simulations in three dimensions.

5.1.4 *Formation of the surface morphology*

The geometrical model presented in subsection 3.2.3 predicts the trajectories of dendrite arms that are confined in the thin coating layer. It indicates which of the 24 possible growth directions are most competitive for a certain orientation of the crystal with respect to the plane of the coating and which growth directions therefore dominate the microstructure. The key factor for the selection of the most competitive dendrite growth directions is the velocity a tip adopts when it is forced to grow along a boundary. Therefore, the relationship for the tip velocity as function of the incidence angle α, which was determined through phase filed simulations (Equation 4.3), has been implemented into the geometrical model. The other crucial point in the geometrical model is the criterion for the emission of secondary branches. The applied criterion states that the formation of secondary arms is possible when the angle between primary and secondary arms is smaller than 90°. This criterion is justified by observations made in the directional solidification of Al-50wt%Zn bulk samples where it was shown that the secondary branches preferentially adopt angles of 61°, or 68° but never 90° even though every primary growth direction has two theoretically possible secondary directions located at 90° [Monachon 06]. Angles much smaller than 60° between the primary and secondary branches are not observed in directional solidification experiments. The obvious presence of such small angles in the Al-Zn-Si coating system (see hereafter) justifies however the use of a criterion allowing all angles smaller than 90°. Nevertheless, this criterion is not perfect. As shown in section 4.2.3, the experimentally observed dominant dendrite growth directions were reasonable well reproduced, at least for grains having {111} and {110} crystallographic planes close to the coating plane, see Figure 4-38. The agreement is less perfect in cases where {100} crystallographic planes were aligned with the coating plane. In this case, where the in-plane anisotropy of the interface stiffness is weak and the observed dendrite pattern is accordingly blurred, it can occur that the geometrical model proposes directions of side branches that are not observed in real coatings. Indeed, it seems that in the case of weak in-plane anisotropy, the selection of the secondary branches does not only depend on the angles between primary and secondary branches and the angle between secondary branches and the coating plane, but also on the angle between the secondary branches and the growth front / grain envelope. For grains of such orientation, one often observes sidebranches forming a small angle with the primary arm on the micrographs. In this case, primary and secondary arms correspond to two neighboring growth directions in the center of which a ⟨110⟩ direction is located, see Figure 3-7, e.g. [230] and [320] around [110]. The geometrical model however selects sometimes other secondary arms that are better aligned with the coating plane (smaller α), but include a larger angle with the primary arm

and hence also with the normal to the grain envelope. The experimentally observed growth along directions that are close to the normal of the grain envelope is typical for low anisotropy microstructures where a transition from purely dendritic growth towards cellular / seaweed growth occurs.

The geometrical model does not only predict the predominant dendrite growth directions but also the surface appearance. Since the crystallographic dendrite growth directions are hardly ever perfectly aligned with the coating plane, they tend to follow either the boundary with the substrate or the free boundary. The geometrical model distinguishes areas where the dendrite arms primarily grow along the boundary with the substrate and areas where they grow primarily along the free boundary. The geometrical model generally well reproduces the experimental observations about the surface appearance. This is clearly the case for the grains where also the selection of the predominant growth directions is in good agreement with the experimental results. In areas where the geometrical model predicts growth along the free boundary, the micrographs show a shiny surface appearance with a well aligned dendrite pattern. In areas where the model predicts growth along the boundary with the steel substrate, the dull, bumpy surface appearance is predominant. The humps visible in the dull areas are presumably due to secondary branches which are emitted form the dendrite arms growing along the boundary with the steel substrate.

There is an important difference between the pattern predicted by the geometrical model and the experimental observation in the shiny sectors. In the geometrical model, dendrite arms projected in one of the boundaries grow continuously along this boundary over long distances. The experimental observations made by AFM and SEM show however that even dendrite arms well aligned at the surface of the coating are interrupted after at maximum a couple of hundred μm, see Figure 4-13. The dendrite arms are overtaken either by arms approaching from the sides or from below, i.e. from within the coating. Whereas the first of these two cases also occurs in the geometrical model, the second situation is impossible in the configuration simulated by the geometrical model. In the reality however, it seems as if the dendrite arms rather zig-zag between the two boundaries confining the melt. In the case of shiny surface appearance, the long segments of the zig-zag structure are well aligned with the free boundary whereas in dull areas, long segments grow along the boundary with the substrate. This zig-zag structure is not properly captured by the geometrical model since only one layer of dendrite arms is allowed to grow within the coating thickness. Hence, stopping of dendrite arms following a boundary

by arms emerging from within the coating is not possible. This phenomenon is also not shown in the phase field simulations of cross sections through the coating layer, unless the incidence angle α of the considered dendrite tip is chosen very large. The reason for this may lie in the fact that the phase field simulations were conducted with a 4-fold anisotropy and a two dimensional geometry. 3D simulations with an appropriate anisotropy function, such as the one presented in section 4.2.1, might lead to a branching behavior that is closer to the experimental observations.

From the above discussion, it becomes clear that the surface appearance of the Al-Zn-Si coatings is primarily due to the surface topography. The surface topography is the result of the solidification shrinkage. Before solidification and hence solidification shrinkage occurs, the coating does not present any topography since it is in the fully liquid state. As will be discussed in detail in section 5.2.3, the solidification shrinkage needs to be compensated by an inflow of melt towards the moving solid-liquid interface. In the solidification of thin coatings, the shrinkage is not compensated from the bulk melt ahead of the solidification front, but by decreasing the level of the free boundary in between the solidifying dendrite arms. Dendritic growth occurring either along the free boundary or along the coating-substrate boundary therefore also affects the way how the solidification shrinkage is distributed within the coating. If the tips grow along the free boundary of the coating, the resulting dendrite arms are very close to the initial surface level of the melt layer. The solidification shrinkage is then compensated by a decrease in the melt level around the developing dendrite arms. In dull areas, where the dendrite tips move primarily along the interface with the boundary, the secondary dendrite arms emitted towards the free boundary reach the free boundary about 40 μm behind the primary dendrite tips, see Figure 4-36. In the 40 μm between the primary tips and the impingement of the secondary arms on the free boundary, a non-negligible solid fraction is already reached and the respective solidification shrinkage takes place. This solidification shrinkage leads to a decrease of the level of the free boundary even before the secondary dendrites impinge on it. Therefore, the maximum level of the humps in the dull areas is expected to be slightly lower than the maximum level of the dendrite arms aligned along the free boundary in the shiny areas. This reasoning is confirmed by the surface topography measurements on a sample with well pronounced shiny and dull sectors. The experimental result indicates that the visible dendrite arms in the shiny sectors are at a higher level than the humps created by the secondary arms in the dull sectors; see Figure 4-10 a).

5.2 Mechanisms leading to intragranular misorientations

In this section, three different mechanisms which could be responsible for the formation of intragranular misorientations are discussed in the light of the experimental and numerical findings presented in chapter 4 and discussed in section 5.1. The first two mechanisms to be discussed, which are subsequently called microsegregation hypothesis and thermomechanical hypothesis, have been suggested by Sémoroz et al. [Sémoroz1 01] and were already briefly introduced in section 2.4. Further on, another mechanism involving the effect of the solidification shrinkage on the growing dendrite arms is discussed in a third subsection.

5.2.1 *Microsegregation hypothesis*

The microsegregation hypothesis formulated by Sémoroz et al. [Sémoroz1 01] has been briefly introduced in section 2.4. It states that the observed misorientations may be due to systematic concentration gradients in the coating layer which are the result of the microsegregation taking place during the dendritic solidification. Concentration gradients in a solid-solution crystal can lead to distortions of the crystal lattice and hence to misorientations if the solute element has a different atomic radius than the base element. This is the case in Al-Zn(-Si) alloys where an increase of the Zn concentration decreases the lattice parameter by about 2% per atomic fraction, see Figure 2-14. Considering the strong microsegregation occurring in the Al-Zn(-Si) system, it has been shown in section 2.4, that the microsegregation is theoretically sufficient to cause misorientation rates in the order of 5°/mm such as the ones observed experimentally. However, in order to produce a misorientation pattern showing systematic rotations of the crystal lattice towards the substrate when moving along dendrite arms, the Zn concentration needs to increase systematically from the free boundary to the boundary with the substrate. This is a necessary condition for the validity of the microsegregation hypothesis, which is however not verified by the new experimental findings on the microsegregation pattern obtained by WDS and GDOES. GDOES, a technique that was not yet available at the time of the earlier studies conducted by Sémoroz et al. [Sémoroz1 01], shows that there are two minima of the Zn concentration / maxima of the Al concentration, Figure 4-15. They are located close to the two boundaries confining the coating layer, but not exactly on the boundaries. The global microsegregation pattern is about symmetrical with respect to the plane of the coating and should therefore not lead to systematic misorientations.

More localized WDS mappings (Figure 4-17) show that the microsegregation is slightly different in shiny and dull areas. In shiny areas where the growth of the primary dendrites occurs principally along the free boundary, the minimum Zn concentration occurs close to the free boundary. In areas of growth along the boundary with the substrate, the global minima of the Zn concentration is present close to this boundary. If the microsegregation were responsible for the misorientations, different misorientation patterns would be observed in shiny and dull sectors. This is however not the case.

A further piece of evidence that the microsegregation cannot be responsible for the intragranular misorientations observed in Al-Zn-Si coatings is provided by the misorientations that are observed in Zn-0.2wt.%Al coatings. Zn-0.2wt.%Al coatings are also applied on steel sheets for corrosion protections by the hot dipping process. They have a similar thickness of about 20 μm as the Al-Zn-Si coatings studied here and they do also show a dendritic solidification morphology. Figure 5-6 shows that the Zn grains also exhibit strong intragranular misorientations. The misorientations follow the same pattern as in Al-Zn-Si coatings, i.e. from the center to the periphery, the crystal undergoes a rotation towards the substrate around an axis lying in the plane of the coating and being about perpendicular to the radial direction. By analogy, one can assume that the mechanism leading to the misorientations in Zn coatings is the same as in the Al-Zn-Si coatings. The microsegregation within the dendrite arms is however much less pronounced in Zn-0.2wt.%Al coatings since the maximum solubility of Al in the β-Zn phase is only 2.8 at.%, as compared to 67at.% Zn in α-Al. Unlike for solid solutions of Zn in α-Al (see Figure 2-14), no experimental data are available for the dependence of the lattice parameter of the β-Zn phase with respect to the Al concentration. As a first approximation, one can however estimate the lattice parameter through Vegard's law [Vegard 21], which posits that there is a linear relationship for the lattice parameter between the constituents of an alloy in the case of a solid solution. Using Vegard's law and making the extreme assumption that the Al concentration increases from 0 to 2.8 at.% from the free boundary to the boundary with the substrate, one finds that the maximum possible misorientation rate $\partial \tau / \partial x$ is about 1.6°/mm. This is considerably smaller than the experimentally observed misorientation rates. Therefore, one can assume that the microsegregation is not solely responsible for the misorientations in Zn-0.2wt.%Al coatings. Considering the analogy of Zn-0.2wt.%Al and Al-Zn-Si coatings, this indicates that other mechanisms than microsegregation are also involved in the formation of intragranular misorientations in Al-Zn-Si coatings.

a)   b)
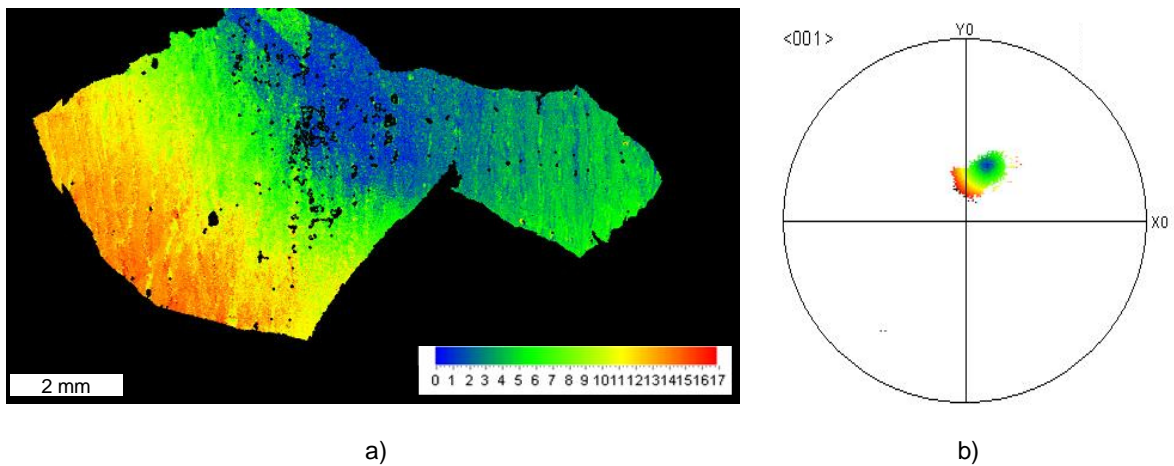
Figure 5-6 a) EBSD misorientation map of a grain in a Zn-0.2wt%Al coating showing strong intragranular misorientations. **b)** The corresponding ⟨001⟩ pole figure. The grains in Zn coatings show the same convex misorientation pattern as the grains in Al-Zn-Si coatings.

5.2.2   *Thermomechanical hypothesis*

Sémoroz et al. [Sémoroz1 01] presented a second hypothesis for the formation of intragranular misorientations in Al-Zn-Si coating systems. The hypothesis is based on the accumulation of dislocations of a particular orientation, so-called geometrically necessary dislocations (GND) that lead to a distortion of the crystal lattice and eventually to intragranular misorientations. In order to cause a misorientation pattern such as the one typically observed in Al-Zn-Si coatings, dislocations of edge-type having their excess atomic plane oriented towards the free boundary need to be present in the coating, see Figure 2-13 a). For the creation of dislocations, plastic deformation of the sample is required. Sémoroz et al. proposed that thermal stresses lead to plastic deformation and possibly to the accumulation of excess dislocations in the coating layer. This argument is based on the fact that the thermal expansions coefficients of the Al-Zn-Si coating and the steel substrate are significantly different. As described in section 2.4, the cooling form the solidification temperature to ambient temperature leads to a difference in thermal strain of about 0.7% between substrate and coating. Since the substrate is much more rigid than the coating due to its thickness and composition, the strain is almost entirely accommodated by the coating. The strain, which is of tensile nature in the coating, is sufficient to lead to plastific deformation and hence to the creation, movement and accumulation of dislocations in the coating. Sémoroz et al. [Sémoroz1 01] did not describe in detail the mechanism that leads to the formation and accumulation of dislocations of one sign. In this

section, the conditions under which the plastic deformation due to the thermal strain takes place are analyzed and the misorientations that are possible due to these deformations are discussed in the light of the experimental observations.

In order to understand the effect of the plastic deformation on the coating layer, it is important to remember how the dendrite network is formed. The solidification experiments showed that the dendrite network forms very quickly at a considerable undercooling and hence rapidly reaches a significant solid fraction. The dendrite network is established at an almost uniform temperature of about 535 to 530 °C, see section Figure 4-43. Thermal stresses / strains are hence not significant during the formation of the dendrite network since this process is essentially isothermal. This means that the orientation within the initial dendrite network is uniform and that no misorientations are present. As has been shown in sections 4.2.2 and 5.1.3, the dendrite tips do not establish contact with the boundaries during growth but remain separated from them by a thin layer of solute-rich liquid. Immediately after the formation of the dendrite network there is hence very little contact between the solid dendrites and the substrate. Based on the assumptions on the interface energies made in section 5.1.3, one can assume that coalescence between the dendrite network and the substrate occurs relatively late in the solidification interval. The major part of the thermal strain induced in the coating layer occurs hence in the fully solid state, i.e. below the eutectic temperature. Accordingly, the misorientations needed to build up in the solid state. Therefore, the coating on which the thermal strain is applied, can be viewed as an α-Al single crystal with eutectic islands (or liquid islands in the beginning) as inclusions.

In industrial coatings, the misorientations are often of continuous nature along dendrite arms. The variation of orientation from one end of a grain to the other can easily reach 20 degrees whereas, if only thermomechanical aspects are considered, the orientation is uniform immediately after the formation of the dendrite network. Therefore, the amount of misorientation with respect to the initial orientation occurring during cooling must be strongly dependent on the position. Due to the fact that the misorientations are continuous along the dendrite arms from the nucleation center to the periphery of the grain along all primary dendrite growth directions, it is sensible, however not strictly imperative, that the orientation at the nucleation center should correspond roughly to the initial orientation of the dendrite network. This means that during cooling, no misorientation occurs at the nucleation center whereas the misorientation becomes stronger and stronger along the dendrite arms. In order to realize such important differences in misorientation, two

mechanisms are conceivable. To visualize them, one can divide a dendrite arm into segments and study the misorientation that each of these segments needs to undergo. As a first possibility, one can imagine that each of the segments passes independently from its initial orientation to the final orientation, see Figure 5-7 a). As mentioned before, this means that the increment of misorientation $d[\mathbf{M}]^n$ actually occurring locally depends strongly on the position. This seems implausible since the supposed driving force for the formation of misorientations, the thermal strain (Eq. 2.20), is uniform all over the coating.

a)   b)
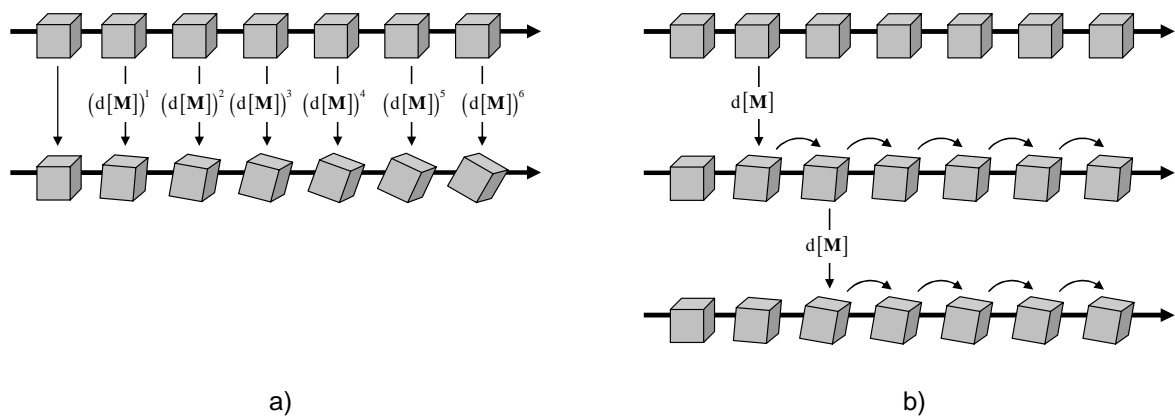
Figure 5-7 Schematic representation of mechanisms leading to a continuous variation of the crystal orientation along a dendrite trunk. **a)** Mechanism transforming each segment of an dendrite arm individually into the final orientation. The amount of misorientation required is strongly dependent on the position within the dendrite arm. **b)** Mechanism where each segment undergoes the same amount of misorientation. The new orientation must however be transmitted to all other segments towards the periphery of the grain in order to realize a continuous variation of orientation.

Secondly, one could assume that the same amount of misorientation $d[\mathbf{M}]$ occurs in each segment but that the misorientation propagates into each following segment along the already entirely established dendrite arm, see Figure 5-7 b). This possibility is in accordance with the uniform thermal strain as the driving force. However, the mechanism of propagation of the new orientation to the following segments is not evident considering that the entire dendrite arm is already formed when the misorientations are introduced. When introducing a misorientation, e.g. through the introduction of geometrically necessary dislocations, into a segment which has initially a uniform crystal orientation such as in the situation depicted in Figure 5-8 a), the segment deforms macroscopically. The propagation of a misorientation of e.g. 5° to the next segment would be trivial if the dendrite arm were a freestanding cantilever. In this case, the dendrite would just bend, see Figure 5-8 b), and the right segment would automatically adopt the crystal orientation imposed on its left by the misoriented segment. However, the coating cannot bend since it

is mechanically confined by the much more rigid steel substrate. The propagation of the misorientation along the dendrite arm is only possible if shear, which does not affect the crystal orientation, occurs in parallel. The amount of shear corresponds to the shear that is required to pass from the gray, dashed shape of Figure 5-8 c) into the solid black shape. The corresponding shear strain ε_{xy} is about:

$$\varepsilon_{xy} = \frac{1}{2}\left(\frac{\partial u_x}{\partial y} + \frac{\partial u_y}{\partial x}\right) \approx \frac{1}{2}\left(\frac{\partial u_y}{\partial x}\right) \approx \frac{1}{2}\tan\tau \qquad (5.4),$$

where τ is the misorientation imposed by the preceding segment. In order to propagate a relatively moderate misorientation of $\tau = 5°$ along a denrite arm, a shear strain $\varepsilon_{xy} = 4.4$ % is necessary. This shear deformation is significantly larger than the tensile strain of about 0.7 % that is imposed by the difference in thermal contraction of the coating and the substrate. It is therefore hard to imagine how misorientations up to 20° can propagate along the dendrite network.
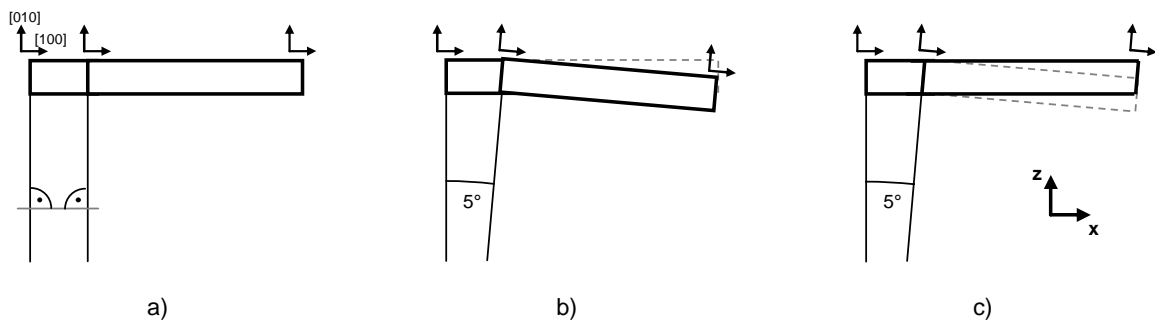
Figure 5-8 Schematic representation of the thought experiment concerning the propagation of misorientations along a dendrite arm. **a)** Situation prior to the formation of misorientations. The crystal orientation is uniform. **b)** Misorientations lead to a macroscopic distortion of the left segment. In the absence of a substrate, the right segment would bend. **c)** Due to the presence of the substrate, the propagation of the misorientation can only occur if shear in the crystal allows maintaining its initial shape.

This theoretical argument or thought experiment is confirmed by the new results of the re-solidification experiments conducted under modified stress conditions, see section 4.3.2. In samples, on which plastic deformation is imposed by two brass disks during solidification and cooling to the ambient temperature, the observed misorientations are not significantly different from those in samples re-solidified without any mechanical constraint or from those in samples solidified under industrial conditions. One has to admit that the brass disks probably do not completely eliminate the thermal strain due to the different thermal contraction behavior of the steel substrate and the Al-Zn-Si coating since

the expansion coefficient of the brass is not exactly as high as the one of the coating. The resulting misorientations were strongly affected by the presence of the brass disks even if in addition some limited plastic deformation in the brass disks would occur. The experimental results show however that the misorientation is not significantly affected by the brass disks, see Table 4-3. The combination of the experimental evidence and the theoretical considerations allows concluding that the thermal strain due to the different thermal expansion properties of substrate and coating is not responsible for the observed continuous and cumulative variations of crystallographic orientation.

Nevertheless, the thermal strain, which is estimated at about 0.7%, see section 2.4, is largely sufficient to cause plastic deformation in the coating. The deformation, which is of tensile nature, applies on the dendrite network. The dendrite network can be considered, at least locally, as a single crystal. It is well-known that uniaxial tensile deformation of single crystals can lead to variations of the crystal orientation within the specimen. Upon tensile deformation, the angle between the normal of the slip plane and the tensile direction increases whereas the angle between the slip direction and the tensile direction decreases. This reorientation of the crystal is systematically shown in Figure 5-9. In a tensile test, the misorientation is accumulated towards both ends of the specimen whereas the orientation remains uniform in the central area where only shear occurs. Towards both ends of the specimen, both bending and shear occur. The bending moment there can lead to the introduction of geometrically necessary dislocations and hence to misorientations. A typical feature of the misorientations observed in tensile tests is, that the crystal orientation at both ends of the crystal remains the same during deformation. Tensile deformation of single crystals does therefore not lead to continuous and progressive misorientations, but only to misorientations that are neutralized by misorientations of the opposite sense occurring farther in the crystal.

Such structures consisting of misoriented areas which are surrounded by two areas of the identical, initial orientation are indeed observed experimentally in Al-Zn-Si coatings. Figure 4-27 c) and d) as well as Figure 5-9 a) show EBSD maps of a cross section through a coating where several inclined, misoriented zones are visible. Under the assumption that the tensile direction corresponds to the axis of the dendrite arm (which is nearly aligned with the plane of the metallographic section), it turns out that the Schmid factor of the supposedly activated slip system is higher in the inclined misoriented areas (blue in Figure 5-9 a) than in the areas showing the base orientation (green). This indicates that plastic deformation, i.e. the activation of slip systems, occurred preferentially in the misoriented

(blue) zones. In the case of an uniaxial tensile deformation imposed at the extremity of a specimen, the misoriented zone stretches the entire central part of the specimen and the actual misorientations only occur in two limited areas towards the ends of the specimen. In the strained Al-Zn-Si coatings however, misoriented zones alternate with zones that conserved the initial orientation. This may be due to the different ways how the tensile deformation is applied. In a tensile specimen, the deformation is applied at the ends of the sample, whereas in the coating layers, the deformation is applied all along the boundary with the substrate. This constraining boundary seems to limit the size of the misoriented zones and favors the formation of repeated small misoriented zones. Further on, the fact that the misoriented zones are not in relationship with the microsegregation / dendrite structure indicates that observed deformation occurred in the fully solid state and hence probably during the cooling from the eutectic to ambient temperature.
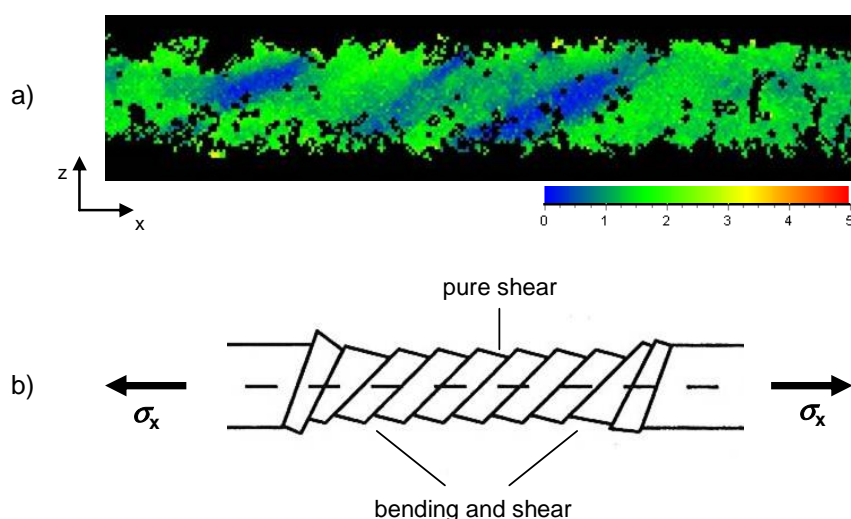
Figure 5-9 a) EBSD misorientation map taken parallel to a primary dendrite arm in a cross section through the Al-Zn-Si coating. It shows a banded misorientation pattern. **b)** Schematic representation of variations of orientations that occur during the tensile deformation of a single crystal specimen. In the central where pure shear occurs, the crystal orientation is uniform. Misorientations are present on the sides of the specimen where bending and shear occurs. In the two areas where variations of orientation occur, the sense of rotation are opposite.

In summary, one can conclude that the thermal strains are not responsible for the continuous and cumulative misorientations observed in Al-Zn-Si coatings. However, they may be responsible for banded misorientation structures such as the one displayed in Figure 4-27.

5.2.3 Solidification shrinkage hypothesis

Up to now, microsegregation and thermal stresses, which are both of particular importance in Al-Zn-Si coatings, have been discussed, and have finally been dismissed as mechanisms for the formation of the experimentally observed misorientations since they are not in sufficient accordance with the new experimental and numerical results reported previously in this work. As an alternative, a new hypothesis related to the solidification shrinkage and the proximity of the free surface is proposed here. The discussion of this mechanism is structured in the following steps:

- presentation of how the solidification shrinkage is compensated in Al-Zn-Si coatings.

- estimation of how much solidification shrinkage can be expected at the grain envelope during the solidification of the coating.

- the forces that can be expected in the liquid-air interface.

- the mechanical response of the dendrite arms to these forces.

- and finally, the discussion of the solidification shrinkage mechanism in the light of the experimental results presented in chapter 4.

Compensation of the solidification shrinkage in Al-Zn-Si coatings

Al-Zn-Si coatings exhibit particularly strong intragranular misorientations when compared to those in metal castings such as Ni-base single crystal turbine blades, see section 2.4. Another particularity of coating systems is that the solidification shrinkage is accommodated differently than in bulk solidification. For most metals, the molar volume decreases by a couple of percent upon solidification. In the solidification of bulk samples, the solidification shrinkage is compensated by an inflow of liquid metal antiparallel to the moving solid-liquid interface. Depending on the solidification velocity and the size of the casting, this can lead to a significant melt flow over considerable distances. In massive castings, this phenomenon may lead to the formation of shrinkage cavities in the areas solidifying last if they are not in contact with the free surface. In thin coatings, it is easier to compensate the solidification shrinkage by lowering the level of liquid metal in the coating, since this reduces the distance over which the melt needs to be transported.
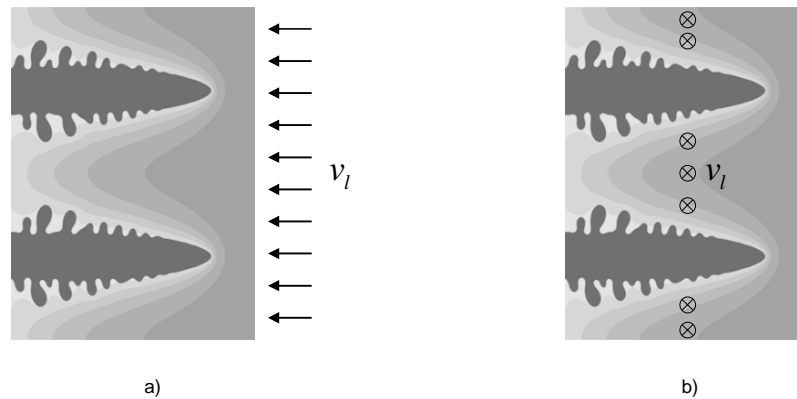
Figure 5-10 Schematic representation of the inflow of melt towards the moving solid-liquid interface with a velocity v_l in order to compensate the solidification shrinkage. **a)** In bulk solidification, the inflow of melt occurs perpendicular to the solidification front. **b)** In thin coatings, the inflow of melt occurs from the free boundary. Thereby, the level of the melt-air interface is decreased.

As already mentioned in section 5.1.4, this phenomenon leads to the formation of a surface topography following the dendrite pattern of the coating layer. If the tips of the dendrites grow close to the free boundary and dendrite arms are hence present along the boundary, a decrease of the liquid-air interface can occur only in between the dendrite arms. This leads to a curved liquid-air interface that is inclined at the triple point between solid, liquid and air, see Figure 5-11.
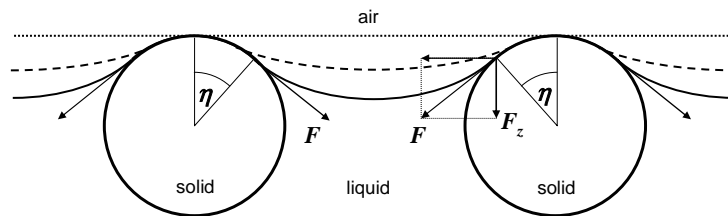
Figure 5-11 Schematic cross section through two dendrite arms growing into the undercooled melt. The solidification shrinkage leads to a depression of the melt level and to a curved liquid-air interface in between the dendrite arms. As the solidification shrinkage proceeds, the liquid-air interface evolves to a more and more curved shape (dotted line → dashed line → solid line).

Neglecting the presence of an oxide skin, Equation 5.2 predicts that the slope of the liquid-air interface is tangential to the solid at the point of contact between solid, liquid and air. If there is a tension F present in the liquid-air interface at the triple point, F can be divided into a horizontal component that is balanced by an opposite force on the other side of the dendrite arms and a vertical component F_z which contributes to a resulting vertical force on the dendrite arm. The exact situation at the triple point and the nature of the tension in the interface will be discussed in detail further down in this section. First, the

location where the most important part of the solidification shrinkage occurs will be discussed here.

As pointed out in section 5.1.3, the entire dendrite network forms very quickly in between 535 and 530°C. In a very short time, a solid fraction in the order of 25% is realized in the coating. Afterwards, the dendrite morphology evolves only by thickening and ripening of the dendrite arms. With respect to the solidification shrinkage and the surface topography, three different zones can be distinguished during the quick growth of the grains, see Figure 5-12. Far outside the grain envelope (region 1), the level of the free boundary corresponds to the initial melt level since it is not yet affected by the solidification. In the area just behind the grain envelope (region 2), a significant solid fraction is established. Therefore, considerable solidification shrinkage occurs there. In this zone, the liquid-air interface is in movement and depresses in between the already established dendrite tips / arms. Farther within the semi-solid grain (region 3), the solid fraction reaches its equilibrium value for the actual temperature, and from now on, the solid fraction increases only slowly with the decrease of the temperature. The liquid-air interface and hence the surface topography of the still semi-solid coating layer evolve only very slowly in region 3. As will be detailed later on, region 2 is of particular interest for the formation of intragranular misorientations since considerable solidification shrinkage occurs in a short time. Before addressing in detail questions such as the size of region 2, the exact situation at the triple point and the nature of the tension in the interface, we will try to estimate the amount of solidification shrinkage occurring in region 2.
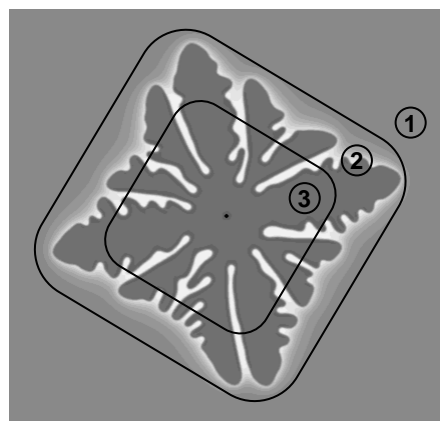
Figure 5-12 Schematic in-plane view of a grain growing in an undercooled Al-Zn-Si melt. Three different stages can be identified: (1) The areas away from the grain envelope are not yet affected by the solidification shrinkage. (2) Just behind the grain envelope the solid fraction increases quickly. Therefore, a major part of the solidification shrinkage occurs there. (3) In the mushy zone within the grain, the equilibrium solid fraction is reached. The solidification and hence the solidification shrinkage are slow there.

Amount of solidification shrinkage in the Al-Zn-Si coating

Since there are no literature values available for the solidification shrinkage of the Al-43Zn-1.6Si alloy, it needs to be derived from quantities such as the molar volumes of the melt and the lattice parameter of the solid at the solidification temperature as far as they are known. A detailed presentation of the equations used to calculate the densities of the solid and the liquid phase at the solidification temperature as well as the necessary numerical data are given in the Appendix. By applying the Equations A.1 to A.4 to the numerical values given in Table A-1, the density of the melt at the solidification temperature of 535°C can be determined. A value ρ_{liq} (T=535°C) = 3344 kg/m^3 is obtained thereby for a melt of the nominal concentration. The density of the solid at the solidification temperature is determined through its lattice parameter. The linear extrapolation of the lattice parameter data reported by Murray [Murray 83] allows determining a lattice parameter vs. Zn concentration relationship at 535°C, see Figure 5-13. For the nominal composition, a lattice parameter a = 0.4091 nm is thereby found. Through Equation A.5, a density ρ_{sol} (T=535°C) = 3513 kg/m^3 is obtained for the solid phase at the given temperature. This density is of course larger than the density of the melt calculated above. The resulting total solidification shrinkage amounts hence to 5.1%.
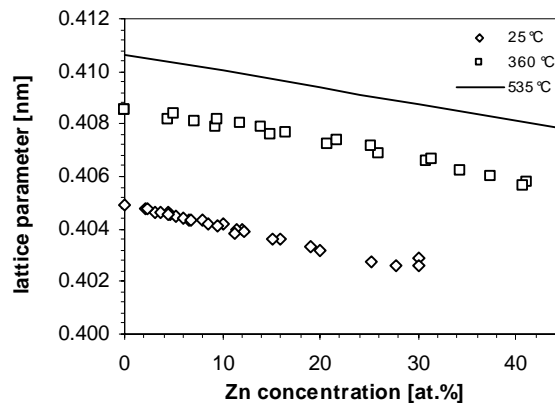
Figure 5-13 Experimental lattice parameter for a binary Al-Zn alloy at T=25 °C and T=360 °C. Data taken from [Murray 83]. The relationship between lattice parameter and Zn concentration at T=535°C (solid line) has been extrapolated from the experimental data for lower temperatures.

As it was already mentioned in the previous paragraph, the total solidification shrinkage of 5.1% can be divided in two parts in the case of equiaxed dendritic growth. The first part occurs during the isothermal formation of the dendrite network and is

localized in the areas of the grain envelope. The second part occurs later within the grains, where the solid fraction is uniform but steadily increasing upon cooling. For the formation of intragranular misorientations, the solidification shrinkage occurring at the grain envelope is of particular interest. The solidification shrinkage occurring in the area of the grain envelope can be calculated with equations A.7 and A.8 if the molar volumes of the solid and liquid phase are known at the solidification temperature and at their respective concentrations and volume fractions. This calculation is illustrated in Figure 5-14. For a solidification temperature of T=535°C and the liquidus and solidus concentrations given by the ternary Al-Zn-Si phase diagram (nominal concentration: Al-43.4Zn-1.6Si in wt.% or Al-24Zn-2Si in at.%), one obtains an effective solidification shrinkage of 2.6 % across the grain envelope. This amount of solidification shrinkage is somewhat approximate. In the re-solidification experiments where the solidification temperature of 535°C has been determined, the melt does not exactly exhibit the nominal concentration but is enriched in Zn as it was discussed in section 5.1.3. The higher Zn concentration would lead to a reduced solidification shrinkage across the grain envelope. Therefore, for the further calculations, the very conservative estimation of a solidification shrinkage of 1% has been made.
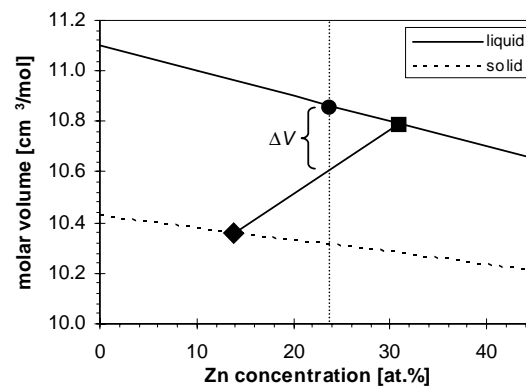
Figure 5-14 Molar volume of solid and liquid as a function of the Zn concentration at T=535°C. Circle: molar volume of the melt prior to solidification. Diamond: molar volume of the solid dendrites behind the grain envelope. Square: molar volume of the interdendritic liquid behind the grain envelope. The molar volume of the solid is obtained from extrapolated lattice parameter data, see Figure 5-13. The molar volume of the melt is obtained through Equations A2 and A.3 (Appendix).

Forces in the liquid-air interface

As already mentioned, tensions present in the liquid-air interface can exert resulting forces on the growing dendrite arms when the liquid-air interface curves under the effect of the solidification shrinkage. Forces in the liquid-air interface could be due to different origins.

Under the assumption that there is no oxide layer at the surface of the liquid metal, the force F in the liquid-gas interface is equal to the surface tension γ_{lg} of the liquid metal. According to Iida and Guthrie [Iida 93] the liquid surface tension of pure Al is $\gamma_{lg}^{Al} = 0.914 \, \text{N/m}$, while it is $\gamma_{lg}^{Zn} = 0.782 \, \text{N/m}$ for Zn and $\gamma_{lg}^{Al} = 0.865 \, \text{N/m}$ for Si at the respective melting points. By weighting the surface tensions of the pure substances according to the atomic fractions present in the given Al-Zn-Si alloy, a surface tension value of $\gamma_{lg}^{Al-Zn-Si} = 0.881 \, \text{N/m}$ is obtained. According to Iida and Guthrie [Iida 93], the surface tensions tend to be smaller than what would be predicted by proportional addition of the pure component surface tensions for most binary alloys. This is often the result of the liquid surface becoming enriched with the component of lower surface tension. Indeed, the literature suggests that the surface tension is 0.84 N/m at the liquidus temperature of an Al-24 at.%Zn binary melt [Pelzel 49].

There is however experimental evidence that the liquid metal is not in direct contact with the surrounding atmosphere. AFM measurements and SE–micrographs, see Figure 4-14 and Figure 5-15 a), show wrinkle structures on the surface of the Al-Zn-Si coatings. The wrinkles resemble the oxide skin wrinkles that Grasso [Grasso 04] observed on liquid bridges between the dendrite arms being pulled apart during hot tearing experiments in Al-alloys, Figure 5-15 b). The observed wrinkles prove the presence of an oxide skin on the melt layer prior to solidification of the coating. The necessary condition for the formation of wrinkles is that the oxide skin is locally in compression. Apparently, this is the case in some spots even though the surface area of the coating increases globally due to the formation of a relief during solidification. For the formation of wrinkles, it is however sufficient that one principal strain component of the biaxial strain state of the oxide skin is compressive. Wrinkles will form perpendicular to the principal direction along which the strain is compressive. In most areas however, the oxide skin undergoes a tensile strain since the surface of the liquid-air interface increases when the level of the melt decreases in between the already established dendrite arms.

a)   b)
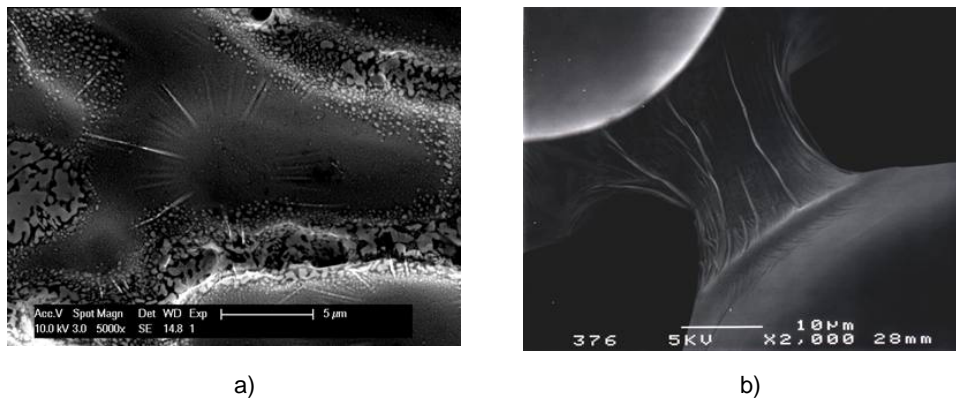
Figure 5-15 The wrinkle structures observed on Al-Zn-Si coatings seem to be due to the compression of the oxide skin. **a)** SE-micrograph taken on the surface of an Al-Zn-Si coating showing wrinkles arranged radially around a hump. **b)** For comparison, oxide skin wrinkles reported by [Grasso 04] on liquid bridges formed between dendrite arms during hot tearing experiments in Al alloys. Micrograph taken from [Grasso 04].

The stress state in the oxide skin is associated to the strain state applied by the solidification shrinkage. In order to determine the stresses/forces developing as a response to the imposed strain, information about the tensile properties of the oxide film is needed. Experimental measurements on the mechanical properties of oxide skins on liquid Al alloys have been reported in a pioneering study of Kahl and Fromm [Kahl 85] and recently by Syvertsen [Syvertsen 06]. Kahl and Fromm measured the force that developed in response to an imposed displacement between two dies positioned at the oxidized surface of an aluminum melt bath. A typical example of a force-displacement curve is given in Figure 5-16. In stage (2), the two dies are put in contact with the oxide skin. In stage (3), the dies are held at constant displacement. The authors argue that the measured force corresponds to the intrinsic tension in the oxide layer. In stage (4) and (5) the dies are displaced at constant speed. The linear increase of the force in the oxide skin in stage (4) seems to correspond to an elastic regime. A maximum force is reached in stage (5). Each peak represents the initiation and propagation of an individual crack in the oxide skin. It is interesting to note that the force is only reduced by 10-15% by these cracks. This means that the newly formed oxide skin is almost immediately as resistant as the other parts of the oxide which have grown during a much longer oxidation time. In section (6), the displacement of the dies is stopped and the force remains almost constant at a level near the maximum force. This experiment essentially shows that the oxide skin behaves in tension as an elastic / perfectly plastic material. Once plasticity, i.e. cracking and re-formation of the oxide skin occurs, the stress level remains independent of the deformation history.
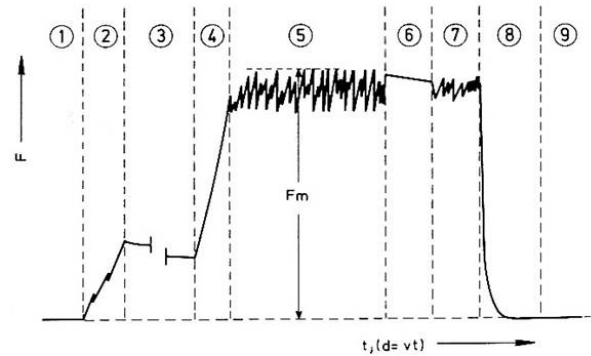
Figure 5-16 Measured force vs. time curve of an oxide skin on an Al melt. In stages 4, 5 and 7, a constant strain rate is applied. In these areas, the curve corresponds hence to a force displacement curve. The experiment shows that the tensile behavior of the oxide skin is elastic / perfectly plastic. Figure taken from [Kahl 85].

Recently, more quantitative experiments using a setup similar to the one of Kahl and Fromm [Kahl 85] have been conducted by Syvertsen [Syvertsen 06]. These experiments provided more accurate results for the mechanical properties of the oxide skin. According to Syvertsen, the measured surface skin strength λ can be expressed by the following relationship:

$$\lambda = \gamma_{l-ox} + \sigma_{ox} \, d_{ox} + \gamma_{ox-g} \tag{5.5},$$

where σ_{ox} is the tensile strength and d_{ox} the thickness of the oxide layer. The surface skin strength λ has been directly measured for pure Al, industrially pure Al, Al-Si alloys and Al-Si-Mg alloys at various temperatures from the melting point up to the 950°C [Syvertsen 06]. All alloys except the ones containing Mg showed a constant λ up to a transition temperature. Above the transition temperature, λ increases linearly with temperature, probably due to oxide skin thickening. The transition temperature is depending on the alloy composition and is found between 720 and 820°C. The constant λ value below the transition temperature shows only small variations on the alloy composition and is in general about $\lambda = 0.72$ N/m. As mentioned above, the addition of Si has little effect on the measured oxide skin strength. Other authors [Divandari 04] point out that Zn also has only a minimal effect on the oxidation behavior of liquid Al. Therefore, we conclude that the oxide skin strength λ of Zn-rich Al alloys are comparable to those determined by Syvertsen [Syvertsen 06], i.e. in the order of $\lambda = 0.72$ N/m.

Mechanical response of the dendrite arms

Considering the shape of the topography profiles measured on Al-Zn-Si coatings, see e.g. Figure 4-12, it becomes clear that the strain in the oxide skin during the formation of the topography is certainly high enough in order to reach the plastic zone in the force-displacement curve of the oxide skin. Therefore, one can assume that a tension of about λ = 0.7 N/m is present in the oxide skin at the moment when the important part of solidification shrinkage takes place just behind the envelope of the fast growing grain. The oxide skin is forced to follow the melt level decreasing in between the dendrite arms and stretches therefore around the now protruding dendrite arms. The tension present in the oxide skin is applied on the dendrite arms in the triple points where dendrite, melt and the oxide skin meet as it is visualized in Figure 5-11.

The vertical component F_z of the tension λ is of particular interest due to its effect on the growing dendrite arm:

$$F_z = \lambda \sin \eta \qquad\qquad (5.6),$$

where η is the inclination of the oxide skin at the solid-liquid-air triple point. In order to estimate the resulting force, it is essential to know η. Of course, it is impossible to measure the actual η value behind the grain envelope during solidification. In order to get a realistic estimate of η, one can refer to topography profiles taken on the surface of Al-Zn-Si coatings. In fact, once the oxide skin comes in contact with the dendrite arm, the shape of the dendrite arm does probably not change anymore in the areas spanned by the oxide skin and the inclination of the surface remains constant afterwards. Approximate values of the inclination η have been related the solidification shrinkage $\Delta V/V$ by measuring the slope of an experimentally determined surface profile according to the method visualized in Figure 5-17. The surface profile shown in Figure 5-17 has been measured in a shiny zone about perpendicular to the growth directions of the dendrite arms. It can be assumed that the straight line connecting the tops of the humps corresponds about to the level of the melt layer prior to solidification. During solidification, the melt level recedes in between the dendrite arms. At a certain stage during solidification, the shrinkage volume ΔV is assumed to correspond to the grey volume in Figure 5-17. Given that the thickness of the coating is known (about 20 μm), this allows determining the relative solidification shrinkage $\Delta V/V$. The inclination η of the surface is measured at the locations where the lower line delimiting the grey area in Figure 5-17 intersects the surface profile.
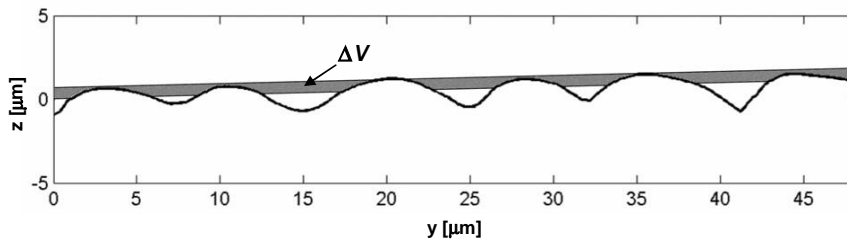
Figure 5-17 Schematic illustration of the determination of a relationship between solidification shrinkage $\Delta V/V$ and the inclination η of the oxide skin. For a given volume of shrinkage, the inclination of the dendrite surface / the oxide skin can be determined.

By averaging the η values measured on several dendrite humps and performing this operation for different liquid heights, a curve relating the solidification shrinkage to the inclination of oxide skin can be determined, see Figure 5-18. In order estimate the inclination of the oxide skin behind the grain envelope, it is necessary to know the solidification shrinkage occurring across the grain envelope. In the previous section, an approximate estimate for the solidification shrinkage of about 2.6% was made. As it was discussed before, this value probably overestimates the solidification shrinkage. For the further calculations a very conservative estimate of 1% shrinkage across the grain envelope has been made. According to Figure 5-18, 1% shrinkage corresponds to an inclination $\eta = 17°$ respectively $\sin\eta = 0.29$. Therefore, a vertical force F_z of about 0.21 N/m can be expected at the contour of the dendrite tip, see Equation 5.6.
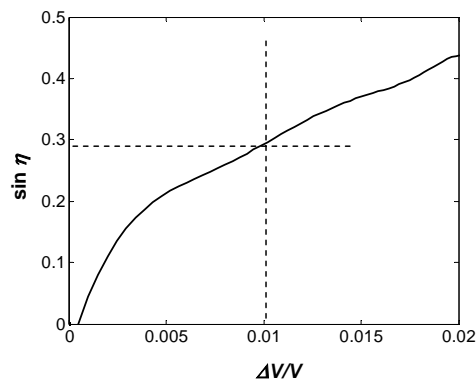
Figure 5-18 Relationship between the solidification shrinkage $\Delta V/V$ and the inclination of the oxide skin $\sin\eta$ determined from the experimentally measured profile shown in Figure 5-17.

In order to estimate the mechanical response of a dendrite arm, a clear idea of the contour on which the vertical force F_z applies is required. It is considered that the vertical force acts above all in the area where strong solidification shrinkage occurs and where the oxide skin is therefore necessarily strained in tension. The phase field results show that the

largest solidification rate and hence solidification shrinkage occurs in a zone of about 40 μm behind the envelope formed by the dendrite tips, see Figure 4-36. In order to have an idea of the lateral spread of a dendrite tip, in-plane phase field simulations have been conducted, see Figure 5-19.

a)   b)
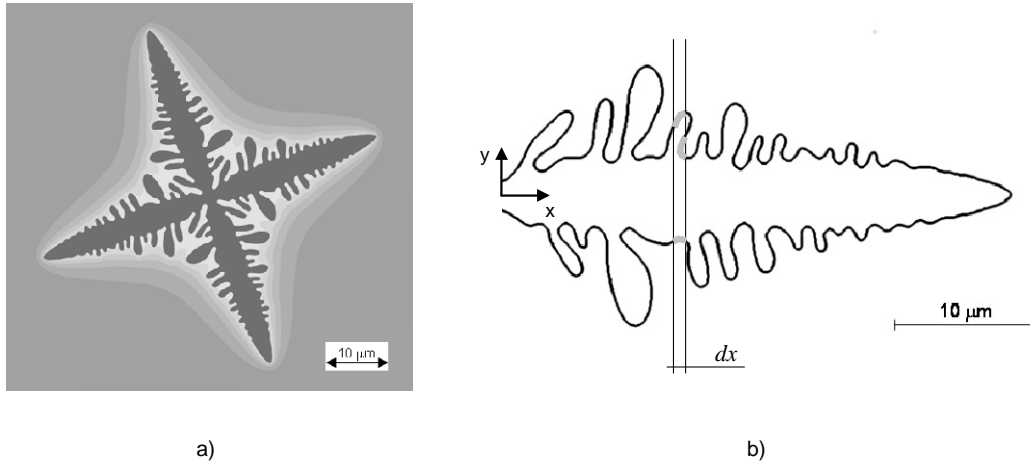
Figure 5-19 a) Phase field simulations showing the concentration field of an unconstrained dendrite at a realistic undercooling of 550°C. **b)** Contour of one of the dendrite arms. The dendrite arm has a total length of 36 μm. The determination of *ds/dx* is illustrated schematically. For a certain *dx*, *ds* corresponds to the sum of the segments of the dendrite contour which are indicated in grey.

Figure 5-19 b) shows the contour of a dendrite arm growing into a binary melt undercooled at 550°C. By applying the vertical force F_z piecewise on the contour the bending moment $M_y(x)$ can be calculated along the dendrite arm:

$$M_y(x) = -F_z \int_x^{x_{tip}} \int_{\xi_1}^{x_{tip}} \frac{\mathrm{d}s}{\mathrm{d}x}(\xi_2)\,\mathrm{d}\xi_2\,\mathrm{d}\xi_1 \qquad (5.7),$$

ξ_1 and ξ_2 are auxiliary integration variables and $\frac{\mathrm{d}s}{\mathrm{d}x}(x)$ is an function describing the length of the segments of the dendrite contour as a function of x. This function has been determined according to the method illustrated schematically in Figure 5-19 b). The bold line in Figure 5-20 shows the bending moment along the dendrite arm for the given dendrite contour. For comparison, the resulting moment for a hypothetical cylindrical dendrite arm (no side branches $\Rightarrow \frac{\mathrm{d}s}{\mathrm{d}x} = 2$) of the same length is given by the thin line.
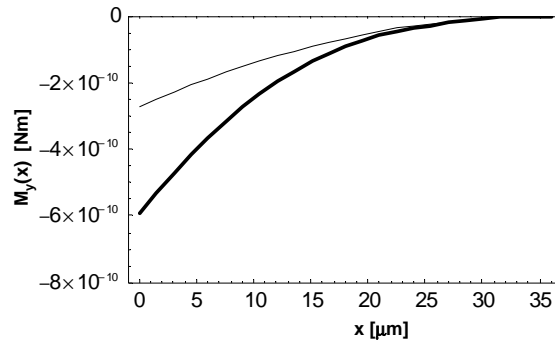
Figure 5-20 Bold line: bending moment developing along the dendrite arm shown in Figure 5-19 b) upon the application of a vertical force F_z=0.21 N/m on the dendrite contour. Thin line: bending moment for a dendrite arm of identical length but without side branches.

For the described dendrite geometry, a maximum bending moment of about $M_y\left(x=0\right)=-6.10^{-6}\,\mathrm{Nm}$ is reached. From the bending moment, the stresses in the dendrite arm can be calculated if the mechanical properties of the crystal are known. Different possibilities are conceivable for the mechanical response of the dendrite arm with respect to the bending moment. If the crystal exhibits a sufficient mechanical resistance, the behavior of the dendrite arm is purely elastic. In this case, the stress and strain fields in the crystal are proportional, see Figure 5-21, and the following stress profile occurs in the crystal:

$$\sigma_{xx} = -z\frac{M_y}{I_{yy}}$$ (5.8),

where I_{yy} is the second moment of area around the neutral axis. If one assumes that a dendrite has locally a circular cross-section the second moment of area becomes $I_{yy} = \pi/4\ r_d^4$. If a dendrite diameter $d = 2\,r_d = 5\,\mu\mathrm{m}$ is assumed, the yield stress of the crystal needed to be as high as 49 MPa in order to remain in the elastic regime. The assumption of a diameter of 5 μm is realistic but conservative, see Figure 5-2, since spots of a lower diameter are likely to occur in a dendrite arm.

If the yield stress is below 49 MPa, plastic deformation occurs in the dendrite arm. In the simple case of elastic-perfectly plastic deformation, which is realistic at the given high temperature, the center of the dendrite arm is subject of elastic deformation whereas plastification occurs in the peripheral areas outside a certain radius *d*, Figure 5-21. For a given moment and geometry, *d* can be calculated if the yield strength of the crystal is known. For low yield strengths, *d* approaches zero, the elastic zone hence vanishes and plastic deformation occurs throughout the dendrite arm. In structural mechanics, complete

failure of the element occurs in this case since the strain is not related to the stress anymore and very large deformations occur if the bending moment is maintained. In our case, the deformation is stopped if the surface is flattened by the bending of the dendrite arm or when the dendrite arm touches the substrate. For the numerical values derived above, complete plasticity occurs if the yield stress of the dendrite is below about 19 MPa.
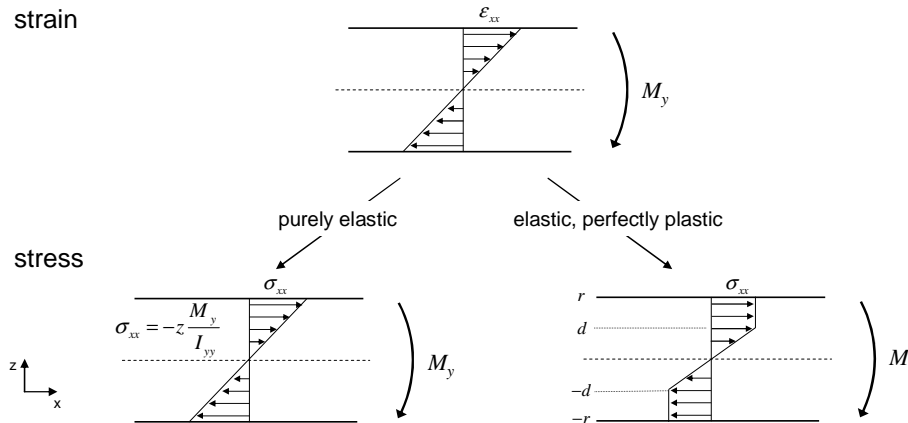
Figure 5-21 Strain and stress fields in sections along a dendrite. Depending on the mechanical properties of the dendrite crystal, the applied bending moment can lead to either purely elastic (left) or to elastic and plastic (right) deformation.

Unfortunately, there are no literature data of the mechanical properties of the Al-Zn-Si crystals at the temperature of interest (~530°C). However, the high temperature mechanical behavior of other Al-based solid solution alloys has been reported in literature. In general, Al alloys show an elastic - perfectly plastic behavior near the solidus temperature. The yield strength σ strongly depends on the plastic strain rate $\dot{\varepsilon}^p$ which follows a so-called Ludwik type law [Ludwig1 05]:

$$\dot{\varepsilon}^p = A \exp\left(\frac{-Q}{RT}\right)\left(\frac{\sigma}{s_0}\right)^n \tag{5.9}.$$

A, Q, s_0 and n are material parameters reported that have been determined for AA3104 [Van Haaften 02], Al-Cu [Ludwig1 05] and AA5182 [Ludwig2 05] alloys in the fully solid state. The above equation allows to extrapolate the behaviour of the solid to temperatures in the two phase area of the phase diagram. In Figure 5-22, the strain rate vs. yield stress relationship at the respective solidus temperature is plotted for these three Al-alloys. The figure shows that the three alloys follow the same trend, and one can assume that the Al-Zn-Si alloy shows a similar behaviour. In order to reach a yield stress of 20 MPa as required to avoid complete plasticity of a dendrite arm, very high strain rates in the order

of 0.1 s^{-1} (10 %/s) are required. At lower strain rates, the yield stress drops significantly. One can therefore assume that plastic deformation can occur in the dendrite crystal as a response to the forces that are generated by the solidification shrinkage.
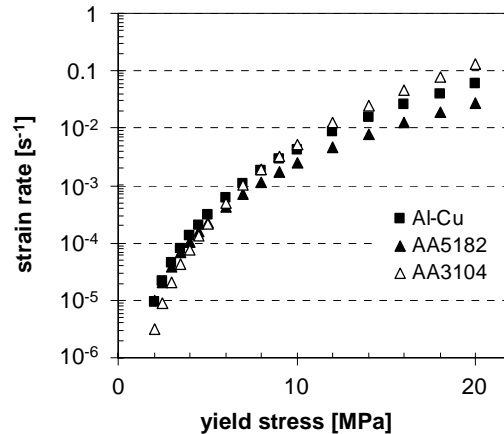
Figure 5-22 Yield stress vs. strain rate plotted for different Al-alloys at 535°C. The date points have been calculated by Equation 5.9 with numerical values determined experimentally by [Van Haaften 02], [Ludwig1 05] and [Ludwig2 05].

In order to discuss the effect of the bending moment on the crystal orientation, the dendrite arms are regarded as single crystal elements in which plastic deformation occurs by creation, movement and accumulation of dislocations. Dislocation sources (e.g. Frank-Read sources) are important for the plastic deformation. Under the effect of a sufficiently high resolved shear stress τ_{rss} in a certain slip plane, they emit a dislocation loops. The dislocation loop has edge character in the areas where the dislocation line is perpendicular to τ_{rss} and screw character in the area where the dislocation line is parallel to τ_{rss}. In a longitudinal section along the crystal / dendrite arm, the dislocations can therefore be visualized as pure edge dislocations, see Figure 5-23. The dislocation loop increases its size if τ_{rss} is larger than the critical resolved shear stress τ_{crss}, i.e. if yielding can occur, which is the case according to the above estimations. Supposed that the bending moment M_y is negative, dislocations with an excess atomic plane oriented downwards (in the –z direction) move towards the boundaries of the crystal whereas dislocations with an excess plane oriented upwards (+z direction) move towards the central fiber of the bent element, see Figure 5-23 a). The movement of dislocations leads to a pile-up of dislocations of one sign in the central area of the crystal. The dislocation segments moving to the boundaries of the crystal reach the solid-liquid interface and annihilate there as it is shown in Figure 5-24. Thereby, a pure edge dislocation moving towards the center of dendrite arm is the

only thing that remains from the dislocation loop of originally mixed character.

a)

b)
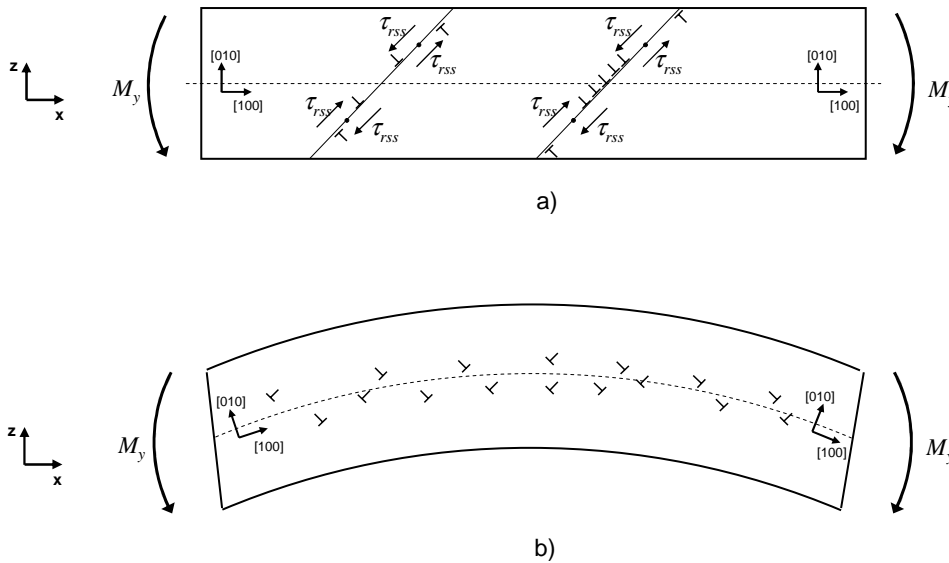
Figure 5-23 Schematic representation of the proposed dislocation movement occurring within the crystal under the effect of a bending moment. **a)** Under the effect of a the resolved shear stress in the activated slip system, dislocations with their excess plane oriented upwards move to the center of the crystal, whereas dislocations with their excess plane oriented downwards move the boundaries of the crystal. **b)** The resulting dislocation arrangement supposed that two slip systems were activated during plastic deformation. The accumulation of dislocations having their excess atomic plane oriented upwards leads to an gradient of crystallographic orientation.

Figure 5-23 b) shows a dislocation arrangement which can result in the bending of a single crystal dendrite arm. In the displayed case, two families of edge dislocations originating from two different activated slip systems are present in the crystal. Since they all have their excess plane oriented upwards, a distortion of the crystal lattice and hence a small variation of orientation is occurring. The resulting dislocation arrangement resembles to the one proposed by Sémoroz et al. [Sémoroz1 01], see Figure 2-13 a), except that the excess atomic planes of the edge dislocations can not be exactly normal to the axis of the dendrite since they need to be normal to the slip plane, which in turn is necessarily inclined with respect to the axis of the dendrite. The plausibility of such a dislocation arrangement due to a bending moment on single crystal beams with dimensions on the order of microns has been shown in the literature by numerical simulations [Yefimov 04] and by experimental investigations [Motz 05].
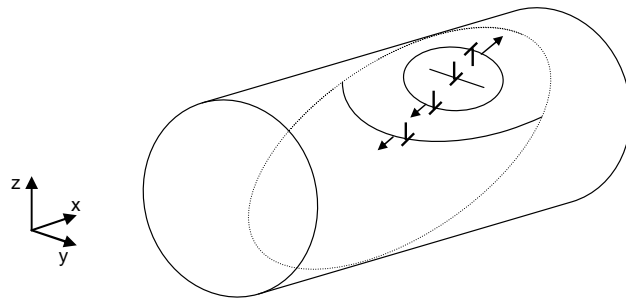
Figure 5-24 Schematic representation of a dislocation loop increasing its size under the effect of a bending moment -M_y within a dendrite arm. Part of the dislocation loop annihilates at the intersection of the slip plane with the solid-liquid interface limiting dendrite arm (dotted line). What remains in the end is a dislocation of pure edge character moving towards the center of the dendrite arm.

Experimental evidences

The objective of this paragraph is to discuss the experimental findings with respect to the crystallographic orientation reported in subsection 4.1.5 in the light of the above proposed solidification shrinkage mechanism which states that the misorientations are due to a decrease of the liquid level, and hence the oxide skin, in a zone of about 40 μm behind the grain envelope. This mechanism explains well the continuous misorientations observed along dendrite arms and the small discrete, but cumulative misorientations occurring across individual dendrite arms (cases 1 and 2a in Figure 4-18). In both cases, the misorientation axes are almost parallel to the plane of the coating and nearly perpendicular to the predominant dendrite growth direction. The observed misorientation axis corresponds well to the mechanical response of a freestanding dendrite tip that is subject to the application of a force in the –z (vertical) direction. The two other types of misorientations identified on the EBSD maps, i.e. the large, discrete misorientations of unspecified rotation axis and the banded misorientation structures (cases 2b and 3 in Figure 4-18 respectively) can not be related to the solidification shrinkage mechanism. Experimental investigations showed however that the latter type seems to be related mechanical strains on the dendrite network in the fully solid state, see 5.2.2, whereas one can assume that unspecified events in early stages of solidification are responsible for the first of these two.

The solidification shrinkage mechanism postulates that the misorientations are established very early in the solidification process, namely just behind the envelope of the developing grain. This is in good accordance with the experimental observation that eventual subgrain boundaries follow the dendrite structure, see Figure 4-19. The subgrain

boundaries indicate that dendrite tips growing in close proximity can adopt significantly different crystal orientations. This is easily possible in the early stage of solidification when coalescence of neighboring dendrite arms has not yet occurred. In later stages of solidification when the dendrite arms are coalesced, it is difficult to imagine how clear-cut subgrain boundaries can form across a coalesced dendrite pattern.

As already mentioned, the misorientation axes are in general in the plane of the coating and approximately perpendicular to the predominant dendrite growth direction. Figure 4-21 shows however, that the secondary branches can also affect the misorientation axis. The presence of secondary arms only on one side of a primary branch shifts the misorientation axis towards the secondary branches. This phenomenon can also be explained by the solidification shrinkage mechanism. If secondary arms develop only towards one side of the primary arm, the vertical force applied on the dendrite contour leads to an additional torsional moment in the primary arm. It seems plausible that this torsional moment contributes to the plastic deformation in the dendrite arm and thereby shifts the misorientation axis.

As already mentioned above, the systematic cumulative misorientations can either occur continuously along individual dendrite arms, Figure 4-22, or step by step by small discrete, but cumulative misorientations occurring across the dendrite arms. The latter can lead to a so-called "tile pattern" that is shown in Figure 4-23. This kind of misorientation pattern occurs in particular if two neighboring growth directions are equally competitive, which leads to repeated lateral branching in the development of the dendrite structure. The detailed analysis by EBSD shows that the small discrete misorientations occur at branching necks of the dendrites, see Figure 4-23 to 4-25. This is in good accordance with the solidification shrinkage mechanism since the bending of the dendrite arm due to the vertical forces will have the tendency to localize in areas where the cross-section of the dendrite arm is minimal, i.e. in branching necks.

A necessary condition for the validity of the solidification shrinkage mechanism as the cause for the observed crystallographic misorientations, is that the developing dendrite network is in contact with the free boundary, i.e. with the oxide skin, in the zone behind the advancing grain envelope. From the presence of shiny and dull zones, it has been concluded in section 5.1.4 that growth occurs preferentially along either the free boundary or the boundary with the substrate respectively. Experimental observations made by AFM and SEM show however that growth does not occur exclusively along either of the

boundaries in the respective sectors, see Figure 4-13 and section 5.1.4. In actual fact, the dendrite arms are rather zig-zaging between the two boundaries that confine the melt. In the case of shiny surface appearance, longer segments of the zig-zag structure are well aligned with the free boundary whereas in dull areas, longer segments grow along / towards the boundary with the substrate. However, one can assume that in dull areas also, there are enough points of contact between the developing dendrite network and the oxide skin in order to transmit the forces from the surface to the solid underneath.

The experiments involving re-melting and re-solidification of the Al-Zn-Si coating layer showed that misorientations of the same kind as the ones observed in the industrial process can be reproduced in laboratory. In the light of the solidification shrinkage mechanism, this behavior can be expected since the solidification shrinkage and the oxide skin are equally present in a re-solidification experiment. Further on, it seems plausible that the modified thermal strain conditions imposed by the brass setup does not affect the crystallographic misorientations. On the other hand, there is a clear relationship between the experimentally determined misorientation rate and the cooling rate. For higher cooling rates, higher misorientation rates are observed. This correlation can be understood if one considers the effect of the cooling rate on the dendrite arm spacing a finer dendrite network undergoes plastic deformation more easily. This is even the more true for deformation by bending since the stress in a bent element is inversely proportional to the second moment of area I_{yy} which in turn is proportional to the fourth power of the diameter of dendrite arm, see Figure 5-21. When interpreting the correlation between dendrite arm spacing and misorientation rate, one should however bear in mind that the measured dendrite arm spacing does not exactly correspond to the dendrite arm spacing at the moment of solidification since the dendrite arm spacing increases due to ripening in the semi-solid state [Mortensen 91]:

$$\lambda^3 - \lambda_0^3 = Kt \tag{5.10},$$

where λ_0 is the initial dendrite arms spacing, t is the hold time in the semi-solid state and K is a constant. The correlation between the spacing at the growth front λ_0 and the misorientation rate is therefore not as pronounced as it seems at first glance since the ripening is more important for lower cooling rates.

The analysis of the Al-Zn-Si interlayers re-melted and re-solidified after joining by ultrasonic welding shows misorientation pattern that are substantially different from those

observed in coatings exhibiting free surfaces. In the welded area, showing hardly any misorientation at all are equally present as grains displaying very strong misorientations. Grains without misorientations are not observed in coatings with a free boundary. In the grains with strong misorientations, the misorientations are mainly of discrete nature, i.e. they are made up of very pronounced subgrain boundaries. Unlike in the case of solidification of layers with a free surface, no systematic relationship between the misorientation axes and the dendrite pattern is found. The strong misorientations present in some grains show however that the solidification in a layer confined by two steel substrates is far from the situation occurring in the solidification of bulk samples. The only plausible explanation for the pronounced misorientations is the interaction of the dendrite network with the two steel substrates, with the residual fragments of oxide skin and the pores forming on the oxide skin. The solidification shrinkage, which seems to be responsible for the typical misorientation in coatings with free boundaries is compensated differently in interlayers confined by two steel sheets, namely a) by the formation of pores on or in between the residual oxide fragments and b) by a decrease of the spacing between the two steel substrates. The latter phenomenon is hard to control since the solidification shrinkage at the grain envelope can be completely compensated by approaching the two steel substrates by less than a micron. The mechanical interaction of the approaching rigid steel substrates with the developing dendrite network is however significantly different from the interaction between dendrites and a flexible oxide skin as it happens in the solidification of coatings. Whereas the forces due to the oxide skin apply smoothly along the contour of the dendrite arms leading thereby to relatively continuous misorientations, the approaching steel substrates localize significant strain at specific spots in the dendrite network where the dendrite tip passed closest to the substrates. This may explain the very localized and abrupt misorientations observed in some grains in the re-solidified sandwich samples.

On the other hand, there are grains in re-solidified sandwich samples that hardly show any misorientations at all. One can assume therefore that the solidification shrinkage was compensated in these grains without mechanical interferences with the developing dendrite network. Maybe, the solidification shrinkage was compensated by an inflow of liquid originating from the formation of pores on oxide fragments located far from the moving grain envelope, similarly as it is the case in bulk solidification. In total, one can summarize that the re-solidification experiments on sandwich samples joined by ultrasonic welding did not lead to utterly conclusive results. The findings are however not in contradiction with the solidification shrinkage mechanism that is proposed here as the origin of the intragranular misorientations observed in Al-Zn-Si coating systems.

The solidification shrinkage mechanism that is proposed in order to explain the formation of the substantial and systematic crystallographic misorientations within grains of Al-Zn-Si coatings requires the presence of a free boundary in the immediate vicinity of the growing dendrite tips. This condition is only fulfilled if the melt to be solidified is present under the form of a thin coating layer. As soon as the thickness of the melt layer is larger than a couple of dendrite arm spacings, the effect of the solidification shrinkage on the crystal orientation of the dendrites vanishes. The proposed mechanism can therefore not be applied on the solidification of bulk samples. However, the present work shows that near the solidification front, the dendrite network is very prone to the formation of crystallographic misorientations when forces are applied on the dendrite arms. In the solidification of bulk samples, forces of a different origin may occur such as gravity forces as it was observed in Al-Ni alloy by Billia et al. [Billia 07], see Figure 2-12. Likewise, it seems plausible that the continuous and cumulative misorientations observed in long dendrite arms growing into the platform region of Ni-base single crystal blades [D'Souza 05] are due to forces applied in the tip area of the growing dendrites.

CHAPTER VI

CONCLUSION

During this project, the formation of the microstructure in Al-Zn-Si coatings on steel substrates has been studied. A particular emphasis has been laid on the development of the dendrite network and on the origins of the intragranular misorientations that are very pronounced in the given system. The topic has been investigated on the following three main axes:

- The detailed characterization of the microstructure of coatings solidified under industrial conditions with respect to phases, surface appearance and surface topography, microsegregation and crystallographic misorientations. For this reason, characterization methods such as optical and electron microscopy, laser profilometry, AFM, EDS, WDS, GD-OES as well as EBSD have been applied.

- The modeling of the microstructure formation by the phase field method on the scale of the dendrite tip, and with a geometrical model on the scale of the grain. Further on, inverse modeling has been conducted in order to infer on the anisotropy of the solid-liquid interfacial energy based on the dendrite growth directions that are apparent on the surface of the coating.

- Re-melting / re-solidification experiments conducted in induction and infrared furnaces aimed at studying the behavior of the Al-Zn-Si layers under modified

solidification conditions.

These investigations have led to a deeper understanding of the microstructure formation in the Al-Zn-Si coating system. The main findings are summarized here:

- The present study confirmed the solidification sequence that has previously been reported in the literature [Chen 05]. α-Al dendrites are formed as primary phase, Si particles and finally α-Al-β-Zn-(Si) eutectics appear in the interdendritic areas. At lower temperatures, β-Zn precipitates are formed within the primary dendrites.

- The dendrite network spreads very quickly within the coating layer at a high supersaturation around about 535 to 530°C. As a consequence of the high supersaturation, the internal solid fraction is also high immediately after the formation of the dendrite network. The most substantial increase of the solid fraction occurs just behind the envelope of the growing grain.

- The dendrite tips do not grow along the usual [100] crystallographic directions in the Al-Zn-Si system. The inverse method approach applied in this work allowed determining accurately the preferred crystallographic growth directions from the dendrite morphology that is apparent on the surface of the Al-Zn-Si coatings. The preferred growth directions are located in between neighboring ⟨100⟩ and ⟨110⟩ directions, 28.5° from ⟨100⟩.

- Further on, the inverse method allowed proposing a mathematical expression for the anisotropy of the solid-liquid interfacial energy in the Al-Zn-Si system. The availability of such an expression is a crucial prerequisite for future 3D phase field simulations of the given alloy system. Such simulations are desirable in order to better understand the interaction of the dendrite tips with the confining boundaries.

- 2D phase field simulations suggest that the dendrite tips do not establish contact with the boundaries confining the melt. This is in good accordance with experimental evidence obtained by electron microprobe measurements. In between the dendrite tips and the boundary, a thin layer of solute-rich liquid remains. One can assume that the dendrite arms coalesce with the substrate significantly after the formation of the dendrite network.

- The results of the geometrical model, which are in good agreement with experimental evidence, indicate that the shiny and dull areas observed visually on the surface of the coating are due to dendrite growth occuring primarily along the

free boundary and along the boundary with the substrate respectively. Surface topography measurements show that long uninterrupted dendrite arms growing along a boundary are rare since the velocity of tips growing along a boundary is substantially reduced as compared to dendrite tips growing freely into the bulk melt. Therefore, on can assume that the dendrite network is established by tips that are constantly zig-zagging between the two boundaries.

- It has been shown that the intragranular misorientations observed in Al-Zn-Si cannot originate from the microsegregation occurring in the coating or from the thermomechanical stresses due to the different thermal contraction behavior of substrate and coating.

- As a new hypothesis, it is proposed that the solidification shrinkage is the driving force for the formation of the intragranular misorientations.

- In melt layers exhibiting a boundary that can move freely, the solidification shrinkage is compensated by a decrease of the melt level in between the dendrite arms which leads to the surface topography observed experimentally by laser profilometry and AFM.

- The solidification shrinkage leads to an increase of the surface roughness and hence of the surface area of the coating. Therefore, tensile stresses are present in the oxide skin spanning the surface of the melt. The tensile stresses translate into forces that apply on the dendrite network.

- Since the amount of solidification shrinkage is substantial just behind the grain envelope, the forces lead to a bending moment in the tip area of the growing dendrite arms. It was shown that the bending moment is sufficient to deform plastically the dendrite arm, thereby introducing the geometrically necessary dislocation that lead to the observed variations of the crystallographic orientation.

The present study provides a deeper understanding of the microstructure development in Al-Zn-Si coatings. In particular, the formation of the dendrite network within the confined volume of the coating layer was studied in detail. The insights gained on the microstructure formation allowed concluding on the origins of the typical surface appearance, the spangle pattern, and on the mechanism which is responsible for the formation of the intragranular crystallographic misorientations observed in Al-Zn-Si coatings. For both phenomena, the boundaries confining the coating layer are of crucial importance. Experimental and numerical investigations have shown that the spangle

pattern is a consequence of the atypical dendrite growth directions and the complex branching behavior of the dendrite arms, which lead to preferential dendrite growth along one of the two boundaries. In order to better understand the interaction of a dendrite tip with a boundary, 3D phase field simulations of dendrite arms growing along a boundary are desirable in the future. Such simulations could accurately reproduce the solute rejection around a dendrite tip in interaction with a boundary. By including convective transport and the displacement of the free boundary in a 3D phase field model, the compensation of the solidification shrinkage could also be addressed in such a model. For 3D dendrite growth modeling of the Al-Zn-Si system, the third order cubic harmonics expression for the interfacial energy determined during this study is an essential prerequisite. On a more fundamental level, future 3D phase field simulations would allow more detailed investigations of the relationship between the solid-liquid interfacial energy or the interface stiffness and the preferred crystallographic dendrite growth directions.

As has been shown in this study, the observed pronounced intragranular crystallographic misorientations have their origin in the fact that one of the boundaries confining the melt is free to move. This allows the compensation of the solidification shrinkage by a decrease of the melt level in between the growing dendrites which leads to mechanical forces on the dendrite arms. The proposed mechanism requires the presence of a free boundary in close vicinity of the dendrite growth front. This is the case in coating systems, however, it is not the case in bulk solidification where intragranular misorientations can also occur. Future work is required in order to clarify the mechanisms responsible for crystallographic misorientations in massive castings such as Ni-base single crystal turbine blades. Detailed 3D EBSD characterizations of the misorientations, which go beyond what has been reported in the literature so far, would be a first step of future activities in this direction.

APPENDIX

Solidification shrinkage in dendritic growth

As it was described in chapter 5, the solidification shrinkage plays an important role in the microstructure formation of Al-Zn-Si coatings. Therefore, it is worth summarizing the information available in the literature concerning the solidification shrinkage in dendritic growth. In the growth of equiaxed dendritic grains, the solidification shrinkage can be divided in two parts. A first part of the solidification shrinkage occurs during the isothermal formation of the dendrite network and is localized in the area of the moving grain envelope. The second part occurs later within the grains, where the solid fraction is uniform but steadily increasing upon cooling. Since there are no literature values available for the solidification shrinkage of the Al-43Zn-1.6Si alloy, it needs to be derived from quantities such as the molar volumes of the melt and the lattice parameter of the solid at the solidification temperature as far as they are known.

In the theoretical treatment of liquid metals, atomic or molar volumes are more frequently used for describing their properties than the density. The atomic volume V of a pure metal is related to the density ρ by the following relationship:

$$V = \frac{M}{\rho}$$
(A.1),

where M is the molar weight. For an alloy melt, the molar volume becomes [Egry 06]:

$$V_{alloy} = \sum_i x_i V_i + {}^E V_{alloy}$$
(A.2),

where x_i is the atomic fraction of element i, V_i is the molar volume and ${}^E V_{alloy}$ is the so-called excess volume. Generally, ${}^E V_{alloy}$ is a small correction in the order of a few percents, which can either be negative or positive. According to the literature [Iida 93], negative ${}^E V_{alloy}$ values have been observed for alloys forming stable intermetallic compounds. The largest positive ${}^E V_{alloy}$ values are reported for alloy systems exhibiting a miscibility gap. Alloy systems with important solid solubility show typically small excess volumes [Iida 93]. Based on these considerations, one can assume that the ${}^E V_{alloy}$ term is negligible in the Al-Zn-Si system even though there are no experimental data available for this system. In the case of negligible excess volume, the above equation reduces to a simple linear

combination of the molar volumes which is often referred to as Vegard's law.

It is found that the molar volume of the elements V_i is linearly dependent on temperature [Iida 93]:

$$V_i = V_{m,i}\left(1 + \alpha_{v,i}\left(T - T_m\right)\right) \tag{A.3},$$

where $V_{m,i}$ is the molar volume of the liquid at the melting point, $\alpha_{v,i}$ is the volume expansion coefficient and T_m is the melting point of the element. Values for $V_{m,i}$ and $\alpha_{v,i}$ can be found in the literature and are repeated in Table A-1.

	$V_{m,i}$ [10^{-6} m^3/mol]	$\alpha_{v,i}$ [10^{-6} K^{-1}]
Al	11.3	150
Zn	9.94	150
Si	11.1	140

Table A-1 Molar volume and volume expansion coefficients at the respective melting temperatures of the pure substances. Taken from [Iida 93].

From the molar volume, the density of the melt can be calculated through Eq. A.1 using an averaged molar volume M_{alloy}:

$$M_{alloy} = \sum_i x_i M_i \tag{A.4},$$

As there are no experimental results for the density of the solid phase at the solidification temperature, the density needs to be extrapolated from experimental data gathered at lower temperatures. Reliable estimations of the density of solid solution alloys are possible from the lattice parameter data measured for various concentrations and temperatures. Lattice parameter data for the binary Al-Zn system have been determined by Murray [Murray 83] for the temperatures $T = 25°C$ and $T = 360°C$. The results of this study are plotted in Figure 2-14. The author shows that the lattice parameter decreases linearly with increasing Zn concentration and that it increases of course with increasing temperature. From the given data, linear extrapolation allowed determining a lattice parameter vs. Zn concentration relationship at a realistic solidification temperature.

From the lattice parameter a, the density can be calculated through:

$$\rho_{sol} = \frac{M_{alloy}}{a^3 N_a} n \tag{A.5},$$

where M_{alloy} is calculated as in the case of the liquid by Equation A.4, N_a is the Avogadro number and n is the number of atoms per unit cell, which corresponds to 4 in the case of fcc material. From the densities of the solid (Equation A.5) and the liquid (Equation A.1 and A.4), the total solidification shrinkage of the alloy can be calculated.

By combining Equations. A.1 and A.5, the molar volume of the solid is obtained:

$$V_{sol} = \frac{a^3 N_a}{n} \tag{A.6}.$$

In order to better understand the situation at the grain envelope, it is helpful to compare the molar volumes of the solid and the liquid phase at the solidification temperature and at their respective concentrations c_{sol} and c_{liq} which are given by the equilibrium phase diagram. By weighting the molar volume of the solid and the interdendritic liquid according to the phase fractions, the mean molar volume within the mushy grains can be calculated:

$$\overline{V}_{mushy\ zone} = f_s V_{sol}(c_{sol}) + (1 - f_s) V_{liq}(c_{liq}) \tag{A.7},$$

where f_s is the internal solid fraction of the grain. This mean molar volume allows calculating the effective solidification shrinkage occurring across the grain envelope:

$$\left. \frac{\Delta V}{V} \right|_{grain\ envelope} = \frac{V_{liq}(c_{liq}) - \overline{V}_{mushy\ zone}}{V_{liq}(c_{liq})} \tag{A.8}.$$

As has been shown in section 5.2, the solidification shrinkage at the grain envelope is an important factor for the formation of the intragranular misorientations observed in Al-Zn-Si coatings.

SYMBOLS

Symbol	Unit	Meaning
D_L	m^2/s	diffusion coefficient in the liquid
D_S	m^2/s	diffusion coefficient in the solid
G	K/m	temperature gradient at the interface
G_c	1/m	solute gradient at the interface in the liquid
L	J/mol	latent heat of fusion
$[\mathbf{M}]$	-	orientation / misorientation matrix
P	-	solutal Peclet number
P_t	-	thermal Peclet number
R	m	dendrite tip radius
T_l	K	liquidus temperature
T_s	K	solidus temperature
V	m/s	dendrite tip speed
c_L	-	local liquid concentration in the phase field method
c_l	-	liquidus concentration
c_S	-	local solid concentration in the phase field method
c_s	-	solidus concentration
c_0	-	concentration of the undercooled liquid
f_s	-	solid fraction
h	W/m^{2}K	heat transfer coefficient
k	-	partition coefficient
m	K	liquidus slope
$\mathbf{r}$	-	misorientation axis
x^*	m	interface position
ΔG	J/mol	Gibbs free energy of the transformation
ΔT	K	undercooling

ΔT_0	K	solidification interval
ΔT_k	K	kinetic undercooling
ΔT_r	K	curvature undercooing
Δs_f	J/m^{3}K	volumetric entropy of fusion
Γ	Km	Gibbs-Thomson coefficient
$\Phi_r(\mathbf{n})$	-	normalized generalized interface stiffness
Ω	-	supersaturation of the undercooled melt
α	°	angle between the crystallographic growth direction and a boundary
α_t	m^2/s	thermal diffusivity
β	°	contact angle of the solid on a boundary
γ_{sl}	J/m2	solid liquid interface energy
δ	m	solid-liquid interface thickness
$\varepsilon_1, \varepsilon_2, \varepsilon_3$	-	3D cubic harmonics anisotropy parameters
ε_4	-	2D 4-fold anisotropy parameter
η	°	inclination at the solid-liquid-air triple point
ζ	rad	angle between primary dendrite growth directions
κ	W/mK	thermal conductivity
$\kappa_1, \ \kappa_2$	1/m	principal curvatures
λ	N/m	plastification tension in the oxide skin
λ_i	m	marginal stability wavelength
λ_2	m	dendrite arm spacing
τ	°	misorientation angle
θ	rad	polar angle
ϑ	rad	Bragg angle
ϕ	rad	azimuthal angle
φ	-	phase field variable
$\varphi_1, \phi, \varphi_2$	rad	Euler angles

REFERENCES

[Agapova 89]   E. V. Agapova, G. N. Pankin, V. V. Ponomarev, V. N. Larionov and A.Y. Denisov, Izvestiya Akademii Nauk SSSR. Metally **2**, 104 (1989).

[Agapova 97]   E. V. Agapova, D. M. Tagirova and V. M. Gundyrev, The Physics of Metals and Metallography **84** 171 (1997).

[Akamatsu 95]   S. Akamatsu, G. Faivre, and T. Ihle, Phys. Rev. E **51**, 4751 (1995).

[Asta 02]   M. Asta, J. J. Hoyt, and A. Karma, Phys. Rev. B **66**, 100101 (2002).

[Athreya 04]   B. P. Athreya and J. A. Dantzig, in *Solidification Processes and Microstructures: A Symposium in Honor of Wilfried Kurz*, edited by M. Rappaz, C. Beckermann and R. Trivedi, 357 (TMS, Warrendale PA, 2004).

[Beck 77]   J. V. Beck and K. J. Arnold, Parameter Estimation in Engineering and Science (Wiley, New York NY, 1977).

[Beckermann 99] C. Beckermann, H.-J. Diepers, I. Steinbach, A. Karma and X. Tong, J. Comp. Phys. **154**, 468 (1999).

[Billia 07]   B. Billia, J. Gastaldi, H. Nguyen-Thi, T. Schenk, G. Reinhart, N. Mangelinck, B. Grushko, H. Klein, J. Härtwig and J. Baruchel, submitted for publication (2007).

[Boettinger 02] W. J. Boettinger, J. A. Warren, C. Beckermann and A. Karma, Annu. Rev. Mater. Res. **32**, 163 (2002).

[Brener 96]   E. Brener, H. Müller-Krumbhaar, and D. Temkin, Phys. Rev. E **54**, 2714 (1996).

[Cahn 74]   J. W. Cahn and D. W. Hoffman, Acta Metall. **22**, 1205 (1974).

[Chen 05]   R. Y. Chen and D. J.Willis, Met. Mat. Trans. A **36**, 117 (2005).

[Cleary 85]   H. J. Cleary, Microstructural Sci. **12**, 103 (1985).

[Courntey 00]   T. H. Courtney, *Mechanical Behavior of Materials* (McGraw-Hill, Boston MA, 2000).

[Dantzig 00]   J. Dantzig, N. Provatas, N. Goldenfeld, J. C. LaCombe, A. Lupulescu, M. Koss and M. Glicksman, in *Modeling of Casting Welding and Advanced Solidification Processes IX*, edited by P. R. Sahm, P. N. Hansen and J. G. Conley, 453 (Shaker, Aachen, 2000).

[Davidchack 00] R. L. Davidchack and B. B. Laird, Phys. Rev. Lett. **65**, 4751 (2000).

[Divandari 04]   M. Divandari and J. Campbell, Int. J. Cast Met. Res. **17**, 182 (2004).

[Dragnevski 02]   K. Dragnevski, A. M. Mullis, D. J. Walker and R. F. Cochrane, Acta Mater. **50**, 3743 (2002).

[D'Souza 05]   N. D'Souza, M. Newell, K. Devendra, P. A. Jennings, M. G. Ardakani and B. A. Shollock, Mat. Sci. Eng. A **413-414**, 567 (2005).

[Echebarria 04]   B. Echebarria, R. Folch, A. Karma and M. Plapp, Phys. Rev. E **70**, 061604 (2004).

[Egry 06]   I. Egry and J. Brillo, in *Modeling of Casting, Welding and Advanced Solidification Processes XI*, edited by C. A. Gandin and M. Bellet, 1181 (TMS, Warrendale PA, 2006)

[Fabietti 91]   L. M. Fabietti and J. A. Sekhar, in Nature and Properties of Semi-Solid Materials, edited by J. A. Sekhar and J. Dantzig, (TMS, Warrendale PA, 1991).

[Fehlner 76]   W. R. Fehlner and S. H. Vosko, Can. J. of Phys. **54**, 2159 (1976).

[Glicksman 89]   M. E. Glicksman and N. B. Singh, J. Cryst. Growth **98**, 277 (1989).

[Gonzales 06]   F. Gonzales, and M. Rappaz, Met. Mat. Trans. A **37**, 2797 (2006).

[Grasso 04]   P.-D. Grasso, *Coalescence and mechanical behavior of semi-solid aluminium alloys in relation to hot tearing* (PhD thesis EPFL, Lausanne, 2004).

[Haxhimali 06]   T. Haxhimali, A. Karma, F. Gonzales and M. Rappaz, Nature Materials **5**, 6 (2006).

[Henry1 98]   S. Henry, T. Minghetti, and M. Rappaz, Acta Mater. **46**, 6431 (1998).

[Henry2 98]   S. Henry, P. Jarry, and M. Rappaz, Met. Mat. Trans. A **29**, 2807 (1998).

[Henry 99]   S. Henry, *Etude de la Germination et de la Croissance maclées dans les Alliages d'Aluminium* (PhD thesis EPFL, Lausanne, 1999).

[Herring 51]   C. Herring, in *The physics of powder metallurgy*, edited by W. E. Kingston (McGraw-Hill, New York, 1951).

[Hoffman 72]   D. W. Hoffman and J. W. Cahn, Surface Science **31**, 368 (1972).

[Hoyt 01]   J. J. Hoyt, M. Asta, and A. Karma, Phys. Rev. Lett. **86**, 5530 (2001).

[Hoyt 03]   J. J. Hoyt, M. Asta, and A. Karma, Mat. Sci. Eng. R **41**, 121 (2003).

[Iida 93]   T. Iida and R. I. L. Guthrie, *The physical properties of liquid metals* (Clarendon Press, Oxford 1993).

[Jacot 06]   A. Jacot, in *Virtual Fabrication of Aluminium Products*, edited by J. Hirsch (Wiley-VCH, Weinheim, 2006).

[Karma 97]   A. Karma and W.-J. Rappel, J. Cryst. Growth **174**, 54 (1997).

[Karma 98]   A. Karma and W.-J. Rappel, Phys. Rev. E **57**, 4323 (1998).

[Karma 01]   A. Karma, Phys. Rev. Lett. **87**, 115701 (2001).

[Kessler 88]   D. A. Kessler, J. Koplik, and H. Levine, Adv. Phys. **37**, 255 (1988).

[Kobayashi 93]   R. Kobayashi, Physica D **63**, 410 (1993).

[Kurz 86]   W. Kurz, B. Giovanola and R. Trivedi, Acta Metall. **34**, 823 (1986).

[Kurz 98]   W. Kurz, *Fundamentals of Solidification* (Trans Tech, Uetikon-Zürich, 1998).

[Laird 05]   B. B. Laird and R. L. Davidchack, J. Phys. Chem. B **109**, 17802 (2005).

[Langer 77]   J. S. Langer and H. Müller-Krumbhaar, J. Cryst. Growth **42**, 11 (1977).

[Langer 86]   J. S. Langer, in *Directions in Condensed Matter, 164* (World Scientific, Singapore, 1986).

[Lipton 87]   J. Lipton, W. Kurz and R. Trivedi, Acta Metall. **35**, 957 (1987).

[Liu 01]   S. Liu, R. E. Napolitano, and R. Trivedi, Acta Mater. **49**, 4271 (2001).

[Löffler 91]   H. Löffler, R. Ramlau, Cryst. Res. Technol. **26**, 81 (1991).

[Löffler 95]   H. Löffler, *Structure and Structure Development of Al-Zn alloys*, (Akademie Verlag, Berlin 1995).

[Ludwig1 05]   O. Ludwig, J.-M. Drezet, C. L. Martin and M. Suery, Met. Mat. Trans. A **36**, 1525 (2005).

[Ludwig2 05]   O. Ludwig, J.-M. Drezet, P. Ménésès, C. L. Martin and M. Suery, Mat. Sci. Eng. A **413-414**, 174 (2005).

[Marder 00]   A. R. Marder, Prog. Mat. Sci. **45**, 191 (2000).

[Monachon 06]   C. Monachon and F. Gonzales, oral communication (2006).

[Morris 04]   J. R. Morris and R. E. Napolitano, JOM **56**, 40 (2004).

[Mortensen 91]   A. Mortensen, Met. Trans. A **22**, 569 (1991).

[Motz 05]   C. Motz, T. Schöberl and R. Pippan, Acta Mater. **53**, 4269 (2005).

[Mullins 63]   W. W. Mullins and R. F. Sekerka, J. Appl. Phys. **34**, 323 (1963).

[Mullins 64]   W. W. Mullins and R. F. Sekerka, J. Appl. Phys. **35**, 444 (1964).

[Mullis 01]   A. M. Mullis, D. J. Walker, S. E. Battersby and R. F. Cochrane, Mat. Sci. Eng. A **304-306**, 245 (2001).

[Murray 83]   J. L. Murray, Bulletin of Alloy Phase Diagrams **4**, 55 (1983).

[Muschol 92]   M. Muschol, D. Liu, and H. Z. Cummins, Phys. Rev. A **46**, 1038 (1992).

[Napolitano 00] R. E. Napolitano and R. J. Schaefer, J. Mat. Sci. **35**, 1641 (2000).

[Napolitano 02] R. E. Napolitano, S. Liu, and R. Trivedi, Interface Sci. **10**, 217 (2002).

[Napolitano 04]   R. E. Napolitano and S. Liu, Phys. Rev. B **70**, 214103.1 (2004).

[Nestler 00]   B. Nestler, A. A. Wheeler, Physica D **138**, 114 (2000).

[Newell 05]   M. Newell, K. Devendra, P. A. Jennings and N. D'Souza, Mat. Sci. Eng. A **412**, 307 (2005).

[Papapetrou 35]   A. Papapetrou, Z. Kristallographie **92**, 89 (1935).

[Paul 93]   U. Paul, P. R. Sahm, D. Goldschmidt, Mat. Sci. Eng. A **173**, 49 (1993).

[Pelzel 49]   E. Pelzel, Berg- und Hüttenmännische Monatshefte **93**, 10 (1949).

[Plapp 02]   M. Plapp and A. Karma, Phys. Rev. E **66**, 061608-1 (2002).

[Porter 91]   F. Porter, *Zinc Handbook* (Marcel Dekker, New York, 1991).

[Provatas 98]   N. Provatas, N. Goldenfeld and J. Dantzig, Phys. Rev. Lett. **80**, 3308 (1998).

[Randle 00]   V. Randle, in *Electron Backscatter Diffraction in Materials Science*, edited by A. J. Schwartz, M. Kumar and B. L. Adams, 19 (Kluwer Academic, New York NY, 2000).

[Rappaz 86]   M. Rappaz and E. Blank, J. Cryst. Growth **74**, 67 (1986).

[Rappaz 95]   M. Rappaz, J.-L. Desbiolles, J.-M. Drezet, Ch.-A. Gandin, A. Jacot and Ph. Thévoz, in *Modeling of Casting, Welding and Advanced Solidification Processes VII*, edited by M. Cross and J. Campbell, 449 (TMS, Warrendale PA, 1995).

[Saito 88]   Y. Saito, G. Goldbeck-Wood and H. Müller-Krumbhaar, Phys. Rev. A **38**, 2148 (1988).

[Sekerka1 05]   R. F. Sekerka, Cryst. Res. Technol. **40**, 291 (2005).

[Sekerka2 05]   R. F. Sekerka, J. Cryst. Growth **275**, 77 (2005).

[Selverian 87]   J. H. Selverian, M. R. Notis and A. R. Marder, J. Mat. Eng. **9**, 133 (1987).

[Selverian 88]   J. H. Selverian, A. R. Marder and M. R. Notis, Met. Trans. A **19**, 1193 (1988).

[Selverian 89]   J. H. Selverian, A. R. Marder and M. R. Notis, Met. Trans. A **20**, 543 (1989).

[Sémoroz 00]   A. Sémoroz, S. Henry, and M. Rappaz, Met. Mater. Trans. A **31**, 487 (2000).

[Sémoroz1 01]   A. Sémoroz, Y. Durandet, and M. Rappaz, Acta Mater. **49**, 529 (2001).

[Sémoroz2 01]   A. Sémoroz, *Experimental study and modelling of nucleation and growth during solidification of Al and Zn coatings* (PhD thesis EPFL, Lausanne, 2001).

[Simerska 78]   M. Simerska, P Bartuska and V. Synecek, Acta Crystall. A **34**, 304 (1978).

[Siredey 93]   N. Siredey, M. Boufoussi, S. Denis and J. Lacaze, J. Cryst. Growth **130**, 132 (1993).

[Smithells 99]   E. A. Brandes and G. B. Brook (Eds.), *Smithells Metals Reference Book* (Butterworth-Heinemann, Oxford, 1999).

[Suzuki 93]   T. Suzuki, in *Ternary Alloys*, edited by G. Petzow and G. Effenberg, 338 (VCH, Weinheim, 1993).

[Syvertsen 06]   M. Syvertsen, Met. Mater. Trans B **37**, 495 (2006).

[Tiaden 98]   J. Tiaden, B. Nestler, H.-J. Diepers and I. Steinbach, Physica D 115, **73** (1998).

[Tiller 53]   W. A. Tiller, K. A. Jackson, J. W. Rutter and B. Chalmers, Acta Met. **1**, 428 (1953).

[Townsend 95]   H. E. Townsend and A. R. Borzillo, in *Galvatech '95 Conf. Proc.*, 171 (ISS, Warrendale PA, 1995).

[Trivedi 94]   R. Trivedi and W. Kurz, Int. Mat. Rev. **39**, 49 (1994).

[Utter 02]   B. Utter and E. Bodenschatz, Phys. Rev. E **66**, 051604_1 (2002).

[Vegard 21]   L. Vegard, Z. Phys **5**, 17 (1921).

[Van Haaften 02]   W. M. Van Haaften, B. Magnin, W. H. Kool and L. Katgerman, Met. Mat. Trans. A **33**, 1971 (2002).

[Wagner 04]   A. Wagner, B. A. Shollock and M. McLean, Mat. Sci. Eng. A **374**, 270 (2004).

[Warren 95]   J. A. Warren and W. J. Boettinger, Acta Mater. **43**, 689 (1995).

[Wehling 99]   B. Wehling, R. Hüttner and A. Angerbauer, La Revue de Métallurgie **96-1**, 57 (1999).

[Werkstoff 05]   Werkstoff-Datenblatt, CuZn39Pb3, Deutsches Kupferinstitut, www.kupfer-institut.de (2005).

[Willis 98]   D. J. Willis, in *Galvatech '98 Conf. Proc.*, 337 (ISIJ, Chiba, 1998).

[Woodruff 73]   D. P. Woodruff, *The solid-liquid interface*, (Cambridge University Press, London, 1973).

[Yefimov 04]   S. Yefimov, E. Van der Giessen and I. Groma, Modeling Simul. Mater. Sci. Eng. **12**, 1069 (2004).

[Zytkiewicz 02]   Z. R. Zytkiewicz, Thin Solid Films **412**, 37 (2002).

CURRICULUM VITAE

Christoph Niederberger

born: March 28, 1979

place of birth: Stans (NW), Switzerland

Education

1998-2003   Master in Materials Science and Engineering,
                  Ecole Polytechnique Fédérale de Lausanne, Lausanne, Switzerland

2000-2001   Studies in Materials Science and Engineering, exchange student program
                  Carnegie Mellon University, Pittsburgh PA, USA

Professional activities

2002-2003   Trainee, Process Technologies Group, Technology Center,
                  ALSTOM Switzerland, Baden, Switzerland

2003-2007   Research assistant / PhD student, Computational Materials Laboratory,
                  Ecole Polytechnique Fédérale de Lausanne, Lausanne, Switzerland